

REDUCTION AND RECONSTRUCTION
METHODS FOR SIMULATION AND CONTROL OF
FLUIDS

ZHANHUA MA

A DISSERTATION
PRESENTED TO THE FACULTY
OF PRINCETON UNIVERSITY
IN CANDIDACY FOR THE DEGREE
OF DOCTOR OF PHILOSOPHY

RECOMMENDED FOR ACCEPTANCE
BY THE DEPARTMENT OF
MECHANICAL AND AEROSPACE ENGINEERING

ADVISOR: CLARENCE W. ROWLEY

NOVEMBER 2010

UMI Number: 3435965

All rights reserved

INFORMATION TO ALL USERS

The quality of this reproduction is dependent upon the quality of the copy submitted.

In the unlikely event that the author did not send a complete manuscript and there are missing pages, these will be noted. Also, if material had to be removed, a note will indicate the deletion.



UMI 3435965

Copyright 2010 by ProQuest LLC.

All rights reserved. This edition of the work is protected against unauthorized copying under Title 17, United States Code.



ProQuest LLC
789 East Eisenhower Parkway
P.O. Box 1346
Ann Arbor, MI 48106-1346

© Copyright by Zhanhua Ma, 2010. All rights reserved.

Abstract

In this thesis we develop model reduction/reconstruction methods that are applied to simulation and control of fluids. In the first part of the thesis, we focus on development of dimension reduction methods that compute reduced-order models (at the order of $10^{1\sim 2}$) of systems with high-dimensional states (at the order of $10^{5\sim 8}$) that are typical in computational fluid dynamics. The reduced-order models are then used for feedback control design for the full systems, as the control design tools are usually applicable only to systems of order up to 10^4 .

First, we show that a widely-used model reduction method for stable linear time-invariant (LTI) systems, the approximate balanced truncation method (also called balanced POD), yields identical reduced-order models as Eigensystem Realization Algorithm (ERA), a well-known method in system identification. Unlike ERA, Balanced POD generates sets of modes that are useful in controller/observer design and systems analysis. On the other hand, ERA is more computationally efficient and does not need data from adjoint systems, which cannot be constructed in experiments and are often costly to construct and simulate numerically. The equivalence of ERA and balanced POD leads us to further design a version of ERA that works for unstable (linear) systems with one-dimensional unstable eigenspace and is equivalent to a recently developed version of balanced POD for unstable systems.

We consider further generalization of balanced POD/ERA methods for linearized time-periodic systems around an unstable orbit. Four algorithms are presented: the lifted balanced POD/lifted ERA and the periodic balanced POD/periodic ERA. The lifting approach generates a LTI reduced-order model that updates the system once every period, and the periodic approach generates a periodic reduced-order model. By construction the lifted ERA is the most computationally efficient algorithm

and it does not need adjoint data. By removing periodicity in periodic balanced POD/ERA algorithms, they can be applied to linear time-varying systems.

A motivating and model problem of stabilization of an unstable vortex shedding cycle with high average lift is then shown as an application of the lifted ERA method. We consider the flow past a flat plate at a post-stall angle of attack with periodic forcing at the trailing edge. The Newton-GMRES method is used to find a high-lift unstable orbit at a forcing period slightly larger than the natural period. A six-dimensional reduced-order model is constructed using lifted ERA to reconstruct the full (with a dimension about 1.4×10^5) linearized input-output dynamics about the orbit. An observer-based feedback controller is then designed using the reduced-order model. Simulation results show that the controller stabilizes the unstable orbit, and the reduced-order model correctly predicts the behavior of the full simulation.

The second part of the thesis addresses a different type of reduction, namely symmetry reduction. In particular, we exploit symmetries to design special numerical integrators for a general class of systems (Lie-Poisson Hamiltonian systems) such that conservation laws, such as conservation of energy and momentum, are obeyed in numerical simulations. The motivating problem is a system of N point vortices evolving on a sphere that possesses a Lie-Poisson Hamiltonian structure. The design approach is a variational one at the Hamiltonian side that directly discretizes the corresponding Lie-Poisson variational principle, in which the Lie-Poisson system is regarded as a system reduced from a full canonical Hamiltonian system by symmetry. A modified version of Lie-Poisson variational principle is also proposed in this work. By construction the resulting integrators will not only simulate the Lie-Poisson dynamics, but also reconstruct some dynamics for the full system or the dual system (the so called Euler-Poincaré reduced Lagrangian system). The in-

tegrators are then applied to a free rigid body rotation problem and to simulations of the dynamics of N point vortices on a sphere. Numerical results show that some of the integrators preserve the conservative quantities well in these applications.

Acknowledgments

First and foremost, I would like to thank my advisor Professor Clancy Rowley for his constant guidance and support over the years. Whenever I needed help, Clancy was always willing to spend hours with me discussing research problems in detail. I am also grateful for the constant encouragement and great research freedom Clancy has provided, without which my thesis would not be as topically diverse as it is. Last but not least, I am deeply indebted to Clancy for his patient teaching on coding, writing papers, collaboration, presentation, and even Matlab and L^AT_EX skills.

I would like to thank my readers Professor Philip Holmes and Professor Alexander Smits for their helpful comments, and Professor Naomi Leonard and Professor Luigi Martinelli for being my examiners. I am grateful for my former advisors Professor Zhuoping Yu and Professor Banavara Shashikanth for their support and encouragement over the years.

I would like to thank Professor Gilead Tadmor and Professor Tim Colonius for their valuable comments and suggestions on my project of feedback flow control using reduced-order models. I am also thankful for Dr. Won Tae Joe for help on setting up the flow control actuator in the numerical solver. I would like to thank Professor Jerrold Marsden and Dr. Nawaf Bou-Rabee for their insightful suggestions and comments on the Lie-Poisson integrators.

I always enjoyed the collaborative atmosphere in Professor Rowley's group. In particular, I would like to thank Dr. Sunil Ahuja (now at UTRC) and Dr. Miloš Ilak (now at KTH) not only for many helpful and inspirational discussions but also for sharing up and down moments over the years. I am grateful for Dr. Kunihiro (Sam) Taira (now at Honda), Dr. Sunil Ahuja, Steven Brunton and Jonathan Tu for the immersed boundary solver (both the Fortran and C++ versions) and related post-

processing modules, such as the Arnoldi iteration method in C++ by Jonathan. Professor Mingjun Wei (now at New Mexico State University) also provided helpful comments and suggestions when he was here. Thanks to Sunil and Steve for feedback on my thesis drafts of some chapters. Additionally, I always enjoyed the time we spent together for beer and wings at the Ivy Inn.

Special thanks to my Graduate Administrators Jessica O’Leary (now at the Bendheim Center for Finance) and Jill Ray for their tremendous help all the time, and special thanks to Bill Wichser for invaluable computing support almost twenty-four hours a day, seven days a week.

I am grateful to the support from my friends here in Princeton, in Shanghai and in many other places in the world. Finally, I would not have reached this point without the invaluable support from my family all the time. I dedicate this dissertation to my parents and my sister.

I gratefully acknowledge the support of this work by NSF Grant CMS-0347239, AFOSR Grants FA9550-05-1-0369 and FA9550-07-1-0127, the Princeton University first-year graduate fellowship, and the Daniel & Florence Guggenheim Foundation Fellowship awarded by the MAE department. This dissertation carries the number T-3223 in the records of the Department of Mechanical and Aerospace Engineering.

Dedicated to my parents and my sister.

Contents

Abstract	iii
Acknowledgements	vi
Contents	ix
List of Figures	xiv
List of Tables	xvii
1 Overview	1
1.1 Motivation	1
1.1.1 Model reduction methods for feedback flow control	2
1.1.2 Geometric integrators for Lie-Poisson Hamiltonian systems: a variational approach	4
1.2 Outline and contributions	6
2 Background: Balanced truncation for model reduction of linear time-invariant systems	9
2.1 Petrov-Galerkin projection approach applied to linear systems . . .	11
2.2 Exact balanced truncation	16
2.2.1 Balanced truncation for unstable systems.	18
2.3 Snapshot-based approximate balanced truncation (balanced POD) .	19
2.3.1 Outline of the balanced POD algorithm	20

2.3.2	Method of output projection for systems with high-dimensional outputs	23
2.3.3	Balanced POD for unstable systems	24
2.4	Challenges to balanced truncation methods	25
2.5	Summary	28
3	Adjoint-free snapshot-based balanced truncation for linear time-invariant systems	30
3.1	Eigensystem realization algorithm as adjoint-free snapshot-based approximate balanced truncation	32
3.1.1	The eigensystem realization algorithm	32
3.1.2	Theoretical equivalence between ERA and balanced POD . .	34
3.1.3	Comparison between ERA and balanced POD	35
3.2	A modified ERA method using pseudo-adjoint modes	39
3.2.1	Transformed approximate Gramians	40
3.3	A numerical example: two-dimensional flow past a flat plate	44
3.3.1	Model problem and parameters	44
3.3.2	Input and output	45
3.3.3	Reduced-order models	46
3.3.4	Model performance	49
3.4	ERA for neutrally stable/unstable systems	53
3.5	Summary	56
4	Snapshot-based balanced truncation for linear time-periodic systems	58
4.1	Motivation and background	58

4.2	Snapshot-based balanced truncation for periodic systems, using a lifting approach	61
4.2.1	The lifting approach	61
4.2.2	Factorization of empirical Gramians using snapshot-based matrices	63
4.2.3	Balanced truncation using the method of snapshots	66
4.2.4	Output projection method	68
4.2.5	Algorithm summary: the lifted BPOD	72
4.2.6	The neutrally stable/unstable case	73
4.3	An alternative algorithm: a periodic approach	75
4.3.1	The neutrally stable/unstable case	77
4.3.2	Comparison with the lifting approach	79
4.4	Numerical examples	80
4.4.1	Example 1: A randomly generated system	80
4.4.2	Example 2: Application to the Ginzburg-Landau equation (a neutrally stable case)	82
4.5	ERA for linear time-periodic systems	86
4.5.1	Lifted ERA for linear time-periodic systems	88
4.5.2	Periodic ERA for linear time-periodic systems	90
4.6	Summary	93

5 Feedback control of flow past a flat plate with open-loop periodic forcing 95

5.1	Main procedures of the model-based feedback control design approach	96
5.1.1	Step I: Solve for periodic orbits by using the Newton-GMRES method	99

5.1.2	Step II: The linearized time-periodic system with an affine control input	102
5.1.3	Step III: Snapshot-based approximate balanced truncation for the linearized time-periodic system	106
5.1.4	Step IV and V: Observer-based feedback control design and implementation.	108
5.2	Observer-based feedback control results	112
5.2.1	Stable and unstable periodic orbits	112
5.2.2	Reduced-order models	114
5.2.3	Observer-based feedback control results	120
5.3	Summary	124
6	Variational Lie-Poisson Hamiltonian integrators	125
6.1	Introduction	125
6.2	Background: Lie-Poisson systems	127
6.2.1	Preliminaries	127
6.2.2	Conservation laws	130
6.2.3	Lie-Poisson Variational Principle	130
6.2.4	Why variational Lie-Poisson integrators?	131
6.3	Variational Lie-Poisson integrators on $G \times \mathfrak{g}^*$	133
6.4	Variational Lie-Poisson integrators on $\mathfrak{g} \times \mathfrak{g}^*$	142
6.5	Lie-Poisson integrators on \mathfrak{g}^* based on discretized variational principles	148
6.5.1	Integrators on \mathfrak{g}^* based on the Lie-Poisson variational principle	148
6.5.2	Integrators on \mathfrak{g}^* based on a modified Lie-Poisson variational principle	151
6.6	Numerical examples	155
6.6.1	Example 1: Free Rigid Body Rotation	155

6.6.2	Example 2: Dynamics of N point vortices on a sphere	159
6.7	Summary	169
7	Conclusions and future work	172
7.1	Conclusions	172
7.2	Future research directions	174
A	Equivalence between the ROM for projected stable dynamics and the stable part of a ROM for the full unstable system	177
B	Periodic balanced truncation for linear time-periodic systems: the neutrally stable/unstable case	179
C	Proofs of preservation of a symplectic two-form along a Lie-Poisson flow.	185

List of Figures

3.1	Transformed Gramian matrices.	43
3.2	Flow past a plate example: the stable steady state and the actuator.	45
3.3	First two primal and adjoint/pseudo-adjoint modes.	48
3.4	Comparison of Gramians.	49
3.5	2-norm error plots for the reduced-order models.	51
3.6	The first output from the impulse-response simulation.	51
3.7	Singular-value plots.	52
4.1	Primal and adjoint impulse-response simulations for the lifting approach.	65
4.2	Primal impulse-response simulations for the periodic approach.	76
4.3	Example 1: Error plots for lifting and periodic approaches.	82
4.4	Example 1: T -periodic vs time-invariant output projection.	82
4.5	Example 2: Nonlinear and linearized GL dynamics.	85
4.6	Example 2: 2-norm error plots for reduced GL by lifted BPOD.	86
4.7	Example 2: Error plots for reduced GL by lifted BPOD.	87
4.8	Input-output impulse-response simulations for the lifted ERA.	90
4.9	Input-output impulse-response simulations for the periodic ERA.	91
5.1	Schematic of control system setup.	104

5.2	Feedback control block diagram for the reduced-order model.	109
5.3	Feedback control block diagram for the full linearized model.	111
5.4	Feedback control block diagram for the full nonlinear model.	112
5.5	The stable periodic orbit for the baseline actuation-free case.	112
5.6	The lift coefficient trajectory for $T_f = T_0$ case.	114
5.7	Orbit I: The unstable periodic orbit at period $T_f = 1040$ time steps.	114
5.8	Orbit II: The stable periodic orbit at period $T_f = 1040$ time steps.	115
5.9	Transiton from Orbit I to Orbit II	115
5.10	Vorticity fields of orbit I and II at time phase 0.	116
5.11	Impulse responses with unprojected and project initial conditions.	117
5.12	Reduced-order model properties.	118
5.13	Impulse-response outputs of the reduced and full linear system.	120
5.14	Observer-based feedback control on the reduced-order model and the full linear system.	122
5.15	Stabilization of the unstable periodic orbit I.	123
6.1	Relations between Euler-Lagrange, canonical Hamiltonian, Euler- Poincaré and Lie-Poisson systems.	129
6.2	The almost commuting cube that links the full/reduced Lagrangian/Hamil- tonian sides in both continuous and discrete domains.	140
6.3	Relations between Euler-Poincaré (E-P) systems, Lie-Poisson (L-P) systems, VEP on \mathfrak{g} and VLP on $\mathfrak{g} \times \mathfrak{g}^*$	147
6.4	Free rigid body example: Evolution of conserved quantities in simu- lations.	159
6.5	Free rigid body example: The trajectories of $\Pi(t)$ versus time.	160
6.6	Free rigid body example: Error plots.	160
6.7	6-point vortex on a sphere example: The inclined ring case.	166

6.8	6-point vortex on a sphere example: The trajectory of each vortex. .	166
6.9	6-point vortex on a sphere example: Evolution of conserved quantities in simulations.	168
6.10	6-point vortex on a sphere example: The trajectory of the first point vortex versus time.	169
6.11	6-point vortex on a sphere example: Simulation results of the MLP on \mathfrak{g}^* with $\beta = 1/2$	170
6.12	6-point vortex on a sphere example: Error plots.	171

List of Tables

3.1	Comparison of the computational costs of approximate balanced truncation and ERA.	47
-----	---	----

Chapter 1

Overview

1.1 Motivation

From the dynamical systems point of view, research problems in fluid dynamics are challenging often due to the highly nonlinear dynamics described by the governing differential equations. Closed-form analytical solutions are rarely available in engineering applications. However, in many fluid dynamics problems, the flow is dominated by low-dimensional coherent structures (Holmes *et al.*, 1996), or there are symmetries in the models such that the dynamics obey certain conservational laws (Arnold, 1998; Marsden & Ratiu, 1994). Mathematical tools developed in dynamical systems, control theory and geometric mechanics can be applied to these problems to extract the key coherent structures and conservational laws, and in turn substantially simplify the problems. On the other hand, to solve problems that arise in fluid dynamics, the existing mathematical tools are often not directly applicable or sufficient, and new tools need to be developed. The interactive iteration between solving specific problems in fluid dynamics and development of general

mathematical tools has been our main research interest. In particular, in this thesis we consider reduction and reconstruction methods with application to simulation and control of fluids.

1.1.1 Model reduction methods for feedback flow control

In a broad sense, flow control “refers to any mechanism that manipulates a fluid flow into a state with desired flow properties” (Kim & Bewley, 2007) for purposes of, among many others, drag reduction, lift enhancement, noise/vibration reduction, and mixing enhancement. Considering the practically limited energy resources and the huge amount of fuel consumption in transportation on our planet, flow control has been not surprisingly one of the most active research areas in fluid dynamics in the last a few decades; see Gad-el Hak (2000) for early developments. In the last decade, besides developments in passive control and open-loop active control, closed-loop (feedback) active control has become the main research focus (Kim & Bewley, 2007; Cattafesta *et al.*, 2008; Choi *et al.*, 2008; Sipp *et al.*, 2010), thanks to fast developments in flow control actuators and sensors in experiments, as well as increasing modeling and computation power in simulations. Among other feedback control methods, model-based feedback control makes it possible to apply sophisticated control design tools from modern control theory. The challenge, however, is that those tools are often directly applicable only to systems with dimension not higher than 10^4 , while dynamic models in computational fluid dynamics are typically at the order of $10^{5\sim 8}$. One solution is to develop reduced-order models (at the order of $10^{1\sim 2}$) that capture the dominant low-dimensional coherent structures (if they exist) and in turn accurately reconstruct the input-output dynamics of the full systems. Based on these models, one can design model-based feedback control laws for the full systems. This reduced-order model based feedback control design

approach has been applied to a variety of problems of flow control about steady states, e.g. stabilization of globally unstable flow (Henningson & Åkervik, 2008), suppression of transition to turbulence (Ilak, 2009), noise reduction in cavity flow (Rowley & Juttijudata, 2005; Samimy *et al.*, 2007), drag reduction in boundary layers (Bagheri *et al.*, 2009a), and stabilization of an unstable steady state and suppression of vortex shedding behind a flat plate (Ahuja & Rowley, 2010).

As a generalization to model reduction methods for feedback control around steady states, in this thesis we develop model reduction methods for high-dimensional periodic systems (Chapter 4), and then realize model-based feedback control of periodic orbits found in systems governed by Navier-Stokes equations (Chapter 5). Besides theoretical interest, in practice, control of unstable periodic orbits can serve as a starting point for chaos control and control of turbulent flows. Also, recent research results (Joe *et al.*, 2008; Taira *et al.*, 2010) show that periodic forcing at the trailing/leading edge of an airfoil can result in high-lift periodic orbits. It is thus desirable to realize feedback control that can enlarge the region of attraction of the stable orbits, speed up convergence to the stable orbits, or stabilize the unstable orbits. Besides the model reduction methods and feedback control design, we will also introduce a necessary intermediate step on how to find unstable periodic orbits in such high-dimensional systems.

Another important topic in model reduction is to improve the methods such that they are more computationally efficient and easily applicable in both simulations and experiments. In fact, in experiments certain types of data, such as data from adjoint systems, are not available, which restricts the use of those otherwise efficient methods, among which we will focus on the snapshot-based approximate balanced truncation method (Rowley, 2005). We will devote Chapter 3 and parts of Chapter 4 to this topic.

1.1.2 Geometric integrators for Lie-Poisson Hamiltonian systems: a variational approach

In the second topic in this thesis, we consider the application of a different type of system reduction/reconstruction method that is based on symmetry to simulations for inviscid fluids. In particular, we develop special integrators for Lie-Poisson Hamiltonian systems and apply them to simulations of dynamics of N point vortices on a sphere, such that the conservation laws are preserved at the discrete level.

The point vortex model was introduced by Helmholtz (1858) more than one and half centuries ago. In the past two decades, by using tools developed in dynamical systems, geometric mechanics and numerical analysis, researchers have concluded a number of substantial results on the dynamics of N point vortices (Newton, 2001). For the dynamics of N point vortices in the plane, whose canonical Hamiltonian structure was introduced by Kirchhoff (1876), the non-integrability and chaotic dynamical behavior for general $N > 3$ cases has been noticed and studied in detail since the early 1980's (Ziglin, 1980; Aref & Pomphrey, 1982). The dynamics of N point vortices on a spherical shell with radius R is a generalization of the planar case (in which R is infinite) and an important topic in geophysical fluid dynamics modeling long time evolution of atmospheric and oceanographic flows with coherent structures. The equations of motion are presented in Bogomolov (1977) (almost precisely one century after Kirchhoff (1876)). In the last several decades much theoretical analysis on the problem of N point vortices on the sphere has been performed, especially on the integrability/non-integrability, and fixed and relative equilibria and their stability. See, for example, the introduction and references in Newton (2001, 2010).

The N -vortex on a sphere system possesses a Lie-Poisson Hamiltonian structure

(Pekarsky & Marsden, 1998). Due to the non-integrability and complex nonlinear feature of a general system of N point vortices, further understanding on this topic naturally requires applications of numerical techniques. However, most commonly used ODE integrators, such as the standard Runge-Kutta fourth order methods, can not correctly capture the qualitative behavior of the system. More precisely, during simulations using those integrators, the Hamiltonian structure of the system of N point vortices is not preserved, and some important theoretically conserved quantities of the system, such as the Hamiltonian function, also drift unboundedly. It is thus desirable to develop *geometric integrators* to preserve some or all of the geometric properties along the solution flows in numerical simulations. For the planar N point vortices problem, since the Hamiltonian structure is canonical, those geometric integrators developed for canonical Hamiltonian systems can be applied. Results include the symplectic integrators introduced in Pullin & Saffman (1991), the integrators developed by a splitting method in Zhang & Qin (1993), and the variational integrator for the planar point vortices as a degenerate Lagrangian system introduced in Rowley & Marsden (2002). However, as to the geometric simulation of point vortices on the sphere, whose Hamiltonian structure is not canonical but Lie-Poisson, to our knowledge little work has been done except that in Patrick (2000); Newton & Khushalani (2002) the splitting method (McLachlan, 1993; Reich, 1993) is applied for simulations. The application of splitting method to general Lie-Poisson systems is however restrictive, since it requires the system to have a separable Hamiltonian function.

In this work we thus develop geometric integrators for general finite-dimensional Lie-Poisson systems by using a systematic variational approach on the Hamiltonian side. In the development the Lie-Poisson systems are regarded as reduced systems resulting from symmetry reduction of canonical Hamiltonian systems. Versions of

variational principles for Lie-Poisson systems are then discretized to obtain integrators. The integrators by construction reconstruct some dynamics of the corresponding full canonical Hamiltonian systems or the dual reduced Lagrangian systems.

1.2 Outline and contributions

This thesis consists of two parts. In the first part, from Chapter 2 to Chapter 5, we present improvement and generalization to a widely used model reduction method, the snapshot-based approximate balanced truncation method (balanced POD). In Chapter 5, the generalized method is also applied to feedback control for high-lift vortex shedding cycles in a flow past an inclined plate with periodic forcing. In the second part, Chapter 6, we construct families of geometric integrators for Lie-Poisson Hamiltonian systems using a variational approach on the Hamiltonian side, such that conservational laws can be preserved at the discrete level. The algorithms are applied to simulations of N point vortices interacting on a sphere.

Detailed outline and contributions of each chapter are listed below.

Chapter 2. We present a review of projection-based model reduction methods, including the method using global eigenmodes, the POD/Galerkin method (Section 2.1), and in particular the balanced truncation method for linear time-invariant (LTI) systems (Section 2.2). We then review the snapshot-based approximate balanced truncation method, i.e., balanced POD, in Section 2.3. A list of challenging open problems is given at the end of the chapter in Section 2.4, as a guideline for our work in the next chapters.

Chapter 3. The key contribution here is, for stable LTI systems, we show that

theoretically the eigensystem realization algorithm (ERA) generates reduced-order models identical to those of balanced POD. Compared to balanced POD, the key advantage of the ERA algorithm is that it is adjoint free and computationally much more efficient. This work was done jointly with Sunil Ahuja, where MZH established the equivalence and SA validated the relation in a numerical experiment. Furthermore, in Section 3.4 a version of ERA applicable to systems with one-dimensional neutral stability/instability is also presented.

Chapter 4. The contribution here is the generalization of the balanced POD algorithm for model reduction of linear, time-periodic systems. Four algorithms, i.e., the lifted balanced POD (Section 4.2), the periodic balanced POD (Section 4.3), the lifted ERA and the periodic ERA (Section 4.5), are proposed. They are applicable to linear periodic systems with high dimensional states (at the order of $10^{5\sim 7}$) that may also have high dimensional outputs and be neutrally stable/unstable. The work on lifted balanced POD was done jointly with Gilead Tadmor, who besides other insightful discussions also suggested the lifting approach, and how to “un-lift” the reduced-order models. Numerical experiments on the lifted/periodic balanced POD method are given in Section 4.4. The lifted/periodic ERA are by construction equivalent to lifted/periodic balanced POD in the sense that theoretically they yield identical models; however the ERA methods are adjoint-free and therefore more computationally efficient. Furthermore, the periodic balanced POD/ERA can be directly applied to linear time-varying systems by removing assumption of periodicity in computation procedures.

Chapter 5. The contribution here is that we design feedback control for stabilization of an unstable vortex shedding cycle that has a high average lift, based

on reduced-order models obtained by using lifted ERA. The model problem we consider is a two-dimensional flow past a flat, inclined plate, with an open-loop periodic forcing at the trailing edge. By using Newton-GMRES method for periodic systems, we first show that there exist high-lift stable and unstable periodic solutions for the system with open-loop periodic forcing. After linearization around the unstable orbit, we apply the lifted ERA method to obtain reduced-order models. A reduced-order model is used to reconstruct the input-output dynamics of the full linearized system, based on which an observer-based feedback controller is designed. The controller is then applied onto the full linearized model and finally onto the full nonlinear model to stabilize the unstable orbit.

Chapter 6. The contribution here is a systematic development of three families of geometric integrators for Lie-Poisson Hamiltonian systems, using a variational approach on the Hamiltonian side. While designing the integrators, we consider Lie-Poisson systems as reduced systems of full canonical Hamiltonian systems, and some integrators also numerically reconstruct part of the full dynamics. These integrators are applicable to geometric simulations of Lie-Poisson Hamiltonian systems, including those that are computationally difficult or impossible to be transformed into the corresponding Lagrangian (i.e., Euler-Poincaré) formation. Numerical examples, one on a free rigid body rotation simulation and the other on the simulation of N point vortices on a sphere, are presented to validate the algorithms.

Chapter 7. The conclusions of this work and outlook for future work are presented in this final chapter.

Chapter 2

Background: Balanced truncation for model reduction of linear time-invariant systems

In the area of model-based feedback flow control of fluids, substantial developments have taken place in the last decade. For instance, see the recent reviews by Kim & Bewley (2007); Cattafesta *et al.* (2008); Choi *et al.* (2008); Sipp *et al.* (2010). In many applications, the focus is on how to apply actuation to maintain the flow around a steady state or an orbit of interest, for instance to delay transition to turbulence, or control separation on a bluff body. Model-based linear control theory provides efficient tools for the analysis and design of feedback controllers, such as Linear-Quadratic Regulator (LQR) and Linear-Quadratic-Gaussian (LQG). However, a significant challenge is that models for flow control problems are often very high dimensional, e.g., on the order of $\mathcal{O}(10^{5\sim 9})$, so large that it becomes computationally infeasible to apply linear control techniques. To address this issue, model reduction, by which a low-order approximate model is obtained, is therefore widely

employed.

Among other model reduction techniques, such as singular perturbation and Hankel norm reduction methods, the projection-based method is a widely used approach, which involves projecting a model onto a set of modes. These may be global eigenmodes of a linearized operator (Åkervik *et al.*, 2007), modes determined by proper orthogonal decomposition (POD) of a set of data (Holmes *et al.*, 1996), and variants of POD, such as including shift modes (Noack *et al.*, 2003). In particular, an efficient projection-based method for linear control systems is balanced truncation (Moore, 1981). Compared to most other methods, including POD, balanced truncation has key advantages, such as *a priori* error bounds, and guaranteed stability of the reduced-order model (if the original high-order system is stable). While this method is computationally intractable for systems with very large state spaces (dimension $\gtrsim 10^5$), recently an algorithm for computing approximate balanced truncation from snapshots of linearized and adjoint simulations has been developed (Rowley, 2005) and successfully applied to a variety of high-dimensional (for instance, up to 10^7) flow control problems (Ilak & Rowley, 2008; Ahuja & Rowley, 2010; Bagheri *et al.*, 2009a). In this method, sometimes called balanced POD, one obtains two sets of modes (primal and adjoint) that are bi-orthogonal, and uses those for projection of the governing equations. Balanced POD typically produces models that are far more accurate and efficient than standard POD models, in the sense that the number of modes needed to capture the dynamics in balanced POD is much less than that in POD. Detailed comparisons can be found in Rowley (2005) and Ilak & Rowley (2008). For instance, in Ilak & Rowley (2008), a 3-mode balanced POD model captures the transient growth in a linearized channel flow nearly perfectly, while for a standard POD model, 17 modes were required.

In this chapter we will first review the main idea of projection-based model reduction

and introduce several widely used projection-based model reduction methods in Section 2.1. Then, in particular, we will focus on the method of balanced truncation in Section 2.2 and 2.3. Review of existing balanced truncation algorithms leads to a list of interesting challenges and open problems (not complete in any sense) in Section 2.4. The list will serve as a starting point for further improvement and generalization of the algorithms, which is our main task in the following three chapters.

2.1 Petrov-Galerkin projection approach applied to linear systems

For discussions in this and next chapter, we will consider a discrete-time, high-dimensional, linear time-invariant (LTI) system, described by

$$\begin{aligned} x(k+1) &= Ax(k) + Bu(k) \\ y(k) &= Cx(k), \end{aligned} \tag{2.1}$$

where the high-dimensional state $x(k) \in \mathbb{C}^n$ can be, for instance, flow variables at all gridpoints of a simulation, $k \in \mathbb{Z}$ is the time step index, $u(k) \in \mathbb{C}^p$ a vector of inputs (for instance, actuators or disturbances), and $y(k) \in \mathbb{C}^q$ a vector of outputs (for instance, sensor measurements, or other measurable quantities as linear functions of the state). We consider a discrete-time setting, because data from numerical simulations or experiments are essentially discrete in time. This system may arise, for instance, by discretizing the Navier-Stokes equations in time and space, and linearizing about a steady solution, as will be demonstrated in the example in Section 3.3. The system (2.1) is *asymptotically stable* (and indeed *exponentially stable*) if the spectral radius $\rho(A) < 1$, i.e., all eigenvalues of A are located inside a

unit circle. It is *neutrally stable* or *unstable* if $\rho(A) = 1$, or $\rho(A) > 1$, respectively.

In this work, the goal of model reduction, especially for feedback control design purposes, is to obtain an approximate model that captures the dynamic relationship between inputs u and outputs y , but with a much smaller state dimension:

$$\begin{aligned} x_r(k+1) &= A_r x_r(k) + B_r u(k) \\ y(k) &= C_r x_r(k), \end{aligned} \tag{2.2}$$

where the reduced state variable $x_r(k) \in \mathbb{C}^r$, $r \ll n$.

In particular, we consider a standard *Petrov-Galerkin projection* approach that forms reduced order models (2.2) by projections onto a r -dimensional subspace spanned by columns of a matrix $\Phi_r \in \mathbb{C}^{n \times r}$, along a direction that is orthogonal to a r -dimensional subspace spanned by columns of another matrix $\Psi_r \in \mathbb{C}^{n \times r}$. The bases Φ_r, Ψ_r are bi-orthogonal, i.e.,

$$\Psi_r^* \Phi_r = I_{r \times r}, \tag{2.3}$$

where the asterisk denotes an adjoint matrix satisfying the inner product relations $\langle a, \Psi_r b \rangle_{\mathbb{C}^n} = \langle \Psi_r^* a, b \rangle_{\mathbb{C}^r}$, for $a \in \mathbb{C}^n, b \in \mathbb{C}^r$. With the approximation $x(k) \approx \Phi_r x_r(k)$ at every time k , and applying the bi-orthogonality relation (2.3), one generates reduced-order models of the form

$$\begin{aligned} x_r(k+1) &= \Psi_r^* A \Phi_r x_r(k) + \Psi_r^* B_r u(k) \\ y(k) &= C_r \Phi_r x_r(k). \end{aligned} \tag{2.4}$$

This bi-orthogonal projection approach can be also used for model reduction of non-linear systems. When $\Psi_r = \Phi_r$, the Petrov-Galerkin projection is just an orthogonal Galerkin projection.

Different projection-based model reduction methods employ different bases Φ and Ψ (“modes”) and in turn generate different reduced-order models. The most widely

applied projection-based methods include: (i) method using global eigenmodes (Åkervik *et al.*, 2007), (ii) proper orthogonal decomposition (POD)/Galerkin approach (Holmes *et al.*, 1996), and (iii) balanced truncation (Moore, 1981). In this subsection we briefly review the first two methods in the following discussion to understand their strength and weakness as model reduction methods. See Barbagallo *et al.* (2009) for a detailed comparison of performance among these methods in a problem of closed-loop control of an open cavity flow.

Petrov-Galerkin Projection using global eigenmodes. The global eigenmode approach has been applied to construct reduced-order models for stability analysis and control for Navier-Stokes systems, such as for cavity flows (Åkervik *et al.*, 2007; Barbagallo *et al.*, 2009), for flow over a smooth bump (Ehrenstein & Gallaire, 2008), and for the Blasius boundary layer (Henningson & Åkervik, 2008). Global eigenmodes and the corresponding adjoint modes are indeed the right and left eigenvectors of the state transition matrix A . By using the bi-orthogonal global eigenmodes and adjoint modes for projection, one obtains a reduced-order model (2.4) where the reduced transition matrix $A_r = \Psi_r^* A \Phi_r$ is a diagonal matrix of leading eigenvalues of A , supposing there are no repeated eigenvalues. By construction, this eigenmode approach generates a reduced-order model that captures well the uncontrolled *system dynamics* described by

$$x(k+1) = Ax(k), \quad (2.5)$$

and therefore suits best for stability analysis of a steady state, about which the linear system (2.1) is obtained by linearization. However, since the projection does not include any information about the control input (characterized by B) and the system output (characterized by C), it is not a natural choice as a model reduction method to capture the input-output dynamics. Indeed, the system dynamics is the

“internal” dynamics, and important modes for stability analysis might be difficult to be excited or suppressed by control inputs, or to be observed through system outputs. On the other hand, the important modes for control or measurement purposes might be negligible in stability analysis.

As to numerics, for high-dimensional linear systems such as those obtained by linearizing Navier-Stokes equations about a steady state, the eigenmodes can be computed by Krylov methods, e.g. the Arnoldi iteration method (Trefethen & Bau, 1997; Lehoucq *et al.*, 1998).

Note that recently Rowley *et al.* (2009) presented a spectral analysis for nonlinear flows using Koopman modes, which can be regarded as a nonlinear generalization of global eigenmodes of a linearized system.

POD/Galerkin approach. Proper orthogonal decomposition, also known as principal component analysis or Karhunen-Loève transformation, was first introduced to the fluids community by Lumley (1967, 1970). It has since been widely used in fluid problems for study of dominant, low-dimensional coherent structures and model reduction (see Sirovich (1987); Aubry *et al.* (1988); Moin & Moser (1989); Holmes *et al.* (1996), among others); see recent surveys on a variety of applications of the POD/Galerkin approach to model reduction and control in fluids in Siegel *et al.* (2008); Barbagallo *et al.* (2009). Theoretical details of this approach can be found in Sirovich (1987); Holmes *et al.* (1996).

POD provides an *orthogonal* set of modes. Reduction of the original linear or nonlinear system is realized by an orthogonal, Galerkin projection using the leading modes. In typical applications, the POD modes are the leading orthonormal eigenvectors of XX^* , where the columns of X are the snapshots taken from simulations

of the original system. By construction, the POD models can be computed directly from experimental data, and can be applied to both nonlinear and linear systems.

POD modes are optimal in the sense that the orthogonal projection using these modes captures the most *energy* in the snapshots (Holmes *et al.*, 1996). Modes are ranked by their inherent energy content. However, reduced-order models obtained by the POD/Galerkin approach do not necessarily capture the input-output *dynamics* of the original system, as the most important modes for control or measurement purposes can be of very small energy, as shown in Smith *et al.* (2005); Ilak & Rowley (2008). For linear systems as (2.1), if the snapshots are taken from impulse-response simulations, then the leading POD modes will contain the most important modes for capturing the actuation (Rowley, 2005), as the simulation data includes B, AB, \dots , the information on how the system will be excited by actuations. However, the POD modes may still not capture the influence of system outputs. Reduced-order models by POD/Galerkin approach for a linear system can be unstable even if the original system is stable (Smith, 2003). Note that variants of POD have been developed to improve the performance of reduced-order models, such as including shift modes (Noack *et al.*, 2003; Siegel *et al.*, 2003; Luchtenburg *et al.*, 2009; Tadmor *et al.*, 2010), double POD (Siegel *et al.*, 2008), and calibration methods applied to POD (Galletti *et al.*, 2004; Couplet *et al.*, 2005; Cordier *et al.*, 2010).

Regarding numerics, the method of snapshots (Sirovich, 1987) is widely used to compute POD modes for high-dimensional systems. The main idea of this method is that instead of solving the $n \times n$ dimensional eigenvalue problem for XX^* , one solves an eigenvalue problem for X^*X where the dimension m is much smaller, assuming the number of snapshots m is much smaller than the system dimension n , and then reconstructs a basis for an m -dimensional subspace.

Having reviewed the other major projection-based model reduction methods, we now consider the method of balanced truncation in the following paragraphs and explain why it will be our focus.

2.2 Exact balanced truncation

For a *stable* LTI system (2.1), define its controllability and observability Gramians by a pair of symmetric, positive-semidefinite matrices

$$W_c := \sum_{i=0}^{\infty} A^i B B^* (A^i)^* ; \quad W_o := \sum_{i=0}^{\infty} (A^i)^* C^* C A^i, \quad (2.6)$$

where the asterisk $*$ stands for adjoint of a matrix. The controllability Gramian provides a measure of the influence of a sequence of input history on the current state(i.e., to what degree each state is excited by inputs), and the observability Gramian measures the influence of an initial state on future outputs with zero control input (i.e., to what degree each state excites future outputs). The larger eigenvalues of the controllability(observability) Gramian correspond to the more controllable (observable) states. Note that the Gramians are solutions of discrete Lyapunov equations:

$$\begin{aligned} A W_c A^* - W_c + B B^* &= 0; \\ A^* W_o A - W_o + C^* C &= 0. \end{aligned} \quad (2.7)$$

A balanced truncation (Moore (1981)) involves first a coordinate transformation Φ , called the balancing transformation, that can be computed by solving the eigenvalue problem

$$W_c W_o \Phi = \Phi \Sigma^2 = \Phi \begin{bmatrix} \sigma_1^2 & & \\ & \ddots & \\ & & \sigma_n^2 \end{bmatrix}, \quad (2.8)$$

where the Hankel singular values $\sigma_1 \geq \dots \geq \sigma_n \geq 0$ are invariant under coordinate transformations. The transformed Gramians $W_c \mapsto \Phi^{-1}W_c(\Phi^{-1})^*$ and $W_o \mapsto \Phi^*W_o\Phi$ are “balanced” in the sense that they are identical and diagonal:

$$\Phi^{-1}W_c(\Phi^{-1})^* = \Phi^*W_o\Phi = \Sigma.$$

A reduced-order model in the form (2.4) is then obtained in the new coordinates by truncating both the least controllable and least observable states that correspond to the smallest Hankel singular values and having little effect on the input-output behavior. Geometrically, it is obtained by considering a subspace spanned by the r leading balancing modes, i.e., the r leading columns of Φ , and projecting the dynamics (2.1) onto this subspace using the r leading adjoint modes given by leading columns of $\Psi = (\Phi^{-1})^*$.

Main features. The reduced-order, balanced model keeps the most controllable and observable states, and is therefore ideal for capturing the input-output dynamics of the original system. Quantitatively, the balanced truncation procedure guarantees an *a priori* upper bound of error between the original system and the reduced-order model:

$$\|G(t) - G_r(t)\|_\infty < 2 \sum_{k=r+1}^n \sigma_k,$$

where $G(t)$ and $G_r(t)$ are the impulse-response matrices of the original system and the reduced-order model, respectively. Another feature of balanced truncation is that the reduced-order model inherits the stability of the original system, as long as the truncation is executed at an order between two distinguished Hankel singular values. In contrast, the problem of losing stability can happen to other model reduction methods, such as reported in Smith (2003) when developing POD/Galerkin models close to a stable equilibrium. More details of exact balanced truncations

can be found in Dullerud & Paganini (1999); Zhou *et al.* (1996).

Restrictions to applications. For large-dimensional systems (e.g. on the order of $10^{6\sim 9}$) such as those arise from numerical discretization in fluid systems, to realize exact balanced truncation as above becomes computationally intractable, due to difficulties mainly in (i) solving the large-dimensional Lyapunov equations (2.7) for Gramians and storing them, and (ii) solving the large-dimensional eigenvalue problem (2.8). A snapshot-based approximate balanced truncation algorithm was therefore developed by Rowley (2005). We will review the algorithm in Section 2.3.

2.2.1 Balanced truncation for unstable systems.

Balanced truncation has been extended for linear, unstable systems (Zhou *et al.*, 1999; Ahuja & Rowley, 2010) by decomposing the system into a stable subsystem and an unstable subsystem.

If it is unstable, the system (2.1) can be decoupled into an n_s -dimensional stable subsystem and an n_u -dimensional unstable subsystem as

$$\begin{aligned} \begin{bmatrix} x_s(k+1) \\ x_u(k+1) \end{bmatrix} &= \begin{bmatrix} A_s & 0 \\ 0 & A_u \end{bmatrix} \begin{bmatrix} x_s(k) \\ x_u(k) \end{bmatrix} + \begin{bmatrix} B_s \\ B_u \end{bmatrix} u(k) \\ y(k) &= y_s(k) + y_u(k) = \begin{bmatrix} C_s & C_u \end{bmatrix} \begin{bmatrix} x_s(k) \\ x_u(k) \end{bmatrix} \end{aligned} \quad (2.9)$$

by a coordinate transformation

$$x(k) = T \begin{bmatrix} x_s(k) \\ x_u(k) \end{bmatrix} = \begin{bmatrix} T_s & T_u \end{bmatrix} \begin{bmatrix} x_s(k) \\ x_u(k) \end{bmatrix}, \quad (2.10)$$

where $T_s \in \mathbb{C}^{n \times n_s}$ and $T_u \in \mathbb{C}^{n \times n_u}$ are matrices of stable and unstable right eigen-

vectors of A . Here $A_s = (S_s^* T_s)^{-1} S_s^* A T_s^*$, $A_u = (S_u^* T_u)^{-1} S_u^* A T_u^*$, $B_s = (S_s^* T_s)^{-1} S_s^* B$, $B_u = (S_u^* T_u)^{-1} S_u^* B$, $C_s = C T_u$ and $C_u = C T_s$, where $\begin{bmatrix} S_s & S_u \end{bmatrix}^* = T^{-1}$, $S_s \in \mathbb{C}^{n \times n_s}$ and $S_u \in \mathbb{C}^{n \times n_u}$ consisting of stable and unstable left eigenvectors of A . The transformed system is decoupled, as all n_s eigenvalues of A_s are inside the unit circle, while all n_u eigenvalues are on or outside the circle.

In the new coordinates, one can realize balanced truncation on both of the subsystems respectively, as in Zhou *et al.* (1999), by defining generalized Gramians in the frequency domain for both the stable and unstable subsystem. However, in many physical applications, the unstable dynamics is of small dimension (e.g. at the order of $10^{1 \sim 2}$), and is crucial for stabilization purpose. Thus, alternatively one can choose to keep the unstable dynamics *exactly*, and just realize a usual balanced truncation of order r , $r \ll n_s$, for the n_s -dimensional stable dynamics (Ahuja & Rowley, 2010). Finally the “partially-balanced” truncated system of order $(r + n_u)$ shall be transformed back into the original coordinates. See computational details in the subsection 2.3.3.

Also note that the generalized Gramians in the frequency domain defined in Zhou *et al.* (1999) have poles on the imaginary axis if A has eigenvalues on the imaginary axis (for the continuous case). The method given in Zhou *et al.* (1999) is thus not directly applicable to the neutrally stable case.

2.3 Snapshot-based approximate balanced truncation (balanced POD)

A snapshot-based approximate balanced truncation algorithm (“*balanced POD*”) was introduced by Rowley (2005) for applications to high-dimensional LTI systems

with high-dimensional outputs or inputs. Since its introduction, balanced POD has been successfully applied in a variety of feedback flow control problems in simulations, such as suppression of transition to turbulence in a channel flow (Ilak, 2009), stabilization of unstable steady flow past a flat plate (Ahuja & Rowley, 2010), control of the convectively unstable flat-plate boundary layer (Bagheri *et al.*, 2009a), and suppression of the instability of separated flow past cavity (Barbagallo *et al.*, 2009).

2.3.1 Outline of the balanced POD algorithm

We first outline the main procedures of the algorithm:

- **Step 1:** *Collect snapshots.* Run impulse-response simulations of the primal system (2.1) and collect $m_c + 1$ snapshots of *states* $x(k)$ in $m_c P + 1$ steps:

$$X = \begin{bmatrix} B & A^P B & A^{2P} B & \dots & A^{m_c P} B \end{bmatrix}, \quad (2.11)$$

where P is the sampling period. In addition, run impulse-response simulations for the adjoint system

$$z(k+1) = A^* z(k) + C^* v(k) \quad (2.12)$$

and collect $m_o + 1$ snapshots of states $z(k)$ in $m_o P + 1$ steps:

$$Y = \begin{bmatrix} C^* & (A^*)^P C^* & (A^*)^{2P} C^* & \dots & (A^*)^{m_o P} C^* \end{bmatrix}. \quad (2.13)$$

- **Step 2:** *Compute modes by the method of snapshots.* Calculate the generalized Hankel matrix,

$$H = Y^* X. \quad (2.14)$$

Compute the singular value decomposition of H :

$$H = U\Sigma V^* = \begin{bmatrix} U_1 & U_2 \end{bmatrix} \begin{bmatrix} \Sigma_1 & 0 \\ 0 & 0 \end{bmatrix} \begin{bmatrix} V_1^* \\ V_2^* \end{bmatrix} = U_1 \Sigma_1 V_1^* \quad (2.15)$$

where the diagonal matrix $\Sigma_1 \in \mathbb{R}^{n_1 \times n_1}$ is invertible and includes all non-zero singular values of H , $n_1 = \text{rank}(H)$, and $U_1^* U_1 = V_1^* V_1 = I_{n_1 \times n_1}$. Choose $r \leq n_1$. Let U_r and V_r denote the sub-matrices of U_1 and V_1 that include their first r columns, and Σ_r the first $r \times r$ diagonal block of Σ_1 . Calculate

$$\Phi_r = X V_r \Sigma_r^{-\frac{1}{2}}; \quad \Psi_r = Y U_r \Sigma_r^{-\frac{1}{2}}. \quad (2.16)$$

where the columns of Φ_r and Ψ_r are respectively the first r primal and adjoint modes of system (2.1). The two sets of modes are bi-orthogonal: $\Psi_r^* \Phi_r = I_{r \times r}$.

- **Step 3: Petrov-Galerkin Projection.** The system matrices in the reduced order model (2.2) are computed by

$$A_r = \Psi_r^* A \Phi_r; \quad B_r = \Psi_r^* B; \quad C_r = C \Phi_r. \quad (2.17)$$

Balanced POD employs the low-rank feature of Gramians (and in turn generalized Hankel matrices) for typical high-dimensional systems modeled in physics problems. Assume the number of snapshots $m_o + 1$, $m_c + 1$ are much smaller than the system dimension n , and the input and output dimensions are moderate (see the case for high-dimensional outputs/inputs in 2.3.2). In balanced POD, the $n \times n$ controllability/observability Gramians are approximated by the empirical Gramians (Lall *et al.*, 2002)

$$W_{ce} = X X^*; \quad W_{oe} = Y Y^*. \quad (2.18)$$

The empirical Gramians themselves are never computed. Instead, only the low-rank factors X and Y are constructed by snapshots. The Hankel singular values

and balancing modes are then computed by the method of snapshots (Sirovich, 1987) that also saves much computational cost, as the $n \times n$ dimensional eigenvalue problem is reduced to a much smaller, $q(m_o + 1) \times p(m_c + 1)$ dimensional problem of SVD. The resulting reduced-order model is balanced in the sense that Φ_r and Ψ_r *exactly* balance the approximate Gramians W_{ce} and W_{oe} , as shown in Rowley (2005); see more discussion in Section 3.2.

Some historical notes. Compared to other numerical methods for balanced truncation, such as Laub *et al.* (1987); Tombs & Postlethwaite (1987); Safonov & Chiang (1989) where essentially a Cholesky decomposition is used to obtain (exact) Gramian factors, balanced POD constructs approximate factors by collecting snapshots through impulse response simulations. Therefore balanced POD is valid for high-dimensional systems that are neither controllable nor observable, which is typically the case. Note that besides the snapshot-based method, there are other low-rank, iterative methods for approximating Gramians by solving Lyapunov equations, including Krylov subspace methods (Hu & Reichel, 1992; Jaimoukha & Kasenally, 1994) and low-rank Smith (LRS) methods (Penzl, 2000; Gugercin *et al.*, 2003). An interesting observation is that, for continuous systems, the low-rank Smith method can be regarded as a special case of the snapshot-based method, in which the trapezoidal rule is used to discretize in time, as introduced by Daniel Sorenson and then mentioned in Antoulas (2005), Section 12.4.5. In this sense, the approximate balanced truncation method most similar to balanced POD is the low rank square root method presented in Penzl (2006), where the method of snapshots is used together with approximate factors of Gramians that are computed by low-rank Smith methods.

2.3.2 Method of output projection for systems with high-dimensional outputs

For a system in the form (2.1), the output dimension, q , can also be very large. For instance, the outputs can be set identical to the states (e.g. the whole flow field) for study of the system dynamics or for full-state feedback control design. In such cases, the input dimension of the adjoint system (2.12), q , will be so large that it is practically intractable to run the many adjoint simulations to collect snapshots needed for approximate balanced truncation. To solve this problem, Rowley (2005) proposed an *output projection* method. It employs a standard POD procedure to find an optimal, orthogonal projection P of rank r_{op} , $r_{op} \ll q$, such that the error between the impulse-response of the original system (2.1) and of the output projected system

$$\begin{aligned} x(k+1) &= Ax(k) + Bu(k); \\ y(k) &= PCx(k) \end{aligned} \tag{2.19}$$

is minimized. The solution is $P = \Theta\Theta^*$, where the columns of $\Theta \in \mathbb{C}^{q \times r}$ are the leading POD modes of the impulse-response matrix of the original system (2.1), i.e., the output dataset from impulse response simulations of (2.1) that can be approximated by CX , given by (2.11). The adjoint system of the output-projected system (2.19) is

$$z(k+1) = A^*z(k) + C^*\Theta v_{r_{op}}(k) \tag{2.20}$$

where the adjoint control input $v_{r_{op}}$ is only r_{op} -dimensional. Thus, by output projection, only r_{op} adjoint simulations are needed.

Note that there is a “dual” case corresponding to a linear system with high-dimension states and inputs, but only few outputs. Examples include systems with distributed disturbances that affect the entire state simultaneously. An *input projection* is then

needed to project inputs onto leading POD modes of the dataset of outputs obtained in adjoint impulse-response simulations.

2.3.3 Balanced POD for unstable systems

For high-dimensional systems with a small dimension of instability, Ahuja & Rowley (2010) suggest keeping the unstable dynamics exactly and realize balanced truncation for the high-dimensional stable dynamics, as mentioned in Section 2.2. However, in computations, the n_s -dimensional stable subsystem given in (2.9) should not be explicitly formed, due to the high computational cost to obtain the stable right and left eigenvectors of A . Instead, Ahuja & Rowley (2010) suggest directly projecting out the unstable dynamics from the full system dynamics. The first step is to compute the few unstable right and left eigenvectors of A to construct T_u and S_u , the unstable right and left eigenspaces of A . This is computationally tractable by applying Krylov methods, for example, the Arnoldi iteration method (Trefethen & Bau, 1997) to the operator A and its adjoint A^* . Then, one computes a projection operator onto $E^s(A)$, the stable subspace of A , by

$$\mathbb{P}_s = I_{n \times n} - T_u(S_u^* T_u)^{-1} S_u^*. \quad (2.21)$$

\mathbb{P}_s projects the dynamics of system (2.1) onto the stable subspace of A to produce

$$\begin{aligned} x_s(k) &= A x_s(k) + \mathbb{P}_s B u_s(k); \\ y_s(k) &= C \mathbb{P}_s x_s(k) \end{aligned} \quad (2.22)$$

where $x_s = \mathbb{P}_s x$. Correspondingly, the adjoint \mathbb{P}_s^* projects the dynamics of the adjoint system (2.12) onto $E^s(A^*)$, the stable subspace of A^* , by

$$z_s(k+1) = A^* z_s(k) + \mathbb{P}_s^* C^* v(k), \quad (2.23)$$

where $z_s = \mathbb{P}_s^* z$. Snapshot-based balanced truncation can be realized in the projected system (2.22). Note that in the impulse responses of the projected system (2.22), to suppress numerical errors accumulated in the unstable directions, one may project the states onto the stable subspace of A or A^* from time to time in simulations.

Let the columns of matrices $\Phi_{1r}, \Psi_{1r} \in \mathbb{C}^{n \times r}$ correspond to the leading r bi-orthogonal balancing and adjoint modes of the projected system (2.22). It is shown in (Ahuja & Rowley, 2010) that the reduced model of order $(r + n_u)$ for the original system (2.1) can be obtained in the form (2.4), where

$$\Phi_r = \begin{bmatrix} \Phi_{1r} & T_u \end{bmatrix}, \quad \Psi_r^* = \begin{bmatrix} \Psi_{1r}^* \\ (S_u^* T_u)^{-1} S_u^* \end{bmatrix}. \quad (2.24)$$

By using properties of left/right eigenvectors, the final reduced-order model reads

$$\begin{aligned} x_r(k+1) &= \begin{bmatrix} \Psi_{1r}^* A \Phi_{1r} & 0 \\ 0 & (S_u^* T_u)^{-1} S_u^* A T_u \end{bmatrix} x_r(k) + \begin{bmatrix} \Psi_{1r}^* \\ (S_u^* T_u)^{-1} S_u^* \end{bmatrix} B u(k); \\ y(k) &= C \begin{bmatrix} \Phi_{1r} & T_u \end{bmatrix} x_r(k), \end{aligned} \quad (2.25)$$

where $(S_u^* T_u)^{-1} S_u^* A T_u = \Lambda_u \in \mathbb{C}^{n_u \times n_u}$, a diagonal matrix with unstable eigenvalues of A , supposing there are no repeated eigenvalues.

2.4 Challenges to balanced truncation methods

Balanced truncation exhibits several useful properties: there is a guaranteed upper error bound, and the stability of the reduced-order model is guaranteed. In applications, the balanced POD algorithm can be used to realize approximate balanced truncations for high-dimensional systems that are unstable and with high-

dimensional outputs, and has been successfully applied in a variety of flow control problems, as reviewed in Section 2.3. However, balanced truncation and the balanced POD algorithm summarized above have limitations, especially in situations in which only experimental data is available. We outline several of the main challenges below. In the following three chapters, we will present techniques that address the first two challenges.

1. Snapshot-based approximate balanced truncation for experiments.

Snapshot-based approximate balanced truncation (balanced POD) requires impulse-response data from an adjoint system. However, in experiments, adjoint information is not available. This restricts the application of balanced POD to experimental data. In Section 3.1, we present an effective way to circumvent this problem by connecting the eigensystem realization algorithm to balanced POD (Ma *et al.*, 2010a).

2. Generalization to time-periodic/time-varying linear systems.

Exact and approximate balanced truncation for general linear, time-varying systems is still an open problem. Theoretical progress on this topic has been reported in, for example, Verriest & Kailath (1983); Shokoohi *et al.* (1983); Sandberg & Rantzer (2004); Sandberg (2006). The simplest form of a time-varying system is a time-periodic system. Exact and approximate balanced truncation methods for periodic systems have been developed in, e.g., Longhi & Orlando (1999); Farhood *et al.* (2005); Chahlaoui & Van Dooren (2006). However, the existing algorithms are restrictive in the sense that they are either not suitable for systems with high-dimensional states and/or outputs/inputs, or not valid for neutrally stable/unstable systems. The neutrally stable case is especially important because by Floquet theory (Hartman, 1964), linearization even about an asymptotically stable periodic orbit results in a neutrally stable

time-periodic system. Further, no applications to high-dimensional physical systems have been reported. In Chapter 4, we will present versions of balanced POD algorithms for linear time-periodic systems, as generalization of balanced POD for LTI systems, and illustrate numerical examples to validate the algorithms; in Chapter 5 we will then apply the algorithms to feedback control of flow past a flat plate with open-loop periodic forcing.

Balanced truncation for other linear systems, such as interconnected systems, has been reported in Sandberg & Murray (2007).

3. **Generalization to nonlinear systems.** Balanced truncation is a method for linear systems. Several ideas have been proposed to generalize the method to nonlinear systems, mainly using the following approaches.

The first approach is to directly project nonlinear dynamics onto modes determined by balanced truncation to a linearized system around a steady state of the nonlinear system. In a recent example using the complex Ginzburg-Landau equation (Ilak *et al.*, 2010), this approach captures well the nonlinear, transient dynamics by projecting the nonlinear complex Ginzburg-Landau equation onto balancing modes corresponding to the equilibrium at the origin. In general, however, there is no guarantee that the balancing modes for linearized systems about an equilibrium can capture the nonlinear dynamics in the whole domain. Improvements can be to add “shift modes” (Noack *et al.*, 2003) to include the influence of the mean-field, and to include balancing modes for linearized systems about other equilibria of the system and incorporate all the modes using an interpolation scheme (Morzyński *et al.*, 2006; Luchtenburg *et al.*, 2006).

The second approach is to define generalized Gramians for nonlinear systems

and then realize generalized balanced truncation, as in Scherpen (1993); Lall *et al.* (2002); Verriest & Gray (2004); Fujimoto & Tsubakino (2008). This is still a developing area, where different versions of generalized Gramians and balanced realizations exist (mainly due to the complexity of nonlinear systems). No applications to high-dimensional systems, such as problems encountered in fluids simulation and experiments, have been reported. In this thesis we will not consider the problem of nonlinear balanced truncation. However it is listed here as an interesting direction for future work.

Other interesting open problems include, e.g., robust reduced-order models by balanced truncation, and using reduced-order models for actuator/sensor optimization.

2.5 Summary

In this chapter we reviewed balanced truncation, a projection-based model reduction method that captures well the input-output dynamics of linear time-invariant control systems. In particular, the balanced POD algorithm, an snapshot-based approximate balanced truncation method, can be applied to model reduction for high-dimensional (up to the order of 10^7) linear time-invariant systems with high-dimensional outputs or inputs. Those systems need not to be controllable or observable, and can be unstable as well.

On the other hand, we list several intriguing open problems in balanced truncation in Section 2.4. In Chapter 3, we will provide a solution to the first problem, i.e., snapshot-based approximate balanced truncation for experiments, by proposing an adjoint-free balanced truncation algorithm that is suitable for application to experimental data and computationally more efficient. In Chapter 4, we will provide a

partial solution to the second problem, i.e., generalization to time-periodic/time-varying linear systems, by proposing versions of balanced truncation algorithms for linear, time-periodic systems. In Chapter 5, we then apply an algorithm developed in Chapter 4 to feedback control design for a flow past a plate with periodic forcing.

Chapter 3

Adjoint-free snapshot-based balanced truncation for linear time-invariant systems

In this chapter we consider the first challenge to balanced truncation methods listed in Section 2.4: While effective in many examples, balanced POD faces the challenge for use with experimental data. The main restriction is that balanced POD requires snapshots of impulse-response data from an adjoint system, and adjoint information is not available for experiments.

To address this issue, here we describe an algorithm widely used for system identification and model reduction, the eigensystem realization algorithm (ERA) (Juang & Pappa, 1985). This algorithm has been used for problems in fluid mechanics, primarily as a system-identification technique for flow control Cattafesta *et al.* (1997); Cabell *et al.* (2006), but also for model reduction Gaitonde & Jones (2003); Silva & Bartels (2004). Our main result, presented in Section 3.1, is that, for linear

systems, ERA theoretically produces *exactly the same* reduced-order models as balanced POD, with *no need of an adjoint system*, and at *an order of magnitude lower* computational cost. This result implies that one can realize approximate balanced truncation even in experiments, and can also improve computational efficiency in simulations. We note that ERA and snapshot-based approximate balanced truncation have been applied together in a model reduction procedure in Djouadi *et al.* (2008). However, the theoretical equivalence between these two algorithms was not explored in that work.

We present a comparison between balanced POD and ERA, and show that if adjoint information is available, balanced POD also has its own advantages. In particular, balanced POD provides sets of bi-orthogonal primal/adjoint modes for the linear system, and can be directly generalized to unstable systems. In Section 3.2, we discuss a modified ERA algorithm that, in the absence of adjoint simulations, uses “pseudo-adjoint modes” to compute reduced order models; however, this method does not produce balanced models, and performs worse than balanced POD in examples. In Section 3.3, we illustrate these methods using a numerical example of the two-dimensional flow past an inclined plate, at a low Reynolds number. Finally, in Section 3.4 we propose a version of ERA that can be applied to systems with one-dimensional instability.

Main results in Sections 3.1, 3.2 and 3.3 are reported in Ma *et al.* (2010*a*).

3.1 Eigensystem realization algorithm as adjoint-free snapshot-based approximate balanced truncation

In this section, we first summarize the steps involved in the eigensystem realization algorithm (ERA) (Juang & Pappa, 1985) and then present the main result of this Chapter, i.e., the equivalence between ERA and snapshot-based approximate balanced truncation (balanced POD).

ERA has been used both for system identification and for model reduction, and it is well known that the models produced by ERA are approximately balanced (Shokoochi & Silverman, 1987; Juang, 1994). Here we show further that, theoretically, ERA produces exactly the same reduced order models as balanced POD. This equivalence indicates that ERA can be regarded as an approximate balanced truncation method, in the sense that, before truncation, it implicitly realizes a coordinate transformation under which a pair of approximate controllability and observability Gramians are exactly balanced. This feature distinguishes ERA from other model reduction methods that first realize truncations and then balance the reduced order models. Note that in ERA the Gramians, and the balancing transformation itself, are never explicitly calculated, as we will also show in the following discussions.

3.1.1 The eigensystem realization algorithm

The eigensystem realization algorithm (ERA) was proposed in Juang & Pappa (1985) as a system identification and model reduction technique for linear time-invariant (LTI) systems. The algorithm follows three main steps (Juang & Pappa,

1985; Juang, 1994):

- **Step 1:** Run impulse-response simulations/experiments of the LTI system (2.1) for $(m_c + m_o)P + 2$ steps, where m_c and m_o respectively reflect how much effect is taken for considering controllability and observability, and P again is the sampling period. Collect the snapshots of the *outputs* y in the following pattern:

$$\begin{aligned} & (CB, \quad CAB, \quad CA^P B, \quad CA^{P+1} B, \quad \dots \\ & CA^{m_c P} B, \quad CA^{m_c P+1} B, \quad \dots \quad CA^{(m_c+m_o)P} B, \quad CA^{(m_c+m_o)P+1} B) . \end{aligned} \quad (3.1)$$

The terms $CA^k B$ are commonly called *Markov parameters*.

- **Step 2:** Construct a generalized Hankel matrix $H \in \mathbb{C}^{q(m_o+1) \times p(m_c+1)}$

$$H = \begin{bmatrix} CB & CA^P B & \dots & CA^{m_c P} B \\ CA^P B & CA^{2P} B & \dots & CA^{(m_c+1)P} B \\ \vdots & \vdots & \ddots & \vdots \\ CA^{m_o P} B & CA^{(m_o+1)P} B & \dots & CA^{(m_c+m_o)P} B \end{bmatrix}. \quad (3.2)$$

Compute the SVD of H , exactly as in (2.15), to obtain U_1 , V_1 , Σ_1 . Let $r \leq \text{rank}(H)$. Let U_r and V_r denote the sub-matrices of U_1 and V_1 that include their first r columns, and Σ_r the first $r \times r$ diagonal block of Σ_1 .

- **Step 3:** The reduced A_r , B_r and C_r in (2.2) are then defined as

$$\begin{aligned} A_r &= \Sigma_r^{-\frac{1}{2}} U_r^* H' V_r \Sigma_r^{-\frac{1}{2}}; \\ B_r &= \text{the first } p \text{ columns of } \Sigma_r^{\frac{1}{2}} V_r^*; \\ C_r &= \text{the first } q \text{ rows of } U_r \Sigma_r^{\frac{1}{2}} \end{aligned} \quad (3.3)$$

where

$$H' = \begin{bmatrix} CAB & CA^{P+1}B & \dots & CA^{m_c P+1}B \\ \vdots & \vdots & \ddots & \vdots \\ CA^{m_o P+1}B & CA^{(m_o+1)P+1}B & \dots & CA^{(m_c+m_o)P+1}B \end{bmatrix}, \quad (3.4)$$

which can again be constructed directly from the collected snapshots (3.1).

3.1.2 Theoretical equivalence between ERA and balanced POD

For comparison, recall the balanced POD procedures outlined in Section 2.3.1. The first observation is that, with X and Y given by (2.11) and (2.13), the generalized Hankel matrices obtained in balanced POD and ERA, respectively by (2.14) and (3.2), are theoretically identical. The theoretical equivalence between the two algorithms then follows immediately: First, H' given in (3.4) satisfies $H' = Y^*AX$, which implies the matrices A_r obtained in the two algorithms are identical. To show the equivalence of B_r , first note that the SVD (2.15) leads to $\Sigma_1^{-\frac{1}{2}}U_1^*H = \Sigma_1^{\frac{1}{2}}V_1^*$, which, by definition of U_r , V_r , Σ_r , implies $\Sigma_r^{-\frac{1}{2}}U_r^*H = \Sigma_r^{\frac{1}{2}}V_r^*$. (Note that it does *not* imply $H = U_r\Sigma_rV_r^*$, since $U_rU_r^*$ is not the identity.) Thus, in balanced POD, $B_r = \Psi_r^*B = \Sigma_r^{-\frac{1}{2}}U_r^*Y^*B$, which equals the first p columns of $\Sigma_r^{-\frac{1}{2}}U_r^*H = \Sigma_r^{\frac{1}{2}}V_r^*$, which is the B_r given by ERA. Similarly, the SVD (2.15) leads to $HV_1\Sigma_1^{-\frac{1}{2}} = U_1\Sigma_1^{\frac{1}{2}}$ and then $HV_r\Sigma_r^{-\frac{1}{2}} = U_r\Sigma_r^{\frac{1}{2}}$. Thus, in balanced POD, $C_r = C\Phi_r = CXV_r\Sigma_r^{-\frac{1}{2}}$, which equals the first q rows of $HV_r\Sigma_r^{-\frac{1}{2}} = U_r\Sigma_r^{\frac{1}{2}}$, the C_r given by ERA. In summary, we have:

Theorem 3.1.1. *The reduced system matrices A_r , B_r and C_r generated in balanced POD and ERA, respectively by (2.17) and (3.3), are theoretically identical.*

In model reduction procedures, balanced POD *exactly* balances a pair of approx-

imate Gramians given by (2.18) (Rowley (2005); Section 3.2). This equivalence thus describes precisely in what sense ERA is an approximate balanced truncation method.

In practice, these two algorithms may generate slightly different reduced order models, because the Hankel matrices calculated in the two algorithms are usually not exactly the same, due to small numerical inaccuracies in adjoint simulations, and/or in matrix multiplications needed to compute the sub-blocks in the Hankel matrices. In the following discussions, we compare these two algorithms in more detail.

3.1.3 Comparison between ERA and balanced POD

While ERA and balanced POD produce theoretically identical reduced-order models, the techniques differ in several important ways, both conceptually and computationally. Neither ERA nor balanced POD calculate Gramians explicitly, but balanced POD constructs approximate controllability and observability matrices X and Y^* , from which one calculates the generalized Hankel matrix H and balancing transformation. Balanced POD thus incurs additional computational cost, because one needs to construct the adjoint system (2.12), run adjoint simulations for Y , and then calculate each block of H by matrix multiplication. Thus we see that the advantages of ERA include:

1. **Adjoint-free:** ERA is a feasible balanced truncation method for experiments, since it needs only the output measurements from the response to an impulsive input. Note that ERA has been successfully applied in several flow control experiments (Cattafesta *et al.*, 1997; Cabell *et al.*, 2006), as a system-identification technique rather than a balanced-truncation method. In practice, input-output sensor responses are often collected by applying a broad-

band signal to the inputs, and the ARMARKOV method (Akers & Bernstein, 1997; Lim *et al.*, 1998) can then be used to identify the Markov parameters, or even directly the generalized Hankel matrix, from the input-output data history.

2. **Computational efficiency:** For large problems, typically the most computationally expensive component of computing balanced POD is constructing the generalized Hankel matrix H in (2.14), as this involves computing inner products of all of the (large) primal and adjoint snapshots with each other. ERA is significantly more efficient at constructing the matrix H in (3.2), since only the first row and last column of block matrices, i.e., the $(m_c + m_o + 1)$ Markov parameters, need be obtained by matrix multiplication. All the other $m_c \times m_o$ block matrices in H are copies of other blocks, and need not be recomputed. For balanced POD, the matrix H is obtained by computing all the $(m_c + 1) \times (m_o + 1)$ matrix multiplications (inner products) between corresponding blocks in Y^* and X in (2.14). Thus, for example, if $m_c = m_o = 200$, the computing time needed for constructing H in ERA will be about only 1% of that in balanced POD. This reduced time could be a great advantage for real-time model reduction and control applications. See Table 3.1 for a detailed comparison on computational efficiency between balanced POD and ERA in the example of the flow past an inclined flat plate.

At the same time, balanced POD also provides its own advantages:

1. **Sets of bi-orthogonal primal/adjoint modes:** Balanced POD provides sets of bi-orthogonal primal/adjoint modes, the columns of Φ_r and Ψ_r . In comparison, without the adjoint system, ERA cannot provide the primal and adjoint modes. At best, the primal modes may be computed, using the

first equation in (2.16), if the matrix X (2.11) is stored (in addition to the Markov parameters). But the adjoint modes cannot be computed without solutions of the adjoint system. In this sense, balanced POD incorporates more of the physics of the system (the two sets of bi-orthogonal modes), while ERA is purely based on input-output data of the system. The primal/adjoint modes together can be useful for system analysis and controller/observer design purposes in several ways: for instance, in flow control applications, a large-amplitude region from the most observable mode (the leading adjoint mode) can be a good location for actuator placement. Also, as mentioned in Section 2.4, although balanced POD is a linear method, a nonlinear system can be projected onto these sets of modes to obtain a nonlinear low-dimensional model. For instance, the transformation $x = \Phi_r x_r$, $x_r = \Psi_r^* x$ can be employed to reduce a full-dimensional nonlinear model $\dot{x} = f(x)$ to a low-dimensional system $\dot{x}_r = \Psi_r^* f(\Phi_r x_r)$. Finally, if parameters (such as Reynolds number or Mach number) are present in the original equations, balanced POD can retain these parameters in the reduced-order models. When the values of parameters change, the reduced order model by balanced POD may still be valid and perform well; see Ilak & Rowley (2008) for an application to linearized channel flow. More discussions following this topic will be presented in Section 3.2.

2. **Unstable systems:** Balanced POD has been extended to unstable systems (Ahuja & Rowley (2010); see 2.3.3). In that case, one first calculates the right/left eigenvectors corresponding to the unstable eigenvalues of the state-transition matrix A , using direct/adjoint simulations. Using these eigenvectors, the system is projected onto a stable subspace and then balanced truncation is realized for the stable subsystem. ERA for general unstable systems is still an open problem, if adjoint operators are not available. However, we

note that, once the stable subsystem is obtained, ERA can still be applied to it and efficiently realize its approximate balanced truncation; see application in Ahuja (2009). See Section 3.4 for more discussions. In Section 3.4 we will also present a version of ERA for neutrally stable/unstable systems with one-dimensional neutral stability/instability.

ERA for systems with high-dimensional outputs. For system with high-dimensional outputs, such as using states as outputs, the number of rows of generalized Hankel matrices H and H' can be too large for SVD calculation. The method of output projection developed in balanced POD (Rowley (2005); see Section 2.3.2) can be directly incorporated into ERA as follows: First, run impulse response simulations of the original system and collect Markov parameters as usual. Then, compute the leading POD modes of the dataset of Markov parameters and stack them as columns of a matrix Θ . Left multiply those Markov parameters by Θ^* to project the outputs onto these POD modes. A generalized Hankel matrix is then constructed using these modified Markov parameters, and the usual steps of ERA follow.

On the other hand, unlike in balanced POD, an “input projection” method (see Section 2.3.2) for systems with high-dimensional control inputs/disturbance is not straightforwardly available for ERA, due to the lack of the adjoint system. For feedback control design problems, a practical treatment can be to compromise some freedom of the control inputs, such that a smaller number of impulse responses is needed; see Chapter 5 for more details.

3.2 A modified ERA method using pseudo-adjoint modes

We have seen that one of the drawbacks of ERA is that it does not provide modes that could be used, for instance, for projection of nonlinear dynamics, or to retain parameters in the models. More precisely, using ERA, one may still obtain primal modes $\Phi_1 = XV_1\Sigma_1^{-1/2}$ as in balanced POD (see (2.15–2.16)), as long as the state snapshots are collected and stored in X as in (2.11). But it is not possible to obtain the corresponding adjoint modes Ψ_1 necessary for projection, without performing adjoint simulations to gather snapshots for the matrix Y as (2.13). To find the adjoint modes, one idea, proposed in Or *et al.* (2008), is to define a set of approximate adjoint modes using the Moore-Penrose pseudo-inverse of Φ_1 :

$$\tilde{\Psi}_1 = \Phi_1(\Phi_1^*\Phi_1)^{-1}. \quad (3.5)$$

We will call the adjoint modes as defined above the *pseudo-adjoint modes* corresponding to the modes Φ_1 . The system matrices of a r -dimensional reduced-order model ($r \leq \text{rank}(H)$) generated by this approach then read

$$A_r = \tilde{\Psi}_r^* A \Phi_r; \quad B_r = \tilde{\Psi}_r^* B; \quad C_r = C \Phi_r, \quad (3.6)$$

where Φ_r and $\tilde{\Psi}_r$ are respectively the first $n \times r$ sub-blocks of $\Phi_1, \tilde{\Psi}_1$.

While this idea produces a set of modes that can be used for projection, we show here that the resulting transformation is *not* a balancing transformation, and does not produce models that are an approximation to balanced truncation. In fact, the resulting models are closer to those produced by the standard POD/Galerkin method: as with standard POD/Galerkin, the method performs well as long as the most controllable and most observable directions coincide. However, when these di-

rections differ (as is the case for many problems of interest, including the example in Section 3.3), the method performs poorly. These systems in which controllable and observable directions do not coincide are precisely the systems for which balanced POD and ERA give the most improvement over the more traditional POD/Galerkin approach.

3.2.1 Transformed approximate Gramians

First, let us recall in what sense the balanced POD procedures described in Section 2.3 are approximations to balanced truncation. Recall that we have an approximation of the controllability and observability Gramians, factored as

$$W_c = XX^*, \quad W_o = YY^*, \quad (3.7)$$

where X and Y are the matrices of snapshots from (2.11) and (2.13). In balanced POD, we define the primal modes as columns of $\Phi_1 = XV_1\Sigma_1^{-\frac{1}{2}}$, and the adjoint modes as columns of $\Psi_1 = YU_1\Sigma_1^{-\frac{1}{2}}$, where U_1 , V_1 , and Σ_1 are defined in (2.15). We will assume in this section that the number of columns of X and Y (the number of snapshots, m_c and m_o , respectively) is smaller than the number of rows (the state dimension, n), which is always true for the large fluid systems of interest here.

Then balanced POD is an approximation to balanced truncation in the following sense: as shown in the appendix of Rowley (2005) (the proof of Proposition 2), we may construct a full (invertible, $n \times n$) transformation

$$T = \begin{bmatrix} \Phi_1 & \Phi_2 \end{bmatrix} \quad (3.8)$$

by choosing Φ_2 such that $\Psi_1^*\Phi_2 = 0$. That is, columns of Φ_2 are orthogonal to the adjoint modes, which are columns of Ψ_1 . Define Ψ_2 as the last $n - r$ rows of the

inverse transformation T^{-1} . T^{-1} then has the form

$$T^{-1} = \begin{bmatrix} \Psi_1^* \\ \Psi_2^* \end{bmatrix} \quad (3.9)$$

where Ψ_1 is the matrix of adjoint modes. Then, Proposition 2 of Rowley (2005) states that the transformed approximate Gramians (3.7) have the form

$$T^{-1}W_c(T^{-1})^* = \begin{bmatrix} \Sigma_1 & 0 \\ 0 & M_1 \end{bmatrix}, \quad T^*W_oT = \begin{bmatrix} \Sigma_1 & 0 \\ 0 & M_2 \end{bmatrix}, \quad (3.10)$$

and furthermore the product of the approximate Gramians, in the transformed coordinates, is

$$T^{-1}W_cW_oT = \begin{bmatrix} \Sigma_1^2 & 0 \\ 0 & 0 \end{bmatrix}. \quad (3.11)$$

In this sense, the transformation T balances the approximate Gramians as closely as possible: the Gramians are block diagonal, and the upper-left blocks are equal and diagonal. Furthermore, all of the states in the lower-right block (i.e., involving M_1 and M_2 above) are either unobservable or uncontrollable, as they do not appear in the product of the Gramians.

However, if the pseudo-adjoint modes $\tilde{\Psi}_1$ are used in place of the true adjoint modes Ψ_1 , then this result does not hold, as we now show. Note that, in order for the first block of rows of T^{-1} to equal $\tilde{\Psi}_1^*$, we must now define

$$\tilde{T} = \begin{bmatrix} \Phi_1 & \tilde{\Phi}_2 \end{bmatrix} \quad (3.12)$$

where $\tilde{\Psi}_1^*\tilde{\Phi}_2 = 0$. Since the range of $\tilde{\Psi}_1$ equals the range of Φ_1 , this is then equivalent to choosing $\tilde{\Phi}_2$ such that its columns are orthogonal to the columns of Φ_1 (the *primal* modes), while when the “true” adjoint modes are used, columns of Φ_2 are chosen to be orthogonal to the *adjoint* modes Ψ_1 .

Defining $\tilde{\Psi}_2$ by

$$\tilde{T}^{-1} = \begin{bmatrix} \tilde{\Psi}_1^* \\ \tilde{\Psi}_2^* \end{bmatrix}, \quad (3.13)$$

one can then show that, as long as $\text{rank}(X) \leq \text{rank}(Y)$ ¹, the transformed Gramians have the form

$$\tilde{T}^{-1}W_c(\tilde{T}^{-1})^* = \begin{bmatrix} \Sigma_1 & 0 \\ 0 & \tilde{M}_1 \end{bmatrix}, \quad \tilde{T}^*W_o\tilde{T} = \begin{bmatrix} \Sigma_1 & M_3 \\ M_3^* & \tilde{M}_2 \end{bmatrix}, \quad \tilde{T}^{-1}W_cW_o\tilde{T} = \begin{bmatrix} \Sigma_1^2 & \Sigma_1 M_3 \\ \tilde{M}_1 M_3^* & 0 \end{bmatrix}, \quad (3.14)$$

with

$$M_3 = \Sigma_1 \Psi_1^* \tilde{\Phi}_2, \quad (3.15)$$

where $\Psi_1 = YU_1\Sigma_1^{-1/2}$ are the true adjoint modes. Note that, when the true adjoint modes are used to define the inverse (3.9), then $M_3 = 0$, since $\Psi_1^*\Phi_2 = 0$. However, when pseudo-adjoint modes are used, then M_3 is no longer zero, and in fact, can be quite large.

An example is shown in Figure 3.1, which shows the magnitude of the elements of the transformed Gramians, where X and Y in (3.7) are chosen at random. Note that when true adjoint modes are used, the transformed Gramians are equal and diagonal, while when the pseudo-adjoint modes are used, the off-diagonal blocks of the transformed observability Gramian, and the product of the Gramians, have significant magnitude.

Thus, when pseudo-adjoint modes are used, the resulting transformation is not, in general, a balancing transformation: even though the upper-left blocks of the transformed Gramians are still equal and diagonal, the transformed observability Gramian is not block diagonal, and so its eigenvalues and eigenvectors do not cor-

¹If $\text{rank}(X) > \text{rank}(Y)$, then the situation is worse, and the transformed controllability Gramian is not block diagonal, nor does its upper-left block equal Σ_1 .

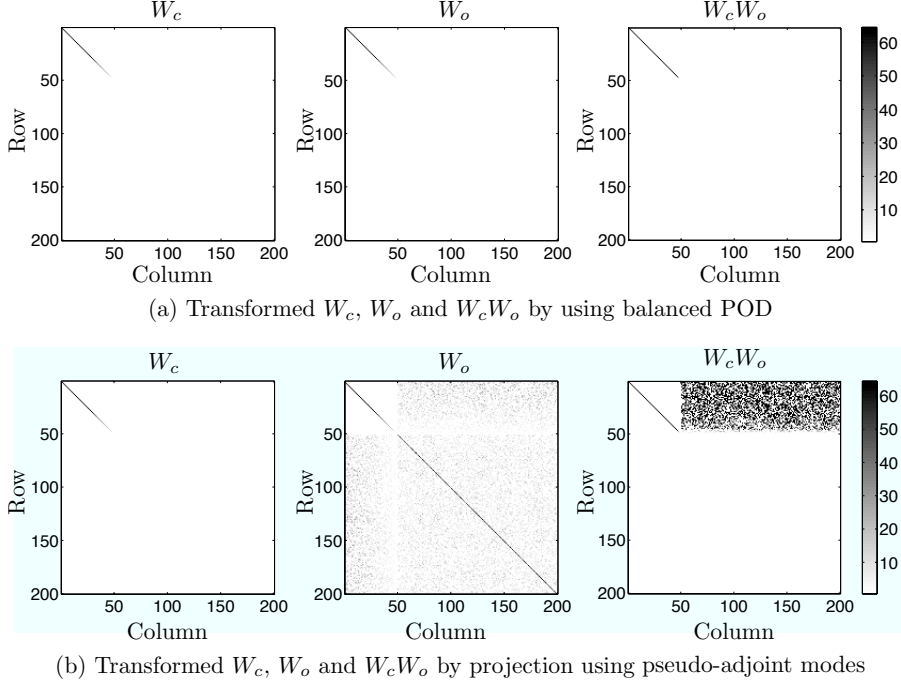


Figure 3.1: Transformed Gramian matrices: (a) using true adjoint modes (eq. (3.10–3.11)) and (b) using pseudo-adjoint modes (eq. (3.14)). Here, X and Y in (3.7) are random matrices with $n = 200$ states and $m_c = m_o = 50$ snapshots.

respond to those of the transformed controllability Gramian. Note that this is the whole point of balanced truncation: to transform to coordinates in which the most controllable directions (dominant eigenvectors of W_c) correspond to the most observable directions (dominant eigenvectors of W_o). Therefore, while the approximate balanced truncation procedure described in Section 2.3.1 exactly balances the approximate Gramians (and so does ERA), transforming by pseudo-adjoint modes does not represent balancing in any meaningful sense.

Note that the matrix M_3 describes the degree to which projection using pseudo-adjoint modes fails to balance the approximate Gramians. This matrix equals zero if the adjoint modes (columns of Ψ_1) are spanned by the primal modes (columns of Φ_1). However, M_3 is the largest when the dominant adjoint modes (columns of Ψ_1) are nearly orthogonal to the dominant primal modes (columns of Φ_1). Unfortunately, this is the case in many problems of interest, in particular those involving non-

normality: the directions spanned by the primal modes often do not coincide with the directions spanned by the adjoint modes.

In the next section, we apply this approach to the flow past a flat plate, and compare it to the methods described in Section 3.1.

3.3 A numerical example: two-dimensional flow past a flat plate

In this section, we illustrate the application of ERA as an approximate balanced truncation method using a numerical example, by obtaining reduced-order models of a large-dimensional fluid system. We compare the resulting models with those obtained using the balanced POD method of Rowley (2005), ERA with pseudo-adjoint modes as described in Section 3.2, and the standard POD/Galerkin method (Holmes *et al.*, 1996).

3.3.1 Model problem and parameters

The model problem that we consider is a two-dimensional uniform flow over a flat plate inclined at an angle $\alpha = 25^\circ$, at a low Reynolds number $Re = 100$. At these conditions, the flow asymptotically reaches a stable steady state, the streamlines of which are plotted in Figure 3.2. The numerical method used for all computations is a fast formulation of the immersed boundary projection method developed by Colonius & Taira (2008), and solves for the vorticity field at each time step. We treat farfield boundary conditions using the multiple-grid scheme described in Colonius & Taira (2008) (Section 4) with five nested grids, each with 250×250 points. The

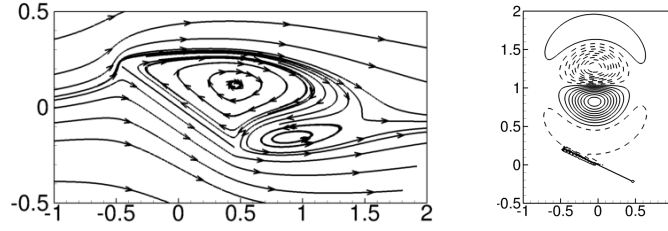


Figure 3.2: Streamlines of the stable steady state past a flat plate at $\alpha = 25^\circ$ (left), and the contour-lines of the vorticity field obtained from an impulsive input to the actuator (right).

finest grid covers the region $[-2, 3] \times [-2.5, 2.5]$, and the largest grid covers the region $[-32, 48] \times [-40, 40]$, where lengths are non-dimensionalized by the chord of the flat plate, whose center is located at the origin. The time step used for all simulations is 0.01 (nondimensionalized by chord and freestream velocity). The numerical model is the same as that considered in Ahuja & Rowley (2010) where balanced POD is applied for feedback controller design to stabilize an *unstable* steady state corresponding to a high angle of attack, at which there exist a stable vortex shedding cycle and an unstable steady state. However, here we consider the case of a *stable* steady state (with an angle of attack at 25°), for comparison of reduced order models.

3.3.2 Input and output

The governing equations are first linearized about the stable steady state, resulting in a high-dimensional model in the form of equation (2.1), where the state x consists of the discrete vorticity field at the grid points. See Ahuja & Rowley (2010) for the details of the linearized (and adjoint) equations and their numerical formulations. The system input u is a disturbance (or actuator) shown in Figure 3.2, modeled as a localized body force in the vicinity of the leading edge. Its vorticity field consists of two counter-rotating vortices, the circulation of each given by a Gaussian

distribution; see Ahuja & Rowley (2010) for details. We consider the output to be the entire velocity field: this is important for capturing the flow physics, and is often needed to represent cost functions used in optimal control design. Since the output is very high-dimensional, in ERA and balanced POD reduction procedures we use output projection described at the end of Section 3.1, projecting the velocity field onto the leading POD modes of the velocity snapshots obtained from the impulse response simulation.

3.3.3 Reduced-order models

ERA is applied to the full-dimensional linearized system to construct a reduced-order model. With a sampling period of 50 time steps, 400 adjacent pairs of Markov parameters, as in (3.1), are collected from an impulse response simulation. Since these parameters are a projection of the velocity fields onto the leading POD modes, for an output projection of order m , the number of inner products required is $4m \times 10^2$ for construction of each H and H' (see Section 3.1.3).

For comparison, balanced POD is also used to compute the same reduced-order models. Adjoint simulations are performed with the POD modes as initial conditions to compute the matrix Y of (2.13). The matrices X and Y are assembled by stacking 200 snapshots from the linearized and each of the adjoint simulations, and in turn, the generalized Hankel matrix $H = Y^*X$ is computed. For an output projection of order m , the number of inner products required to compute H is $4m \times 10^4$, which is 50 times more than that to compute H and H' in total for ERA.

We also compare reduced-order models using standard POD modes, and ERA with pseudo-adjoint modes, as described in Section 3.2. The first 100 primal modes are used to compute the pseudo-adjoint modes..

Steps in computing reduced-order models	Approximate time (CPU hours)	
	balanced POD	ERA
1. Linearized impulse response	2	4
2. Computation of POD modes	2	2
3. Adjoint impulse responses (10 in number)	30	-
4. Computation of the Hankel matrix	7	0.2
5. Singular value decomposition	0.05	0.05
6. Computation of modes	1	-
7. Computation of models	0.02	0.02

Table 3.1: Comparison of the computational times required for various steps of the algorithms using balanced POD and ERA. The times are given for a 10-mode output projected system. The Hankel matrices are constructed using: 200 state-snapshots from each linearized and adjoint simulations for balanced POD, and 400 Markov parameters (outputs) for ERA.

For the given case, a comparison between the computational cost using ERA and using balanced POD is shown in Table 3.1. Results verify that ERA substantially improves computational efficiency in forming reduced-order models.

Next, we compare the reduced-order models. Figure 3.3 shows the leading two primal modes and true adjoint modes from balanced POD, compared with the leading two pseudo-adjoint modes. The pseudo-adjoint modes look quite different from the true adjoint modes, and the flow structures actually more closely resemble the leading *primal* modes. This result is not surprising, since the pseudo-adjoint modes are always linear combinations of the snapshots from the primal simulations, while the true adjoint modes are linear combinations of snapshots from adjoint simulations. Following the discussion in the last section, the poor approximation of the adjoint modes suggests that the pseudo-adjoint modes may produce poor reduced order models for this example, as we will verify below.

Figure 3.4 shows the diagonal values of the controllability and observability Gramians, as well as the empirical Hankel singular values, for reduced-order models obtained from three different methods: ERA, balanced POD, and ERA with pseudo-

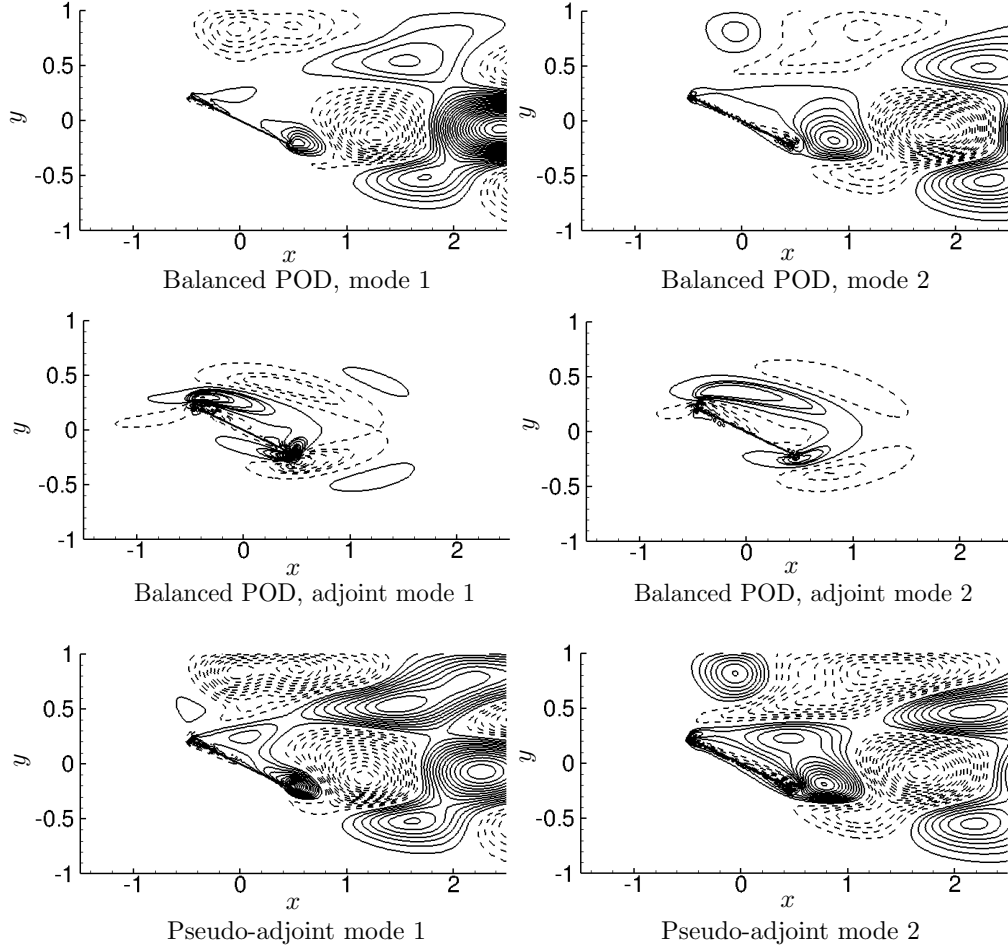


Figure 3.3: The first two primal and adjoint modes computed using balanced POD, and the first two pseudo-adjoint modes computed using (3.5) and the first 100 primal modes. Modes are illustrated using contour plots of the vorticity field.

adjoint modes. The models obtained using ERA are more accurate in the sense that the three sets of curves are almost indistinguishable, for all orders of output-projection. However, for balanced POD, the diagonal values of the observability Gramians are accurate only for certain leading modes, the number of which depends on and increases with the order of output projection. This inaccuracy can be attributed to a slight inaccuracy in the adjoint formulation, which in turn results from an approximation in the multi-domain approach used to treat farfield boundary conditions in the immersed boundary method of Colonius & Taira (2008); see Ahuja & Rowley (2010) for more details. Thus, ERA is advantageous as it does not need

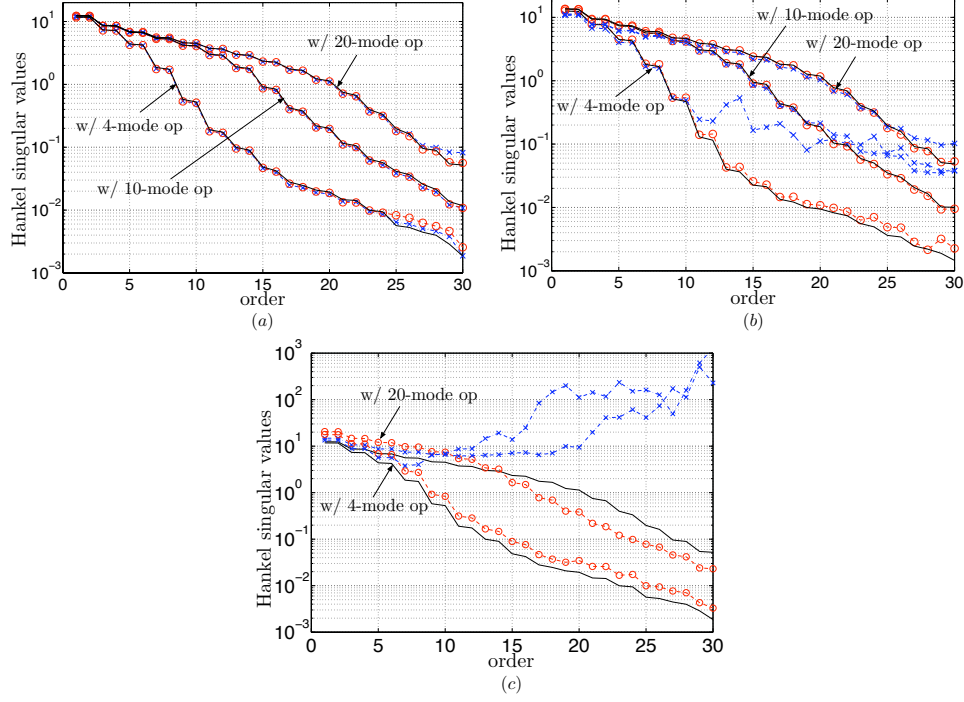


Figure 3.4: Comparison of Gramians computed using (a) ERA, (b) balanced POD, and (c) ERA with pseudo-adjoint modes: The empirical Hankel singular values (—) and the diagonal elements of the controllability (---, \circ) and observability (---, \times) Gramians with different order of modes (e.g., 4, 10, 20) in output projection.

any adjoint simulations and results in more balanced Gramians. On the other hand, ERA with pseudo-adjoint modes generates poorly balanced controllability and observability Gramians, as shown in Figure 3.4(c). This is because the leading primal modes and adjoint modes are supported very differently in the spatial domain, and thus the pseudo-adjoint modes, based on linear combination of leading primal modes, poorly approximate the true adjoint modes.

3.3.4 Model performance

We can quantify the performance of the various reduced-order models by computing error norms. One such measure is the 2-norm of the error between the impulse response of the full linearized system, denoted $G(t)$, and that of a reduced order

model with r modes, denoted by $G_r(t)$. We first compute the 2-norm of the error between the full system (with the entire velocity field as output) and the output-projected system of order 20, shown as the horizontal dashed line in Figure 3.5. This is the lower error bound for any reduced order model of the given output-projected system. Results shown in Figure 3.5 indicate that the first several low-order models obtained by ERA and balanced POD generate slightly different 2-norms of error, presumably because of the slight inaccuracy in the adjoint, mentioned previously. For most orders, however, they agree, and both error norms converge to the lower bound as the order of the model increases. By running more simulation tests, we observe that with higher-order output projections, ERA and balanced POD error norms converge to each other faster when the order of the model increases.

Figure 3.5 also shows the 2-norm error plots for models by ERA with pseudo-adjoint modes, using 20-mode output projection, and for models computed using standard POD. Errors of models by ERA with pseudo-adjoint modes converge to the lower bound much slower than ERA/balanced POD. Errors of models by POD do not start converging until more than nearly 20 modes are used, and they converge to a larger error bound than ERA/balanced POD, again because POD models do not capture the input-output dynamics as well as balanced truncation based models.

In the time domain, a comparison of the transient response to an impulsive disturbance is shown in Figure 3.6, in which the first output of the reduced-order model is plotted, for a 16-mode model determined by ERA, and for 30-mode models by POD and ERA with pseudo-adjoint modes. The 16-mode ERA model already accurately predicts the response for all times. The higher-dimensional, 30-mode models using POD and pseudo-adjoint modes are both stable, and perform reasonably well; however, they over-predict the response, particularly after time $t \approx 80$.

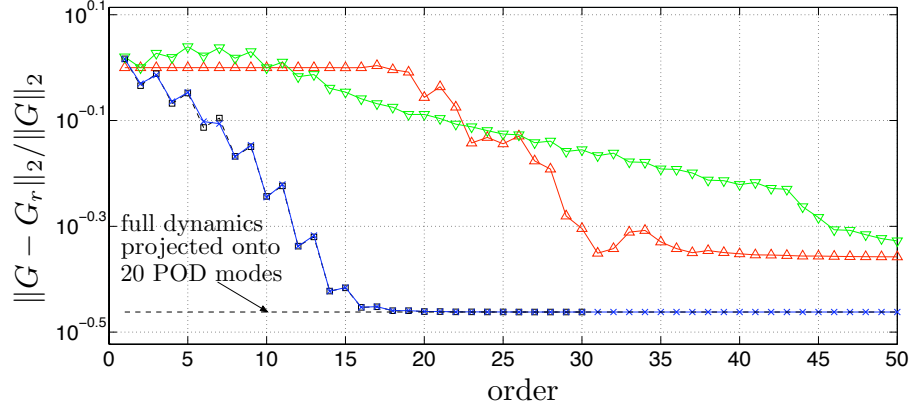


Figure 3.5: H_2 -norm of the error with increasing order of the reduced-order models: exact output of the output-projected system (----, \square), ERA (—, \times), ERA with pseudo-adjoint modes (—, ∇), and POD (—, \triangle). A 20-mode output projection is used in ERA, balanced POD, and ERA with pseudo-adjoint modes.

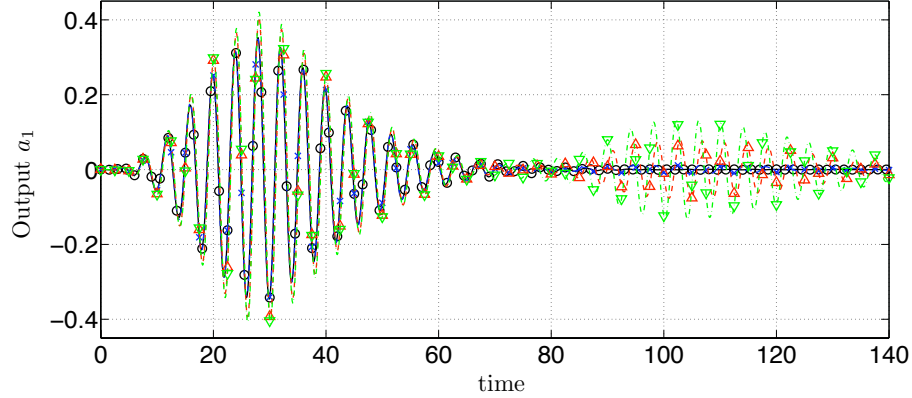


Figure 3.6: The first output, output a_1 , from the impulse-response simulation: results of full-simulation (—, \circ), compared with those of 16-mode reduced order model by ERA (---, \times), 30-mode model by ERA with pseudo-adjoint modes (—, ∇), and 30-mode model by POD (---, \triangle). A 20-mode output projection is used in ERA and ERA with pseudo-adjoint modes.

We also compare the frequency response of reduced-order models to that of the full system, or more precisely, the full output-projected system. One way to represent the response of a single-input multiple-output system is by a singular-value plot, a plot of the maximum singular value of the transfer function matrix as a function of frequency. To generate this plot, a very long simulation of 5×10^5 time steps for the full system is performed, with a random input sampled from a uniform distribution in the range $(-0.5, 0.5)$. The output snapshots are projected onto

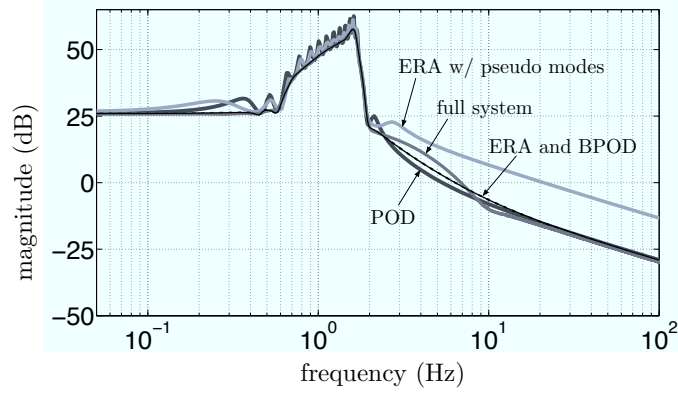


Figure 3.7: Singular-value plots: The full system and 30-mode models obtained using balanced POD, ERA, ERA with pseudo-adjoint modes, and POD, all with a 20-mode output projection. ERA and balanced POD models generate almost identical plots.

leading POD modes. The magnitude of the transfer function is then computed from the cross spectrum of the input and outputs (using the Matlab command `tfestimate`). Finally, singular-value plots for the full output-projected systems are obtained, with a typical case shown in Figure 3.7.

A typical set of singular-value plots of different reduced order models are presented in Figure 3.7. Results shown in the figure indicate that ERA and balanced POD 30-mode models, are almost identical, and are close to the corresponding full output-projected system. In comparison, Figure 3.7 also shows singular-value plots for 30-mode models by ERA with pseudo-adjoint modes and by POD. Note that for computational feasibility, here the output of the POD model is the first twenty reduced states, i.e., the full-dimensional output of the POD model are projected onto the leading twenty POD modes. The frequency responses of the models by POD and ERA with pseudo-adjoint modes capture the resonant peak, but do not match well for frequencies far away from the resonant peak. These two models both generate spurious peaks in the frequency range of $[0.1, 2]$.

3.4 ERA for neutrally stable/unstable systems

From the discussion in Section 3.1, we know ERA is in general not directly applicable to unstable systems if the adjoint operator is not available. That is because Markov parameters will diverge in impulse responses of the original LTI system (2.1). Furthermore, we cannot apply the method of 2.3.3, as the projection in (2.21) is not available, since the unstable left eigenvectors of A are unknown. One solution to the problem is the observer/controller identification (OCID) introduced in Juang (1994). In OCID, one first designs a feedback control to stabilize the system, and then collects Markov parameters for the closed-loop, stable system. The Markov parameters for the original unstable system are then obtained using closed-loop Markov parameters and the known open-loop forcing and feedback control signals. A recent application of OCID/ERA in feedback control design for cavity flow oscillations is given in Illingworth (2009). However, to obtain a stabilizing feedback control beforehand is often non-trivial. Indeed, if this were simple, one might not need the reduced-order models.

In this section we propose an algorithm to generalize ERA to systems with one dimension of neutral stability/instability. This algorithm will be a counterpart of balanced POD for unstable systems (Section 2.3.3): it decomposes the system dynamics into stable and unstable parts, and balanced truncation is performed only on the stable part. Again, the main feature of this version of ERA is that no adjoint data is needed, as in the original ERA.

We are particularly interested in the one-dimensional neutral stability/instability case, since in many physical applications when a key parameter crosses the bifurcation point, only one stable eigenvalue of the corresponding steady state becomes unstable. Furthermore, as we will discuss in the following chapters, the case of

one-dimensional neutral stability is typical in linearized periodic systems around asymptotically stable orbits, by Floquet theory (Hartman, 1964). These neutrally stable systems are structurally unstable (Guckenheimer & Holmes, 1983) in the sense that with perturbations the neutrally stable eigenvalue becomes either stable or unstable. The perturbed systems are thus either stable or of one-dimensional instability.

In the following discussions, for the case of one-dimensional neutral stability/instability, we show that it is computationally feasible to approximately project a state onto $E^s(A)$, the stable subspace of A , without knowing either the unstable left eigenvector nor the projection \mathbb{P}_s explicitly.

Let $v, w \in \mathbb{C}^{n \times 1}$ be the right and left unstable eigenvector of A . By the power method (Horn & Johnson, 1985), v and w are approximated by the recursive formula

$$\begin{aligned} v_{m+1} &= \frac{1}{(v_m^* v_m)^{1/2}} A v_m; \\ w_{m+1} &= \frac{1}{(w_m^* w_m)^{1/2}} A^* w_m, \end{aligned} \tag{3.16}$$

with $m = 0, 1, 2, \dots$, and any $v_0 \notin E^s(A)$, $w_0 \notin E^s(A^*)$. For a large enough m ,

$$\begin{aligned} v &\approx \prod_{i=0}^{m-1} \left(\frac{1}{(v_i^* v_i)^{1/2}} \right) A^m v_0 := c_v(m) A^m v_0; \\ w &\approx \prod_{i=0}^{m-1} \left(\frac{1}{(w_i^* w_i)^{1/2}} \right) (A^*)^m w_0 := c_w(m) (A^*)^m w_0. \end{aligned} \tag{3.17}$$

A projection onto $E^s(A)$ in the form (2.21) reads

$$\mathbb{P}_s = I_{n \times n} - \frac{v w^*}{w^* v}. \tag{3.18}$$

Thus, for any vector $\alpha \in \mathbb{C}^n$ not in $E^s(A)$ nor $E^s(A^*)$, choose $v_0 = w_0 = \alpha$, and we have

$$\mathbb{P}_s \alpha = \left(I_{n \times n} - \frac{v w^*}{w^* v} \right) \alpha \approx \alpha - \frac{\alpha^* A^m \alpha}{\alpha^* A^{2m} \alpha} A^m \alpha, \tag{3.19}$$

where $A^m\alpha$ and $A^{2m}\alpha$ can be obtained by a control free simulation of $2m$ steps of the original system (2.1), with initial condition α . Thus, even though the left eigenvector w and projection \mathbb{P}_s are not explicitly known, we can compute $\mathbb{P}_s B$ by letting α in (3.19) is equal to B (first consider a single-input case). Then, by (3.1) and projection properties $\mathbb{P}_s^2 = \mathbb{P}_s$ and $\mathbb{P}_s A = A\mathbb{P}_s$, the Markov parameters of the projected system (2.22) are

$$C\mathbb{P}_s A^i \mathbb{P}_s B = CA^i \mathbb{P}_s B, \quad i = 0, 1, P, P+1, \dots \quad (3.20)$$

Let A_r, B_r, C_r be the reduced matrices for the projected system (2.22) determined by ERA. By using the equivalence between ERA and balanced POD for stable systems (indeed, the stable dynamics of A here), the $(r+1)$ -dimensional reduced-order model of the original LTI (2.1) is in the form (2.25) where T_u, S_u are now replaced by v, w , and

$$\Psi_{1r}^* A \Phi_{1r} = A_r; \quad \Psi_{1r}^* B = B_r; \quad C \Phi_{1r} = C_r.$$

See Appendix A for a proof of the above relation. With the approximation (3.17), the final $(r+1)$ -dimensional reduced-order model *by ERA* reads

$$\begin{aligned} x_r(k+1) &= \begin{bmatrix} A_r & 0 \\ 0 & \frac{w_0^* A^{2m+1} v_0}{w_0^* A^{2m} v_0} \end{bmatrix} x_r(k) + \begin{bmatrix} B_r \\ \frac{w_0^* A^m B}{c_v(m) w_0^* A^{2m} v_0} \end{bmatrix} u(k); \\ y(k) &= \begin{bmatrix} C_r & c_v(m) C A^m v_0 \end{bmatrix} x_r(k). \end{aligned} \quad (3.21)$$

The value of $\frac{w_0^* A^{2m+1} v_0}{w_0^* A^{2m} v_0}$ is an approximate solution of the unstable eigenvalue of A .

Above is an extended ERA approach, as *no modes are computed and no adjoint information is needed*. To save computational cost, one can choose $v_0 = w_0 = B$, such that the terms $A^m v_0, A^{2m} v_0, A^m B$ have all been obtained during computations of $\mathbb{P}_s B$. The scaling factor $c_v(m)$ can also be calculated in those computations. For

a multiple-input case where B has more than one column, one repeats the procedure in (3.19) once for each control input to compute $\mathbb{P}_s B$.

Equivalence between ERA and balanced POD for the one-dimensional instability case. Theoretically, the reduced-order model by ERA (3.21) will be identical to that by balanced POD (2.25), if in balanced POD the left/right eigenvector of A are also approximated by the power method as in (3.17) with the same initial guesses v_0 and w_0 , and the projection matrix is obtained by (2.21), with S_u, T_u replaced by w, v . However, if other more efficient methods, e.g. Arnoldi iteration method, are used as eigensolvers in balanced POD, then the resulting models will be different and the computational cost of projection will also be higher in ERA than in balanced POD.

The algorithm proposed here can potentially be applied to systems with higher dimensions of instability by iterating the above approach for the several leading unstable eigenvectors. However, this approach will be computationally expensive due to the iteration procedure. Investigating more efficient ERA algorithms for systems with higher dimensions of instability will be an interesting direction for future work.

3.5 Summary

For linear time-invariant systems, we report that, theoretically, the eigensystem realization algorithm (ERA) and snapshot-based approximate balanced truncation (balanced POD) produce exactly the same reduced order models. This equivalence implies that ERA *exactly* balances a pair of approximate Gramians and thus can be regarded as an approximate balanced truncation method. Compared to balanced

POD, the main features of ERA are that it does not require data from adjoint systems and therefore can be used with experimental data; furthermore, its construction of the generalized Hankel matrix is computationally an order-of-magnitude cheaper than balanced POD. Balanced POD does have its own advantages, however: unlike ERA, it produces sets of bi-orthogonal modes that are useful for system analysis and controller/observer design purposes. We also examine a modified ERA approach in which one constructs sets of bi-orthogonal modes without using adjoint information, using a matrix pseudo-inverse, as in Or *et al.* (2008). Although this approach provides sets of bi-orthogonal modes (primal/pseudo-adjoint modes), in general it can not be regarded as an approximate balanced truncation method, since it does not balance the approximate Gramians.

We have demonstrated the methods on an model problem consisting of a disturbance interacting with the flow past an inclined flat plate. As expected, balanced POD models perform nearly identically to ERA models. The small differences result because the adjoint simulation required for balanced POD is not a perfect adjoint at the discrete level. Both procedures work significantly better than standard POD models, or ERA models using pseudo-adjoint modes for projection.

Finally, we report a version of ERA that can be applied to systems with one-dimensional instability. Unlike balanced POD, ERA for linear systems with unstable dimensions larger than one (but still small, at the order of $10^{1\sim 2}$) is still an open problem. In the next chapter we will also present a generalized version of ERA for linear, time-periodic systems.

Chapter 4

Snapshot-based balanced truncation for linear time-periodic systems

In this chapter we develop snapshot-based approximate balanced truncation methods for linear, time-periodic (LTP) systems in detail. As promised in Section 2.4, these algorithms are generalizations of the balanced POD algorithm for LTI systems. These algorithms will be applied in the next Chapter for reduced-order modeling and observer-based feedback control for periodic orbits, i.e., for vortex shedding cycles in a flow past an inclined plate with periodic open-loop forcing. Inspired by the adjoint-free balanced POD (ERA) for LTI systems we discussed in Chapter 3, here we will also construct ERA algorithms for linear time-periodic systems.

4.1 Motivation and background

Since von Kármán’s pioneering papers on the vortex street behind a bluff body (von Kármán, 1911, 1912), periodic solutions in fluid dynamics have been a focus of re-

search interest, thanks to the rich dynamics, close relations to turbulence, and interest in control of the orbits. Recent examples include periodic shedding in the wake of a bluff body (Barkley & Henderson, 1996; Noack *et al.*, 2003), stable/unstable periodic solutions within plane Couette turbulence (Kawahara & Kida, 2001; Viswanath, 2007), and systems subject to periodic open-loop forcing, e.g., to reduce the drag in a channel flow (Min *et al.*, 2006), or to increase lift or lift-to-drag ratio for wings (Joe *et al.*, 2008; Taira *et al.*, 2010). In particular, in the area of flow control, recent simulation results presented in Joe *et al.* (2008) and Taira *et al.* (2010) show that open-loop, periodic body force actuation at the leading/trailing edge of an inclined wing can result in high-lift, stable vortex shedding cycles. Furthermore, results in those works indicate the possible existence of high-lift, unstable orbits. Encouraged by these results, we are interested in developing model-based feedback control for these periodic systems to expedite the stabilization of stable vortex shedding cycles, to enlarge their region of attraction, and to stabilize the unstable cycles, if they exist. As discussed in the previous chapters, to realize this goal, it is essential to first obtain reliable reduced-order models for the linearized periodic systems to capture the linear input-output dynamics, and balanced truncation is again our choice because it provides an *a priori* input-output error bound, and guarantees stability of the reduced-order model if the full system is stable.

Early theoretical work on balanced truncation of linear time-varying/periodic systems includes Verriest & Kailath (1983); Shokoohi *et al.* (1983). For exponentially stable linear periodic systems, several algorithms based on exact balanced truncation (Lall *et al.*, 1998; Longhi & Orlando, 1999; Varga, 2000; Varga & Van Dooren, 2001; Sandberg & Rantzer, 2004; Farhood *et al.*, 2005) are available for problems with moderate dimensions. For systems with high-dimensional states, low-rank methods have been presented in Chahlaoui & Van Dooren (2006); Kressner (2003).

However the recursive low-rank Gramian algorithm (Chahlaoui & Van Dooren, 2006) and the methods presented in Kressner (2003) will give poor approximations for poorly balanced systems. The recursive low rank Hankel algorithm (Chahlaoui & Van Dooren, 2006) overcomes this problem. However it is not tractable for systems with high-dimensional outputs. The neutrally stable and unstable cases (see below) were not considered in these algorithms.

In this chapter, we introduce three snapshot-based algorithms computing approximate balanced truncations for linear time-periodic systems: the lifted balanced POD algorithm(Section 4.2), the periodic balanced POD algorithm(Section 4.3), and the corresponding lifted/periodic ERA algorithm (Section 4.5.1). These algorithms are applicable to systems with high-dimensional (at the order of $10^{5\sim 7}$) states and outputs, and being neutrally stable or unstable. Again, the balanced POD and ERA algorithms are, by construction, equivalent in the sense that they yield identical reduced-order models. Two numerical examples are shown for validation of the algorithms in Section 4.4. In the next chapter we will further show how to apply the lifted balanced POD/ERA algorithms in feedback control design for a problem of two-dimensional flow past a flat plate with periodic forcing.

The results in Section 4.2 and Section 4.4 are also reported in Ma *et al.* (2010*b*) and Ma & Rowley (2008).

4.2 Snapshot-based balanced truncation for periodic systems, using a lifting approach

We consider linear discrete-time periodic systems

$$x(k+1) = A(k)x(k) + B(k)u(k); \quad y(k) = C(k)x(k), \quad (4.1)$$

with state $x \in \mathbb{C}^n$, input $u \in \mathbb{C}^p$, output $y \in \mathbb{C}^q$, and T -periodic matrix coefficients $A(\cdot), B(\cdot), C(\cdot)$. The transition matrix in (4.1) mapping the state from time i to time j is $F_{(j,i)} := A(j-1)A(j-2) \cdots A(i)$ for $j > i$, where $F_{(i,i)} = I_{n \times n}$. Periodicity implies that the eigenvalues of $F_{(j+T,j)}$ are independent of j . The *neutrally stable* and *unstable* cases where the spectral radius $\rho(F_{(j+T,j)}) = 1$ and $\rho(F_{(j+T,j)}) > 1$, respectively, will be discussed later. For now, assume the system is *exponentially stable*, i.e., $\rho(F_{(j+T,j)}) < 1$. The *controllability* and *observability* Gramians of (4.1) are then well defined and are T -periodic in j (Varga, 2000):

$$\begin{aligned} W_c(j) &:= \sum_{i=-\infty}^{j-1} F_{(j,i+1)} B(i) B(i)^* F_{(j,i+1)}^*; \\ W_o(j) &:= \sum_{i=j}^{\infty} F_{(i,j)}^* C(i)^* C(i) F_{(i,j)}, \end{aligned} \quad (4.2)$$

where $*$ denotes the adjoint operator.

4.2.1 The lifting approach

A standard *lifting* procedure (Meyer & Burrus, 1975) recasts (4.1) in T input-output equivalent LTI forms:

$$\begin{aligned} \tilde{x}_j(t+1) &= \tilde{A}_j \tilde{x}_j(t) + \tilde{B}_j \tilde{u}_j(t); \\ \tilde{y}_j(t) &= \tilde{C}_j \tilde{x}_j(t) + \tilde{D}_j \tilde{u}_j(t), \end{aligned} \quad (4.3)$$

where j is fixed and parameterizes the lifted systems, and the state is periodically sampled from (4.1) as

$$\tilde{x}_j(t) = x(j + tT).$$

In (4.3), the augmented inputs and outputs are

$$\begin{aligned} \tilde{y}_j(t) &= \begin{bmatrix} y(j + tT) \\ y(j + tT + 1) \\ \vdots \\ y(j + (t + 1)T - 1) \end{bmatrix} \\ \tilde{u}_j(t) &= \begin{bmatrix} u(j + tT) \\ u(j + tT + 1) \\ \vdots \\ u(j + (t + 1)T - 1) \end{bmatrix}, \end{aligned} \quad (4.4)$$

and the constant matrices are

$$\begin{aligned} \tilde{A}_j &= F(j + T, j) = A(j + T - 1)A(j + T - 2) \cdots A(j) \\ \tilde{B}_j &= [F(j + T, j + 1)B(j), \cdots, \\ &\quad F(j + T, j + T - 1)B(j + T - 2), B(j + T - 1)] \\ \tilde{C}_j &= \begin{bmatrix} C(j) \\ C(j + 1)F(j + 1, j) \\ \vdots \\ C(j + T - 1)F(j + T - 1, j) \end{bmatrix} \\ \tilde{D}_j &= \begin{bmatrix} 0 & & 0 \\ F_{j,2,1} & 0 & \\ \vdots & \vdots & \ddots \\ F_{j,T,1} & F_{j,T,2} & \cdots & 0 \end{bmatrix}, \end{aligned} \quad (4.5)$$

where $F_{j,i,k} = C(j+i-1)F(j+i-1, j+k)B(j+k-1)$. The lifted setting in form (4.3) is a time- T map from state $x(j+tT)$ to state $x(j+tT+T)$ in the original time-periodic setting in form (4.1). The matrix \tilde{D}_j reflects the effect of control inputs in the time period $[j+tT, j+tT+T-1]$ to the outputs in the same period. The dimensions of the input and output of the lifted setting are Tp and Tq , compared to q and p in the original periodic setting.

Assuming exponential stability, the controllability and observability Gramians of the j -th lifted LTI system are

$$\tilde{W}_{jc} = \sum_{i=0}^{\infty} \tilde{A}_j^i \tilde{B}_j \tilde{B}_j^* \left(\tilde{A}_j^i \right)^* ; \tilde{W}_{jo} = \sum_{i=0}^{\infty} \left(\tilde{A}_j^i \right)^* \tilde{C}_j^* \tilde{C}_j \tilde{A}_j^i. \quad (4.6)$$

The following statement follows from the periodicity of (4.1).

Proposition 4.2.1. $\tilde{W}_{jc} = W_c(j)$ and $\tilde{W}_{jo} = W_o(j)$ for all $j = 1, \dots, T$.

Proposition 4.2.1 enables us to apply LTI balanced truncation, in particular balanced POD (Rowley, 2005), in the lifted domain, while keeping all Gramian computations carried in the original periodic setting, where the dimensions of the input and output are much lower.

4.2.2 Factorization of empirical Gramians using snapshot-based matrices

In snapshot-based methods (e.g. Lall *et al.* (2002); Rowley (2005)), the exact Gramians are substituted by approximate *empirical Gramians* where the infinite series in (4.2) are truncated (Chahlaoui & Van Dooren (2006); Verriest & Kailath (1983);

Shokoohi *et al.* (1983)) at a finite $m < \infty$:

$$\begin{aligned} W_{ce}(j; m) &:= \sum_{i=j-m}^{j-1} F_{(j,i+1)} B(i) B(i)^* F_{(j,i+1)}^*; \\ W_{oe}(j; m) &:= \sum_{i=j}^{j+m-1} F_{(i,j)}^* C(i)^* C(i) F_{(i,j)}. \end{aligned} \quad (4.7)$$

When the system is exponentially stable, truncation is justified by an induced norm bound on the truncation error given below:

Lemma 4.2.2. *Assume that the linear periodic system (4.1) is exponentially stable and let m be an integer multiple of the period, $m = lT$. Then the following induced norm error bounds hold:*

$$\begin{aligned} \frac{\|W_c(j) - W_{ce}(j; m)\|}{\|W_c(j)\|} &\leq \|F_{(j+T,j)}^l\|^2; \\ \frac{\|W_o(j) - W_{oe}(j; m)\|}{\|W_o(j)\|} &\leq \|F_{(j+T,j)}^l\|^2. \end{aligned} \quad (4.8)$$

Proof. By Proposition 4.2.1, $W_c(j) = \tilde{W}_{jc}$. Also, by construction $W_{ce}(j; m) = \tilde{W}_{jce}(l)$, where $\tilde{W}_{jce}(l) := \sum_{i=0}^l \tilde{A}_j^i \tilde{B}_j \tilde{B}_j^* (\tilde{A}_j^i)^*$ is the empirical controllability Gramian of the lifted LTI system at time j . Thus, $W_c(j) - W_{ce}(j; m) = \tilde{W}_{jc} - \tilde{W}_{jce}(l)$. Under any induced norm, $\|\tilde{W}_{jc} - \tilde{W}_{jce}(l)\| = \left\| \sum_{i=l}^{\infty} \tilde{A}_j^i \tilde{B}_j \tilde{B}_j^* (\tilde{A}_j^i)^* \right\| = \left\| \tilde{A}_j^l \tilde{W}_{jc} (\tilde{A}_j^l)^* \right\| \leq \|\tilde{A}_j^l\| \|\tilde{W}_{jc}\| \left\| (\tilde{A}_j^l)^* \right\| = \|\tilde{A}_j^l\|^2 \|\tilde{W}_{jc}\|$. The result for the observability Gramian follows similarly. \square

Empirical Gramians can be factorized using snapshot-based matrices.

Proposition 4.2.3. *Let $B^{(i)}$, $i = 1, \dots, p$, denote the i -th column of B , and let $X^{(i)} \in \mathbb{C}^{n \times m}$ be defined as*

$$X^{(i)}(j; m) := [F_{(j,j-m+1)} B^{(i)}(j-m), F_{(j,j-m+2)} B^{(i)}(j-m+1), \dots, B^{(i)}(j-1)]$$

for each $j = 1, \dots, T$ and the horizon length m . Finally, define the matrix of

snapshots

$$X(j; m) := [X^{(1)}(j; m), \dots, X^{(p)}(j; m)] \in \mathbb{C}^{n \times mp}. \quad (4.9)$$

Then $W_{ce}(j; m) = X(j; m)X(j; m)^*$.

Employing the T -periodicity of $B(\cdot)$ and $F(\cdot, \cdot)$ (e.g. $F_{(j, j-m+T+1)} = F_{(j-T, j-m+1)}$), one observes that the m columns of $X^{(i)}(j; m)$ are snapshots taken at time $j - kT$, $k = 0, \dots, l - 1$ (assuming $m = lT$), in T impulse-response simulations of system (4.1), each initiated at $x(j - m + t) = B^{(i)}(j - m + t - 1)$, $t = 1, \dots, T$. See an illustration in Figure 4.1(a), where the snapshots (columns of $X^{(i)}(j; m)$) are the black dots at times $j - m + T, j - m + 2T, \dots, j$. In total, Tp simulations and mp snapshots are needed to construct $X(j; m)$.

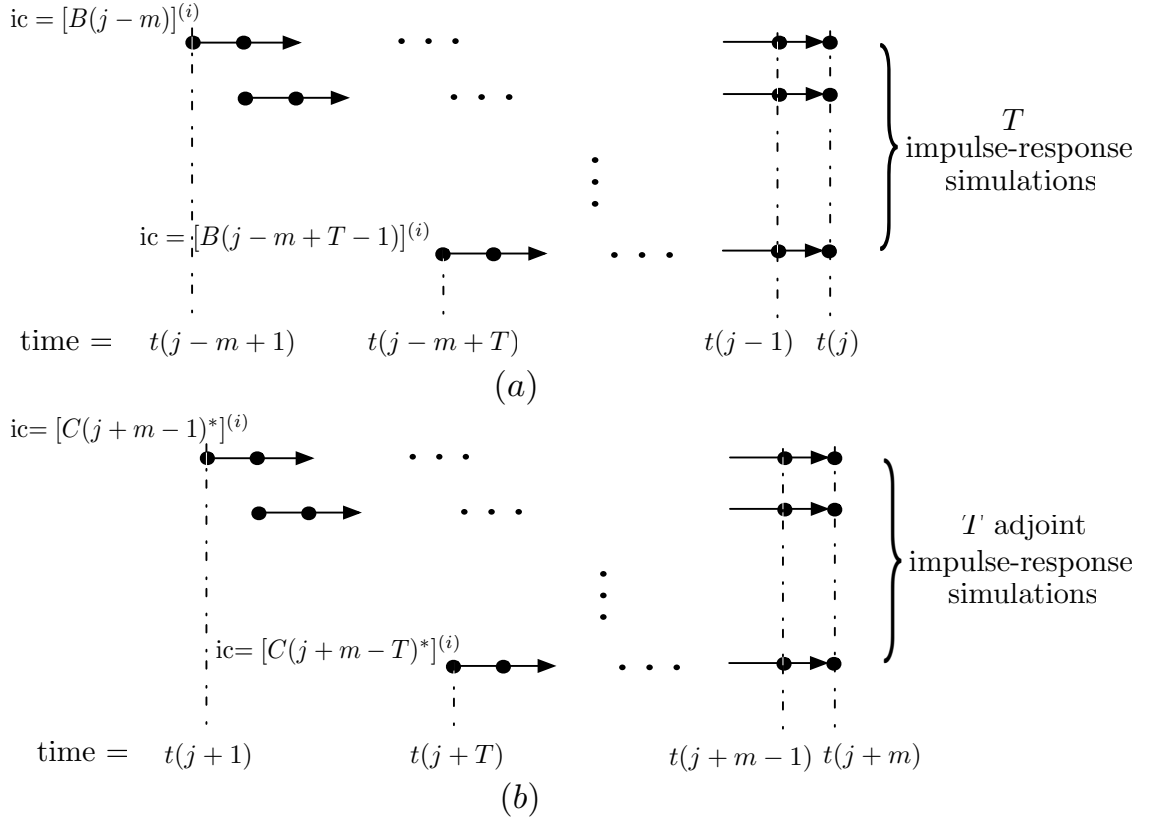


Figure 4.1: (a) The T impulse-response simulations corresponding to the i -th control input. (b) The T adjoint impulse-response simulations corresponding to the i -th adjoint control input.

An analogous observation applies to the empirical observability Gramian.

Proposition 4.2.4. *Let $C^{(i)}$, $i = 1, \dots, q$, denote the i -th row of C , and let $Y^{(i)} \in \mathbb{C}^{n \times m}$ be defined as*

$$Y^{(i)}(j; m) := [F_{(j+m-1,j)}^* C^{(i)}(j+m-1)^*, F_{(j+m-2,j)}^* C^{(i)}(j+m-2)^*, \dots, C^{(i)}(j)^*]$$

for each $j = 1, \dots, T$ and the horizon length m . Finally, let

$$Y(j; m) := [Y^{(1)}(j; m), \dots, Y^{(q)}(j; m)] \in \mathbb{C}^{n \times mq}. \quad (4.10)$$

Then $W_{oe}(j; m) = Y(j; m)Y(j; m)^*$.

As illustrated in Figure 4.1(b), $Y(j; m)$ can be obtained from impulse-response simulations of the *adjoint system*

$$z(k+1) = \hat{A}(k)z(k) + \hat{C}(k)v(k) \quad (4.11)$$

where $k = j, \dots, j+m-1$, $z \in \mathbb{C}^n$, $v \in \mathbb{C}^q$,

$$\hat{A}(k) := A(2j+m-k-1)^*$$

$$\hat{C}(k) := C(2j+m-k-1)^*.$$

The columns of $Y^{(i)}(j; m)$ are the snapshots (the black dots in the plot) taken at times $j+T, j+2T, \dots, j+m$. In total, Tq adjoint simulations and mq snapshots taken at time $j+kT$, $k = 1, \dots, l$ are needed to construct $Y(j; m)$.

4.2.3 Balanced truncation using the method of snapshots

Fix a time index $1 \leq j \leq T$ for lifting. Assume one has computed $X(j; m_c)$ and $Y(j; m_o)$, the factors of the empirical Gramians $W_{ce}(j; m_c), W_{oe}(j; m_o)$ (allowing $m_c \neq m_o$). By Lemma 4.2.2 and Proposition 4.2.1, they are in fact factors that approximate the Gramians of the j -th *lifted LTI* system (4.3), as given in (4.6).

The method of snapshots presented in Rowley (2005) then leads to approximate balanced truncations in the lifted LTI setting, as follows: Compute the SVD

$$Y(j; m_o)^* X(j; m_c) = U \Sigma V^*, \quad (4.12)$$

and the transformations Φ , Ψ that *exactly* balance the empirical Gramians of the lifted system

$$\Phi = X(j; m_c) V \Sigma^{-1/2}; \quad \Psi = Y(j; m_o) U \Sigma^{-1/2}. \quad (4.13)$$

Let Φ_r, Ψ_r be the first r columns of Φ and Ψ , comprising the leading bi-orthogonal balancing and adjoint modes of the j -th lifted system. (Note that to simplify notation, the dependence of $U, V, \Sigma, \Phi, \Psi, \Phi_r, \Psi_r$ on j is suppressed.) The reduced state $\tilde{z}_j(t) \in \mathbb{C}^r$ is defined by the projection $\tilde{z}_j(t) = \Psi_r^* \tilde{x}_j(t) = \Psi_r^* x(j + tT)$ and the estimated full state $x(j + tT) \approx \Phi_r \tilde{z}_j(t)$. The reduced model of order r , in the lifted setting, reads

$$\begin{aligned} \tilde{z}_j(t+1) &= \Psi_r^* \tilde{A}_j \Phi_r \tilde{z}_j(t) + \Psi_r^* \tilde{B}_j \tilde{u}_j(t); \\ \tilde{y}_j(t) &= \tilde{C}_j \Phi_r \tilde{z}_j(t) + \tilde{D}_j \tilde{u}_j(t), \end{aligned} \quad (4.14)$$

In simulations, the reduced output equation in (4.14) shall be lowered to the original periodic setting: For each $i, i = 1, \dots, T$,

$$\begin{aligned} y(j + tT + i - 1) &= C(j + i - 1) F(j + i - 1, j) \Phi_r \tilde{z}_j(t) \\ &\quad + \sum_{k=1}^T \tilde{D}_{j(i,k)} u(j + tT + k - 1), \end{aligned} \quad (4.15)$$

where $\tilde{D}_{j(i,k)}$ denotes the entry of \tilde{D}_j at i -th row and k -th column.

Input-output equivalence of the original system (4.1) to the lifted LTI (4.3) means that the reduced-order LTI system approximates the input-output dynamics of the linear periodic system (4.1). Note that improved numerical stability of the computations above can be achieved by first representing each of the factors $X(j; m_c)$ and

$Y(j; m_o)$ in terms of leading orthogonal bases, obtained, e.g., by SVD or by Krylov methods.

“Un-lift” the reduced LTI system. The reduced-order lifted system updates the state only once every period. However, as described in Ma *et al.* (2010b), it is still possible to “lower” the system to a periodic one, supposing that the balancing requirement is limited to the periodically sampled system (i.e., to the lifted system with the fixed j). The following inductive procedure is one possible solution: Consider T -periodic sets $\{\Phi(k)\}_{k=1}^T$ and $\{\Psi(k)\}_{k=1}^T$. First, fix $\Phi(j) = \Phi_r$ and $\Psi(j) = \Psi_r$. Let $P(j+i)$ be the rank- r orthogonal projection on $\mathcal{I}m(F_{(j+i,j)}\Phi(j))$ and let $\Phi(j+i) = \Psi(j+i) \in \mathbb{C}^{n \times r}$, $i = 1, \dots, T-1$, satisfy $P(j+i) = \Phi(j+i)\Psi(j+i)^*$. Then a periodic realization of the reduced order system can be defined by $A_r(k) := \Psi(k+1)^*A(k)\Phi(k)$, $B_r(k) := \Psi(k+1)^*B(k)$ and $C_r(k) := C(k)\Phi(k)$. This is because, by construction, $A_r(j+T-1) \cdots A_r(j) = \Psi_r^* \tilde{A}_j \Phi_r$, the reduced state transition matrix given in the reduced-order lifted system (4.14).

4.2.4 Output projection method

The lifting approach generates a LTI system (4.3) whose dimension of output is T times larger than that in the periodic setting (4.1); see (4.4). The number of adjoint simulations (see Section 4.2.2) required for the above reduction procedures can thus be untenable, if the period T is large, and/or if the original output in the periodic setting is of high dimension. The latter case happens, for instance, when the original output is set identical to the entire state for system dynamics analysis or full-state feedback control design. A generalization of output projection method (Rowley (2005); also see Section 2.3.2) for periodic systems is therefore necessary.

In the LTI case, Rowley (2005) proposed projecting the output on a few leading POD modes of the output dataset formed by the impulse response simulations. The dimension of the output space is thus reduced by invoking the *kinematic* significance of POD modes, while at that same time we avoid the potential weakness of standard POD/Galerkin models that use POD modes as *dynamic* states. Here we extend the output projection method to periodic systems.

The input-output map of the j -th lifted LTI system (4.3) is determined by the $Tq \times Tp$ dimensional impulse-response matrices $\{\tilde{G}_j(t)\}$. The *output-projected* lifted system

$$\begin{aligned}\tilde{x}_j(t+1) &= \tilde{A}_j \tilde{x}_j(t) + \tilde{B}_j \tilde{u}_j(t); \\ \tilde{y}_j(t)_P &= \tilde{P}_j \left(\tilde{C}_j \tilde{x}_j(t) + \tilde{D}_j \tilde{u}_j(t) \right),\end{aligned}\tag{4.16}$$

is designed to best approximate the exact impulse response of the original lifted system. Ideally, the low-rank orthogonal projection matrix \tilde{P}_j should thus satisfy

$$\tilde{P}_j = \underset{\{\tilde{P}_j \in \mathcal{P}_{\tilde{r}_{op}}\}}{\operatorname{argmin}} \left(\sum_{t=0}^{\infty} \|\tilde{G}_j(t) - \tilde{P}_j \tilde{G}_j(t)\|^2 \right),\tag{4.17}$$

where $\mathcal{P}_{\tilde{r}_{op}}$ is the space of orthogonal projections of rank $\tilde{r}_{op} \ll Tq$. When the Frobenius norm $\|\cdot\|_F$ is used in (4.17), it becomes a standard projection problem. Its solution is $\tilde{P}_j = \tilde{\Theta}_j \tilde{\Theta}_j^*$, where the columns of $\tilde{\Theta}_j$ are the leading \tilde{r}_{op} POD modes of the datasets $\{\tilde{G}_j(i)\}_{i=0}^{\infty}$.

As described above, the optimal \tilde{P}_j is generically a full matrix. Thus, $\tilde{y}_j(t)_P = \tilde{P}_j \tilde{y}_j(t)$ is no longer the lifted representation of the output of a periodic system, and the projected system cannot be "lowered". Rather, for each t , the value of $\tilde{y}_j(t)_P$ is determined by the original response along an entire period. In particular, we lose the ability to compute the Gramian in the original periodic setting. To avoid this problem we impose on (4.17) the additional condition that the projection has

a block diagonal form

$$\tilde{P}_j = \text{diag} \left[\tilde{P}_j(1), \dots, \tilde{P}_j(T) \right], \quad (4.18)$$

where each $q \times q$ diagonal block is a rank- r_{op} orthogonal projection with $\tilde{r}_{op} = r_{op}T$. This enables to lower the projected lifted system (4.16) to an *output-projected time-periodic system*

$$\begin{aligned} x(k+1) &= A(k)x(k) + B(k)u(k); \\ y(k)_P &= P(k)C(k)x(k), \end{aligned} \quad (4.19)$$

where the T -periodic, rank- r_{op} orthogonal projection P is defined by $P(j+tT+i) = P(j+i) := \tilde{P}_j(i+1)$, $i = 0, \dots, T-1$. The constrained optimization problem (4.17) and (4.18) can be solved as unconstrained problems in the periodic setting. First, rewrite $\tilde{G}_j(t)$ as

$$\tilde{G}_j(t) = \left[G(j+tT, j)^\top \quad \dots \quad G(j+(t+1)T-1, j)^\top \right]^\top$$

where each block $G(j+tT+i, j)$, $i = 0, \dots, T-1$, is a $q \times Tp$ matrix. For the periodic system (4.1), define each $G(j+tT+i, j)$ as its impulse-response matrix at time $(j+tT+i)$, since it includes all different responses at the current time respectively to corresponding unit impulse inputs during the whole time period $[j, j+T-1]$. This definition matches that in Bamieh & Pearson (1992). We have

Proposition 4.2.5. *Using the Frobenius norm, the solution of the constrained optimization problem (4.17) and (4.18) is equivalent to the combined solution of the problems*

$$\tilde{P}_j(i+1) = \underset{\{\tilde{P}_j(i+1) \in \mathcal{P}_{r_{op}}\}}{\text{argmin}} \left(\sum_{t=0}^{\infty} \left\| G(j+tT+i, j) - \tilde{P}_j(i+1)G(j+tT+i, j) \right\|_F^2 \right),$$

for $i = 0, \dots, T-1$.

Proof. By direct calculation, and the linearity of the trace operator. \square

The computation of the structurally constrained optimal \tilde{P}_j of the form (4.18) is thus reduced to T unconstrained optimization problems for each $P(k)$, $k = j, \dots, j + T - 1$, in the periodic setting. Following standard POD rationale, the solutions are $P(k) = \Theta(k)\Theta(k)^*$, where the r_{op} columns of $\Theta(k)$ are the leading POD modes of the dataset $\{G(tT + k, j)\}_{t=0}^\infty$, and the approximation error between the output-projected system and the original system is

$$\begin{aligned} \sum_{t=0}^{\infty} \|\tilde{G}_j(t) - \tilde{P}_j \tilde{G}_j(t)\|_F^2 &= \sum_{i=j}^{j+T-1} \sum_{t=0}^{\infty} \left\| G(tT + i, j) - \tilde{P}_j(i+1)G(tT + i, j) \right\|_F^2 \\ &= \sum_{i=j}^{j+T-1} \sum_{m=r_{op}+1}^q \lambda(i)_m, \end{aligned}$$

where for each i , $\lambda(i)_1, \dots, \lambda(i)_q$ are the descending-ordered eigenvalues $\sum_{t=0}^{\infty} G(tT + i, j)G(tT + i, j)^*$. The POD modes can be computed by the method of snapshots Sirovich (1987), applied to datasets comprising the columns of the impulse-response matrices $\{G(tT + i, j)\}_{t=0}^s$. Conveniently, provided that $m_c \geq (s+1)T$, periodicity implies that data required to compute these snapshots have already been obtained during the computation of $X(j; m_c)$, as described in Section 4.2.2. For instance, the matrix $C(j)X(j; m_c)$ includes the columns of matrices $\{G(j + tT, j)\}_{t=1}^{m_c/T}$.

The empirical factor $Y(j; m_o)$ of the corresponding observability Gramian

$$W_{oP}(j) = \sum_{i=j}^{\infty} F_{(i,j)}^* C(i)^* \Theta(i) \Theta(i)^* C(i) F_{(i,j)}$$

is needed in order to realize the snapshot-based approximate balanced truncation for the output-projected system (4.19). This is accomplished with only Tr_{op} ($r_{op} \ll q$) impulse-response simulations of the *projected adjoint time-periodic system* that corresponds to the output-projected system (4.19), i.e.

$$z(k+1) = \hat{A}(k)z(k) + \hat{C}_P(k)v_{r_{op}}(k) \quad (4.20)$$

where $k = j, \dots, j + m_o - 1$, the control input v_{rop} is r_{op} -dimensional, and

$$\begin{aligned}\hat{A}(k) &= A(2j + m_o - k - 1)^*, \\ \hat{C}_P(k) &= C(2j + m_o - k - 1)^* \Theta(2j + m_o - k - 1).\end{aligned}$$

In closing we note that, for additional simplicity and a requirement of a single SVD computation, one can also use a single, time-invariant output projection. Under this constraint, the optimal selection is $P = \Theta \Theta^*$, where the columns of Θ are the leading POD modes of the entire impulse-response $\{\{G(tT + k, j)\}_{t=0}^s\}_{k=j}^{j+T-1}$ of (4.1). This stronger constraint implies further reduction in matching, when compared with the optimal solution in the lifted domain.

4.2.5 Algorithm summary: the lifted BPOD

Following the terminology in Rowley (2005), the approximate balanced truncation method for linear, time-periodic systems using a lifting approach is termed a *lifted balanced POD*. Its main steps include:

- Step 0: Fix a time j , $1 \leq j \leq T$, as the time point for lifting.
- Step 1: Run Tp impulse-response simulations to obtain m_cp snapshots and form the $n \times m_cp$ dimensional $X(j; m_c)$ as described in Section 4.2.2.
- Step 2: Compute $y = Cx$ from stored states in simulations carried to compute $X(j; m_c)$. Solve for the POD problems for the periodically sampled $y(j + tT + i)$, to obtain the output-projection matrices $\Theta(j + i)$, $i = 0, \dots, T - 1$.
- Step 3: Run Tr_{op} impulse-response simulations of the adjoint output-proejected system, to form the $n \times m_or_{op}$ dimensional matrix $Y(j; m_o)$ as described in Section 4.2.2.

- Step 4: Compute the SVD of $Y(j; m_o)^* X(j; m_c)$ and the balancing modes for the lifted system given by (4.13).
- Step 5: Compute the reduced lifted system (4.14). The entries in \tilde{D}_j are outputs that can be collected in direct impulse responses.

Variants include skipping Step 2, when the output dimension in the lifted setting qT is small, and using a single, time-invariant output projection, as discussed in Section 4.2.4. The reduced system can be lowered to a periodic system, e.g., as described in closing Section 4.2.3.

As discussed in Section 2.3.2 for the balanced POD method for LTI systems, one can readily apply a “dual” version of the above algorithm for balanced truncations of linear periodic systems with high-dimensional states and inputs, but only few outputs. *Input projections* are needed to project inputs onto leading POD modes of the dataset of outputs obtained in adjoint impulse-response simulations.

4.2.6 The neutrally stable/unstable case

Consider a linear periodic system (4.1) that arises from linearization of a nonlinear system $x(k+1) = f(x(k))$ around an asymptotically stable periodic orbit. By Floquet theory (Hartman, 1964, §§ IV.6, IX.10), in this case $\tilde{A}_j = F_{(j+T,j)}$ is only neutrally stable, due to *one* unity eigenvalue that corresponds to persisting perturbations along the periodic orbit in the linearization. Balanced truncation cannot be directly applied to a neutrally stable system, as the infinite series used to define Gramians may diverge.

An extended version of balanced POD for unstable LTI systems that have small unstable dimensions is presented in Ahuja & Rowley (2010) (also see Sections 2.2.1,

2.3.3). Following the idea presented in Zhou *et al.* (1999), it decomposes the system dynamics into stable and unstable parts. Then it applies approximate balanced truncation to the stable dynamics while keeping the unstable dynamics exactly. This method is conceptually applied here to periodic systems through the lifted setting, with all computations executed in the periodic setting. First, for a given lifting time j , define a projection onto the stable subspace $E^s(\tilde{A}_j)$ by

$$\mathbb{P}_j = I_{n \times n} - \frac{v_j w_j^*}{w_j^* v_j}, \quad (4.21)$$

where $w_j, v_j \in \mathbb{C}^n$ are the left/right eigenvectors of \tilde{A}_j corresponding to the unity eigenvalue. Dynamics of the neutrally stable lifted system (4.3) is thus restricted to the stable subspace of \tilde{A}_j :

$$\begin{aligned} \tilde{x}_j(t+1)_s &= \tilde{A}_j \tilde{x}_j(t)_s + \mathbb{P}_j \tilde{B}_j \tilde{u}_j(t); \\ \tilde{y}_j(t)_s &= \tilde{C}_j \mathbb{P}_j \tilde{x}_j(t)_s + \tilde{D}_j \tilde{u}_j(t), \end{aligned} \quad (4.22)$$

where $\tilde{x}_j(t)_s = \mathbb{P}_j \tilde{x}_j(t)$. (The dimension of state $\tilde{x}_j(t)_s$ of the projected system is still n .) Lifted balanced POD can be realized to this projected system describing stable dynamics. Let $\Phi_{r_s}^s$ and $\Psi_{r_s}^s$ be the matrices including the leading r_s balancing and adjoint modes of the projected system (4.22). Then, a reduced model of order r , $r = r_s + 1$, for the neutrally stable lifted system (4.3) can be obtained in the form of (4.14), where now

$$\Phi_r = \begin{bmatrix} \Phi_{r_s}^s & v_j \end{bmatrix}; \quad \Psi_r = \begin{bmatrix} \Psi_{r_s}^s & \frac{w_j}{w_j^* v_j} \end{bmatrix}. \quad (4.23)$$

The reduced system keeps the one-dimensional neutrally stable dynamics exactly, while the exponentially stable dynamics is reduced to the order of r_s .

Numerically, the neutrally stable eigenvectors of \tilde{A}_j can be calculated using a Krylov method, or even the power method: By running a control-free simulation of the periodic system (4.1) with an arbitrary initial condition $x(j) \notin E^s(\tilde{A}_j)$, one can

approximate v_j by $x(j + lT)$, with a large l . Similarly, a long-time control-free simulation of the adjoint periodic system (4.11) is needed to approximate w_j . Then, when computing the transformations $\Phi_{r_s}^s$ and $\Psi_{r_s}^s$ for the projected system (4.22), one follows exactly the same procedures given in Section 4.2.5. The only difference is that in the Tp simulations of the periodic system (4.1) described in Section 4.2.2, the states should be projected onto $E^s(\tilde{A}_j)$ by \mathbb{P}_j at time $j - m + T$. The simulations then resume with these states as new initial conditions. Similarly, in the adjoint simulations, the adjoint states should be left-multiplied by \mathbb{P}_j^* at time $j + T$ before the simulations resume.

By construction, this method is applicable to other neutrally stable/unstable periodic systems, with small neutrally stable/unstable dimensions (e.g., at the order of $10^{1\sim 2}$). For unstable systems, in impulse-response simulations one can repeatedly project the states once each period, using \mathbb{P}_j , to numerically confine the dynamics to the stable invariant subspace.

4.3 An alternative algorithm: a periodic approach

The lifting approach enables us to apply LTI balanced truncation methods in the lifted domain. However, unless a “lowering” method, such as the one introduced in Section 4.2.3, is used, the lifted reduced-order system (4.14) updates the reduced-order state indeed only once per period in the periodic setting. This might cause delay in the feedback control input update. To avoid this problem, one can alternatively use a “periodic approach” to construct a time periodic reduced-order model.

By the “periodic approach”, we mean that the Petrov-Galerkin projection and trun-

cation procedure is done at each time step along a whole period. T -periodic balancing transformations are computed and then a T -periodic reduced system is generated. An exact periodic balanced truncation keeps the stability of the original system, and has an upper error bound (Longhi & Orlando (1999); Varga (2000)). Here, we develop a snapshot-based, periodic balanced POD approach.

Consider the exponentially stable case. We need to construct the factors $X(j; m_c)$ and $Y(j; m_o)$ of the Gramians, given by (4.9) and (4.10), now for every $j = 1, \dots, T$. In Section 4.2.2 we show that Tp impulse-response simulations are needed to construct *one* $X(j; m_c)$. Indeed, by employing T -periodicity, one shows quickly that these Tp simulations, each with a different start time and initial condition, are enough to obtain all the m_cpT snapshots needed for construction of *all* the T $X(j; m_c)$ s. The difference is that now each simulation needs to be run for $(m_c - 1)$ steps (see Figure 4.2), and that snapshots are taken *at every time step* in all simulations: For each j , $j = 1, \dots, T$, the m_cp columns of $X(j; m_c)$ are just the m_cp snapshots taken at time $j, j - T, j - 2T \dots$, in the Tp simulations. As before, we suppose m_c to be an integer multiple of the period T .

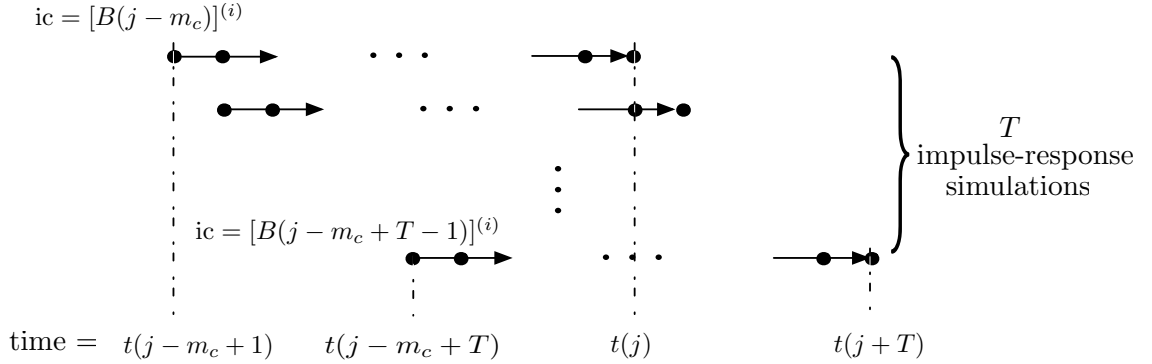


Figure 4.2: The T impulse-response simulations corresponding to the i -th control input, each beginning with a different initial time, for the periodic approach, .

Similarly, to construct $Y(j; m_o)$, $j = 1, \dots, T$, only Tq (or Tr_{oq} , if a output projection is needed) adjoint simulations, as those described in Section 4.2.2, are needed,

each with a different initial time and initial condition, and running for $(m_o - 1)$ steps. For each $j = 1, \dots, T$, all snapshots taken at time $j, j + T, \dots$ shall be collected as columns for $Y(j; m_o)$.

One then performs T SVD calculations:

$$Y(j; m_o)^* X(j; m_c) = U(j) \Sigma(j) V(j)^*, \quad j = 1, \dots, T. \quad (4.24)$$

to calculate the T -periodic balancing transformations

$$\Phi(j) = X(j; m_c) V(j) \Sigma(j)^{-1/2}; \quad \Psi(j) = Y(j; m_o) U(j) \Sigma(j)^{-1/2}. \quad (4.25)$$

Finally, the T -periodic reduced system of order r reads

$$\begin{aligned} x(k+1) &= \Psi_r^*(k+1) A(k) \Phi_r(k) x(k) + \Psi_r^*(k+1) B(k) u(k) \\ y(k) &= C(k) \Phi_r(k) x(k), \end{aligned} \quad (4.26)$$

where $\Phi_r(k)$ and $\Psi_r^*(k)$ are respectively the first r columns and rows of $\Phi(k)$ and $\Psi_{(k)}^*$. The periodic procedure is regarded as approximate balanced truncation because all the T pairs of empirical Gramians, $W_{ce}(j; m_c) = X(j; m_c) X(j; m_c)^*$, $W_{oe}(j; m_o) = Y(j; m_o) Y(j; m_o)^*$ are exactly balanced. One difference between the lifting and periodic approach is that in the lifting approach the pair of bi-orthogonal modes for projection is the balancing/adjoint modes taken at the same time phase; whereas in the periodic approach they are taken from consecutive time phases. By construction, both the time-periodic and the time-invariant output projection methods introduced in Section 4.2.4 are directly applicable to this periodic approach.

4.3.1 The neutrally stable/unstable case

For the neutrally stable case that has one unity eigenvalue in the lifted setting, we outline an algorithm that is a periodic counterpart of the algorithm presented in

Section 4.2.6. Theoretical details can be found in Appendix B. One first runs a pair of control free primal/adjoint simulations of system (4.1), as those described in Section 4.2.6, with initial $x(0) \notin E^s(\tilde{A}_0), z(0) \notin E^s(\tilde{A}_0^*)$, each for a long time $(l+1)T$. The “asymptotic residues” at different time $lT+j, j=1, \dots, T$, are approximations of the neutrally stable right/left eigenvectors v_j, w_j . The T -periodic projection matrices $\{\mathbb{P}_k\}_{k=1}^T$ are then calculated by (4.21). One then executes the periodic balanced truncation procedures given above for the projected, exponentially stable, periodic system

$$\begin{aligned} x(k+1) &= A(k)\mathbb{P}_k x(k) + \mathbb{P}_{k+1} B(k)u(k); \\ y(k) &= C(k)\mathbb{P}_k x(k). \end{aligned} \tag{4.27}$$

Note that by properties of the projections $\{\mathbb{P}_k\}_{k=1}^T$ (see Appendix B), the direct/adjoint impulse-response simulations of (4.27) are indeed the same as those of the original neutrally-stable periodic system, except the initial conditions shall now be left-multiplied by the corresponding \mathbb{P}_{k+1} or \mathbb{P}_k^* . Let $\{\Phi_{r_s}(k)\}_{k=1}^T, \{\Psi_{r_s}(k)\}_{k=1}^T$ be T -periodic pairs of matrices including the T -periodic leading r_s corresponding balancing/adjoint modes of the projected system (4.27). Then, a T -periodic reduced-order model of order $r, r = r_s + 1$, for the original periodic system (4.1) can be obtained in the form of (4.26), where now the T -periodic transformations are

$$\Phi_r(k) = \begin{bmatrix} \Phi_{r_s}(k) & v_k \end{bmatrix}; \quad \Psi_r(k) = \begin{bmatrix} \Psi_{r_s}(k) & \frac{w_k}{w_k^* v_k} \end{bmatrix}. \tag{4.28}$$

Again, for other neutrally stable/unstable systems with small dimensions of neutral stability/unstability, this procedure is also applicable, where the T -periodic projection matrices can be obtained by, e.g., Krylov methods.

4.3.2 Comparison with the lifting approach

Computational cost. Compared to the lifted balanced POD method presented in Section 4.2, the periodic approach is much more computationally expensive, especially when T is large, due to storage of T times more snapshots, and requirement of T SVD computations. We will see in the following numerical example (Section 4.4.1) that although it is more computationally expensive, the periodic approach does not necessarily outperform the lifting approach.

Reduced-order models: Lifted LTI vs time periodic. Reduced-order models yielded by the periodic approach are time T -periodic. That means the reduced states are updated every time step, not once per period as in the lifting approach, unless the lifted system is lowered as discussed at the end of Section 4.2. In feedback control design, the periodic approach therefore avoids potential big delay of control input update caused by updating the states only once a period. The trade-off is that, instead of well-developed control theory for LTI systems, more sophisticated control techniques for time-varying systems should be employed.

Stability Both lifting and periodic approaches are approximate balanced truncation methods, which implies there is no guarantee on the stability of reduced-order models. In the lifting approach, the stability of the reduced-order model is determined by the reduced, lifted transition matrix (see (4.14))

$$\tilde{A}_r = \Psi_r^*(j) \tilde{A}_j \Phi_r(j) = \Psi_r^*(j) A(j+T-1) \cdots A(j) \Phi_r(j),$$

where j is the time index for lifting. Compared to a reduced-order model by exact balanced truncation (where the stability is guaranteed), the only error source of \tilde{A}_r is the pair of approximate balancing/adjoint modes $\Psi_r(j), \Phi_r(j)$ that are computed

using factors of empirical (approximate) Gramians at time j .

In comparison, the stability of the time-periodic, reduced-order model is determined by the T products of periodic transition matrices (see (4.26))

$$\begin{aligned}\tilde{A}_r &= A_r(j+T-1) \cdots A_r(j) \\ &= \Psi_r^*(j)A(j+T-1)\Phi_r(j+T-1) \cdots \Psi_r^*(j+1)A(j)\Phi_r(j).\end{aligned}$$

Here the error in \tilde{A}_r results from using all the T pairs of approximate balancing/adjoint modes $\Phi_r(k), \Psi_r(k)$, $k = 1, \dots, T$. We thus speculate that, due to the involvement of more error sources in \tilde{A}_r and in turn larger error in the eigenvalues of \tilde{A}_r , reduced-order models by the periodic approach is more liable to lose stability than those obtained by the lifting approach. More analysis is needed to make a definite conclusion.

4.4 Numerical examples

To validate and demonstrate the balanced POD algorithms for linear time-periodic systems, we present two numerical examples in this section.

4.4.1 Example 1: A randomly generated system

We first consider the following exponentially stable example (similar to that in Farhood *et al.* (2005)): a linear periodic system (4.1) with period $T = 5$, state dimension $n = 30$, output dimension $q = 30$, control input dimension $p = 1$, and $\{A(k)\}_{k=1}^5$ are randomly generated diagonal matrices with diagonal entries bounded in $[0.16, 0.96]$, guaranteeing exponential stability. The matrices $B(k)$ and $C(k)$ are also randomly generated, with entries bounded in $[0, 1]$.

Using lifted balanced POD, here we pick the “lifting time” $j = 1$. Choose $m_c = m_o = 3T = 15$. Figure 4.3 (a) shows the error plots of the infinity norm, $\|\tilde{G} - \tilde{G}_r\|_\infty / \|\tilde{G}\|_\infty$ versus r , the order of the reduced lifted system. Here \tilde{G}_r is the impulse-response matrix of the reduced lifted system of order r . We see that the snapshot-based balanced truncation gives a good approximation of exact balanced truncation. Further, the balanced POD, even with low orders of output projection r_{op} , generates satisfying results. Recall that, for the lifted system, the order of output projection is $\tilde{r}_{op} = r_{op}T$.

Results using the periodic approach are shown in Figure 4.3 (b) for comparison. Here we lift the reduced periodic system of order r to its lifted LTI setting with lifting time $j = 1$, so that we can compare the periodic and lifting approaches directly. Results show that, with the same reduction order and order of output projection, the lifting approach generates a reduced model whose input-output behavior is closer to that of that full system. Note that we reach the same conclusion in a similar comparison done in the periodic setting. In that comparison, the outputs of the reduced lifted system by lifted balanced POD are first lowered to the periodic setting. Considering also the higher computational cost of the periodic approach, from now on we will focus on the applications of the lifting approach.

Figure 4.4 shows comparisons between lifted balanced POD results with the same order of output projection, one set based on T -periodic projection matrices along one period, and the other using a single time-invariant projection matrix (see Section 4.2.4). For the cases where r_{op} are low, these two approaches give almost identical results, or even the latter one gives better results. However, when the order of output projection r_{op} increases, the results based on T -periodic projection matrices are better than those by a single projection matrix, as we expect.

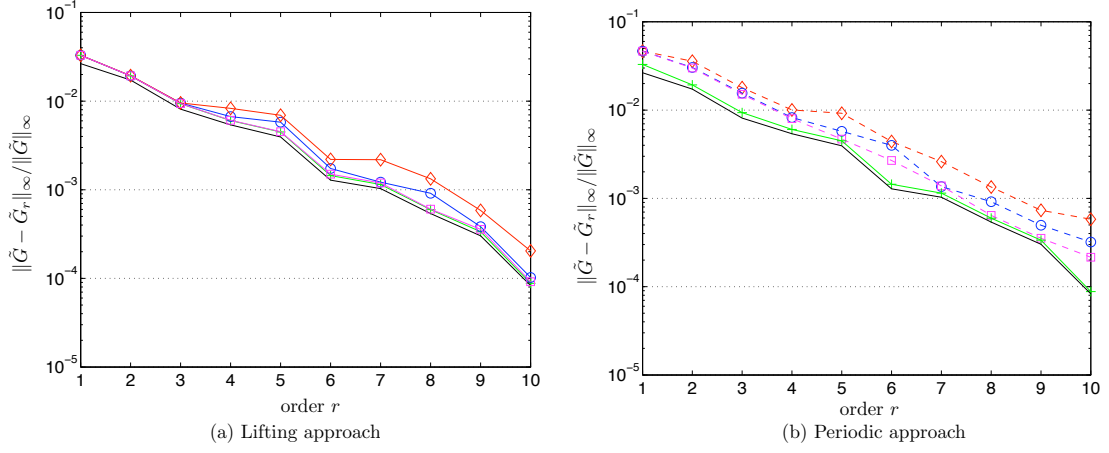


Figure 4.3: Error $\|\tilde{G} - \tilde{G}_r\|_\infty / \|\tilde{G}\|_\infty$, for (a) lifted balanced POD approach, and (b) the periodic approach. $m_c = m_o = 3T$. For exact balanced truncation(+), balanced truncation by the method of snapshots but without output projection(\square), balanced POD with $r_{op} = 1$ (\diamond), balanced POD with $r_{op} = 3$ (\circ), and the lower bound for any model reduction scheme ($-$).

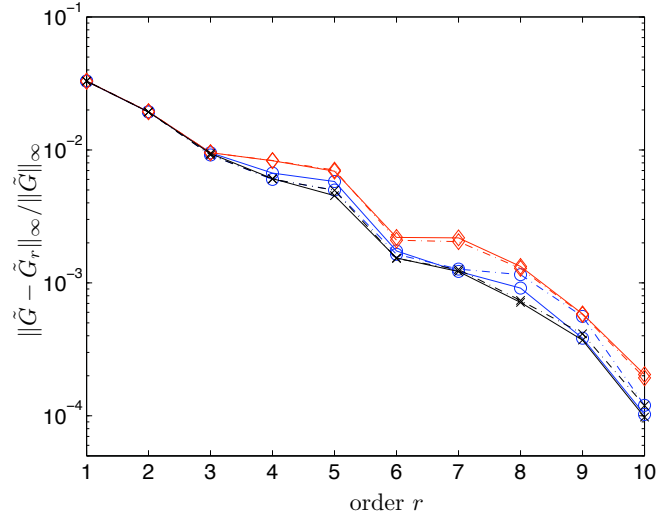


Figure 4.4: Time varying T -periodic output projections versus time-invariant output projections: Error $\|\tilde{G} - \tilde{G}_r\|_\infty / \|\tilde{G}\|_\infty$, by lifted balanced POD with $r_{op} = 1$ (\diamond), with $r_{op} = 3$ (\circ) and with $r_{op} = 5$ (\times). Solid lines correspond to cases using T different projection matrices along one period for the periodic system, and dashed lines using one single projection matrix. The black solid line is the lower bound for any model reduction scheme ($-$).

4.4.2 Example 2: Application to the Ginzburg-Landau equation (a neutrally stable case)

The well-known nonlinear complex Ginzburg-Landau (GL) equation is a one dimensional partial differential equation that demonstrates spatially developing flows

and can be used to study convective/global instabilities in fluids. See recent review papers Chomaz (2005); Bagheri *et al.* (2009b) and the references therein. Consider the complex nonlinear GL equation

$$\frac{\partial q}{\partial t} = -\nu \frac{\partial q}{\partial x} + \gamma \frac{\partial^2 q}{\partial x^2} + \mu(x)q + f(q), \quad (4.29)$$

where $\nu, \gamma \in \mathbb{C}$ are convection and diffusion coefficients, the real “coefficient of stability” $\mu(x) = (\mu_0 - c_u^2) + \mu_2 x^2/2$, and the nonlinear forcing term $f(q) = -a|q|^2 q$. The model parameters $c_u, \mu_0, \mu_2, a \in \mathbb{R}$. The nonlinear GL undergoes a supercritical Hopf bifurcation when the bifurcation parameter μ_0 crosses a critical μ_c : For $\mu_0 < \mu_c$, there is a stable equilibrium; for $\mu_0 > \mu_c$, an asymptotically stable periodic orbit emerges, while the equilibrium loses its stability. The GL is extensively used to model cylinder wakes that have a similar bifurcation behavior: The wake is steady (stable equilibrium) when the Reynolds number is below a critical value. For higher Reynolds numbers, the equilibrium state becomes unstable and a Karman vortex street (stable periodic orbit) appears. The parameter μ_0 in GL can be linked to the Reynolds number (Roussopoulos & Monkewitz, 1996).

Bagheri *et al.* (2009b) studied model reduction and controller design for a linear time-invariant GL obtained from linearization about its equilibrium state. Recently, Ilak *et al.* (2010) studied reduced order modeling of the nonlinear, transient dynamics by projecting the nonlinear GL onto balancing modes corresponding to the equilibrium. Here we consider the linear periodic system obtained from linearization about the stable periodic orbit in the $\mu_0 > \mu_c$ case.

The GL is first spatially discretized into a nonlinear ODE system using Hermite collocation (Bagheri *et al.*, 2009b). By choosing the number of Hermite collocation points $n = 50$, we consider the solution of GL in a finite domain for computation $[-20.5644, 20.5644]$. The parameter values used in simulations are $\gamma = 1 - 0.1i$,

$\nu = 2 + 0.6i$, $c_u = 0.3$, $\mu_2 = -0.08$, $a = 0.005$. One computes $\mu_c = 1.1318$ and chooses $\mu_0 = 1.1771 > \mu_c$. These parameters ensure the existence of a nonlinear stable periodic orbit. The Crank-Nicolson method is used for time discretization. With $\Delta t = 0.093271125$, the nonlinear stable orbit has a period $T = 100$. A linear, discrete system that has T -periodic $A(k)$'s is then obtained by linearization about the orbit. Note that the nonlinear term $f(q) = -a|q|^2q$ does not satisfy the Cauchy-Riemann conditions for any $q \neq 0$. Thus, linearization is done for the real and imaginary parts of the GL separately, and the resulting system is real but twice the dimension. We choose the system output y identical to the states, resulting in $C(k)$ s as a time-invariant identity matrix. Suppose a single input case, with a time-invariant $B(k)$ representing a Gaussian distribution $\exp(-[(x + \sqrt{-2\mu_0/\mu_2})/1.6]^2)$, as in Bagheri *et al.* (2009b). The resulting linear, neutrally-stable, time-periodic system is in the form (4.1), with $D(k) = 0$. Figure 4.5(a) and (b) show the nonlinear stable periodic orbit, and the oscillation that persists for the linear, neutrally-stable, periodic system for a control free case. Figure 4.5(c) shows that, for the linear periodic system, with a projected initial condition $q(1) \in E^s(\tilde{A}_1)$ (see Section 4.2.6), the oscillations due to the neutral stability are eliminated to the level of machine precision.

The neutrally stable, linearized GL is then reduced using lifted balanced POD, at the lifting time $j = 1$. Figure 4.6 shows the error plots for reduced lifted systems, in which the impulse-response norm is computed in a finite time window $[0, 30]$ in the lifted setting, which corresponds to 30 periods in the periodic setting. The notation \tilde{G}, \tilde{G}_r refers to the full and reduced lifted systems, respectively. The quantity $\|\tilde{G}_{\text{stab}}\|_2$ is the 2-norm of the (asymptotically stable) full lifted system, in which the outputs are the full impulse-response dynamics after the neutrally stable dynamics have been subtracted out. Figure 4.6 shows that the error norm of a balanced POD

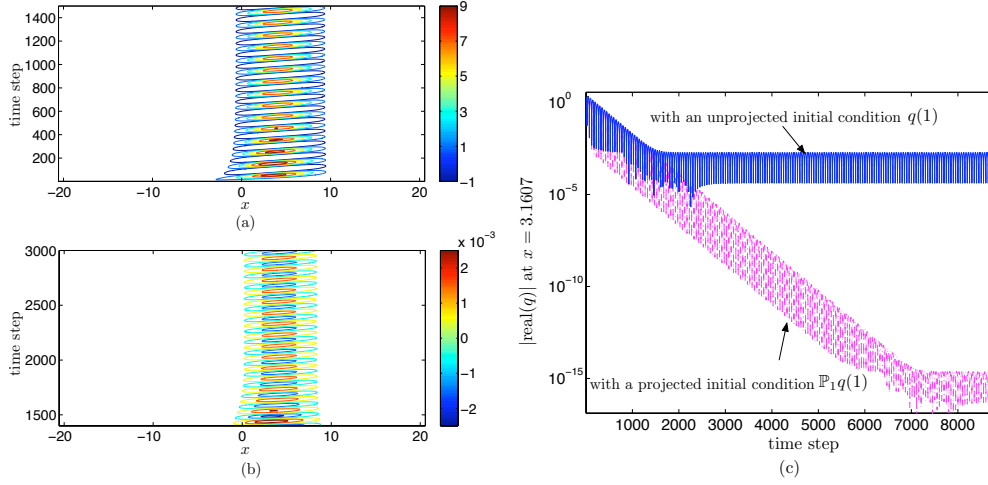


Figure 4.5: (a) Contour plot of $\text{real}(q)$: Nonlinear GL. An asymptotically stable periodic orbit appears when $\mu_0 = 1.1771 > \mu_c$. (b) Contour plot of $\text{real}(q)$: Neutral stability of the linearized periodic GL. With an arbitrary initial condition, a steady oscillation persists. (c) Projected vs unprojected initial conditions for the linear GL: Time evolution of q at a typical position $x = 3.1607$.

with $m_c = m_o = 3T$ and $r_{op} = 3$ is already very close to that of the snapshot-based balanced truncation without output projection, or even the exact balanced truncation. Note that in the case of snapshot-based balanced truncation without output projection, one needs to run $qT = 10^4$ adjoint simulations, while with output projection, one needs to run only $r_{op}T$ adjoint simulations. The exact balanced truncation is done by first explicitly constructing the lifted system, whose input dimension is $pT = 200$ and output dimension is $qT = 10^4$, and then using Matlab command `balreal`.

In this case, the outputs are the states themselves. From (4.15) we obtain the states in the periodic setting. Figure 4.7 shows the state trajectories and error plots in the time domain of the periodic setting, for an impulse-response simulation where the impulse is $u(1) = 1$. We see small “jumps” of the error occurring at time $j + tT$, $t = 0, 1, \dots$ especially at early time stages. These jumps occur because the lifting approach projects states onto the reduced space only once per period, at times

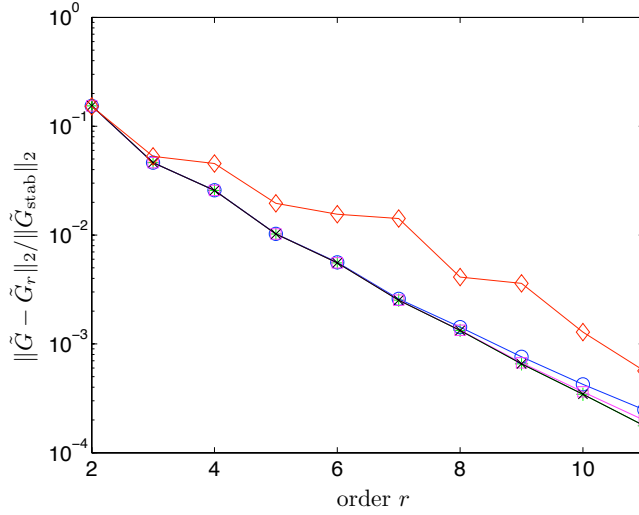


Figure 4.6: Error plots for reduced GL by lifted BPOD, lifting time $j = 1$, $m_c = m_o = 3T$ where $T = 100$: Error norm $\|\tilde{G} - \tilde{G}_r\|_2 / \|\tilde{G}_{\text{stab}}\|_2$, for exact balanced truncation(\times); balanced truncation by the method of snapshots but without output projection($+$); balanced POD with $r_{op} = 1$ (\diamond), balanced POD with $r_{op} = 3$ (\circ); balanced POD with $r_{op} = 5$ (\square).

$j + tT$. The simulation results shown here indicate that the size of the jump does not depend strongly on the order of the output projection used. Indeed, a reduced model of order $r = 4$ using snapshot-based balanced truncation without output projection, or even using exact BT, generates jumps at similar magnitudes as those by a fourth order balanced POD with $r_{op} = 3$ shown in Figure 4.7 (b-II). On the other hand, we see that for higher order models, these jumps decrease significantly, even if a low-order output projection is used.

4.5 ERA for linear time-periodic systems

We showed the equivalence between ERA and balanced POD for LTI systems in Chapter 3. For linear time-periodic systems, it is natural to *construct* ERA-like, adjoint-free versions of the lifted/periodic snapshot-based approximate balanced truncation methods introduced above. The goal is to realize approximate balanced

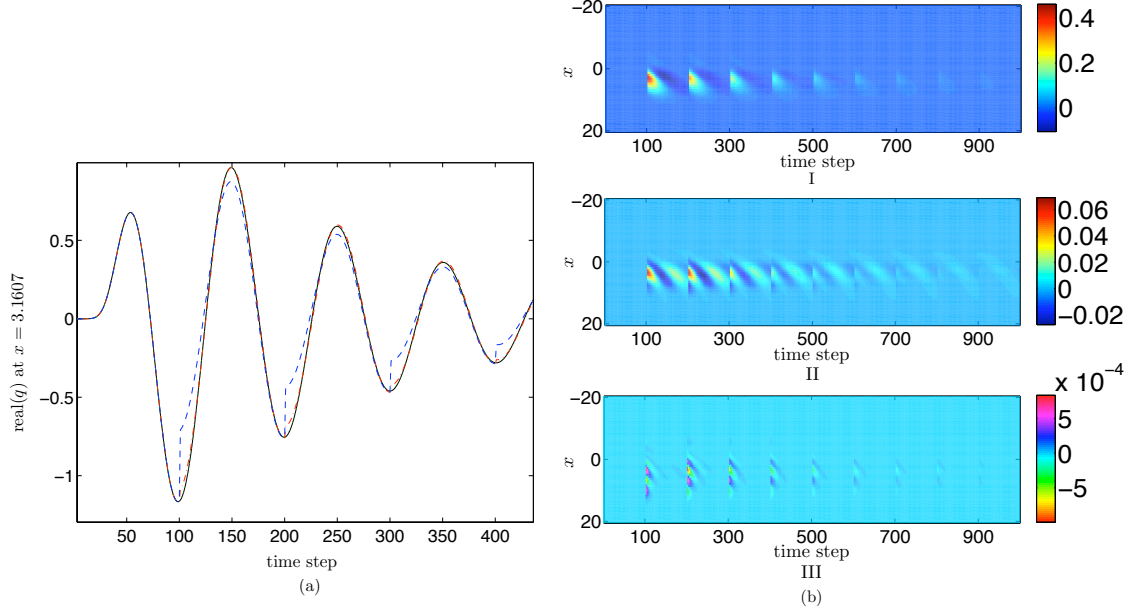


Figure 4.7: Error plots for reduced GL by lifted BPOD, lifting time $j = 1$, $m_c = m_o = 3T$ where $T = 100$: (a) Time evolution of $\text{real}(q)$ at spatial position $x = 3.1607$: full system (—); reduced systems with $r = 4$, $r_{op} = 1$ (---), with $r = 4$, $r_{op} = 3$ (-.-), with $r = 6$, $r_{op} = 1$ (···). The green line is almost on top of the black line. (b) Time evolution of $\text{real}(q_r - q_{\text{full}})$, the real part of errors between full and reduced systems in one impulse-response simulation. (I) $r = 4, r_{op} = 1$; (II) $r = 4, r_{op} = 3$; (III) $r = 11, r_{op} = 3$.

truncation without any adjoint data and at a much lower computational cost. The price is that the bi-orthogonal sets of balancing/adjoint modes will not be available.

There are existing algorithms for linear time-varying/time-periodic systems that are similar to ERA (i.e., based on SVD of generalized Hankel matrices obtained from impulse responses). For instance, the work by Liu (1997); Bauchau & Wang (2008) considers control-free systems. Bauchau & Wang (2008) also presents essentially an output projection method similar to the “time-invariant” version of the output-projection method we introduce here. More general ERA algorithms for linear time-varying/time-periodic control systems can be found in Shokoochi & Silverman (1987); Majji *et al.* (2010), where the reduced models are time-varying/time-periodic (i.e., the “periodic approach”). Here, we will employ the key relations between modes and the SVD factors (4.25) and then systematically construct two versions of ERA,

the lifted/periodic ERA, based on lifted/periodic balanced POD. The lifted/periodic ERA will by construction yield theoretically identical reduced-order models to lifted/periodic balanced POD. The resulting periodic ERA also requires less computational cost than the algorithms developed in (Shokoohi & Silverman, 1987; Majji *et al.*, 2010), and is applicable to systems with one-dimensional neutral stability/instability, as we will shortly see.

4.5.1 Lifted ERA for linear time-periodic systems

In Section 3.1.2, we showed the equivalence between balanced POD and ERA methods for LTI systems. The lifted balanced POD presented in Section 4.2 is conceptually a balanced POD for the lifted LTI system (4.3), so there is naturally an equivalent lifted ERA version that theoretically generates an identical lifted reduced-order model. Again all computations in ERA shall be carried in the periodic setting, as in lifted balanced POD.

The equivalence and feature of T -periodicity can help us to realize the ERA algorithm efficiently. First consider the exponentially stable case. Recall the definition (3.2) and relation $H = Y^*X$, the generalized Hankel matrix for system lifted at time j is (here we set the “sparse sampling parameter” $P = 1$)

$$H_j = \begin{bmatrix} \tilde{C}_j \tilde{B}_j & \tilde{C}_j \tilde{A}_j \tilde{B}_j & \cdots & \tilde{C}_j \tilde{A}_j^{m_c/T} \tilde{B}_j \\ \tilde{C}_j \tilde{A}_j \tilde{B}_j & \tilde{C}_j \tilde{A}_j^2 \tilde{B}_j & \cdots & \tilde{C}_j \tilde{A}_j^{m_c/T+1} \tilde{B}_j \\ \vdots & \vdots & \ddots & \vdots \\ \tilde{C}_j \tilde{A}_j^{m_o/T} \tilde{B}_j & \tilde{C}_j \tilde{A}_j^{(m_o/T+1)} \tilde{B}_j & \cdots & \tilde{C}_j \tilde{A}_j^{(m_c+m_o)/T} \tilde{B}_j \end{bmatrix} = Y^*(j; m_o) X(j; m_c), \quad (4.30)$$

where the factors X and Y are given by (4.9), (4.10). By employing T -periodicity on $A(k)$, $B(k)$ and $C(k)$, one checks that all entries of H_j can be obtained by running pT

input-output impulse-response simulations of the linear periodic system (4.1). For instance, for the i -th control input, do T impulse-response simulations for (4.1) (see Figure 4.8), each beginning at a different time phase in one period, $t = j - T, \dots, j - 1$. At time j , the states are, respectively,

$$B^{(i)}(j - 1), F(j, j - 1)B^{(i)}(j - 2), \dots, F(j, j - T + 1)B^{(i)}(j - T). \quad (4.31)$$

Then continue each of the simulations for $(m_c + m_o - 1)$ steps and take output snapshots at *every time step* from time j to time $(j + m_c + m_o - 1)$. The snapshots are the “building blocks” for the generalized Hankel matrices H_j and $H'_j = Y^*(j; m_o)\tilde{A}_j X(j; m_c)$ (see (3.4)). Then by SVD of H_j (4.12), one readily generates a reduced model of order r following the steps outlined in Section 3.1.1:

$$\begin{aligned} \tilde{A}_{j_r} \left(= \Psi_r^*(j)\tilde{A}_j\Phi_r(j) \right) &= \Sigma(j)_r^{-\frac{1}{2}} U(j)_r^* H'_j V(j)_r \Sigma(j)_r^{-\frac{1}{2}}; \\ \tilde{B}_{j_r} \left(= \Psi_r^*(j)\tilde{B}_j \right) &= \text{the first } Tp \text{ columns of } \Sigma(j)_r^{\frac{1}{2}} V(j)_r^*; \\ \tilde{C}_{j_r} \left(= \tilde{C}_j \Phi_r(j) \right) &= \text{the first } Tq \text{ rows of } U(j)_r \Sigma(j)_r^{\frac{1}{2}}. \end{aligned} \quad (4.32)$$

For the lifted system, there is also $\tilde{D}_{j_r} = \tilde{D}_j$. The entries of \tilde{D}_j (see Section 4.2.1) are outputs that have been collected in impulse response simulations. The model is theoretically identical to the lifted, reduced-order model (4.14) given by balanced POD.

One-dimensional neutral stability/instability case. We extended the ERA algorithm for LTI systems with one-dimensional neutral stability/instability in Section 3.4. To implement the method here, one approximates the blocks in $\mathbb{P}_j \tilde{B}_j$, i.e., $\mathbb{P}_j F(j, j - k + 1)B^{(i)}(j - k)$, $k = 1, \dots, T$, by running T long-time control free simulations for each control input for system (4.1), each with initial conditions $x(j)$ given by (4.31). Operations (see (3.19) and related discussions) on the snapshots taken after enough long periods of simulation yield the projected states. Using

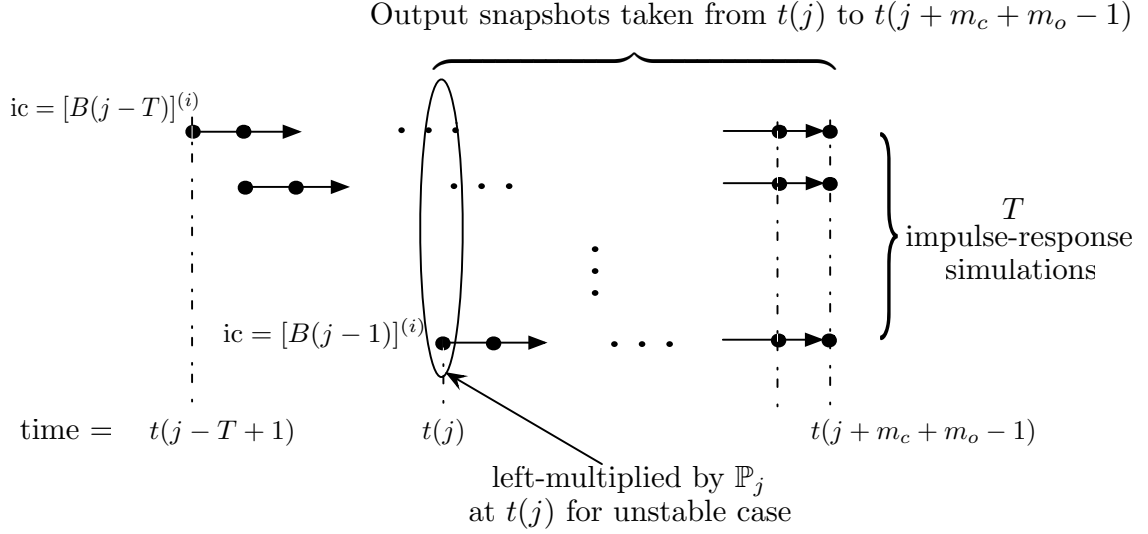


Figure 4.8: The T input-output impulse-response simulations corresponding to the i -th control input, for the lifted ERA method.

these as the projected initial conditions at time j , re-run the simulations, each for $(m_c + m_o - 1)$ steps (see Figure 4.8), and the outputs are the building blocks of the generalized Hankel matrices H_j and H'_j for the projected system (4.22). The final $(r + 1)$ -dimensional reduced-order model includes a r -dimensional reduced order model for the projected system and a one-dimensional model for the neutrally stable/unstable dynamics, whose corresponding A , B and C matrices can also be computed using those long simulation data (see (3.21) and related discussions).

4.5.2 Periodic ERA for linear time-periodic systems

By “symmetry” of the algorithms, the last piece on the map is naturally a “periodic ERA” algorithm that theoretically yields identical time-periodic reduced-order models as periodic balanced POD.

First, consider the exponentially stable case. The first step is to run input-output impulse responses of the LTP (4.1) to obtain T -periodic generalized Hankel matrices

H_j , each in the form (4.30), for every time phase j along one whole period. One checks that by using periodicity as in periodic balanced POD, only Tp simulations are needed to obtain all “building blocks” for all the T generalized Hankel matrices; see illustration in Figure 4.9. Output snapshots are taken at every time step in all simulations, subsets of which are entries of corresponding generalized Hankel matrices.

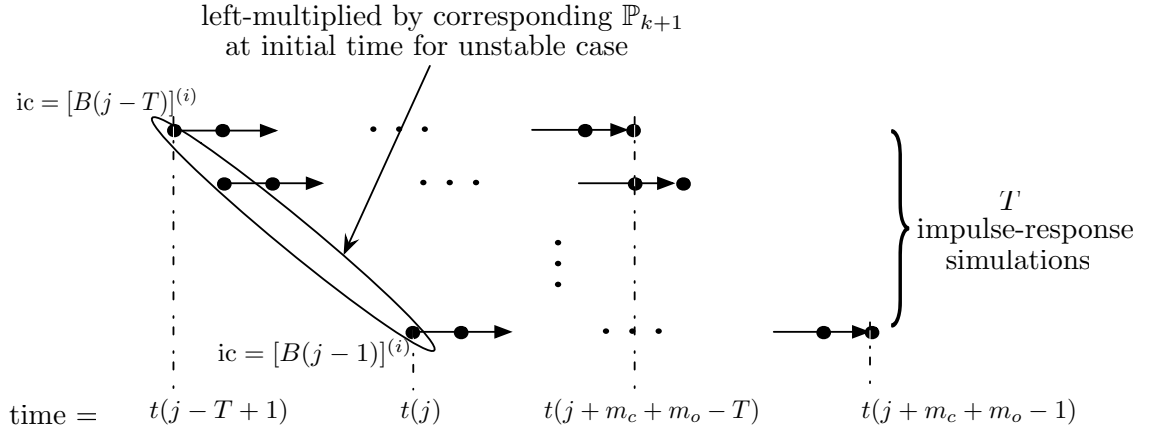


Figure 4.9: The T input-output impulse-response simulations corresponding to the i -th control input, for the periodic ERA method.

One then performs SVD calculations for each H_j , $j = 1, \dots, T$, as in (4.24). Using the mode relations (4.25), one checks that the T -periodic matrices for the periodic reduced model of order r are given by (refer to (4.26))

$$\begin{aligned} A_r(j) & \left(= \Psi_r^*(j+1)A(j)\Phi_r(j) \right) = \Sigma(j+1)_r^{-\frac{1}{2}} U(j+1)_r^* H_j' V(j)_r \Sigma(j)_r^{-\frac{1}{2}}; \\ B_r(j) & \left(= \Psi_r^*(j+1)B(j) \right) = \text{the first } p \text{ columns of } \Sigma(j+1)_r^{\frac{1}{2}} V(j+1)_r^*; \\ C_r(j) & \left(= C(j)\Phi_r(j) \right) = \text{the first } q \text{ rows of } U(j)_r \Sigma(j)_r^{\frac{1}{2}}, \end{aligned} \quad (4.33)$$

where here the H_j' is not $Y^*(j; m_o) \tilde{A}_j X(j; m_c)$ as in the lifted ERA method, but defined by

$$H_j' = Y^*(j+1; m_o) A_j X(j; m_c).$$

The matrices H_j' , $j = 1, \dots, T$, can also be easily constructed using the output

snapshots collected in the above impulse-responses. Again, notice that here we use modes from consecutive time phases for projection (although the modes themselves are not computed).

The B_r and C_r matrices obtained here are the same as those presented in Shokoochi & Silverman (1987); Majji *et al.* (2010). However, while in this algorithm only one SVD (on H_j) is need for each $A_r(j)$, in Shokoochi & Silverman (1987); Majji *et al.* (2010) two SVDs (one on H_j and the other on H'_j) are needed for each $A_r(j)$. This is because the construction of the ERA algorithm here is purely based on the corresponding balanced POD algorithm and the key relation (4.25) between modes and SVD factors, which leads naturally to a simpler form for computing $A_r(j)$. The formulations presented in (4.33) are also more consistent with the original ERA algorithm for LTI systems (see (3.3) in Section 3.1.1). The above method can be directly applied to linear time-varying systems by removing all computational convenience designed for periodic systems.

One-dimensional neutral stability/instability case. As to periodic ERA for systems with one-dimensional neutral stability/instability, one needs to approximate $\mathbb{P}_{j+1}B(j)$, $j = 1, \dots, T$, as projected initial conditions for impulse responses; see Figure 4.9 and the projected periodic system (4.27). Without repeating similar details, we note that the projected initial conditions are computed using the power method approach given in Section 3.4. Tp long-time simulations of the LTP system (4.1) are needed.

Output projection. The output projection method outlined in Section 4.2.4 can be directly applied in lifted/periodic ERA algorithms, where the output snapshots are always collected and POD on the output data sets can thus be done. Also refer

to output projection for ERA to LTI systems in Section 3.1.3 for more details.

4.6 Summary

Versions of snapshot-based approximate balanced truncation methods for high-dimensional linear, time-periodic systems are presented, including the lifted and periodic balanced POD algorithms and the lifted and periodic ERA algorithms. The output projection method for systems with high-dimensional outputs is also generalized here for time-periodic systems. The lifted/periodic balanced POD algorithms are applicable to neutrally stable/unstable systems with a low-dimensional neutrally stable/unstable subspace, while the lifted/periodic ERA is currently applicable only to systems with one-dimensional neutral stability/instability.

The lifting approach is computationally more efficient than the periodic approach. On the other hand, the reduced-order models by the periodic approach update the state every time step, while the models by the lifting approach update the state once a period, which might cause delay in feedback control update. Numerical results show that lifted balanced POD generates low-dimensional models that are close to those obtained by exact balanced truncation, at a much lower computational cost.

By construction, the lifted/periodic ERA yields theoretically identical reduced-order models as lifted/periodic balanced POD. The ERA algorithms do not need adjoint data and by construction are more computationally efficient than balanced POD algorithms; on the other hand lifted/periodic balanced POD provides bi-orthogonal sets of modes that are useful for system analysis and control purposes.

In summary, lifted balanced POD/ERA can be efficient choices for system analysis and feedback control design for linear periodic systems encountered in fluid

mechanics, as long as the potential delay in control update due to lifting does not cause problems. In particular, we will apply the lifted ERA in the next chapter for feedback control of a flow past an inclined plate with open-loop periodic forcing that generates high-lift vortex shedding cycles.

The periodic balanced POD/ERA algorithms can be directly applied to more general linear time-varying systems, by removing the assumption of periodicity in computations. The periodic ERA algorithm is more efficient in computing reduced state transition matrices than those developed in Shokoochi & Silverman (1987); Majji *et al.* (2010).

Chapter 5

Feedback control of flow past a flat plate with open-loop periodic forcing

In this chapter we show how to design a model-based feedback controller to stabilize an unstable periodic orbit found in a high-dimensional system (on the order of 10^5). The lifted ERA method, an adjoint-free approximate balanced truncation method proposed in Section 4.5.1, is applied to compute reduced-order models (with state dimensions smaller than 10) of the unstable time-periodic system, and these models are then used for control design.

As a model problem, we consider a two-dimensional flow past an inclined plate at a post-stall angle of attack, with open-loop periodic actuation at the trailing edge. Our feedback controller will then provide small modifications to the periodic forcing, in order to stabilize a desired periodic orbit. The motivation of the study of this model problem is to develop control design tools for feedback control of wakes of micro-air vehicles at low Reynolds numbers. Recent results from two-dimensional and three-dimensional simulations (Joe *et al.*, 2008; Taira *et al.*, 2010) show that

periodic forcing at the leading or trailing edge of a flat-plate wing can significantly enhance lift. These results are consistent with earlier work reported in experiments and simulations (see references in Joe *et al.* (2008); Taira *et al.* (2010)), although the purpose of most of those works is to reattach the flow or delay separation, not to enhance lift. Furthermore, at different forcing frequencies, besides observed stable high-lift periodic orbits, there are also quasi-periodic solutions with high average lift that suggest the possible existence of unstable, high-lift periodic orbits. In this work we are interested in finding those unstable orbits and then stabilizing them by model-based feedback control. In Joe *et al.* (2008), an ad hoc feedback controller is designed to lock the phase shift between the forcing and lift oscillations. The control design approach applied here is conceptually more systematic and general, as it relies less on specific observation of the system and more on systematic mathematical tools in control theory and dynamical systems.

In Section 5.1 we introduce the main procedures of the model-based feedback control design approach, including key theoretical and numerical details. In Section 5.2 we then present control design results for the specific model problem of flow control described above, including numerical solutions of stable/unstable periodic orbits, a reduced-order model of the unstable linearized time-periodic system corresponding to an unstable orbit, and a feedback controller that stabilizes the unstable orbit.

5.1 Main procedures of the model-based feedback control design approach

The main steps in our control design approach are as follows:

- **Step I:** Find periodic solutions using the Newton-GMRES method.

- **Step II:** Linearize about an orbit that we are interested in. Fix the location of actuators and sensors, and construct a linear time-periodic input-output system.
- **Step III:** Construct a reduced-order model of the linear time-periodic system using the lifted ERA algorithm.
- **Step IV:** Design an observer-based feedback controller using the reduced-order model.
- **Step V:** Apply the feedback controller to the full linearized time-periodic system, and to the full nonlinear system.

As in the numerical example in Section 3.3, the fast formulation of the immersed boundary projection method (IBPM) using a multi-domain scheme (Colonius & Taira, 2008) is used here to solve for the two-dimensional incompressible flow past an inclined plate. Velocities, length and time scales are non-dimensionalized by the free stream velocity U_∞ and the chord length c . The Reynolds number is $Re = 300$, as in Joe *et al.* (2008); Taira *et al.* (2010). The post-stall angle of attack is fixed at $\alpha = 40^\circ$. Three levels of grid domains are used, each with 200×120 grid points. The grid size of the finest domain is $\Delta x = \Delta y = 0.0252$. The finest domain centered at the center of the plate covers $[x_1, x_2] \times [y_1, y_2] = [-1.38302, 3.65698] \times [-1.21861, 1.80539]$ such that the distances between the leading edge of the plate and the left and the lower boundary of the domain are 1 and 1.54 units. The largest domain covers $[8x_1, 8x_2] \times [8y_1, 8y_2]$. The Crank-Nicolson method and the third-order Runge-Kutta method are used for time integration respectively for the linear viscous terms and nonlinear convective terms in the Navier-Stokes equations. The initial time step is $\Delta t = 0.004$, with which actuation-free simulations are run and the time step is slightly adjusted such that the natural vortex shedding period is equal to 900 time

steps. For the input-output system, we consider the states to be the vorticity and stream function on each grid level, and the dimension of the discretized system is about 1.4×10^5 (which is determined by the number of variables at each grid point (2) \times the number of grid points on each level (200×120) \times grid levels (3)). First, for the actuation-free flow past an inclined plate, we write the spatially and temporally discretized nonlinear system as

$$x_{\text{NL}}(k+1) = N(x_{\text{NL}}(k)), \quad (5.1)$$

where $x_{\text{NL}}(k)$ is the the system state, and N is the nonlinear, spatially discretized Navier-Stokes operator combined with the time stepper that updates the state. Let $\Omega(k, x_{\text{NL}_0})$ be a solution, where k is time step and $x_{\text{NL}_0} = x_{\text{NL}}(0)$ is the initial condition. The vortex shedding cycle behind the plate at a post-stall angle of attack corresponds to a stable T_0 -periodic orbit of system (5.1), i.e., $\Omega(T_0 + k, \bar{x}_{\text{NL}_0}) = \Omega(k, \bar{x}_{\text{NL}_0})$, where \bar{x}_{NL_0} is a state on the periodic orbit, and T_0 is the natural period of vortex shedding in terms of time steps. See a typical snapshot of the vorticity shedding contours in Figure 5.1 in Section 5.1.2.

The discrete dynamical system with an open-loop periodic forcing is of the form

$$x_{\text{NL}}(k+1) = N(x_{\text{NL}}(k)) + Bf(k) \quad (5.2)$$

where B is a function of the distribution matrix B_0 representing the localized body force actuation close to the leading/trailing edge. The form of this function is determined by the time stepper. Here the body force is applied to a point on the extended line of the plate close to the trailing edge (i.e., behind the trailing edge of the plate) and is set upstream-directed; see a schematic in Figure 5.1 in Section 5.1.2. This configuration is consistent with that in Joe *et al.* (2008) where results show that in the two-dimensional case, upstream forcing at the trailing edge

is more effective for lift enhancement than downstream forcing. The distribution of the localized force in the domain is given by a discrete delta function $\delta(r)$ (Roma *et al.*, 1999) where r is the distance to the actuation location. The periodic forcing is given by

$$f(k) = \frac{1}{2} \left[1 - \cos \left(\frac{2\pi}{T_f} k \right) \right], \quad (5.3)$$

where T_f is the forcing period. Periodic waveforms other than sinusoidal can be found in, for example, Joe *et al.* (2009), where a waveform is calculated through an adjoint-based optimization procedure.

The strength of the actuation may be quantified by the ratio between the momentum input by the forcing and that of the free stream, called the momentum coefficient

$$C_\mu = \frac{\rho u_{\text{act}}^2 \sigma}{\frac{1}{2} \rho U_\infty^2 c}, \quad (5.4)$$

where $\sigma = \Delta x$ is the effective actuator width determined by the delta function $\delta(r)$. The velocity u_{act} is measured by the nearly constant actuator velocity obtained by a long simulation with a constant forcing $f(k) = 1$ and zero background flow ($U_\infty = 0$); see Taira *et al.* (2010). With $u_{\text{act}} \approx 0.6$ and $\sigma = 0.0252$, $C_\mu \approx 1.8\%$. Since the value is small, the momentum added by the actuation, even with a constant $f(k) = 1$, is small compared to the free stream momentum.

5.1.1 Step I: Solve for periodic orbits by using the Newton-GMRES method

Let $\Omega_f(k, x_{\text{NL0}})$ be a solution of the periodically perturbed system (5.2), where k is the time step and x_{NL0} is the initial condition. For a forcing period T_f (see (5.3)), the periodic solution of (5.2), if it exists, shall also have a period that is an integer multiple of T_f . In particular, we are interested in periodic solutions with a period

equal to the forcing period T_f , i.e., satisfying

$$\mathfrak{F}(x_{\text{NL}}) := \Omega_f(T_f, x_{\text{NL}}) - x_{\text{NL}} = 0, \quad (5.5)$$

that have high average lift. In this case, T_f can be regarded as an additional unknown, and the system (5.5) of n equations, with unknowns $x \in \mathbb{R}^n$ and $T_f \in \mathbb{R}$, does not have a unique solution. To eliminate the indeterminacy, a “phase condition” (Doedel *et al.*, 1991) is added as follows:

$$\langle x_{\text{NL}} - x_{\text{NL}}^{\text{ref}}, v(x_{\text{NL}}^{\text{ref}}) \rangle = 0, \quad (5.6)$$

where $x_{\text{NL}}^{\text{ref}}$ is a reference state, and $v(x_{\text{NL}})$ is a vector field determined by the nonlinear system $\dot{x}_{\text{NL}} = v(x_{\text{NL}})$ that is the continuous-time version of (5.1). The phase condition defines a Poincaré section, such that the periodic solution, if it exists, corresponds to a fixed point of the Poincaré map. On the other hand, if we seek a T_f -periodic solution for a given forcing period T_f , then the phase condition is not needed, since the problem becomes that of finding a fixed point of the time- T_f map by solving (5.5).

For both cases, to solve the high-dimensional nonlinear equations (5.5) (on the order of 10^5 in this work) is numerically challenging. In large-scale computational fluid dynamics problems, widely-used numerical methods for finding steady solutions include the Newton-Krylov methods (Trefethen & Bau, 1997; Kelley, 2003) and the method of selective frequency damping (Åkervik *et al.*, 2006). See recent applications in Ahuja & Rowley (2010); Bagheri *et al.* (2009c). The Newton/Newton-Krylov method has been applied to find stable/unstable periodic solutions in problems such as the plane Couette turbulence (Kawahara *et al.*, 2006; Viswanath, 2007) and thermal convection in an annulus (Sánchez *et al.*, 2004). In this work, we will apply a Newton-Krylov method to find periodic solutions by solving sys-

tem (5.5)(coupled with equation (5.6) if T_f is not specified).

To solve (5.5) by the Newton method, one iteratively updates the solution x by

$$x^{i+1} = x^i - D\mathfrak{F}(x^i)^{-1}\mathfrak{F}(x^i), \quad (5.7)$$

where the superscript stands for the i -th iteration and $D\mathfrak{F}(x)$ is the Jacobian matrix of $\mathfrak{F}(x)$. For large-scale problems, it is computationally infeasible to invert the Jacobian directly. Instead, one solves for h in the linear system

$$D\mathfrak{F}(x^i) \cdot h = \mathfrak{F}(x^i) \quad (5.8)$$

so that $x^{i+1} = x^i - h$. Iterative solvers, such as the Krylov-subspace based methods, are often used to solve the linear system (5.8). In particular, in this work we will use a Krylov method, the Generalized Minimal Residual Method (GMRES) (Saad & Schultz, 1986). The GMRES method has a fast convergence property when it is applied to a system $Ax = b$ where most eigenvalues of A are clustered together. For the system (5.2) that models the Navier-Stokes equations with a periodic forcing input, we expect that most of the eigenvalues of the Jacobian of its solution $\Omega_f(T_f, x)$ are clustered close to the origin when T_f is large, due to the dissipative terms in the Navier-Stokes operator. The Newton-GMRES method applied here (Kelley, 2003) also includes a line search method, the Armijo rule, that determines the step length parameter $\lambda \in [0, 1]$ for updating $x^{i+1} = x^i - \lambda h$. In implementation, the Newton-GMRES method is a computational wrapper around the Navier-Stokes solver (5.2) that updates $x(k_0 + T_f) = \Omega_f(T_f, x(k_0))$ from $x(k_0)$.

A significant challenge of applying the Newton-GMRES method to the large-scale fluid problem is that it requires reasonable initial guesses to obtain convergent solutions. In this work we first run a simulation of the system (5.2) with the forcing period $T_f = T_0$. The solution is not periodic but quasi-periodic. We then use states

at different time phases of the solution as initial guesses of states on periodic orbits, and we use the natural shedding period T_0 as the initial guess of the period of the orbit. The Newton-GMRES method is then applied to solve the $(n+1)$ -dimensional problem, i.e., the system (5.5) and the phase condition (5.6), for periodic solutions (\bar{x}, \bar{T}_f) . Once one or more solutions are obtained, a continuation study follows, with T_f as the bifurcation parameter. Periodic solutions with different forcing periods are obtained in turn.

5.1.2 Step II: The linearized time-periodic system with an affine control input

A linearized, time-periodic system about a T_f -periodic orbit of (5.2) is in the form

$$x(k+1) = A(k)x(k), \quad (5.9)$$

where the T_f -periodic matrix A is the Jacobian of the nonlinear operator N (the open-loop periodic forcing term $Bf(k)$ does not depend on x_{NL}). The nonlinearity of N arises from the convective term $q \times \omega$ in the vorticity transport equation, where q is the flux and ω is the vorticity. The linearized form of the convective term around the orbit at time step k is $\delta q(k) \times \omega_0(k) + q_0(k) \times \delta \omega(k)$, where $q_0(k), \omega_0(k)$ correspond to the baseline state on the T_f -periodic orbit, and $\delta q(k)$ and $\delta \omega(k)$ correspond to the linearized state $x(k)$.

Stability. The original actuation-free system (5.1) has a stable T_0 -periodic orbit. By Floquet theory, its linearized T_0 -periodic system is neutrally stable, with one unity eigenvalue corresponding to perturbations in the direction of the periodic orbit. However, an important observation is that the system (5.9) that is linearized

about an orbit for the forced system (5.2) is in general not neutrally stable. That is because the neutrally stable linearized system about the unforced baseline orbit is structurally unstable (Guckenheimer & Holmes, 1983). Then, by regarding the forcing term $Bf(k)$ in (5.2) as a perturbation, the perturbed linearized system in the form of (5.9) will generically be either stable or unstable, depending on the magnitude of the perturbed unity eigenvalue.

The eigenvalues mentioned above are of the lifted matrix $\tilde{A}_0 = A(T_f - 1) \cdots A(0)$, i.e., the time- T_f map of the linear time-periodic system (5.9). The dominant eigenvalues and eigenvectors of the time- T_f map can be found using Arnoldi iteration (Trefethen & Bau, 1997), a Krylov-subspace method developed by Arnoldi (1951). Early work on stability analysis of periodic orbits in two-dimensional open flows can be found in Tuckerman & Barkley (2000) and the references therein. Arnoldi iteration is also used in the GMRES procedure to iteratively find the solution for a linear system.

Linear time-periodic control system. To stabilize an unstable orbit, we add a one-dimensional affine control input to the linearized system (5.9) also through a localized body force with the same distribution B as in (5.2). The linear time-periodic control system reads

$$\begin{aligned} x(k+1) &= A(k)x(k) + Bu(k); \\ y(k) &= Cx(k), \end{aligned} \tag{5.10}$$

where $A(k)$ is T_f -periodic, $u(k) \in \mathbb{R}$ and B and C are constant matrices. The output is $y(k) = Cx(k)$. For the model problem, we consider an ideal case that there are two y -direction flux sensors located at downstream positions with coordinates of $(1.5, 0)$ and $(2, 0)$, such that they will be in the wake flow actuated by the body force. The linear control system has input dimension $p = 1$ and output dimension $q = 2$. Note

that the total body force actuation for the nonlinear system is $B(f(k) + u(k))$; see a schematic of the set up in Figure 5.1.

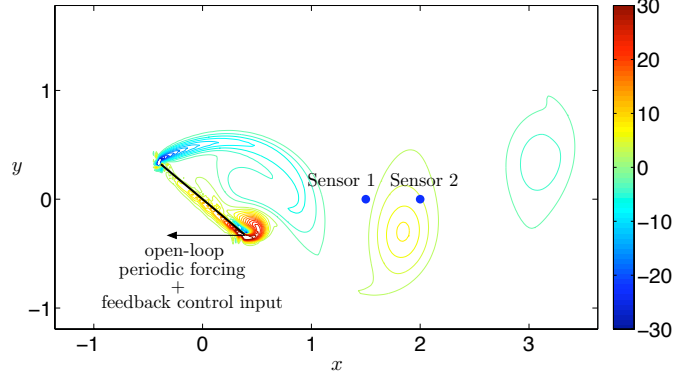


Figure 5.1: Setup of the open-looping forcing, feedback control and sensors. The contour plot shows a typical vorticity field snapshot taken in an actuation-free vortex shedding cycle.

Recall from Section 4.2.1 that the corresponding lifted system (which is time-invariant) will have $pT_f = T_f$ dimensional inputs and $qT_f = 2T$ dimensional outputs. As mentioned in the previous chapter, for a large T_f (e.g., typically on the order of 10^3 here), to run T_f impulse responses for system (5.10) to collect Markov parameters of the lifted system will be computationally expensive. In practice, here we make a compromise on the control freedom by allowing $u(k)$ to change only once every s time steps, with an s such that $T_s = T_f/s$ is on the order of 10, i.e., we add an actuation that is slowly varying relative to time steps, but rapidly varying relative to the period of the orbit. With this restriction, the linear control system (5.10) can be “lifted” (denoted by the check mark) to a T_s -periodic system in which one step corresponds to s steps in (5.10):

$$\begin{aligned}\check{x}(i+1) &= \check{A}(i)\check{x}(i) + \check{B}(i)\check{u}(i); \\ \check{y}(i) &= \check{C}(i)\check{x}(i) + \check{D}(i)\check{u}(i),\end{aligned}\tag{5.11}$$

where

$$\tilde{x}(i) = x(is), \quad \tilde{u}(i) = u(is), \quad \tilde{y}(i) = \begin{bmatrix} y(is) \\ y(is+1) \\ \vdots \\ y((i+1)s-1) \end{bmatrix}. \quad (5.12)$$

The $\check{A}(i), \check{B}(i), \check{C}(i), \check{D}(i)$ matrices are now all T_s -periodic. For instance,

$$\check{A}(i) = A((i+1)s-1) \cdots A(is) = F_{((i+1)s, is)}, \quad \check{B}(i) = \sum_{j=1}^s F_{((i+1)s, is+j)} B(is+j-1). \quad (5.13)$$

The big-step T_s -periodic representation (5.11) is further lifted to a LTI system (see (4.3)), where we choose the lifting time to be 0:

$$\begin{aligned} \tilde{x}(t+1) &= \tilde{A}_0 \tilde{x}(t) + \tilde{B}_0 \tilde{u}(t); \\ \tilde{y}(t) &= \tilde{C}_0 \tilde{x}(t) + \tilde{D}_0 \tilde{u}(t), \end{aligned} \quad (5.14)$$

with

$$\begin{aligned} \tilde{x}(t) = \check{x}(tT_s) = x(T_f t), \quad \tilde{u}(t) &= \begin{bmatrix} \check{u}(tT_s) \\ \check{u}(tT_s+1) \\ \vdots \\ \check{u}((t+1)T_s-1) \end{bmatrix} = \begin{bmatrix} u(tT_f) \\ u(tT_f+s) \\ \vdots \\ u((t+1)T_f-s) \end{bmatrix}, \\ \tilde{y}(t) &= \begin{bmatrix} \check{y}(tT_s) \\ \vdots \\ \check{y}((t+1)T_s-1) \end{bmatrix} = \begin{bmatrix} y(tT_f) \\ \vdots \\ y((t+1)T_f-1) \end{bmatrix}, \end{aligned} \quad (5.15)$$

and $\tilde{A}_0, \tilde{B}_0, \tilde{C}_0, \tilde{D}_0$ are constant matrices. For instance,

$$\begin{aligned} \tilde{B}_0 &= \begin{bmatrix} \check{F}_{(T_s, 1)} \check{B}(0) & \cdots & \check{F}_{(T_s, T_s-1)} \check{B}(T_s-2) & \check{B}(T_s-1) \end{bmatrix} \\ &= \begin{bmatrix} F_{(T_f, s)} \check{B}(0) & \cdots & F_{(T_f, T_f-s)} \check{B}(T_s-2) & \check{B}(T_s-1) \end{bmatrix}. \end{aligned} \quad (5.16)$$

Now only T_s impulse responses for system (5.11) are needed to collect Markov parameters for the lifted LTI representation. One impulse response beginning at time step i for system (5.11) corresponds to a simulation for system (5.10) beginning at time step is , with $u(k) = 1$ for $k \in [is, (i+1)s - 1]$ and $u(k) = 0$ for $k \geq (i+1)s$.

Note that one can choose different lifting times and construct different lifted LTI systems. However the input-output behavior of those systems would essentially be the same, as different lifting times just correspond to different reference points of the time- T_f map on the same orbit.

5.1.3 Step III: Snapshot-based approximate balanced truncation for the linearized time-periodic system

A lifted ERA procedure (see Section 4.5.1) is then executed to obtain reduced-order lifted LTI models of system (5.14). Due to the restriction on the control input $u(k)$, the original periodic system (5.10) is conceptually lifted twice as described above. For reference, we list a summary of the implementation procedure of the lifted ERA method as follows, based on discussions in Section 4.5.1. (The steps with an asterisk mark are needed for systems that have one unstable eigenvalue, but can be skipped for stable systems.)

- **Step III.1:** Run s simulations for system (5.10), each beginning at time step is , $i = 0, \dots, T_s - 1$ with zero initial conditions, and $u(k) = 1$ for $k \in [is, (i+1)s - 1]$ and $u(k) = 0$ for $k \in [(i+1)s, T_f]$. Collect the end state of each simulation $x_i(T_f) = \check{F}_{(T_s, i+1)} \check{B}(i) = F_{(T_f, (i+1)s)} \check{B}(i)$. Store the outputs at every time step in the simulations.

- **Step III.2*:** Run s control-free simulations for system (5.10), each beginning at time 0, with initial conditions $x_i(0)$ given by the corresponding $x_i(T_f)$ collected in the previous step. Each simulation runs for $4m$ steps, where m is a large enough integer multiple of the period T_f , except that the simulation with the initial condition $x_0(0)$ runs for $(4m + T_f)$ steps for later use. In each simulation, store the states $x_i(2m)$ and $x_i(4m)$. Store $x_0(4m + T_f)$. Also, store the outputs $y_0(2m), \dots, y_0(2m + T_f - 1)$.
- **Step III.3*:** Project each of the initial states $x_i(0)$ used in the previous step onto the stable subspace of the lifted transition matrix \tilde{A}_0 by

$$\mathbb{P}_s x_i(0) = x_i(0) - x_i(m) \frac{\langle x_i(0), x_i(2m) \rangle}{\langle x_i(0), x_i(4m) \rangle}.$$

- **Step III.4:** Run s control-free simulations of (5.10), each beginning at time 0, with initial condition given by corresponding $\mathbb{P}_s x_i(0)$ computed in the previous step. Each simulation runs for $(2m - 1)$ steps. Store the outputs at every time step during each simulation.
- **Step III.5:** Construct the Hankel matrices H_0 and H'_0 of the lifted system (5.14) (see (4.30)) using the outputs collected in the previous step. With one SVD calculation on H_0 , compute the lifted reduced-order model of order r for the stable dynamics using (4.32).

- **Step III.6***: Construct the lifted one-dimensional unstable dynamics by (See (2.25) and (3.21))

$$\begin{aligned}\tilde{x}_u(t+1) &= \frac{\langle x_0(0), x_0(4m+T_f) \rangle}{\langle x_0(0), x_0(4m) \rangle} \tilde{x}_u(t) + \frac{\left\langle x_0(0), \begin{bmatrix} x_0(2m) & \dots & x_{T_s-1}(2m) \end{bmatrix} \right\rangle}{\langle x_0(0), x_0(4m) \rangle} \tilde{u}(t); \\ \tilde{y}_u(t) &= \begin{bmatrix} y_0(2m) \\ \vdots \\ y_0(2m+T_f-1) \end{bmatrix} \tilde{x}_u(t),\end{aligned}\tag{5.17}$$

where $x_0(0)$, $x_0(4m+T_f)$, $x_i(2m)$ and $y_0(2m+i)$, $i = 0, \dots, T_s - 1$ are from Step III.2.

- **Step III.7**: The final $(r+1)$ -dimensional, lifted reduced-order model is a combination of the two decoupled models obtained in Step III.5 and Step III.6. The final output equation includes a $\tilde{D}_r = \tilde{D}_0$ (see (4.14)), whose entries are the outputs stored in Step III.1.

If the system is linearized from a stable orbit, then the steps 2 and 3 for the projection and step 6 for the unstable dynamics modeling can be skipped.

5.1.4 Step IV and V: Observer-based feedback control design and implementation.

In most engineering applications, the state of the full system is unknown, and thus a full-state feedback controller that updates the control input based on the current state is not directly applicable. Instead, one typically uses an observer-based feedback controller to update the feedback control inputs based on the sensor measurements (outputs). For the lifted reduced-order models, standard design tools for LTI control systems (Skogestad & Postlethwaite, 2005) can be applied. Figure 5.2

illustrates the structure of an observer-based feedback controller for the reduced system. The reduced-order observer reads

$$\begin{aligned}\hat{\tilde{x}}_r(t+1) &= \tilde{A}_r \hat{\tilde{x}}_r(t) + \tilde{B}_r \tilde{u}(t) + L(\tilde{y}(t) - \hat{\tilde{y}}(t)); \\ \hat{\tilde{y}}(t) &= \tilde{C}_r \hat{\tilde{x}}_r(t) + \tilde{D}_r \tilde{u}(t),\end{aligned}\tag{5.18}$$

where $\hat{\tilde{x}}_r$ is the estimate of \tilde{x}_r and $\hat{\tilde{y}}$ is the estimate of output \tilde{y} . The matrices K and L are respectively the control gain and the observer gain. We emphasize that one step for the reduced lifted model corresponds to one whole period T_f in the original periodic setting.

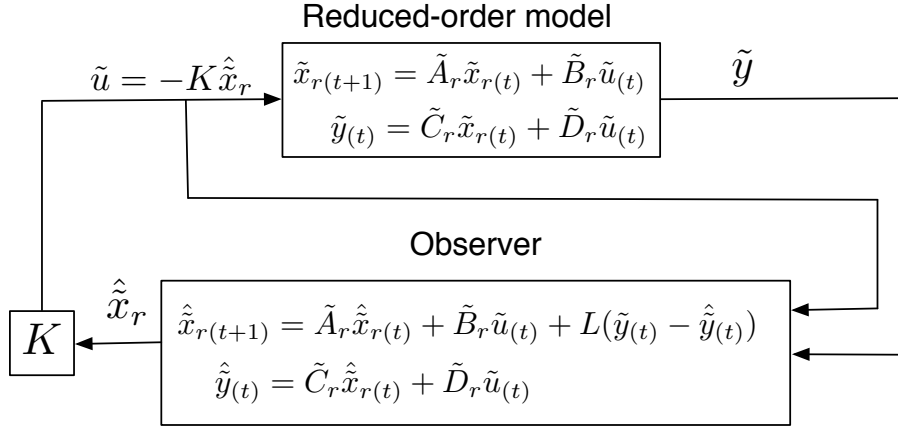


Figure 5.2: Block diagram for observer-based feedback control for the reduced-order model.

By the separation principle (Skogestad & Postlethwaite, 2005), the control gain K and observer gain L can be designed separately. First, the control gain K can be computed by design of a Linear Quadratic Regulator (LQR) with $\tilde{u} = -K\tilde{x}$ (full-state feedback) that minimizes the cost function

$$J = \sum_{t=0}^{\infty} (\tilde{x}_r(t)^T Q \tilde{x}_r(t) + \tilde{u}(t)^T R \tilde{u}(t))\tag{5.19}$$

subject to the state dynamics $\tilde{x}_r(t+1) = \tilde{A}_r \tilde{x}_r(t) + \tilde{B}_r \tilde{u}(t) = (\tilde{A}_r - \tilde{B}_r K) \tilde{x}_r(t)$. By specifying weight matrices Q and R , one can compute K by solving this optimization problem using Matlab command `dlqr`, which essentially solves an algebraic Riccati

equation.

In the current work, the observer gain L is computed by pole placement (Matlab command `place`) that specifies the eigenvalues of the close-loop state transition matrix $(\tilde{A}_r - L\tilde{C}_r)$ of the observer. The observer gain can be obtained by other methods, such as by design of a Linear Quadratic Estimator (LQE) that is based on an assumption that the noises in the states and outputs can be represented by stochastic Gaussian processes.

Based on the assumption that the reduced-order lifted LTI model captures well the input-output dynamics of the full time-periodic system, we apply the controller designed for the reduced-order model to the full linearized time-periodic system (5.10), as illustrated in Figure 5.3. Notice that the the full linearized time-periodic system sends the stored outputs for the *past whole period* to the observer once per period. Then the reduced-order model based observer (in a lifted setting) updates the reduced state estimate, and in turn updates the control input sequence for the full system for the *next whole period*. Also note that here we only allow $u(k)$ to change once every s steps. Thus the observer updates a control input sequence with $T_s = T_f/s$ entries for the full system for the next whole period, each entry acting on the full system for s steps.

The controller is designed for the linearized time-periodic system about an unstable periodic orbit we are interested in. The controller is expected to be able to stabilize the periodic orbit in its neighborhood in the state space where the linear dynamics is dominant, so it is reasonable to expect the linearized model to remain valid for the full nonlinear system, as long as the controller is capable of suppressing the instability. The full nonlinear model with open-loop periodic forcing (5.2), now

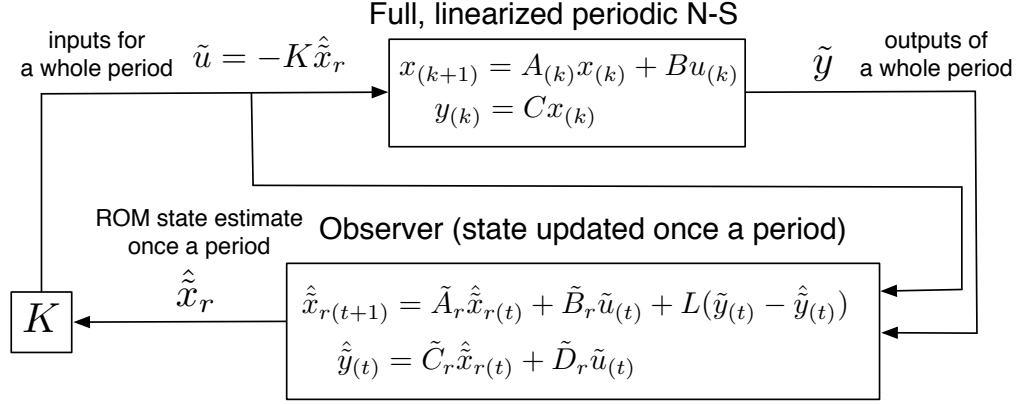


Figure 5.3: Block diagram for observer-based feedback control for the full linearized time-periodic system (5.10).

with the feedback control input, reads

$$\begin{aligned} x_{\text{NL}}(k+1) &= N(x_{\text{NL}}(k)) + Bf(k) + Bu(k); \\ y_{\text{NL}}(k) &= Cx_{\text{NL}}(k), \end{aligned} \tag{5.20}$$

where y_{NL} are the outputs from the nonlinear system, $f(k)$ is the open-loop periodic forcing from (5.3), and $u(k)$ is determined by the feedback controller. The control diagram is shown in Figure 5.4. As in the full linearized system case, the observer is in the lifted setting and updates the state and control inputs once per period, while the full model is running in the periodic setting. Note that before it is sent to the observer, the reference output y_{orb} is subtracted from y_{NL} at the corresponding time phase of the orbit along which the system is linearized. The time phase is determined by the phase of the open-loop sinusoidally periodic forcing.

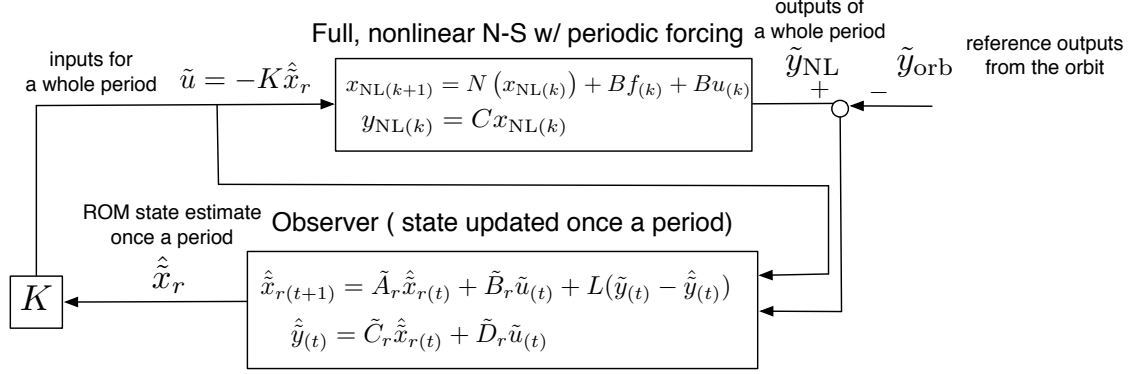


Figure 5.4: Block diagram for observer-based feedback control for the full nonlinear Navier-Stokes model with open-loop periodic forcing.

5.2 Observer-based feedback control results

5.2.1 Stable and unstable periodic orbits

The actuation-free system has a stable periodic orbit with a natural vortex shedding period $T_0 (= 3.6924) = 900$ time steps. Its lift coefficient C_L trajectory is shown in Figure 5.5(a). Consistent with the Floquet theory, a linear stability analysis of the linearized time-periodic system about this orbit by the Arnoldi iteration method shows that it is neutrally stable; see Figure 5.5(b).

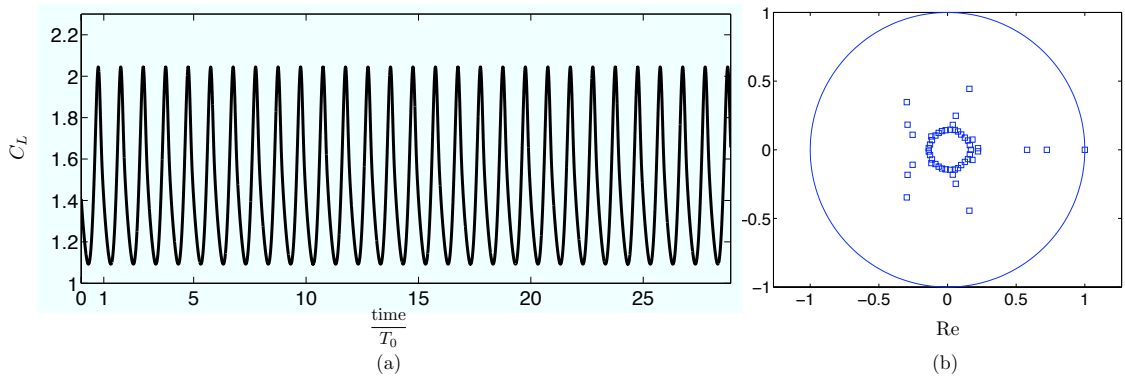


Figure 5.5: The stable periodic orbit for the baseline actuation-free case. (a) The lift coefficient trajectory corresponding to the T_0 -periodic orbit of the nonlinear system (5.2). The average value of the lift coefficient C_L is 1.4530. (b) The leading eigenvalues of the time- T_0 map of the linearized time-periodic system around the orbit.

The Newton-GMRES method is implemented as discussed in Section 5.1.1 to find stable and unstable orbits of the flow with open-loop periodic forcing (5.2). First, we perform a simulation with a forcing period $T_f = T_0$. Its lift coefficient trajectory is shown in Figure 5.6, with an average lift about 13.4% higher than the baseline case (see Figure 5.5). With the $T_f = T_0$ fixed, the Newton-GRMES method is used to solve (5.5) using states corresponding to different phases on the quasi-periodic solution as initial guesses. With T_f fixed, no convergent solution is obtained. However, by regarding the forcing period T_f as an additional unknown and using phase condition (5.6), we find a family of periodic solutions, each with a different period T_f . For instance, one periodic solution, the orbit I with period $T_f = 1040$ time steps, is shown in Figure 5.7(a). Continuation studies using these solutions as starting points and T_f as the bifurcation parameter lead to other periodic solutions. For example, the orbit II shown in Figure 5.8(a) is obtained in this way. Its period is also $T_f = 1040$ time steps. Thus, with forcing period $T_f(= 4.2667) = 1040$ time steps, there are at least two periodic orbits. Both have average lift significantly higher than either the baseline actuation-free case or the $T_f = T_0$ case. The average lift coefficient of the orbit I is 1.8112, higher than that of the orbit II, 1.7812. Figure 5.9 shows a long-term simulation with a forcing period $T_f = 1040$ time steps that begins at a state on the orbit I and eventually converges to the orbit II. Linear stability analyses using the Arnoldi iteration method further show that for the orbit I there is an unstable eigenvalue of the time- T_f map of the linearized time-periodic system, but the linearized time-periodic system about the orbit II is stable; see Figure 5.7(b) and 5.8(b). Neither of them are neutrally stable, as expected in Section 5.1.2.

Figure 5.10 shows the vorticity fields of the orbit I and II, both taken at time phase 0. The noticeable phase difference between these two snapshots (and then

the two orbits) may contribute to the difference in average lift and stability. More detailed analysis on the flow physics is under progress.

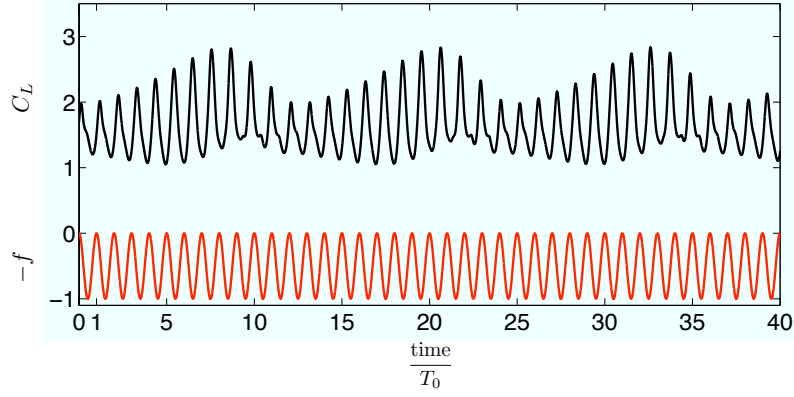


Figure 5.6: The lift coefficient trajectory (—) and the periodic forcing history (—) for the case that the forcing period is equal to the natural period: $T_f = T_0 = 900$ time steps. The approximate average value of the lift coefficient C_L is 1.6480.

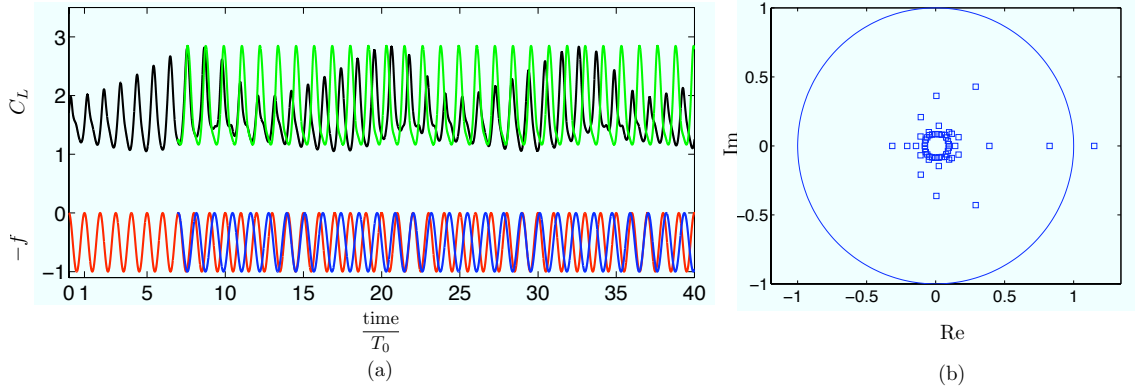


Figure 5.7: Orbit I: The unstable periodic orbit with a forcing period $T_f = 1040$ time steps. (a) The lift coefficient trajectories of the periodic orbit with $T_f = 1040$ time steps (—) and the quasi-periodic case with $T_f = T_0 = 900$ time steps (—), and the actuation history for the periodic orbit with $T_f = 1040$ time steps (—) and for the quasi-periodic case with $T_f = T_0 = 900$ time steps (—). The average value of the lift coefficient C_L of the orbit I is 1.8112. (b) The leading eigenvalues of the time T_f map of the time-periodic system linearized around orbit I.

5.2.2 Reduced-order models

We are interested in the stabilization of the unstable, high-lift orbit I. An unstable linearized time-periodic control system corresponding to orbit I is formed as (5.10).

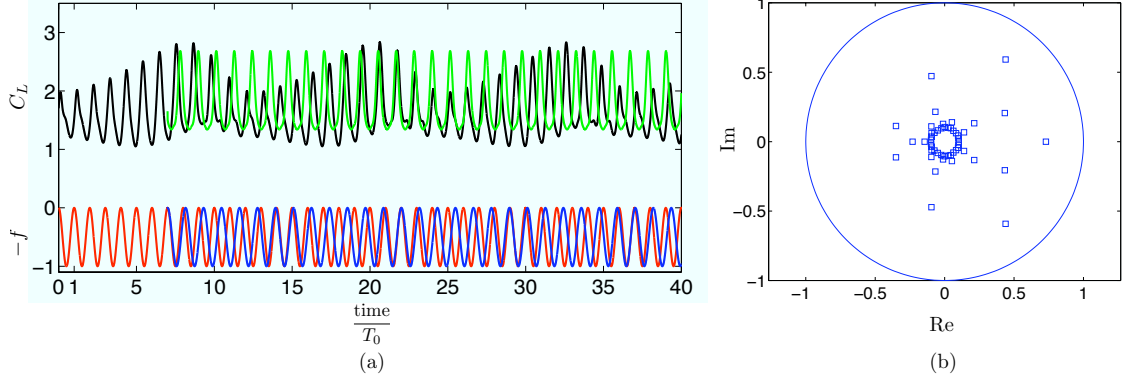


Figure 5.8: Orbit II: The stable periodic orbit with a forcing period $T_f = 1040$ time steps. (a) The lift coefficient trajectories of the periodic orbit with $T_f = 1040$ time steps (—) and the quasi-periodic case with $T_f = T_0 = 900$ time steps (—), and the actuation history for the periodic orbit with $T_f = 1040$ time steps (—) and for the quasi-periodic case with $T_f = T_0 = 900$ time steps (—). The average value of the lift coefficient C_L of the orbit II is 1.7812. (b) The leading eigenvalues of the time T_f map of the time-periodic system linearized around orbit II.

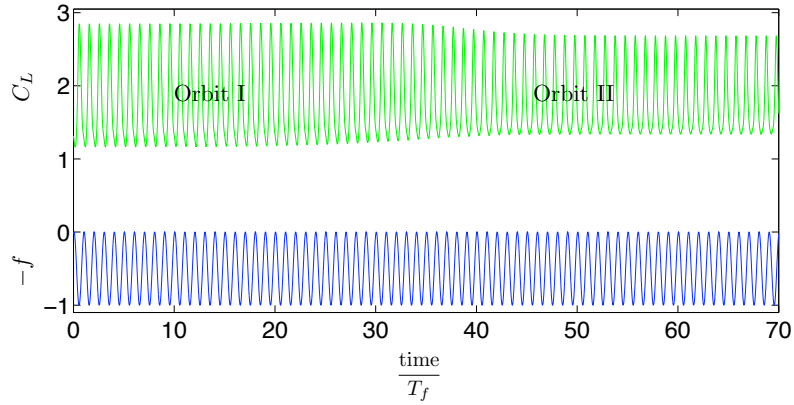


Figure 5.9: The lift coefficient trajectory (—) and the periodic forcing history (—) during the shift from Orbit I to Orbit II. The forcing period is $T_f = 1040$ time steps.

Its lifted, reduced-order model is then obtained by using the lifted ERA method, following the seven steps outlined in Section 5.1.3. We emphasize that the resulting reduced-order model approximates the lifted version of time-periodic system (5.10), whose control input is restricted to change once every s time steps. Equivalently, the reduced system can be regarded as a lifted approximation of the time-periodic system (5.11) with a large time-step corresponding to s real time steps in (5.10). Here we choose the parameter $s = 80 = T_f/13$ time steps such that the control input $u(k)$ is allowed to change only at time steps $k = 0, 80, 160, \dots, 1040, \dots$, thirteen

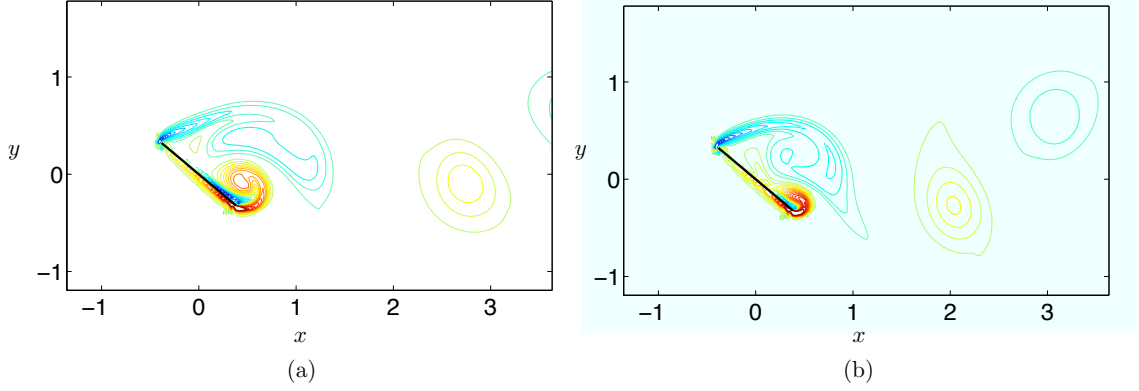


Figure 5.10: The vorticity field of the orbit at time phase 0: (a) Orbit I. (b) Orbit II.

times in one period.

Since the linearized time-periodic system has one unstable dimension, we need to first run an additional set of thirteen simulations, each for $4m$ steps, to project out the components in the unstable direction from the initial conditions for impulse responses; see Section 5.1.3, Steps III.2 and 3. Here we choose $m = 16T_f = 16640$ time steps. Then, thirteen control-free simulations of (5.10) are performed to collect Markov parameters. Each simulation runs for $(2m - 1)$ steps, with projected initial conditions, i.e., $\mathbb{P}F_{(T_f, (i+1)s)}\check{B}_i$, $i = 0, \dots, 12$; see Section 5.1.3, Step III.4. These simulations are indeed impulse responses corresponding to thirteen different time phases of the periodic system (5.11) with large time steps.

Note that for convenience we will denote these simulations with unprojected initial condition $F_{(T_f, (i+1)s)}\check{B}_i$ or with projected initial condition $\mathbb{P}F_{(T_f, (i+1)s)}\check{B}_i$ by “the impulse-response of time phase i with unprojected/projected initial conditions”.

Figure 5.11 shows that the outputs in the impulse-response of time phase 0 with the unprojected initial condition diverge quickly. However, with a projected initial condition, the impulse-response outputs keep decaying at least by the end of the $(2m - 1)$ -steps of the Markov parameter collection process. This result again

supports the argument we proposed in Section 3.4 that a bi-orthogonal projection using unstable left/right eigenvectors can be approximately realized through a power method approach that is adjoint-free and only requires simulations of the primal system.

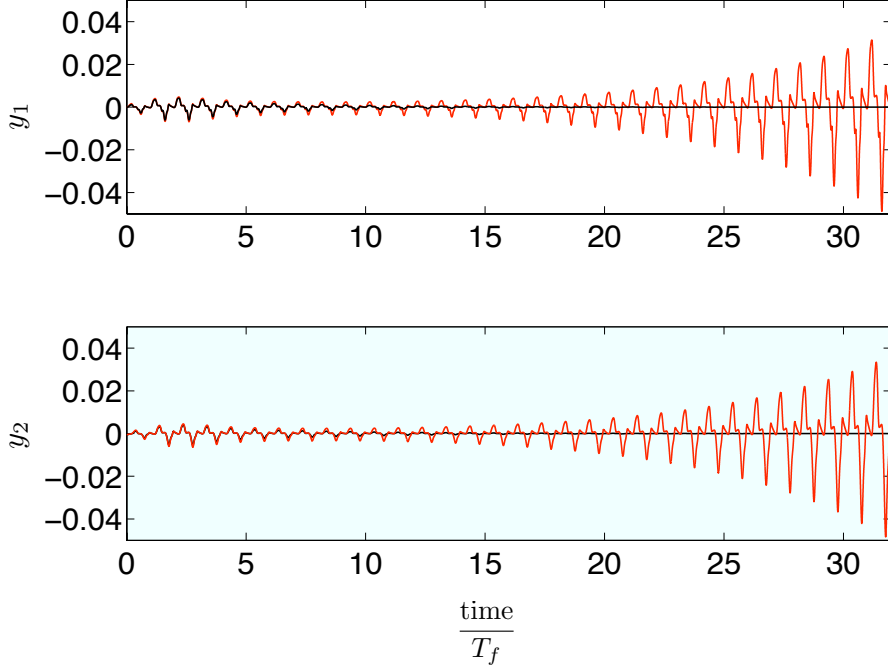


Figure 5.11: The outputs of impulse responses of time phase 0, with unprojected (—) and projected (—) initial conditions. Time period $T_f = 1040$ time steps.

A lifted, 5-dimensional reduced-order model (with $\tilde{A}_r, \tilde{B}_r, \tilde{C}_r, \tilde{D}_r$) for the stable dynamics and a one-dimensional model (with A_u, B_u, C_u) for the unstable dynamics are then computed. The 5-dimensional reduced-order model is perfectly balanced, and the diagonal entries of the reduced-order Gramians are almost identical to the leading Hankel singular values, as shown in Figure 5.12(a). This implies the reduced model captures the most important modes for both controllability and observability for the stable dynamics. On the other hand, the one-dimensional unstable subsystem in the form (5.17) has an eigenvalue, i.e., the value of $\frac{\langle x_0(0), x_0(4m+T_f) \rangle}{\langle x_0(0), x_0(4m) \rangle}$ in (5.17), almost identical to the unstable eigenvalue of the full system (5.10), as shown in

Figure 5.12(b). Furthermore, Figure 5.12(b) also shows that the leading eigenvalues of the 5-dimensional model are also close to the leading stable eigenvalues of the full system.

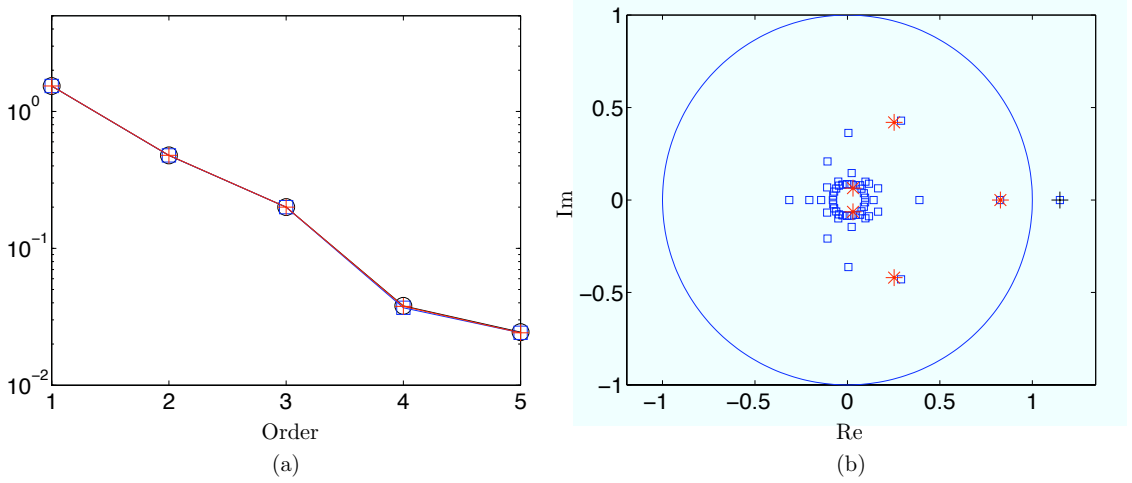


Figure 5.12: Reduced-order model properties. (a) The stable 5-dimensional subsystem: the leading Hankel singular values of the Hankel matrix constructed by Markov parameters (—, \circ), the diagonal entries of the controllability Gramian (—, \square) and those of the observability Gramian (—, $+$). They are almost identical. (b) The leading eigenvalues of the time- T_f map of the full unstable linearized time-periodic system (\square), the eigenvalues of \tilde{A}_r of the stable, reduced 5-dimensional subsystem ($*$), and the eigenvalue of the one-dimensional unstable subsystem ($+$).

Note that for a higher-order reduced model of the stable dynamics, e.g., with a state dimension higher than 10, the \tilde{A}_r matrix will have an unstable eigenvalue that converges to the unstable eigenvalue of the full \tilde{A}_0 quickly as the order r increases. This undesirable effect is not surprising. Even though the Markov parameters (outputs) are collected in impulse responses using projected initial conditions, numerical errors in the unstable direction accumulate with time and are still included in the Markov parameters. However, the Markov parameters are decaying during the impulse responses, which means they are still dominated by the stable dynamics. Also, the unstable eigenvalue does not appear until the order of truncation is higher than 10, which corresponds to very small Hankel singular values (at the order less than 10^{-3}). This indicates that for the stable part of dynamics, the unstable direction is

almost uncontrollable and unobservable, as we expect.

The final, combined 6-dimensional system has a lifted input \tilde{u} with $pT_s = 13$ dimensions, and a lifted output \tilde{y}_r with $qT_f = 2080$ dimensions. We now compare the impulse responses, the most representative simulations for linear control systems, of the reduced-order model and the full linear system. By construction, the impulse response for the first control input of the reduced system corresponds to the impulse response of time phase 0 of the full time-periodic system (5.11), with the unprojected initial condition. Furthermore, it is easy to check that a projection

of the reduced $B = \begin{bmatrix} \tilde{B}_r \\ B_u \end{bmatrix}$ matrix onto the stable 5-dimensional subspace of the

reduced 6×6 state transition matrix results in the matrix $\begin{bmatrix} \tilde{B}_r \\ 0 \end{bmatrix}$, where 0 stands for a zero row vector. Thus, the impulse response for the first control input of the reduced system using the projected reduced B matrix corresponds to the impulse response of time phase 0 of the full time-periodic system (5.11), with projected initial condition. Again, for convenience, we denote the above impulse responses for the reduced system by “impulse response of the reduced model, with projected/unprojected initial conditions”.

The outputs of the impulse responses of the reduced 6-order model match very well the outputs of the corresponding impulse responses of the full time-periodic system (with a dimension of state about 1.4×10^5), for both the projected and the unprojected initial conditions. See Figure 5.13 for an example where the trajectories of the first output are plotted.

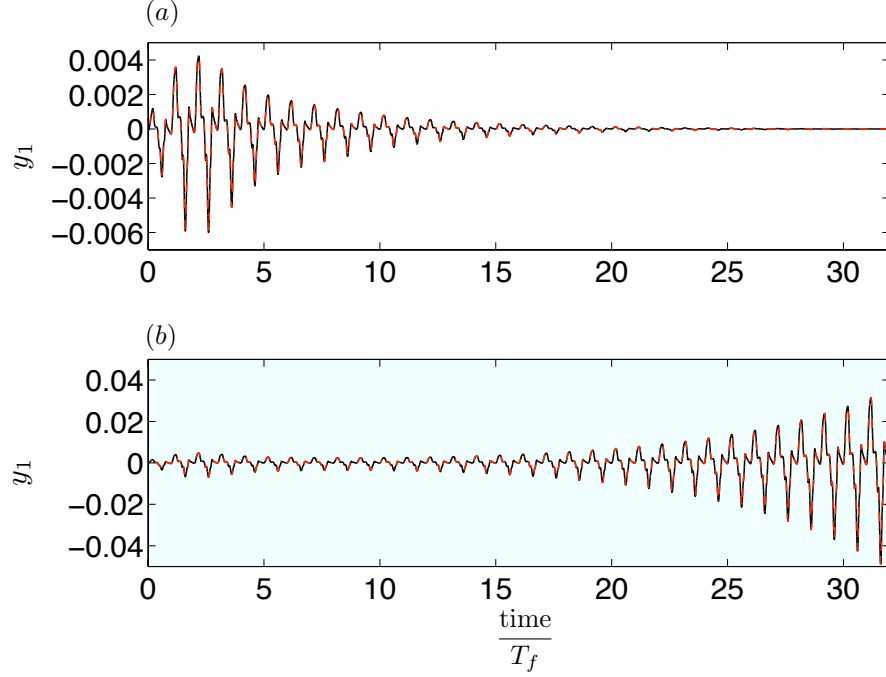


Figure 5.13: The first output y_1 of the impulse response of the 6-order reduced system (---) and that of the impulse response of time phase 0 of the full linear system (—): (a) with the projected initial condition; (b) with the unprojected initial condition. In both cases, the trajectories of y_1 of the reduced-order model and the full system are almost identical.

5.2.3 Observer-based feedback control results

In this section, an observer-based controller for the reduced system is designed using LQR for the control gain K and pole placement for the observer gain L . The weight matrices for LQR (see (5.19)) are chosen as $Q = 5I_{6 \times 6}$ and $R = I_{13 \times 13}$. The observer gain L is obtained by placing the eigenvalues of $(\tilde{A}_r - L\tilde{C}_r)$ at $\text{eig}(\tilde{A})/10$, where $\text{eig}(\tilde{A})$ are the eigenvalues of (\tilde{A}) , such that the eigenvalues of $(\tilde{A}_r - L\tilde{C}_r)$ are close to zero. The controllers can be further tuned and more sophisticatedly designed, such as by adjusting the weight of Q on the unstable dimension of \tilde{x}_r , or by defining $Q = \tilde{C}_r^* \tilde{C}_r$ such that in LQR the “energy of the output” $\sum_{t=0}^{\infty} \tilde{y}_r(t)^* \tilde{y}_r(t)$ is minimized. The observer gain L could also be found using optimal control methods such as LQE (Skogestad & Postlethwaite, 2005). However we emphasize that the main tasks in this work on the model problem are (i) to design a model-based

feedback controller that can stabilize the unstable periodic orbit, and (ii) equally importantly, to test whether a controller designed for the reduced-order model will also work for the full linear system in a dynamically similar way, i.e., if the closed-loop behavior of the full and reduced systems are similar. This will validate our approach of control design for the full system using reduced-order models.

The closed-loop behavior of the full and reduced linear systems are indeed very similar: to demonstrate this, we apply the observer-based controller onto the lifted reduced-order model as illustrated in Figure 5.2. Independently, we apply the same observer-based controller onto the full linear time-periodic system as illustrated Figure 5.3. The control goal is to suppress the diverging impulse responses with unprojected initial conditions (see Figure 5.11). Figure 5.14 shows that the controller indeed stabilizes both the lifted reduced-order model and the full linear time-periodic system. Further, the two output trajectories for the full and reduced-order models are almost identical, and the two control input histories are also very close to each other. This indicates the observer-based reduced-order control system can capture well the closed-loop behavior of the full linear time-periodic system equipped with the same observer-based controller.

As shown in Figure 5.14, the control input is zero until the start of the second period at time $T_f = 1040$ time steps, as the observer begins with a zero reduced state estimate. Then, at time T_f , the observer uses the outputs stored in the first period to update the reduced state estimate, with which the control input signals for the next whole period are computed. Notice that as mentioned before the control inputs here are designed to be constant in every time step interval $[k, k + 80]$, $k = 0, 80, 160, \dots$. Also notice that the control effort for the stabilization is one magnitude smaller than the open-loop periodic forcing.

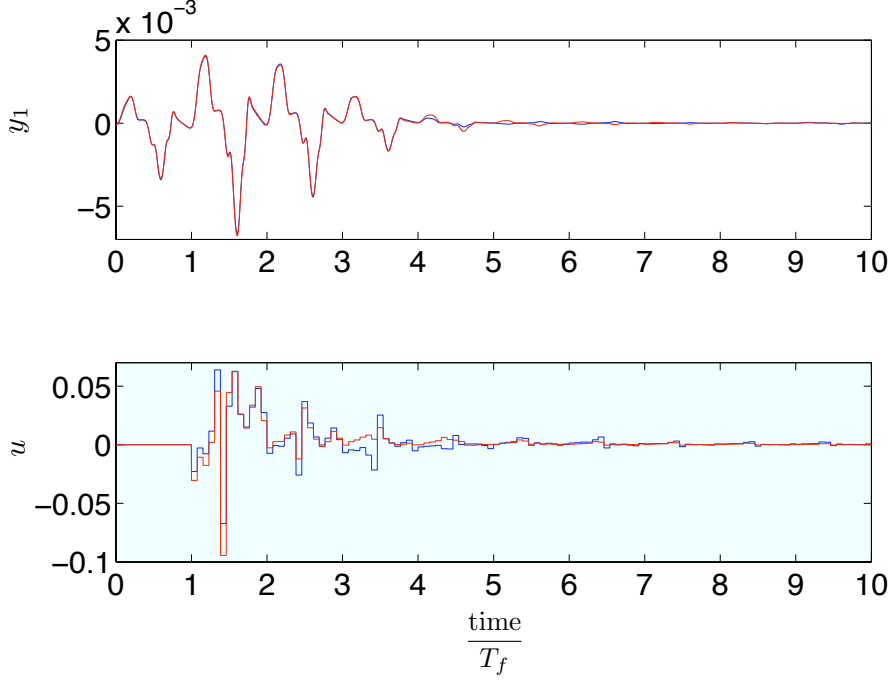


Figure 5.14: The representative output y_1 trajectories and control u trajectories for observer-based feedback control respectively on the reduced-order model (—) and on the full linear time-periodic system (—), for suppressing the otherwise diverging impulse response. Time period $T_f = 1040$ time steps.

Finally, the observer-based controller is applied to the full nonlinear system as illustrated in Figure 5.4. Figure 5.15 shows a typical case in which the controller successfully stabilizes the otherwise unstable orbit. The feedback control input effort is reasonably small compared to the open-loop periodic forcing (except during the first three cycles of application).

Although the current controller stabilizes the desired periodic orbit even for the full nonlinear system, its region of attraction is small. For instance, the controller can not control the system with an initial state on the stable orbit II to evolve to the unstable orbit I. A likely reason is that the controller is intrinsically designed for the linearized time-periodic system. However, nonlinear dynamics dominates if the state is far from the orbit. In such a situation, other control methods, such as open-loop optimal control, could be applied first to bring the system state close to

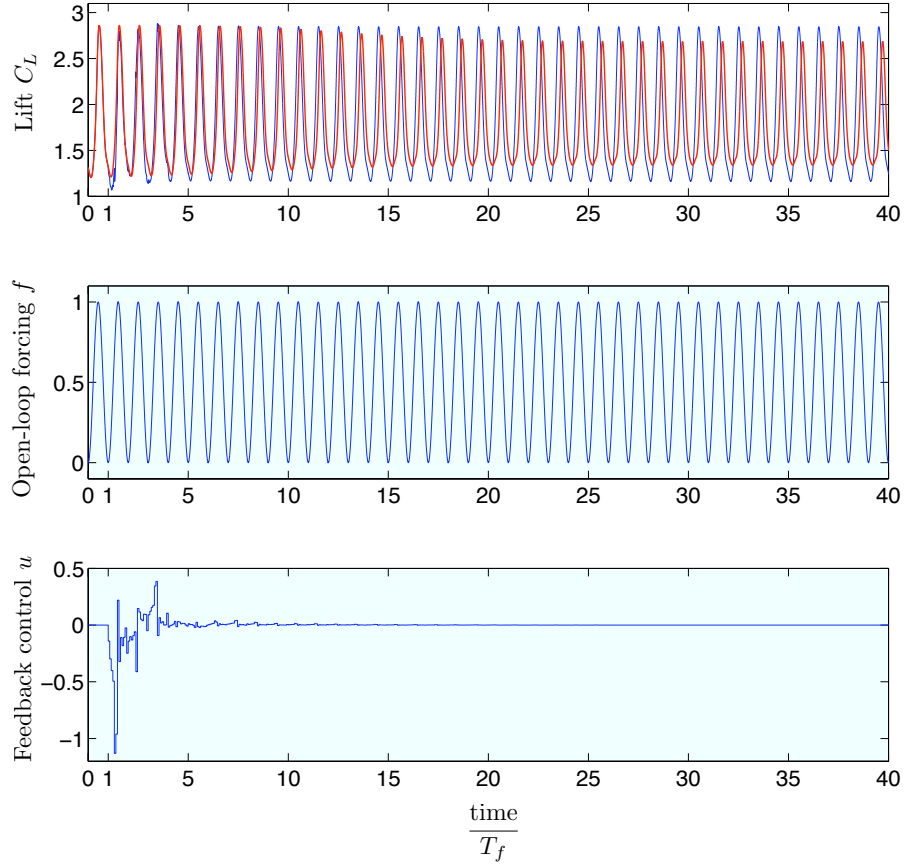


Figure 5.15: Stabilization of the unstable periodic orbit I with the observer-based feedback controller. The top plot shows a comparison between without control (—) and with control on (—). The one without control eventually converges to the stable orbit II. The one with control on converges to the unstable orbit I. Time period $T_f = 1040$ time steps.

the desired orbit, and then the feedback control could be turned on to stabilize the orbit. Also, it would be interesting to compute time-periodic reduced-order models by using the periodic ERA/balanced POD algorithms. With this approach, there would not be a large delay in updating control inputs, as we have with the current approach in which the reduced state is updated only once per period. As mentioned previously, a disadvantage is that control tools for LTI systems would no longer be applicable.

5.3 Summary

In the model problem of flow past a two-dimensional plate with open-loop periodic forcing, we stabilize an unstable high-lift periodic orbit using an observer-based feedback controller. The unstable periodic orbit is found using the Newton-GMRES method. The lifted ERA method, an adjoint-free approximate balanced truncation method proposed in Chapter 4, is applied here to compute a reduced-order model of the unstable linearized time-periodic system corresponding to the unstable orbit. Simulation results show that the reduced-order model captures the full linearized input-output dynamics well. The reduced-order model is then used to design an observer-based feedback controller for the full linearized system. The observer-based feedback controller stabilizes the unstable equilibrium of the lifted full linearized system. Furthermore, the reduced-order lifted model equipped with the observer also captures well the closed-loop input-output behavior of the full linearized time-periodic system equipped with the observer. Finally, the controller is applied to the full nonlinear system to stabilize the unstable high-lift orbit (the orbit I, see Figure 5.7), whose average lift is 24.7% higher than that of the baseline case (see Figure 5.5), 9.90% higher than that of the quasi-periodic case where the forcing period is identical to the natural vortex shedding period (see Figure 5.6), and 1.68% higher than that of the stable orbit II (see Figure 5.8).

The current controller has a relatively small range of region of attraction for the full nonlinear system. Possible improvements include better tuning of the controller and observer gains K , L , the usage of LQE and other linear controller design methods, or nonlinear control techniques to attract the state to a neighborhood of the orbit within which the linearized dynamics dominates such that the feedback controller developed here can be applied for the stabilization.

Chapter 6

Variational Lie-Poisson Hamiltonian integrators

6.1 Introduction

In Chapters 2, 3, 4 and 5, we discussed model dimensional reduction for control systems with high-dimensional states. The reduced-order models can capture (reconstruct) the correct input-output dynamics of the original system. These model reduction methods are therefore applicable to feedback control design for dynamical systems in fluids that are dominated by low-dimensional coherent structures. In this chapter, we consider another important feature in fluidic dynamical systems and its applications. It is well known that the governing equations for ideal fluids and fluid-body interactions (without dissipation) are Hamiltonian, which implies there are symmetry-induced conservation laws in these systems. The conservation laws can include, for example, the conservation of Poisson structure, Hamiltonian function, Casimir function(s), and momentum map(s) (Marsden & Ratiu, 1994).

Practically, most Hamiltonian systems are nonlinear ordinary differential equations (ODEs) or partial differential equations (PDEs) for which closed forms of analytic solutions are not available, and therefore numerical simulations play a crucial role for understanding their behavior. However, standard finite difference schemes, such as Runge-Kutta methods, often cannot satisfy the conservation laws at the discrete level, which can result in qualitatively incorrect behavior: for instance, a conservative Hamiltonian system typically becomes dissipative in simulations. This drawback can be serious, especially in simulations of long-term and/or chaotic Hamiltonian dynamics. To solve this problem, in the last two decades the so-called *geometric integrators* have been developed to preserve some or all of the conservation laws at the discrete level. Specifically, for canonical (symplectic) Hamiltonian systems, this subject is well studied: symplectic integrators can be constructed in a systematic way; see Hairer *et al.* (2006); Leimkuhler & Reich (2004); Marsden & West (2001) and the references therein. However, for more general non-canonical Hamiltonian systems, this is still an open problem.

In this work, we present a variational approach for construction of geometric integrators for *Lie-Poisson Hamiltonian systems*, a special class of non-canonical Hamiltonian systems that plays an important role in fluid dynamics. Lie-Poisson Hamiltonian systems arise in ideal fluid mechanics, such as the Euler equations for an inviscid fluid and the equations of motion for N point vortices on a sphere; rigid body dynamics, such as the Euler equations for free rigid body rotation; and many other settings (Marsden & Ratiu, 1994). Our approach is based on regarding the Lie-Poisson system as a reduced form of a full canonical Hamiltonian system, and then in the resulting integrators some of the dynamics in the “full space” is reconstructed. The approach is systematic and valid for general finite-dimensional Lie-Poisson systems. It is a natural generalization, on the Hamiltonian side, of the

variational approach for integrators of Euler-Poincaré Lagrangian systems developed by Marsden and collaborators in Marsden *et al.* (1999a); Bou-Rabee (2007). Note that the study of geometric integrators for Lie-Poisson systems was originated by Ge & Marsden (1988) using generating functions. Since then, several approaches, including Lie group methods, the splitting method, and integrators based on the Darboux-Lie theorem that converts the Lie-Poisson system into a canonical Hamiltonian system, have been established. However, the latter two approaches are only applicable to Lie-Poisson systems with certain special structure, while the Lie group method does not in general preserve the Lie-Poisson/symplectic structure in simulations. More details and comments can be found, for example, in Hairer *et al.* (2006).

In this chapter, Section 6.2 introduces the background on Lie-Poisson systems. In Section 6.3, 6.4 and 6.5 we present three different categories of Lie-Poisson integrators developed using a variational approach: schemes defined on $G \times \mathfrak{g}^*$, $\mathfrak{g} \times \mathfrak{g}^*$, and \mathfrak{g}^* . In Section 6.6, simulation results are shown for two examples, namely the dynamics of free rigid body rotation, and the dynamics of N point vortices on a sphere. We note that the second example is the main motivating application for this work. Results in this chapter are reported in Ma & Rowley (2010).

6.2 Background: Lie-Poisson systems

6.2.1 Preliminaries

A Lie-Poisson Hamiltonian system is defined on \mathfrak{g}^* , the dual of a Lie algebra \mathfrak{g} . In this work we restrict our study to the case where \mathfrak{g} is finite dimensional, which guarantees the existence of a certain Lie group G such that the \mathfrak{g} is its Lie algebra.

The Poisson bracket form of Lie-Poisson systems is

$$\dot{F}(\mu) = \{F, h\}_{LP}^{\mp}(\mu) \quad (6.1)$$

where the dot stands for time derivative, $\mu \in \mathfrak{g}^*$, $F: \mathfrak{g}^* \rightarrow \mathbb{R}$, $h: \mathfrak{g}^* \rightarrow \mathbb{R}$ is the Hamiltonian function, and the Lie-Poisson structure is

$$\{F, h\}_{LP}^{\mp}(\mu) = \mp \left\langle \mu, \left[\frac{dF}{d\mu}, \frac{dh}{d\mu} \right] \right\rangle, \quad (6.2)$$

in which $dF/d\mu, dh/d\mu \in \mathfrak{g}$, $\langle \cdot, \cdot \rangle : \mathfrak{g}^* \times \mathfrak{g} \rightarrow \mathbb{R}$ is the pairing between elements in a vector space and its dual, and $[\cdot, \cdot] : \mathfrak{g} \times \mathfrak{g} \rightarrow \mathfrak{g}$ is the Lie bracket in \mathfrak{g} . Equivalently, the intrinsic coordinate-free form of Lie-Poisson systems is

$$\dot{\mu} = \pm \text{ad}_{\frac{dh}{d\mu}}^* \mu \quad (6.3)$$

where ad^* stands for the dual of the usual ad operator on \mathfrak{g} . Note that $\text{ad}_a b = [a, b]$ for $a, b \in \mathfrak{g}$.

A key remark is that the Lie-Poisson system on $\mathfrak{g}^* \approx T^*G/G$ can be regarded as a reduced system resulting from *Lie-Poisson reduction* of a canonical Hamiltonian system on the cotangent bundle T^*G in which the Hamiltonian $H : T^*G \rightarrow \mathbb{R}$ is left / right invariant under action of G . The $+/-$ in Lie-Poisson equations (6.3) correspond to the left/right invariant cases respectively. We refer readers to Marsden & Ratiu (1994) for a general discussion on Lie-Poisson systems and Lie-Poisson reduction.

Since a Lie-Poisson system is a reduced Hamiltonian system, it is natural to define a reduced Legendre transform to link the Lie-Poisson system to an Euler-Poincaré system, the corresponding reduced Lagrangian system defined on \mathfrak{g} (Marsden & Ratiu, 1994). An *Euler-Poincaré system* reads

$$\frac{d}{dt} \left(\frac{dl}{d\xi} \right) = \pm \text{ad}_{\xi}^* \frac{dl}{d\xi}, \quad (6.4)$$

where $\xi \in \mathfrak{g}$, $l(\xi)$ is the reduced Lagrangian mapping $\mathfrak{g} \rightarrow \mathbb{R}$, and $+/-$ represents left/right invariant cases, respectively. Then $\mathfrak{g} \approx TG/G$, where TG is the tangent bundle on which the full Lagrangian system is defined, with variable (g, \dot{g}) , $g \in G$, and the reduced variable $\xi(t) = g^{-1}(t)\dot{g}(t) := T_{g(t)}L_{g(t)}^{-1}\frac{dg}{dt} \in \mathfrak{g}$ (for the left-invariant case) or $\xi(t) = \dot{g}(t)g^{-1}(t) := T_{g(t)}R_{g(t)}^{-1}\frac{dg}{dt} \in \mathfrak{g}$ (for the right-invariant case). If the mapping defined by the *reduced Legendre transform* $\mu = dl/d\xi$, $h(\mu) = \langle \mu, \xi \rangle - l(\xi)$ and the inverse transform $\xi = dh/d\mu$, $l(\xi) = \langle \mu, \xi \rangle - h(\mu)$ is a diffeomorphism, the reduced Euler-Poincaré Lagrangian and Lie-Poisson Hamiltonian are hyperregular, and the Euler-Poincaré system (6.4) is equivalent to the Lie-Poisson system (6.3). In summary, for systems with hyperregular Lagrangians/Hamiltonians, the diagram in Figure 6.1 commutes.

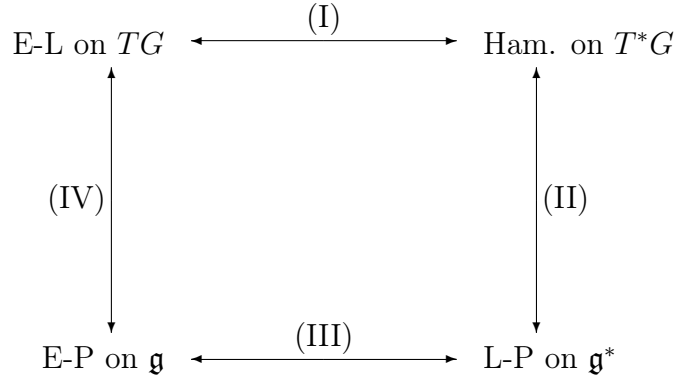


Figure 6.1: Relations between Euler-Lagrange (E-L) systems, canonical Hamiltonian (Ham.) systems, Euler-Poincaré (E-P) systems and Lie-Poisson (L-P) systems. (I): Legendre transform; (II): Lie-Poisson reduction/reconstruction; (III): reduced Legendre transform; (IV): Euler-Poincaré reduction/reconstruction.

We emphasize that the point here is not to regard a Lie-Poisson system as an isolated system, but to relate it to a canonical Hamiltonian system on T^*G by Lie-Poisson reduction/reconstruction and to a reduced Lagrangian system on \mathfrak{g} by the reduced Legendre transform, even if the forms of the canonical Hamiltonian system and the Euler-Poincaré system may be not explicitly known.

6.2.2 Conservation laws

Along solution flows of a Lie-Poisson system, the Lie-Poisson structure is preserved. Its Hamiltonian function is also conserved along the solution flow since $\dot{h} = \{h, h\}_{LP} \equiv 0$. Any *Casimir function* C , defined by $\dot{C} = \{C, K\}_{LP} \equiv 0$ for any real valued function $K : \mathfrak{g}^* \rightarrow \mathbb{R}$, is also conserved if it exists. Furthermore, if the Hamiltonian h is invariant under the action of a symmetry group G_s , then by the Hamiltonian version of Noether's theorem, the corresponding momentum map is conserved along the solution flow too.

Another feature of a Lie-Poisson system is the preservation of its *coadjoint orbits* along solution flows. The solution of a Lie-Poisson system for the left-invariant case (with '+' sign in (6.3)) is in form of

$$\mu(t) = \text{Ad}_{g(t)}^* \mu(t_0), \quad (6.5)$$

where $\mu(t_0)$ is the initial condition, Ad^* , the dual of the adjoint action operator Ad , stands for coadjoint action, and the curve $g(t) \in G$ satisfies $\frac{dg}{dt}(t) = g^{-1}(t)\dot{g}(t) \in \mathfrak{g}$. Starting from $\mu(t_0) \in \mathfrak{g}^*$, the solution stays on $\text{Orb}(\mu(t_0))$, the coadjoint orbit of $\mu(t_0)$. For the right-invariant case, the solution is in form of $\mu(t) = \text{Ad}_{g(t)^{-1}}^* \mu(t_0)$ with $g(t) \in G$ satisfying $\frac{dg}{dt}(t) = \dot{g}(t)g^{-1}(t) \in \mathfrak{g}$. If all the coadjoint orbits are connected, Casimir functions are also preserved along each coadjoint orbit (Marsden & Ratiu, 1994). This is another way to show the Casimir functions are constant along solution flows.

6.2.3 Lie-Poisson Variational Principle

As a counterpart of the well-known Euler-Poincaré variational principle that is equivalent to the Euler-Poincaré equations on the reduced Lagrangian side, Cen-

dra *et al.* (2003) presented the *Lie-Poisson variational principle* on the reduced Hamiltonian side:

$$\delta \int_0^T (\langle \mu(t), \xi(t) \rangle - h(\mu(t))) dt = 0, \quad (6.6)$$

where $\mu \in \mathfrak{g}^*$, h is the reduced Hamiltonian, and for the left-invariant case $\xi = g^{-1}\dot{g} \in \mathfrak{g}$, $g \in G$. Here $\delta\mu$ is arbitrary while $\delta\xi = \dot{\eta} + [\xi, \eta]$, with $\eta = g^{-1}\delta g$ and $\delta g(t)$ arbitrary everywhere except that $\delta g(0) = \delta g(T) = 0$. For the right-invariant case, the above setting is replaced by $\xi = \dot{g}g^{-1} \in \mathfrak{g}$ and $\delta\xi = \dot{\eta} - [\xi, \eta]$ where $\eta = \delta g g^{-1}$. Cendra *et al.* (2003) showed the principle is equivalent to the Lie-Poisson equations (6.3). More precisely, it is equivalent to the pair of equations

$$\dot{\mu} = \pm \text{ad}_\xi^* \mu; \quad (6.7)$$

$$\xi = \frac{dh}{d\mu}. \quad (6.8)$$

The Lie-Poisson principle implies the preservation of a symplectic two-form along the Lie-Poisson flow; see Proposition C.0.7 in Appendix C.

6.2.4 Why variational Lie-Poisson integrators?

Formally, a variational integrator is an integrator obtained by discretization of variational principles. Variational integrators for canonical Hamiltonian systems / full Lagrangian systems are by construction symplectic (Marsden & West, 2001), i.e., they preserve a discrete symplectic two form exactly. This is an appealing property since by backward error analysis (Hairer *et al.*, 2006) it follows that the simulation results are exponentially close to a Hamiltonian system nearby the original one. Following the same spirit, we would like to develop variational Lie-Poisson (VLP) integrators for Lie-Poisson reduced Hamiltonian systems. A cautionary note is that, depending on its construction, the integrators may or may not conserve a discrete

Lie-Poisson structure or symplectic structure. The fundamental reason why certain integrators do not preserve discrete Hamiltonian structures is that, in the discrete setting, Lie algebra elements $\xi \in \mathfrak{g}$ depend on Lie group elements $g \in G$, and therefore variations $\delta\xi$ are not arbitrary, which may cause the issue that the one-form defined by $\delta\xi$ at the discrete level is not closed. We will see details concerning this in Section 6.4, 6.5. To be consistent with the terminology convention in the literature, in this note an integrator will be referred to as a *variational integrator* only when it is obtained by discretization of a variational principle and preserves a Hamiltonian structure.

Note that on the reduced Lagrangian side, i.e., for Euler-Poincaré systems, Marsden and collaborators (Marsden *et al.*, 1999a; Bou-Rabee, 2007) have developed variational integrators by discretizing the Euler-Poincaré variational principle. The work here is a natural analog on the reduced Hamiltonian side. Indeed, if a Lie-Poisson system can be rewritten as an Euler-Poincaré system using the reduced Legendre transform, then those variational Euler-Poincaré integrators are readily applicable. However, it is important to obtain variational Lie-Poisson integrators directly on the reduced Hamiltonian side, especially for cases when the reduced Lagrangian form is not available, due to a degenerate reduced inverse Legendre transform, or it is computationally difficult to invert the transform. For instance, the problem of N point vortices evolving on a sphere (Section 6.6.2) has been shown to be a Lie-Poisson system for the right-invariant case; see, e.g., Pekarsky & Marsden (1998). However, to convert the mechanics to the reduced Lagrangian side using the reduced Legendre transform is computationally complicated; as a result, no Euler-Poincaré form of this system is available so far.

6.3 Variational Lie-Poisson integrators on $G \times \mathfrak{g}^*$

We begin by defining $\Theta : \mathfrak{g}^* \times \mathfrak{g} \rightarrow \mathbb{R}$ by

$$\Theta(\mu, \xi) = \langle \mu, \xi \rangle - h(\mu). \quad (6.9)$$

It is essentially a reduced Lagrangian, expressed in terms of the reduced Hamiltonian. Then, we approximate the variational principle (6.6) by

$$0 = \delta \int_0^T \Theta(\mu(t), \xi(t)) dt = \delta \sum_{k=0}^{K-1} \int_{t_k}^{t_{k+1}} \Theta(\mu(t), \xi(t)) dt \approx \delta \sum_{k=0}^{K-1} \Theta(\mu(t_k), \xi(t_k)) \Delta t, \quad (6.10)$$

where $\Delta t = \frac{T}{K}$ is small, $t_k = k\Delta t$, $k = 0, \dots, K-1$. Consider the left-invariant case where $\xi = g^{-1}\dot{g}$. A natural way to approximate $\xi(t_k)$ is $\xi_k = \xi_k(g_k, g_{k+1}) \approx \xi(t_k)$ where $g_k \approx g(t_k)$. For example, one choice is $\xi_k = g_{k+1}^{-1} \frac{g_{k+1} - g_k}{\Delta t} = \frac{1}{\Delta t} (\text{Id} - g_{k+1}^{-1} g_k)$ where Id is the identity element of G (this choice is consistent with that in Marsden *et al.* (1999a) for variational Euler-Poincaré integrators on G). Note that besides the finite difference approximation, other general methods of relating Lie group and Lie algebra elements are also available, e.g., retraction maps (Shub, 1984) arising from the embedding of the group into a linear space. Define

$$f_{k+1k} = g_{k+1}^{-1} g_k \quad (6.11)$$

and approximate $\xi(t_k) \approx \xi_k = \xi_k(f_{k+1k})$. Let $\mu_k \approx \mu(t_k)$. Note that in the discrete approximation we would like to keep $g_k \in G$, $\xi_k \in \mathfrak{g}$ and $\mu_k \in \mathfrak{g}^*$.

Let

$$\bar{\Theta}_k = \bar{\Theta}(\mu_k, f_{k+1k}) := \Theta(\mu_k, \xi_k) = \langle \mu_k, \xi_k \rangle - h(\mu_k). \quad (6.12)$$

Proposition 6.3.1. *For the left-invariant case, with the above setting, the discrete*

variational principle

$$0 = \delta \sum_{k=0}^{K-1} \bar{\Theta}(\mu_k, f_{k+1k}), \quad (6.13)$$

where

$$\delta f_{k+1k} = -g_{k+1}^{-1} \delta g_{k+1} g_{k+1}^{-1} g_k + g_{k+1}^{-1} \delta g_k, \quad (6.14)$$

δg_k , $k = 1, \dots, K-1$, arbitrary, $\delta g_0 = \delta g_K = 0$ and $\delta \mu_k$, $k = 0, \dots, K-1$, arbitrary, is equivalent to the sets of equations

$$\left\langle \frac{\partial \bar{\Theta}_k}{\partial f_{k+1k}}, f_{k+1k} \eta_k \right\rangle - \left\langle \frac{\partial \bar{\Theta}_{k-1}}{\partial f_{kk-1}}, \eta_k f_{kk-1} \right\rangle = 0, \quad k = 1, \dots, K-1; \quad (6.15)$$

$$\xi_k - \frac{dh_k}{d\mu_k} = 0, \quad k = 0, \dots, K-1, \quad (6.16)$$

where $\eta_k = g_k^{-1} \delta g_k$ and $h_k := h(\mu_k)$.

Proof. Direct calculation leads to (6.14). Then,

$$\begin{aligned} 0 &= \delta \sum_{k=0}^{K-1} \bar{\Theta}(\mu_k, f_{k+1k}) \\ &= \sum_{k=0}^{K-1} \left\langle \delta \mu_k, \frac{\partial \bar{\Theta}_k}{\partial \mu_k} \right\rangle + \sum_{k=0}^{K-1} \left\langle \frac{\partial \bar{\Theta}_k}{\partial f_{k+1k}}, \delta f_{k+1k} \right\rangle \\ &= \sum_{k=0}^{K-1} \left\langle \delta \mu_k, \frac{\partial \bar{\Theta}_k}{\partial \mu_k} \right\rangle + \sum_{k=0}^{K-1} \left\langle \frac{\partial \bar{\Theta}_k}{\partial f_{k+1k}}, (-g_{k+1}^{-1} \delta g_{k+1} g_{k+1}^{-1} g_k + g_{k+1}^{-1} \delta g_k) \right\rangle \\ &= \sum_{k=0}^{K-1} \left\langle \delta \mu_k, \xi_k - \frac{dh(\mu_k)}{d\mu_k} \right\rangle + \sum_{k=1}^{K-1} \left(\left\langle \frac{\partial \bar{\Theta}_k}{\partial f_{k+1k}}, f_{k+1k} \eta_k \right\rangle - \left\langle \frac{\partial \bar{\Theta}_{k-1}}{\partial f_{kk-1}}, \eta_k f_{kk-1} \right\rangle \right) \end{aligned}$$

in which the last step is obtained from (6.12) and by relabelling indices and using the boundary conditions $\delta g_0 = \delta g_K = 0$. Equations (6.15) and (6.16) follow since δg_k , $k = 1, \dots, K-1$, and $\delta \mu_k$, $k = 0, \dots, K-1$, are arbitrary. The derivation from (6.15) and (6.16) to (6.13) is obvious using the relations above. \square

The statement above provides the **Variational Lie-Poisson integrator on $G \times \mathfrak{g}^*$** (6.15) and (6.16) mapping $(\mu_k, f_{k+1k}) \mapsto (\mu_{k+1}, f_{k+2k+1})$ for $k = 0, \dots, K-2$. By

the chain rule and the definition of $\bar{\Theta}_k$, (6.12), the VLP on $G \times \mathfrak{g}^*$ can be rewritten as

$$\left\langle \mu_k \frac{d\xi_k}{df_{k+1k}}, f_{k+1k} \eta_k \right\rangle - \left\langle \mu_{k-1} \frac{d\xi_{k-1}}{df_{kk-1}}, \eta_k f_{kk-1} \right\rangle = 0, \quad k = 1, \dots, K-1; \quad (6.17)$$

$$\xi_k(f_{k+1k}) = \frac{dh(\mu_k)}{d\mu_k}, \quad k = 0, \dots, K-1. \quad (6.18)$$

Proposition 6.3.2. *A symplectic two-form is preserved along a solution sequence of the VLP on $G \times \mathfrak{g}^*$ (6.15) and (6.16).*

Proof. Rewrite the sum in the discrete Lie-Poisson principle (6.13) as

$$S_d(\{g_k, \mu_k\}) = \sum_{k=0}^{K-1} \bar{\Theta}(\mu_k, f_{k+1k}). \quad (6.19)$$

For short, define $\mathbf{v}_k = ((\delta g_k, \delta \mu_k), (\delta g_{k+1}, \delta \mu_{k+1}))$. We have

$$\begin{aligned} dS_d(\{g_k, \mu_k\}) \cdot (\{\delta g_k, \delta \mu_k\}) &= \sum_{k=0}^{K-1} (d\bar{\Theta}(\mu_k, f_{k+1k}) \cdot \mathbf{v}_k) \\ &= \sum_{k=0}^{K-1} \left[\left\langle \frac{\partial \bar{\Theta}}{\partial \mu_k}, d\mu_k \cdot \mathbf{v}_k \right\rangle + \left\langle \frac{\partial \bar{\Theta}}{\partial f_{k+1k}}, df_{k+1k} \cdot \mathbf{v}_k \right\rangle \right] \end{aligned} \quad (6.20)$$

where

$$d\mu_k \cdot \mathbf{v}_k = \delta \mu_k; \quad df_{k+1k} \cdot \mathbf{v}_k = \delta f_{k+1k} = -g_{k+1}^{-1} \delta g_{k+1} g_{k+1}^{-1} g_k + g_{k+1}^{-1} \delta g_k. \quad (6.21)$$

Thus, by direct calculation and the equality of mixed partials,

$$\begin{aligned}
& \mathbf{d}^2 S_d(\{g_k, \mu_k\}) \cdot (\{\delta g_k^1, \delta \mu_k^1\}, \{\delta g_k^2, \delta \mu_k^2\}) \\
&= \sum_{k=0}^{K-1} [d(d\bar{\Theta}(\mu_k, f_{k+1k}) \cdot \mathbf{v}_k^2) \cdot \mathbf{v}_k^1 - d(d\bar{\Theta}(\mu_k, f_{k+1k}) \cdot \mathbf{v}_k^1) \cdot \mathbf{v}_k^2] \\
&= \sum_{k=0}^{K-1} \left[\left\langle \frac{\partial \bar{\Theta}}{\partial f_{k+1k}}, d(df_{k+1k} \cdot \mathbf{v}_k^2) \cdot \mathbf{v}_k^1 - d(df_{k+1k} \cdot \mathbf{v}_k^1) \cdot \mathbf{v}_k^2 \right\rangle \right. \\
&\quad \left. + \left\langle \frac{\partial \bar{\Theta}}{\partial \mu_k}, d(d\mu_k \cdot \mathbf{v}_k^2) \cdot \mathbf{v}_k^1 - d(d\mu_k \cdot \mathbf{v}_k^1) \cdot \mathbf{v}_k^2 \right\rangle \right],
\end{aligned}$$

in which, by definition, $d(d\mu_k \cdot \mathbf{v}_k^2) \cdot \mathbf{v}_k^1 = d(d\mu_k \cdot \mathbf{v}_k^1) \cdot \mathbf{v}_k^2 = 0$, and

$$\begin{aligned}
d(df_{k+1k} \cdot \mathbf{v}_k^2) \cdot \mathbf{v}_k^1 &= d(-g_{k+1}^{-1} \delta g_{k+1}^2 g_{k+1}^{-1} g_k + g_{k+1}^{-1} \delta g_k^2) \cdot \mathbf{v}_k^1 \\
&= -g_{k+1}^{-1} \delta g_{k+1}^2 g_{k+1}^{-1} \delta g_k^1 + g_{k+1}^{-1} \delta g_{k+1}^2 g_{k+1}^{-1} \delta g_{k+1}^1 g_{k+1}^{-1} g_k \\
&\quad + g_{k+1}^{-1} \delta g_{k+1}^1 g_{k+1}^{-1} \delta g_{k+1}^2 g_{k+1}^{-1} g_k - g_{k+1}^{-1} \delta g_{k+1}^1 g_{k+1}^{-1} \delta g_k^2, \\
d(df_{k+1k} \cdot \mathbf{v}_k^1) \cdot \mathbf{v}_k^2 &= -g_{k+1}^{-1} \delta g_{k+1}^1 g_{k+1}^{-1} \delta g_k^2 + g_{k+1}^{-1} \delta g_{k+1}^1 g_{k+1}^{-1} \delta g_{k+1}^2 g_{k+1}^{-1} g_k \\
&\quad + g_{k+1}^{-1} \delta g_{k+1}^2 g_{k+1}^{-1} \delta g_{k+1}^1 g_{k+1}^{-1} g_k - g_{k+1}^{-1} \delta g_{k+1}^2 g_{k+1}^{-1} \delta g_k^1,
\end{aligned}$$

which leads to

$$\mathbf{d}^2 S_d(\{g_k, \mu_k\}) \cdot (\{\delta g_k^1, \delta \mu_k^1\}, \{\delta g_k^2, \delta \mu_k^2\}) = 0. \quad (6.22)$$

On the other hand, along the solution sequence of the discrete Lie-Poisson principle (6.13), by discrete integration by parts, one can rewrite dS_d given in (6.20) as

$$\begin{aligned}
dS_d(\{g_k, \mu_k\}) \cdot (\{\delta g_k, \delta \mu_k\}) &= \theta^+(g_{K-1}, \mu_{K-1}, g_K, \mu_K) \cdot (\delta g_{K-1}, \delta \mu_{K-1}, \delta g_K, \delta \mu_K) \\
&\quad - \theta^-(g_0, \mu_0, g_1, \mu_1) \cdot (\delta g_0, \delta \mu_0, \delta g_1, \delta \mu_1),
\end{aligned}$$

where the one forms on $(G \times \mathfrak{g}^*) \times (G \times \mathfrak{g}^*)$, θ^+ and θ^- , are given by

$$\begin{aligned}\theta^+(g_k, \mu_k, , g_{k+1}, \mu_{k+1}) \cdot ((u_k, w_k), (u_{k+1}, w_{k+1})) &= \left\langle w_{k+1}, \frac{\partial \bar{\Theta}_{k+1}}{\partial \mu_{k+1}} \right\rangle + \left\langle \frac{\partial \bar{\Theta}_k}{\partial f_{k+1k}}, g_{k+1}^{-1} u_{k+1} g_{k+1}^{-1} g_k \right\rangle; \\ \theta^-(g_k, \mu_k, , g_{k+1}, \mu_{k+1}) \cdot ((u_k, w_k), (u_{k+1}, w_{k+1})) &= - \left\langle w_k, \frac{\partial \bar{\Theta}_k}{\partial \mu_k} \right\rangle - \left\langle \frac{\partial \bar{\Theta}_k}{\partial f_{k+1k}}, g_{k+1}^{-1} u_k \right\rangle\end{aligned}$$

where $(u_k, w_k) \in T_{(g_k, \mu_k)}(G \times \mathfrak{g}^*)$. When $K = 1$, we see that along the Lie-Poisson solution sequence

$$\theta^-(g_0, \mu_0, , g_1, \mu_1) \cdot (\delta g_0, \delta \mu_0, \delta g_1, \delta \mu_1) = \theta^+(g_0, \mu_0, , g_1, \mu_1) \cdot (\delta g_0, \delta \mu_0, \delta g_1, \delta \mu_1).$$

So $0 = \mathbf{d}^2 S_d = (\Phi^K)^* \mathbf{d}\theta^+ - \mathbf{d}\theta^+$, where $\Phi^K : (G \times \mathfrak{g}^*) \times (G \times \mathfrak{g}^*) \times \mathbb{Z} \rightarrow (G \times \mathfrak{g}^*) \times (G \times \mathfrak{g}^*)$ is the discrete Lie-Poisson flow map given by the discrete VLP on $G \times \mathfrak{g}^*$ (6.15) and (6.16). It follows that the discrete symplectic two-form $\omega = \mathbf{d}\theta^+$ is preserved along a solution sequence of VLP on $G \times \mathfrak{g}^*$ (6.15) and (6.16). \square

This symplecticity allows us to expect that, by backward error analysis, the solution of VLP on $G \times \mathfrak{g}^*$ is exponentially close to the exact solution of a modified Lie-Poisson system which is close to the original system, and thus the Hamiltonian function and Casimir functions are preserved in simulations in the sense that no unbounded drifts of the values of these functions are generated.

Further, recall the **Discrete Euler-Poincaré integrator (DEP)** on G developed for Euler-Poincaré systems with a reduced Lagrangian $l(\xi(t))$, $\xi \in \mathfrak{g}$ in Marsden *et al.* (1999a). The variational DEP on G is constructed by discretization of the Euler-Poincaré variational principle, the counterpart of the Lie-Poisson variational principle at the reduced Lagrangian side. Still consider the left invariant case, and use the same definition of ξ_k , η_k , f_{k+1k} as in VLP on $G \times \mathfrak{g}^*$. Discretizing the Euler-Poincaré variational principle gives $0 = \delta \sum_{k=0}^{K-1} l(\xi_k)$. With the notation $l_k = l(\xi_k) = \bar{l}(f_{k+1k}) = \bar{l}_k$, the DEP on G integrator derived from the discrete

variational principle for $f_{kk-1} \mapsto f_{k+1k}$ is:

$$\left\langle \frac{d\bar{l}_k}{df_{k+1k}}, f_{k+1k}\eta_k \right\rangle - \left\langle \frac{d\bar{l}_{k-1}}{df_{kk-1}}, \eta_k f_{kk-1} \right\rangle = 0, \quad k = 1, \dots, K-1, \quad (6.23)$$

i.e., by the chain rule,

$$\left\langle \frac{dl_k}{d\xi_k} \frac{d\xi_k}{df_{k+1k}}, f_{k+1k}\eta_k \right\rangle - \left\langle \frac{dl_{k-1}}{d\xi_{k-1}} \frac{d\xi_{k-1}}{df_{kk-1}}, \eta_k f_{kk-1} \right\rangle = 0, \quad k = 1, \dots, K-1. \quad (6.24)$$

In the continuous case, as mentioned in Section 6.2, Lie-Poisson systems and Euler-Poincaré systems are equivalent to each other if the map $\xi \mapsto \mu$ defined by reduced Legendre transform is a diffeomorphism. At the discrete level we have a similar result for hyperregular discrete Lagrangians and Hamiltonians, as follows.

Proposition 6.3.3. *The DEP on G (6.24) and VLP on $G \times \mathfrak{g}^*$ (6.17), (6.18) integrators are equivalent if the map $\xi_k \mapsto \mu_k$ for each k is a diffeomorphism defined by the discrete reduced Legendre transform*

$$\mu_k = \frac{dl_k}{d\xi_k}; \quad (6.25)$$

$$h_k = \langle \mu_k, \xi_k \rangle - l_k \quad (6.26)$$

and the inverse discrete reduced Legendre transform

$$\xi_k = \frac{dh_k}{d\mu_k}; \quad (6.27)$$

$$l_k = \langle \mu_k, \xi_k \rangle - h_k \quad (6.28)$$

where $h_k = h(\mu_k)$ and $l_k = l(\xi_k)$.

Proof. First, consider the transform from DEP on G to VLP on $G \times \mathfrak{g}^*$. At each step, by the Legendre transform (6.25) and (6.26),

$$\frac{dh_k}{d\mu_k} = - \left\langle \frac{dl_k}{d\xi_k}, \frac{d\xi_k}{d\mu_k} \right\rangle + \left\langle \mu_k, \frac{d\xi_k}{d\mu_k} \right\rangle + \xi_k = \xi_k, \quad (6.29)$$

which is (6.18). Also, plugging the discrete reduced Legendre transform (6.25) into

DEP on G (6.24), one obtains the equation (6.17).

The converse transform from VLP on $G \times \mathfrak{g}^*$ to DEP on G with the inverse Legendre transform (6.27) and (6.28) can be shown in a similar way. \square

Theorems 2.1, 2.2 and 2.3 in Marsden *et al.* (1999a) ensure that DEP on G is Lie-Poisson and by discrete reconstruction / reduction it is equivalent to the normal discrete Euler-Lagrange (DEL) equations obtained by discretization of Hamilton's principle. By discrete Legendre transform the DEL is equivalent to the discrete canonical Hamilton (DH) equations at the Hamiltonian side (Marsden & West, 2001). To summarize, we introduce the following almost commuting cube in Figure 6.2 for systems with hyperregular Lagrangians/Hamiltonians. The contribution of this work to this cube includes the construction of VLP on $G \times \mathfrak{g}^*$ through discretization of L-P equations on \mathfrak{g}^* , given by Proposition 6.3.1 and referred to by the relation (X) in the figure, and the relation (VI), given by Proposition 6.3.3, that shows the equivalence between VLP on $G \times \mathfrak{g}^*$ and DEP on G . The symplecticity of VLP on $G \times \mathfrak{g}^*$ is shown directly at the Hamiltonian side by Proposition 6.3.2, and not depending on the equivalence between DEP on G and VLP on $G \times \mathfrak{g}^*$, which will not be valid if either side is a degenerate system.

Remark 6.3.1. Marsden *et al.* (1999a) introduced an algorithm named 'DEP/DLP' for calculating μ_k . In this algorithm, one updates μ_k by a coadjoint action of f_{k+1k} , where f_{k+1k} is obtained by the DEP on G . For the left-invariant case, the discrete coadjoint action is

$$\mu_{k+1} = \text{Ad}_{f_{k+1k}^{-1}}^* \mu_k. \quad (6.30)$$

This DEP/DLP algorithm preserves not only a discrete Lie-Poisson structure but also the coadjoint orbits by construction, which is different from the VLP on $G \times \mathfrak{g}^*$ introduced here. Thus, though DEP on G (e.g. (6.23)) and VLP on $G \times \mathfrak{g}^*$ (e.g.

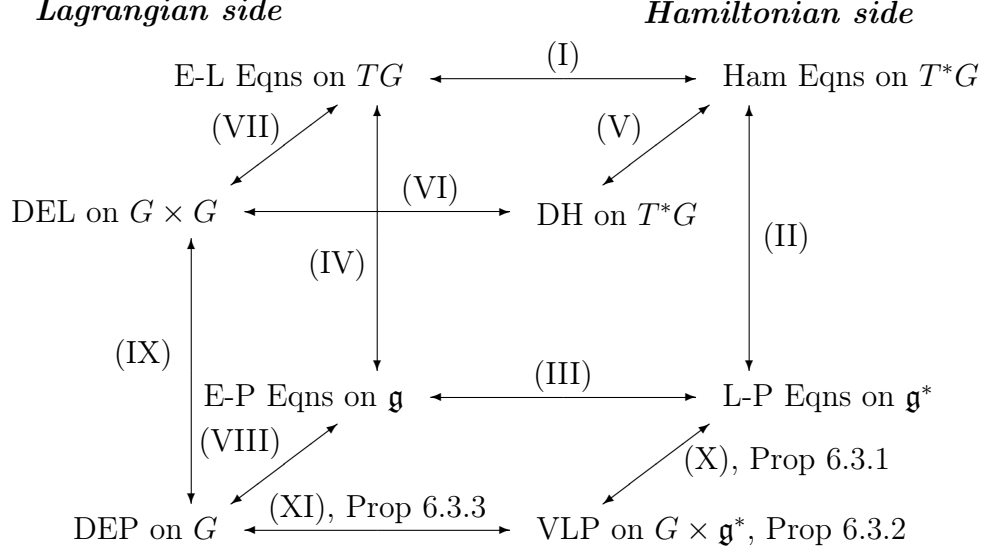


Figure 6.2: The almost commuting cube that links the full/reduced Lagrangian/Hamiltonian sides in both continuous and discrete domains. (I): Legendre transform; (II): Lie-Poisson reduction/reconstruction; (III): reduced Legendre transform; (IV): Euler-Poincaré reduction/reconstruction; (VI): discrete Legendre transform; (IX): discrete reduction/reconstruction at the Lagrangian side; (XI): discrete reduced Legendre transform defined by (6.25)-(6.28); (V), (VII), (VIII) and (X) are transforms between the corresponding continuous and discrete systems.

(6.15) with (6.16)) are equivalent, generally DEP/DLP (e.g. (6.23) with (6.30)) and VLP on $G \times \mathfrak{g}^*$ generate different results of μ_k . Also, compared to VLP on $G \times \mathfrak{g}^*$, which needs to solve for both μ_k and f_{k+1k} implicitly at each time step, DEP/DLP only needs to solve implicitly for f_{k+1k} from its DEP on G integrator. However, the advantage of the VLP on $G \times \mathfrak{g}^*$ introduced here is that it is constructed *directly* from the Lie-Poisson side, so one needs not to convert the Lie-Poisson system into Euler-Poincaré system by Legendre transform, which is necessary for the application of DEP/DLP. When the conversion by Legendre transform is computationally difficult, or even degenerate, this advantage becomes crucial. See the problem of N point vortices interacting on a sphere in Section 6.6.2 as an example.

Remark 6.3.2. For the right-invariant case,

$$\dot{\mu} = -\text{ad}_{\xi}^* \mu, \quad (6.31)$$

where $\xi = dh/d\mu = \dot{g}g^{-1}$. Using the same method as that for the left-invariant

case, with $\xi_k = \xi_k(f_{kk+1})$ where $f_{kk+1} = g_k g_{k+1}^{-1}$, one obtains the VLP on $G \times \mathfrak{g}^*$ for the right-invariant case

$$\left\langle \frac{\partial \bar{\Theta}_k}{\partial f_{kk+1}}, \eta_k f_{kk+1} \right\rangle - \left\langle \frac{\partial \bar{\Theta}_{k-1}}{\partial f_{k-1k}}, f_{k-1k} \eta_k \right\rangle = 0, \quad k = 1, \dots, K-1; \quad (6.32)$$

$$\xi_k - \frac{dh_k}{d\mu_k} = 0, \quad k = 0, \dots, K-1. \quad (6.33)$$

where $\eta_k = \delta g_k g_k^{-1}$. All above results on symplecticity and equivalence to the reduced Lagrangian side hold for the right-invariant case.

Remark 6.3.3. Note that we can obtain higher order VLP integrators on $G \times \mathfrak{g}^*$ by using higher-order approximations of the action integral in the Lie-Poisson variational principle, instead of the Riemann sum approximation in (6.13).

Remark 6.3.4. Bou-Rabee & Marsden (2009) introduced a discrete version of the reduced Hamilton-Pontryagin Principle for the left-invariant case

$$\delta \int_0^T (l(\xi) + \langle \mu, g^{-1} \dot{g} - \xi \rangle) dt = 0, \quad (6.34)$$

where δg , $\delta \mu$, $\delta \xi$ are arbitrary, except that $\delta g = 0$ at endpoints. The VLP on $G \times \mathfrak{g}^*$ given above can also be regarded as a counterpart at the Hamiltonian side to the variational Hamiltonian-Pontryagin integrators in Bou-Rabee & Marsden (2009).

As a summary, we note that VLP on $G \times \mathfrak{g}^*$ is symplectic, and by construction it should be valid for general finite dimensional Lie-Poisson systems. Its drawbacks, however, are (i) the construction of the scheme is quite involved and the scheme is in general implicit. Note that the integrator (6.17) & (6.18) is not directly applicable for simulation due to the η_k terms, the elimination of which depending on individual Lie-Poisson systems. (ii) At each time step a Lie group element, f_{k+1k} or f_{kk+1} , is calculated. Thus a numerical reconstruction is done by the VLP on $G \times \mathfrak{g}^*$ algorithm in simulations, which is unnecessary in applications where only the time evolution of $\mu(t) \in \mathfrak{g}^*$ is concerned. Since the Lie group involved is in general a

manifold but not a vector space, calculation of Lie group elements will also cost much computation effort. See Section 6.6 for numerical examples. This is the motivation of the development of VLP on $\mathfrak{g} \times \mathfrak{g}^*$ and VLP purely on \mathfrak{g}^* , which will be introduced in the next two sections.

6.4 Variational Lie-Poisson integrators on $\mathfrak{g} \times \mathfrak{g}^*$

Consider the left-invariant case. In Section 6.3, we approximate $\xi(t_k)$ in the discrete version of Lie-Poisson variational principle (6.10) by discretizing the relation $\xi = g^{-1}\dot{g}$, which inevitably involves the appearance of Lie group elements in numerical schemes. To avoid that, we start directly from the approximation of $\delta\xi = \dot{\eta} + [\xi, \eta]$, in which $\eta, \xi \in \mathfrak{g}$ and η arbitrary except at the endpoints, such that only Lie algebra elements appear for $\delta\xi$ approximation. The above idea was first introduced by Bourabee (2007) for construction of variational Euler-Poincaré integrators purely on \mathfrak{g} . The work here is a generalization to the reduced Hamiltonian side.

Approximating the Lie-Poisson variational principle (6.6) by

$$\begin{aligned} 0 &= \delta \int_0^T (\langle \mu(t), \xi(t) \rangle - h(\mu(t))) dt = \delta \sum_{k=0}^{K-1} \int_{t_k}^{t_{k+1}} (\langle \mu(t), \xi(t) \rangle - h(\mu(t))) dt \\ &\approx \delta \sum_{k=0}^{K-1} (\langle \mu_{k+\beta}, \xi_{k+\gamma} \rangle - h(\mu_{k+\beta})) \Delta t, \end{aligned} \quad (6.35)$$

where $\mu_{k+\beta} = (1 - \beta)\mu_k + \beta\mu_{k+1}$ and $\xi_{k+\gamma} = (1 - \gamma)\xi_k + \gamma\xi_{k+1}$, $\{\mu_k\}_{k=0}^{K-1} \subset \mathfrak{g}^*$, $\{\xi_k\}_{k=0}^{K-1} \subset \mathfrak{g}$, and $\gamma, \beta \in [0, 1]$ are two parameters, we introduce the following statement:

Proposition 6.4.1. *For the left-invariant case, let the discrete variational principle*

$$\delta \sum_{k=0}^{K-1} (\langle \mu_{k+\beta}, \xi_{k+\gamma} \rangle - h(\mu_{k+\beta})) \Delta t = 0 \quad (6.36)$$

hold with $\delta\mu_{k+\beta} = (1-\beta)\delta\mu_k + \beta\delta\mu_{k+1}$ in which $\delta\mu_k$ arbitrary for $k = 0, \dots, K-1$, and $\delta\xi_{k+\gamma} := (1-\gamma)\delta^+\xi_k + \gamma\delta^-\xi_{k+1}$ in which

$$\begin{cases} \delta^+\xi_k = \frac{\eta_{k+1}-\eta_k}{\Delta t} + \text{ad}_{\xi_{k+\alpha}} \eta_k; \\ \delta^-\xi_k = \frac{\eta_k-\eta_{k-1}}{\Delta t} + \text{ad}_{\xi_{k+\alpha}} \eta_k, \end{cases} \quad (6.37)$$

$\alpha \in [0, 1]$, i.e.,

$$\delta\xi_{k+\gamma} = \frac{\eta_{k+1}-\eta_k}{\Delta t} + (1-\gamma)\text{ad}_{\xi_{k+\alpha}} \eta_k + \gamma\text{ad}_{\xi_{k+1+\alpha}} \eta_{k+1}, \quad (6.38)$$

where $\eta_k = g_k^{-1}\delta g_k \in \mathfrak{g}$, $g_k \in G$, δg_k arbitrary for $k = 1, \dots, K-1$ and $\delta g_0 = \delta g_K = 0$. Then, the discrete variational principle is equivalent to the sets of equations on $\mathfrak{g} \times \mathfrak{g}^*$

$$\frac{1}{\Delta t}(\mu_{k+\beta} - \mu_{k-1+\beta}) = \text{ad}_{\xi_{k+\alpha}}^* ((1-\gamma)\mu_{k+\beta} + \gamma\mu_{k-1+\beta}), \quad k = 1, \dots, K-1 \quad (6.39)$$

$$\xi_{k+\gamma} = \left. \frac{dh}{d\mu} \right|_{\mu_{k+\beta}}, \quad k = 0, \dots, K-1. \quad (6.40)$$

Proof. The conditions on $\{\delta g_k\}$ imply that η_k is arbitrary for $k = 1, \dots, K-1$ and $\eta_0 = \eta_K = 0$. Then, the result follows by direct calculation similar to that in the proof of Proposition 6.3.1 and using the conditions on $\delta\mu_k$, and η_k . \square

Note that the $\delta\xi_k$ given in (6.38) was first proposed by Bou-Rabee (2007). Though in this setting we have a whole family of integrators on $\mathfrak{g} \times \mathfrak{g}^*$, (6.39) & (6.40), with three parameters $\alpha, \beta, \gamma \in [0, 1]$, only certain subsets of it will preserve a discrete Hamiltonian structure.

Proposition 6.4.2. *With $\alpha = 0$, $\gamma = \frac{1}{2}$, the integrators on $\mathfrak{g} \times \mathfrak{g}^*$, (6.39) & (6.40), preserve a symplectic two-form along its solution sequence.*

Proof. Define

$$S_d(\{g_k, \xi_k, \mu_k\}) = \sum_{k=0}^{K-1} \Theta(Y((\mu_k, \mu_{k+1}), X(\xi_k, \xi_{k+1}))) \quad (6.41)$$

where $Y((\mu_k, \mu_{k+1}) = \mu_{k+\beta}$, $X(\xi_k, \xi_{k+1}) = \xi_{k+\gamma}$. Define

$$\mathbf{v}_k = ((\delta g_k, \delta^+ \xi_k, \delta \mu_k), (\delta g_{k+1}, \delta^- \xi_{k+1}, \delta \mu_{k+1})),$$

such that

$$dX \cdot \mathbf{v}_k = (1 - \gamma)\delta^+ \xi_k + \gamma\delta^- \xi_{k+1} = \delta \xi_{k+\gamma}; \quad dY \cdot \mathbf{v}_k = \delta \mu_{k+\beta}. \quad (6.42)$$

where $\delta^+ \xi_k$, $\delta^- \xi_k$ and $\delta \xi_{k+\gamma}$ are given by (6.37) and (6.38). Similar to that in Proposition 6.3.2, we have

$$\begin{aligned} & \mathbf{d}^2 S_d(\{g_k, \xi_k, \mu_k\}) \cdot (\{\delta g_k^1, (\delta^+ \xi_k)^1, (\delta^- \xi_k)^1, \delta \mu_k^1\}, \{\delta g_k^2, (\delta^+ \xi_k)^2, (\delta^- \xi_k)^2, \delta \mu_k^2\}) \\ &= \sum_{k=0}^{K-1} [d(d\Theta(Y, X) \cdot \mathbf{v}_k^2) \cdot \mathbf{v}_k^1 - d(d\Theta(Y, X) \cdot \mathbf{v}_k^1) \cdot \mathbf{v}_k^2] \\ &= \sum_{k=0}^{K-1} \left[\left\langle \frac{\partial \Theta}{\partial X}, d(dX \cdot \mathbf{v}_k^2) \cdot \mathbf{v}_k^1 - d(dX \cdot \mathbf{v}_k^1) \cdot \mathbf{v}_k^2 \right\rangle + \left\langle \frac{\partial \Theta}{\partial Y}, d(dY \cdot \mathbf{v}_k^2) \cdot \mathbf{v}_k^1 - d(dY \cdot \mathbf{v}_k^1) \cdot \mathbf{v}_k^2 \right\rangle \right]. \end{aligned}$$

Consider the case when $\alpha = 0$. By direct calculation, $d(dX \cdot \mathbf{v}_k^2) \cdot \mathbf{v}_k^1 - d(dX \cdot \mathbf{v}_k^1) \cdot \mathbf{v}_k^2 = \frac{1}{\Delta t} Q + P$ with

$$\begin{aligned} Q &= (1 - 2\gamma)(\text{ad}_{\eta_{k+1}^2} \eta_{k+1}^1 + \text{ad}_{\eta_k^2} \eta_k^1 + \text{ad}_{\eta_k^1} \eta_{k+1}^2 + \text{ad}_{\eta_{k+1}^1} \eta_k^2); \\ P &= (1 - \gamma)(\text{ad}_{\xi_k} \text{ad}_{\eta_k^2} \eta_k^1 + \text{ad}_{\eta_k^1} \text{ad}_{\xi_k} \eta_k^2 + \text{ad}_{\eta_k^2} \text{ad}_{\eta_k^1} \xi_k) \\ &\quad + \gamma(\text{ad}_{\xi_{k+1}} \text{ad}_{\eta_{k+1}^2} \eta_{k+1}^1 + \text{ad}_{\eta_{k+1}^1} \text{ad}_{\xi_{k+1}} \eta_{k+1}^2 + \text{ad}_{\eta_{k+1}^2} \text{ad}_{\eta_{k+1}^1} \xi_{k+1}) = 0 \end{aligned}$$

where $\eta_k^i = g_k^{-1} \delta g_k^i$, and the Jacobi identity is used in the last equality. Also, it is clear that $d(dY \cdot \mathbf{v}_k^2) \cdot \mathbf{v}_k^1 = d(dY \cdot \mathbf{v}_k^1) \cdot \mathbf{v}_k^2 = 0$. Thus, when $\gamma = \frac{1}{2}$, $Q = 0$ and $\mathbf{d}^2 S_d = 0$. It implies, by the same argument used in the proof of Proposition 6.3.2, that along a solution sequence of VLP on $\mathfrak{g} \times \mathfrak{g}^*$ with $\alpha = 0$, $\gamma = \frac{1}{2}$, a symplectic two-form $\omega = \mathbf{d}\theta^+ = -\mathbf{d}\theta^-$ is preserved, where the one forms θ^+ and θ^- on $(G \times \mathfrak{g} \times \mathfrak{g}^*) \times (G \times \mathfrak{g} \times \mathfrak{g}^*)$

are

$$\begin{aligned}
& \theta^+(g_k, \xi_k, \mu_k, g_{k+1}, \xi_{k+1}, \mu_{k+1}) \cdot ((u_k, v_k, w_k), (u_{k+1}, v_{k+1}, w_{k+1})) \\
&= \beta \left\langle w_{k+1}, \xi_{k+\frac{1}{2}} - \frac{dh}{d\mu} \Big|_{k+\beta} \right\rangle + \left\langle \frac{1}{2} \text{ad}_{\xi_{k+1}}^* \mu_{k+\beta} + \frac{1}{\Delta t} \mu_{k+\beta}, g_{k+1}^{-1} u_{k+1} \right\rangle; \\
& \theta^-(g_k, \xi_k, \mu_k, g_{k+1}, \xi_{k+1}, \mu_{k+1}) \cdot ((u_k, v_k, w_k), (u_{k+1}, v_{k+1}, w_{k+1})) \\
&= (1 - \beta) \left\langle w_k, \frac{dh}{d\mu} \Big|_{k+\beta} - \xi_{k+\frac{1}{2}} \right\rangle + \left\langle \frac{1}{\Delta t} \mu_{k+\beta} - \frac{1}{2} \text{ad}_{\xi_k}^* \mu_{k+\beta}, g_k^{-1} u_k \right\rangle,
\end{aligned}$$

where $(u_k, v_k, w_k) \in T_{(g_k, \xi_k, \mu_k)}(G \times \mathfrak{g} \times \mathfrak{g}^*)$. \square

We thus have a whole family of symplectic, **variational Lie-Poisson integrators** on $\mathfrak{g} \times \mathfrak{g}^*$ for the left-invariant case

$$\frac{1}{\Delta t}(\mu_{k+\beta} - \mu_{k-1+\beta}) = \frac{1}{2} \text{ad}_{\xi_k}^* (\mu_{k+\beta} + \mu_{k-1+\beta}), \quad k = 1, \dots, K-1 \quad (6.43)$$

$$\xi_{k+\frac{1}{2}} = \frac{dh}{d\mu} \Big|_{\mu_{k+\beta}}, \quad k = 0, \dots, K-1. \quad (6.44)$$

where $\beta \in [0, 1]$.

Following the approach of Bou-Rabee (2007) on the Euler-Poincaré side, a symplectic, variational Euler-Poincaré (VEP) integrator on \mathfrak{g} for the left-invariant case can be presented in the form

$$\frac{1}{\Delta t} \left(\frac{dl}{d\xi} \Big|_{\xi_{k+\frac{1}{2}}} - \frac{dl}{d\xi} \Big|_{\xi_{k-\frac{1}{2}}} \right) = \frac{1}{2} \text{ad}_{\xi_k}^* \left[\frac{dl}{d\xi} \Big|_{\xi_{k+\frac{1}{2}}} + \frac{dl}{d\xi} \Big|_{\xi_{k-\frac{1}{2}}} \right], \quad k = 1, \dots, K-1. \quad (6.45)$$

The following statement, again based on a pair of discrete reduced Legendre transforms, shows the equivalence of the VEP on \mathfrak{g} and the VLP on $\mathfrak{g} \times \mathfrak{g}^*$.

Proposition 6.4.3. *The VEP on \mathfrak{g} (6.45) and VLP on $\mathfrak{g} \times \mathfrak{g}^*$ (6.43), (6.44) integrators are equivalent if the map $\xi_k \mapsto \mu_k$ for each k is a diffeomorphism defined by*

the discrete reduced Legendre transform

$$\mu_{k+\beta} = \left. \frac{dl}{d\xi} \right|_{\xi_{k+\frac{1}{2}}} ; \quad (6.46)$$

$$h(\mu_{k+\beta}) = \langle \mu_{k+\beta}, \xi_{k+\frac{1}{2}} \rangle - l(\xi_{k+\frac{1}{2}}), \quad (6.47)$$

and the inverse discrete reduced Legendre transform

$$\xi_{k+\frac{1}{2}} = \left. \frac{dh}{d\mu} \right|_{\mu_{k+\beta}} ; \quad (6.48)$$

$$l(\xi_{k+\frac{1}{2}}) = \langle \mu_{k+\beta}, \xi_{k+\frac{1}{2}} \rangle - h(\mu_{k+\beta}). \quad (6.49)$$

Proof. By direct calculation as that in the proof of Proposition 6.3.3. \square

Figure 6.3 illustrates the relation between VEP on \mathfrak{g} and VLP on $\mathfrak{g} \times \mathfrak{g}^*$ for systems with hyperregular Lagrangians/Hamiltonians, by a commuting square. Our contribution here includes the relation (IV) and the construction of VLP on $\mathfrak{g} \times \mathfrak{g}^*$ through Proposition 6.4.1, and the relation (III) that shows the equivalence between VEP on \mathfrak{g} and VLP on $\mathfrak{g} \times \mathfrak{g}^*$ given by Proposition 6.4.3. Also, Proposition 6.4.2 shows the symplecticity of VLP on $\mathfrak{g} \times \mathfrak{g}^*$ directly from the Hamiltonian side. Notice that unlike VLP on $G \times \mathfrak{g}^*$ or DEP on G that numerically gives reconstruction information, here everything stays in the reduced space.

Remark 6.4.1. For the right-invariant case where $\delta\xi = \dot{\eta} - [\xi, \eta]$, assume

$$\delta\xi_{k+\gamma} = \frac{\eta_{k+1} - \eta_k}{\Delta t} - (1 - \gamma) \text{ad}_{\xi_{k+\alpha}} \eta_k - \gamma \text{ad}_{\xi_{k+1+\alpha}} \eta_{k+1} \quad (6.50)$$

where $\eta_k = \delta g_k g_k^{-1}$. Following the same process for the left-invariant case, with

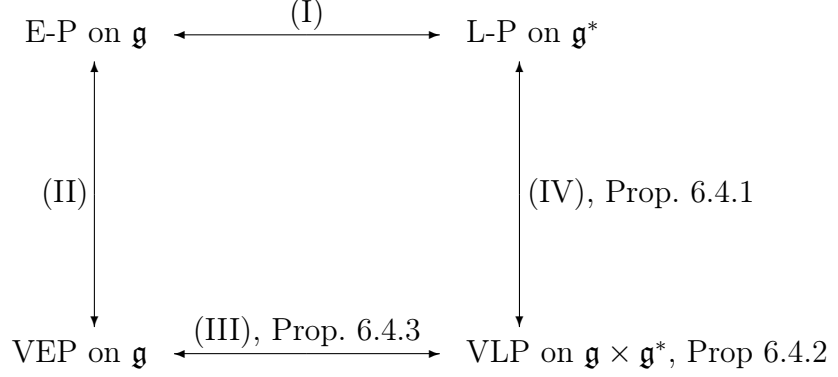


Figure 6.3: Relations between Euler-Poincaré (E-P) systems, Lie-Poisson (L-P) systems, VEP on \mathfrak{g} and VLP on $\mathfrak{g} \times \mathfrak{g}^*$. (I): reduced Legendre transform; (III): discrete reduced Legendre transform defined by (6.46)-(6.49); (II) and (IV): transforms between corresponding continuous and discrete systems.

$\alpha = 0$, $\gamma = \frac{1}{2}$, one obtains the symplectic VLP on $\mathfrak{g} \times \mathfrak{g}^*$ for the right-invariant case

$$\frac{1}{\Delta t}(\mu_{k+\beta} - \mu_{k-1+\beta}) = -\frac{1}{2} \text{ad}_{\xi_k}^* (\mu_{k+\beta} + \mu_{k-1+\beta}), \quad k = 1, \dots, K-1 \quad (6.51)$$

$$\xi_{k+\frac{1}{2}} = \left. \frac{dh}{d\mu} \right|_{\mu_{k+\beta}}, \quad k = 0, \dots, K-1. \quad (6.52)$$

Remark 6.4.2. Though in general the VLP on $\mathfrak{g} \times \mathfrak{g}^*$ (6.43)&(6.44) is implicit, for the case $\beta = 0$, the integrator will be semi-explicit: the equation (6.44) updating ξ_k is explicit while the equation (6.43) updating μ_k is implicit. In special cases the scheme can be *explicit* due to certain special structure of Lie algebra. See examples in Section 6.6 for details.

Compared with VLP on $G \times \mathfrak{g}^*$, the main advantages of the VLP on $\mathfrak{g} \times \mathfrak{g}^*$ are that it is easier to construct, sometimes explicit, and not involved with Lie group elements. The drawback is that it still needs to ‘unnecessarily’ compute those Lie algebra elements $\{\xi_k\}$. Though the computation is not so costly as that for Lie group elements since the Lie algebra is a vector space, the dimension of the numerical scheme on $\mathfrak{g} \times \mathfrak{g}^*$ will be double of that of the original Lie-Poisson system on \mathfrak{g}^* . Naturally, one would like to develop variational Lie-Poisson integrators purely on

\mathfrak{g}^* , which is the topic we will turn to in the next section.

6.5 Lie-Poisson integrators on \mathfrak{g}^* based on discretized variational principles

6.5.1 Integrators on \mathfrak{g}^* based on the Lie-Poisson variational principle

Consider the left-invariant case. Instead of (6.38), approximate $\delta\xi_{k+\gamma} := (1 - \gamma)\delta^+\xi_k + \gamma\delta^-\xi_{k+1}$ in which

$$\begin{cases} \delta^+\xi_k = \frac{\eta_{k+1} - \eta_k}{\Delta t} + \text{ad}_{\xi_{k+\alpha}} \eta_k; \\ \delta^-\xi_k = \frac{\eta_k - \eta_{k-1}}{\Delta t} + \text{ad}_{\xi_{k-1+\alpha}} \eta_k, \end{cases} \quad (6.53)$$

i.e.,

$$\delta\xi_{k+\gamma} = \frac{\eta_{k+1} - \eta_k}{\Delta t} + (1 - \gamma)\text{ad}_{\xi_{k+\alpha}} \eta_k + \gamma\text{ad}_{\xi_{k+\alpha}} \eta_{k+1}, \quad (6.54)$$

Proposition 6.5.1. *For the left-invariant case, let the discrete variational principle (6.36) hold with $\delta\mu_{k+\beta} = (1 - \beta)\delta\mu_k + \beta\delta\mu_{k+1}$ in which $\delta\mu_k$ are arbitrary for $k = 0, \dots, K - 1$, and $\delta\xi_{k+\gamma}$ are given by (6.54) in which $\eta_k = g_k^{-1}\delta g_k$, $g_k \in G$, δg_k are arbitrary for $k = 1, \dots, K - 1$ and $\delta g_0 = \delta g_K = 0$. Then, the discrete variational principle is equivalent to the following sets of equations on $\mathfrak{g} \times \mathfrak{g}^*$*

$$\frac{1}{\Delta t}(\mu_{k+\beta} - \mu_{k-1+\beta}) = (1 - \gamma)\text{ad}_{\xi_{k+\alpha}}^* \mu_{k+\beta} + \gamma\text{ad}_{\xi_{k-1+\alpha}}^* \mu_{k-1+\beta}, \quad k = 1, \dots, K - 1 \quad (6.55)$$

$$\xi_{k+\gamma} = \left. \frac{dh}{d\mu} \right|_{\mu_{k+\beta}}, \quad k = 0, \dots, K - 1. \quad (6.56)$$

Proof. By direct calculation similar to that in the proof of Propositions 6.3.1 and 6.4.1. \square

When $\alpha = \gamma$, the above integrators on $\mathfrak{g} \times \mathfrak{g}^*$ (6.55)&(6.56) becomes purely defined on \mathfrak{g}^* for the left-invariant case:

$$\frac{1}{\Delta t}(\mu_{k+\beta} - \mu_{k-1+\beta}) = (1-\gamma) \text{ad}_{\frac{dh}{d\mu}|_{\mu_{k+\beta}}}^* \mu_{k+\beta} + \gamma \text{ad}_{\frac{dh}{d\mu}|_{\mu_{k-1+\beta}}}^* \mu_{k-1+\beta}, \quad k = 1, \dots, K-1. \quad (6.57)$$

Unfortunately, this integrator on \mathfrak{g}^* is not symplectic:

Proposition 6.5.2. *The integrator on \mathfrak{g}^* (6.57) is not symplectic for any $\gamma \in [0, 1]$.*

Proof. We follow the same arguments as in the proof of Proposition 6.4.2, and only need to show that $\mathbf{d}^2 S_d \neq 0$ for any $\gamma \in [0, 1]$. The only difference here is that $\delta^+ \xi_k$, $\delta^- \xi_k$ and $\delta \xi_{k+\gamma}$ are now given by (6.53) and (6.54). This change does not affect the fact $d(dY \cdot \mathbf{v}_k^2) \cdot \mathbf{v}_k^1 = d(dY \cdot \mathbf{v}_k^1) \cdot \mathbf{v}_k^2 = 0$. However, the Q and P terms in the expression $d(dX \cdot \mathbf{v}_k^2) \cdot \mathbf{v}_k^1 - d(dX \cdot \mathbf{v}_k^1) \cdot \mathbf{v}_k^2 = \frac{1}{\Delta t} Q + P$ now become

$$Q = (1 - 2\gamma)(\text{ad}_{\eta_{k+1}^2} \eta_{k+1}^1 - \text{ad}_{\eta_k^2} \eta_k^1 + \text{ad}_{\eta_k^1} \eta_{k+1}^2 - \text{ad}_{\eta_k^1} \eta_{k+1}^1)$$

and

$$P = \text{ad}_{\xi_{k+\gamma}} \left[(1 - \gamma) \text{ad}_{\eta_k^2} \eta_k^1 + \gamma \text{ad}_{\eta_{k+1}^2} \eta_{k+1}^1 \right] + \text{ad}_{\eta_{k+\gamma}^1} \left[(1 - \gamma) \text{ad}_{\xi_k} \eta_k^2 + \gamma \text{ad}_{\xi_{k+1}} \eta_{k+1}^2 \right] \\ - \text{ad}_{\eta_{k+\gamma}^2} \left[(1 - \gamma) \text{ad}_{\xi_k} \eta_k^1 + \gamma \text{ad}_{\xi_{k+1}} \eta_{k+1}^1 \right].$$

The term Q vanishes only if $\gamma = 1/2$. However, when $\gamma = 1/2$, by the Jacobi identity,

$$P = \frac{1}{4}(\text{ad}_{\xi_k} \text{ad}_{\eta_{k+1}^2} \eta_{k+1}^1 + \text{ad}_{\eta_{k+1}^2} \text{ad}_{\eta_k^1} \xi_k + \text{ad}_{\eta_{k+1}^1} \text{ad}_{\xi_k} \eta_k^2 \\ + \text{ad}_{\xi_{k+1}} \text{ad}_{\eta_k^2} \eta_k^1 + \text{ad}_{\eta_k^2} \text{ad}_{\eta_{k+1}^1} \xi_{k+1} + \text{ad}_{\eta_k^1} \text{ad}_{\xi_{k+1}} \eta_{k+1}^2),$$

and it does not vanish for arbitrary $\eta_k^i, \eta_{k+1}^i, i = 1, 2$. Thus, for any $\gamma \in [0, 1]$, $\frac{1}{\Delta t}Q + P \neq 0$, and it follows immediately that $\mathbf{d}^2 S_d \neq 0$. \square

When $\gamma = 1/2$, the term $\frac{1}{\Delta t}Q$, which dominates when Δt is small, vanishes. In particular, when $\gamma = 1/2, \beta = 0$, the integrator on \mathfrak{g}^* is just the trapezoidal rule:

$$\frac{1}{\Delta t}(\mu_k - \mu_{k-1}) = \frac{1}{2} \left(\text{ad}_{\frac{dh}{d\mu}|_{\mu_k}}^* \mu_k + \text{ad}_{\frac{dh}{d\mu}|_{\mu_{k-1}}}^* \mu_{k-1} \right), \quad k = 1, \dots, K-1, \quad (6.58)$$

In examples given in Section 6.6 we will see that the trapezoidal rule, though not exactly symplectic, preserves conserved quantities well in simulations of Lie-Poisson systems.

Remark 6.5.1. Similarly, for the right-invariant case, by approximating

$$\delta \xi_{k+\gamma} = \frac{\eta_{k+1} - \eta_k}{\Delta t} - (1 - \gamma) \text{ad}_{\xi_{k+\alpha}} \eta_k - \gamma \text{ad}_{\xi_{k+\alpha}} \eta_{k+1}, \quad (6.59)$$

where $\eta_k = \delta g_k g_k^{-1}$, and letting $\alpha = \gamma$ we obtain integrators on \mathfrak{g}^* for the right-invariant case

$$\frac{1}{\Delta t}(\mu_{k+\beta} - \mu_{k-1+\beta}) = -(1 - \gamma) \text{ad}_{\frac{dh}{d\mu}|_{\mu_{k+\beta}}}^* \mu_{k+\beta} - \gamma \text{ad}_{\frac{dh}{d\mu}|_{\mu_{k-1+\beta}}}^* \mu_{k-1+\beta}, \quad k = 1, \dots, K-1. \quad (6.60)$$

Analysis on symplecticity gives the same results as presented in Proposition 6.5.2.

Remark 6.5.2. To construct integrators purely on \mathfrak{g}^* by discretizing the Lie-Poisson variational principle, one can also directly use the scheme developed in Section 6.4 with $\alpha = \gamma$. However, numerical results for free rigid body rotation example by this scheme with typical values of $\alpha = \gamma$ and β , for example $\alpha = \gamma = \beta = 1/2$, etc, give discouraging results, such as dissipating Hamiltonian and Casimir functions. Besides, for the general $\alpha = \gamma \neq 0$ case, theoretical analysis for checking symplecticity of the scheme, such as that in the Proof of Proposition 6.5.2, will be much more involved since, by definition of $\delta \xi_{k+\gamma}$ given in (6.38), terms including ξ_{k+2} will appear in equations like (6.42) that define dX .

6.5.2 Integrators on \mathfrak{g}^* based on a modified Lie-Poisson variational principle

The Lie-Poisson variational principle (6.6) involves both $\mu \in \mathfrak{g}^*$ and $\xi \in \mathfrak{g}$ and is equivalent to the pair of equations (6.7) and (6.8), which is always trivially equivalent to the Lie-Poisson equations (6.3) in the continuous case. However, as we see in Section 6.3 and 6.4, due to the appearance of ξ , discretization of this variational principle in general leads to a pair of difference equations involving not only the elements in \mathfrak{g}^* but also Lie group elements or Lie algebra elements, which prevents us from obtaining integrators purely on \mathfrak{g}^* . To overcome this difficulty, we introduce a modified version of the Lie-Poisson variational principle that includes only the $\mu \in \mathfrak{g}^*$ elements, such that the discretization of this principle naturally leads to integrators purely on \mathfrak{g}^* .

Proposition 6.5.3. *The Lie-Poisson equation (6.3) for the left-invariant case is equivalent to the **modified Lie-Poisson variational principle***

$$\delta \int_0^T \left(\left\langle \mu(t), \frac{dh}{d\mu}(t) \right\rangle - h(\mu(t)) \right) dt = 0 \quad (6.61)$$

where $\mu \in \mathfrak{g}^*$ and $\frac{dh}{d\mu} = g^{-1}\dot{g} \in \mathfrak{g}$, $g \in G$, with restricted variations $\delta\mu$ defined by $(d^2h/d\mu^2)\delta\mu = \delta \left(\frac{dh}{d\mu} \right) = \dot{\eta} + [\frac{dh}{d\mu}, \eta]$ where $\eta = g^{-1}\delta g$, $\delta g(t)$ arbitrary everywhere except that $\delta g(0) = \delta g(T) = 0$. The Lie-Poisson equation (6.3) for the right-invariant case is equivalent to (6.61) with the above setting replaced by $\frac{dh}{d\mu} = \dot{g}g^{-1} \in \mathfrak{g}$, $\frac{d^2h}{d\mu^2}\delta\mu = \delta \left(\frac{dh}{d\mu} \right) = \dot{\eta} - [\frac{dh}{d\mu}, \eta]$ where $\eta = \delta g g^{-1}$.

Proof. Consider the left-invariant case. Start from the principle,

$$\begin{aligned}
0 &= \delta \int_0^T \left(\left\langle \mu, \frac{dh}{d\mu} \right\rangle - h(\mu) \right) dt \\
&= \int_0^T \left(\left\langle \delta\mu, \frac{dh}{d\mu} \right\rangle + \left\langle \mu, \delta \left(\frac{dh}{d\mu} \right) \right\rangle - \left\langle \delta\mu, \frac{dh}{d\mu} \right\rangle \right) dt \\
&= \int_0^T \left\langle \mu, \dot{\eta} + \left[\frac{dh}{d\mu}, \eta \right] \right\rangle dt \\
&= \int_0^T \left\langle -\dot{\mu} + \text{ad}_{\frac{dh}{d\mu}}^* \mu, \eta \right\rangle dt + \langle \mu, \eta \rangle \Big|_0^T.
\end{aligned}$$

This leads to the Lie-Poisson equation $\dot{\mu} = \text{ad}_{\frac{dh}{d\mu}}^* \mu$ on $[0, T]$ since η is arbitrary on the time interval except $\eta(0) = \eta(T) = 0$. The converse direction can also be proved using the relation obtained above. Proof for the right-invariant case follows the same process. \square

Proposition 6.5.4. *The modified Lie-Poisson variational principle (6.61) given in Proposition 6.5.3 implies that along a Lie-Poisson flow a symplectic two-form is preserved.*

Proof. See the proof of Proposition 6.5.4 in Appendix C. \square

The next step is to discretize the modified Lie-Poisson variational principle to obtain integrators on \mathfrak{g}^* . Define $\mu_{k+\beta}$ the same as in the last section. We have:

Proposition 6.5.5. *For the left-invariant case, consider the discrete variational principle*

$$\delta \sum_{k=0}^{K-1} \left(\left\langle \mu_{k+\beta}, \frac{dh}{d\mu} \Big|_{\mu_{k+\beta}} \right\rangle - h(\mu_{k+\beta}) \right) \Delta t = 0, \quad (6.62)$$

with $\delta\mu_{k+\beta} = (1 - \beta)\delta\mu_k + \beta\delta\mu_{k+1}$, where $\delta\mu_k$ is restricted such that $\delta\frac{dh}{d\mu} \Big|_{\mu_{k+\beta}} :=$

$(1 - \beta)\delta^+ \frac{dh}{d\mu} \Big|_{\mu_k} + \beta\delta^- \frac{dh}{d\mu} \Big|_{\mu_{k+1}}$ in which

$$\begin{cases} \delta^+ \frac{dh}{d\mu} \Big|_{\mu_k} = \frac{\eta_{k+1} - \eta_k}{\Delta t} + \text{ad}_{\frac{dh}{d\mu} \Big|_{\mu_k}} \eta_k; \\ \delta^- \frac{dh}{d\mu} \Big|_{\mu_k} = \frac{\eta_k - \eta_{k-1}}{\Delta t} + \text{ad}_{\frac{dh}{d\mu} \Big|_{\mu_k}} \eta_k, \end{cases}$$

i.e.,

$$\delta \frac{dh}{d\mu} \Big|_{\mu_{k+\beta}} = \frac{\eta_{k+1} - \eta_k}{\Delta t} + (1 - \beta) \text{ad}_{\frac{dh}{d\mu} \Big|_{\mu_k}} \eta_k + \beta \text{ad}_{\frac{dh}{d\mu} \Big|_{\mu_{k+1}}} \eta_{k+1}, \quad (6.63)$$

where $\eta_k = \delta g_k g_k^{-1}$, $\delta g_k \in G$ arbitrary for $k = 1, \dots, K-1$ and $\delta g_0 = \delta g_K = 0$. The discrete variational principle is equivalent to the set of difference equations on \mathfrak{g}^*

$$\frac{1}{\Delta t}(\mu_{k+\beta} - \mu_{k-1+\beta}) = \text{ad}_{\frac{dh}{d\mu} \Big|_{\mu_k}}^* ((1 - \beta)\mu_{k+\beta} + \beta\mu_{k-1+\beta}), \quad k = 1, \dots, K-1 \quad (6.64)$$

Proof. Start from (6.62),

$$\begin{aligned} 0 &= \delta \sum_{k=0}^{K-1} \left(\left\langle \mu_{k+\beta}, \frac{dh}{d\mu} \Big|_{\mu_{k+\beta}} \right\rangle - h(\mu_{k+\beta}) \right) \\ &= \sum_{k=0}^{K-1} \left(\left\langle \delta \mu_{k+\beta}, \frac{dh}{d\mu} \Big|_{\mu_{k+\beta}} \right\rangle + \left\langle \mu_{k+\beta}, \delta \frac{dh}{d\mu} \Big|_{\mu_{k+\beta}} \right\rangle - \left\langle \delta \mu_{k+\beta}, \frac{dh}{d\mu} \Big|_{\mu_{k+\beta}} \right\rangle \right) \\ &= \sum_{k=0}^{K-1} \left\langle \mu_{k+\beta}, \frac{\eta_{k+1} - \eta_k}{\Delta t} + (1 - \beta) \text{ad}_{\frac{dh}{d\mu} \Big|_{\mu_k}} \eta_k + \beta \text{ad}_{\frac{dh}{d\mu} \Big|_{\mu_{k+1}}} \eta_{k+1} \right\rangle \\ &= \sum_{k=1}^{K-1} \left(\left\langle \frac{1}{\Delta t}(\mu_{k-1+\beta} - \mu_{k+\beta}) + (1 - \beta) \text{ad}_{\frac{dh}{d\mu} \Big|_{\mu_k}}^* \mu_{k+\beta} + \beta \text{ad}_{\frac{dh}{d\mu} \Big|_{\mu_k}}^* \mu_{k-1+\beta}, \eta_k \right\rangle \right. \\ &\quad \left. + \left\langle -\frac{\mu_\beta}{\Delta t} + (1 - \beta) \text{ad}_{\frac{dh}{d\mu} \Big|_{\mu_0}}^* \mu_\beta, \eta_0 \right\rangle + \left\langle \frac{\mu_{K-1+\beta}}{\Delta t} + \beta \text{ad}_{\frac{dh}{d\mu} \Big|_{\mu_K}}^* \mu_{K-1+\beta}, \eta_K \right\rangle \right). \end{aligned}$$

The conditions on δg_k imply that η_k is arbitrary for $k = 1, \dots, N-1$ and $\eta_0 = \eta_K = 0$. Thus, the equations (6.64) follow. The derivation in the reverse direction can be done in a similar way. \square

The set of difference equations (6.64) obtained above is a Lie-Poisson integrator

purely on \mathfrak{g}^* , referred to as *Modified Lie-Poisson (MLP) integrator on g^** . The symplecticity of this family of schemes can be checked by the approach we used in the proof of Proposition 6.5.2. Here we give a positive result for a special case.

Proposition 6.5.6. *Suppose the discrete inverse Legendre transform (6.48)&(6.49) is invertible at each time k . If a finite dimensional Lie-Poisson system for the left-invariant case has a quadratic Hamiltonian $h(\mu)$, then, with $\beta = 1/2$, the MLP on \mathfrak{g}^* (6.64) applied to this system preserves a discrete symplectic two-form along its solution sequence.*

Proof. The discrete Hamiltonian $h_k = h(\mu_k)$ is also a quadratic function of μ_k . In the inverse discrete reduced Legendre transform (6.48)&(6.49) defined in Proposition 6.4.3, if h_k is quadratic, $\xi_{k+\frac{1}{2}} = \frac{dh}{d\mu}|_{\mu_{k+\beta}}$ implies $\xi_k = \frac{dh}{d\mu}|_{\mu_k}$ when $\beta = 1/2$. It is then readily seen that the MLP (6.64) can be equivalently rewritten in the form of the VEP (6.45), which is symplectic. \square

Explicitly, the MLP on \mathfrak{g}^* with $\beta = 1/2$ for the left-invariant case reads

$$\frac{1}{\Delta t}(\mu_{k+\frac{1}{2}} - \mu_{k-\frac{1}{2}}) = \frac{1}{2} \text{ad}^*_{\frac{dh}{d\mu}|_{\mu_k}} \left(\mu_{k+\frac{1}{2}} + \mu_{k-\frac{1}{2}} \right). \quad k = 1, \dots, K-1 \quad (6.65)$$

Note that it is a two-step scheme.

Remark 6.5.3. For the right-invariant case where $\delta\mu = -\text{ad}^*_{\eta}\mu$, $\delta\left(\frac{dh}{d\mu}\right) = \dot{\eta} - [\frac{dh}{d\mu}, \eta]$, assume

$$\delta\frac{dh}{d\mu}|_{\mu_{k+\beta}} = \frac{\eta_{k+1} - \eta_k}{\Delta t} - (1-\beta) \text{ad}^*_{\frac{dh}{d\mu}|_{\mu_k}} \eta_k - \beta \text{ad}^*_{\frac{dh}{d\mu}|_{\mu_{k+1}}} \eta_{k+1}, \quad (6.66)$$

where $\eta_k = \delta g_k g_k^{-1}$. Following the same process for the left-invariant case one obtains the MLP on \mathfrak{g}^* for the right-invariant case

$$\frac{1}{\Delta t}(\mu_{k+\beta} - \mu_{k-1+\beta}) = -\text{ad}^*_{\frac{dh}{d\mu}|_{\mu_k}} ((1-\beta)\mu_{k+\beta} + \beta\mu_{k-1+\beta}), \quad k = 1, \dots, K-1 \quad (6.67)$$

The MLP on \mathfrak{g}^* with $\beta = 1/2$ for the right-invariant case is

$$\frac{1}{\Delta t}(\mu_{k+\frac{1}{2}} - \mu_{k-\frac{1}{2}}) = -\frac{1}{2} \text{ad}^*_{\frac{dh}{d\mu}} \Big|_{\mu_k} \left(\mu_{k+\frac{1}{2}} + \mu_{k-\frac{1}{2}} \right). \quad k = 1, \dots, K-1 \quad (6.68)$$

6.6 Numerical examples

Here we test the Lie-Poisson integrators developed in previous sections, including the variational integrators VLP on $G \times \mathfrak{g}^*$ and VLP on $\mathfrak{g} \times \mathfrak{g}^*$, and the trapezoidal rule (an integrator on \mathfrak{g}^*) and MLP on \mathfrak{g}^* with $\beta = 1/2$.

6.6.1 Example 1: Free Rigid Body Rotation

The dynamics of the free rigid body rotation forms a left-invariant Lie-Poisson system (Marsden & Ratiu, 1994). In this example $g = R \in G = \text{SO}(3)$ (R is the rotation matrix), $\mu = \hat{\Pi} \in \mathfrak{g}^* = \mathfrak{so}(3)^*$ where $\Pi = (\Pi^1, \Pi^2, \Pi^3) \in \mathbb{R}^3$ is the angular momentum expressed in the body-fixed frame and ‘ $\hat{\cdot}$ ’ is the hat map defined in Marsden & Ratiu (1994), $\xi = g^{-1}\dot{g} = \hat{\Omega} \in \mathfrak{g} = \mathfrak{so}(3)$ where $\Omega = \frac{dh}{d\Pi} \in \mathbb{R}^3$ is the body angular velocity, and the reduced Hamiltonian is

$$h(\Pi) = \frac{1}{2} \left(\frac{(\Pi^1)^2}{\mathbb{I}^1} + \frac{(\Pi^2)^2}{\mathbb{I}^2} + \frac{(\Pi^3)^2}{\mathbb{I}^3} \right). \quad (6.69)$$

where \mathbb{I}^i , $i = 1, 2, 3$, are the principal moments of inertia of the rigid body. The equation of motion is the Euler equation for a rigid body:

$$\dot{\Pi} = \Pi \times \Omega = \Pi \times \frac{dh(\Pi)}{d\Pi} \quad (6.70)$$

or equivalently $\dot{\hat{\Pi}} = \text{ad}^*_{\hat{\Omega}} \hat{\Pi} = \text{ad}^*_{\frac{dh(\hat{\Pi})}{d\hat{\Pi}}} \hat{\Pi}$. The system has the Casimir function $|\Pi|^2/2$ (conservation of the magnitude of the angular momentum in the body frame).

Schemes of VLP on $G \times \mathfrak{g}^*$

Recall from Section 6.2 that for the left-invariant case, $f_{k+1k} = g_{k+1}^{-1}g_k$, $\eta_k = g_k^{-1}\delta g_k$. To approximate $\xi(t_k) = g(t_k)^{-1}\dot{g}(t_k)$ by $\xi_k \in \mathfrak{g}$, i.e., keeping ξ_k skew-symmetric, we set an intermediate variable

$$\xi_k^I = g_{k+1}^{-1} \frac{g_{k+1} - g_k}{\Delta t} = \frac{1}{\Delta t}(\text{Id} - f_{k+1k}),$$

where Id is the 3×3 identity matrix, and thus

$$\xi_k = \frac{1}{2} (\xi_k^I - (\xi_k^I)^T) = \frac{1}{2\Delta t} (f_{k+1k}^T - f_{k+1k}) \in \mathfrak{g}. \quad (6.71)$$

The VLP on $G \times \mathfrak{g}^*$ (6.15)&(6.16) is thus in the form

$$\langle \hat{\mathbf{\Pi}}_k, (f_{k+1k}\eta_k)^T - f_{k+1k}\eta_k \rangle - \langle \hat{\mathbf{\Pi}}_{k-1}, (\eta_k f_{kk-1})^T - \eta_k f_{kk-1} \rangle = 0, \quad k = 1, \dots, K-1; \quad (6.72)$$

$$\frac{1}{2\Delta t} (f_{k+1k}^T - f_{k+1k}) = \frac{dh_k}{d\hat{\mathbf{\Pi}}_k}, \quad k = 0, \dots, K-1. \quad (6.73)$$

which will be solved for $f_{k+1k} \in G$ and $\hat{\mathbf{\Pi}}_k \in \mathfrak{g}^*$ at each time step. For two skew-symmetric matrices \mathbf{A} and \mathbf{B} , $\langle \mathbf{A}, \mathbf{B} \rangle = \frac{1}{2} \text{Trace}(\mathbf{A}^T \mathbf{B})$. Equation (6.72) thus becomes

$$\text{Trace} \left[\left((\hat{\mathbf{\Pi}}_k - \hat{\mathbf{\Pi}}_k^T) f_{k+1k} - f_{kk-1} (\hat{\mathbf{\Pi}}_{k-1} - \hat{\mathbf{\Pi}}_{k-1}^T) \right) \eta_k \right] = 0, \quad k = 1, \dots, K-1. \quad (6.74)$$

Defining (Lee *et al.*, 2005) $g_k^\epsilon = g_k e^{\epsilon \gamma_k}$ where $\gamma_k \in \mathfrak{so}(3)$, we get $\delta g_k = dg_k^\epsilon / d\epsilon|_{\epsilon=0} = g_k \gamma_k$, and thus $\eta_k = g_k^{-1} \delta g_k = \gamma_k \in \mathfrak{so}(3)$ is skew-symmetric. Therefore, the matrix $\left((\hat{\mathbf{\Pi}}_k - \hat{\mathbf{\Pi}}_k^T) f_{k+1k} - f_{kk-1} (\hat{\mathbf{\Pi}}_{k-1} - \hat{\mathbf{\Pi}}_{k-1}^T) \right)$ in (6.74) must be symmetric, i.e.,

$$\hat{\mathbf{\Pi}}_k f_{k+1k} - f_{k+1k}^T \hat{\mathbf{\Pi}}_k^T = f_{kk-1} \hat{\mathbf{\Pi}}_{k-1} - \hat{\mathbf{\Pi}}_{k-1}^T f_{kk-1}^T, \quad k = 1, \dots, K-1. \quad (6.75)$$

Schemes of VLP on $\mathfrak{g} \times \mathfrak{g}^*$

The VLP on $\mathfrak{g} \times \mathfrak{g}^*$ (6.43)&(6.44) is ready for simulation. Here we choose $\beta = 0$, which gives a semi-explicit scheme (explicit in updating ξ_k and implicit in updating $\hat{\Pi}_k$):

$$\frac{1}{\Delta t}(\hat{\Pi}_k - \hat{\Pi}_{k-1}) = \frac{1}{2} \text{ad}_{\xi_k}^* \left(\hat{\Pi}_k + \hat{\Pi}_{k-1} \right), \quad k = 1, \dots, K-1 \quad (6.76)$$

$$\xi_{k+1} = 2 \frac{dh_k}{d\hat{\Pi}_k} - \xi_k, \quad k = 0, \dots, K-1. \quad (6.77)$$

Further, by the fact that $\hat{\mathbf{c}} = \text{ad}_{\hat{\mathbf{a}}}^* \hat{\mathbf{b}}$ is equivalent to $\mathbf{c} = -\hat{\mathbf{a}}\mathbf{b}$ for $\mathbf{a}, \mathbf{b}, \mathbf{c} \in \mathbb{R}^3$, the above scheme can be rewritten as an *explicit* one:

$$\Pi_k = (\text{Id} + \frac{\Delta t}{2} \xi_k)^{-1} (\text{Id} - \frac{\Delta t}{2} \xi_k) \Pi_{k-1}, \quad k = 1, \dots, K-1 \quad (6.78)$$

$$\xi_{k+1} = 2 \frac{dh_k}{d\Pi_k} - \xi_k, \quad k = 0, \dots, K-1. \quad (6.79)$$

Notice that $(\text{Id} + \frac{\Delta t}{2} \xi_k)^{-1} (\text{Id} - \frac{\Delta t}{2} \xi_k)$ is a *Cayley transform* $\text{Cay}(\Delta t \xi_k)$ mapping $\Delta t \xi_k \in \mathfrak{g} = \mathfrak{so}(3)$ to elements in the orthogonal group $G = \text{SO}(3)$. Thus (6.78) is in the form $\Pi_k = \text{Cay}(\xi_k) \Pi_{k-1}$, implying that the Casimir function $|\Pi|^2/2$ will be preserved *exactly* in simulation.

Schemes of Lie-Poisson integrators on \mathfrak{g}^*

For the free rigid-body case, the trapezoidal rule (6.58), a not exactly symplectic integrator on \mathfrak{g}^* , is

$$\frac{1}{\Delta t}(\Pi_{k+1} - \Pi_k) = \frac{1}{2} \left(\Pi_k \times \frac{dh_k}{d\Pi_k} + \Pi_{k+1} \times \frac{dh_{k+1}}{d\Pi_{k+1}} \right), \quad (6.80)$$

and the MLP on \mathfrak{g}^* with $\beta = 1/2$ (6.65) for the free rigid-body case is a two-step method:

$$\frac{1}{\Delta t} \left(\Pi_{k+\frac{1}{2}} - \Pi_{k-\frac{1}{2}} \right) = \frac{1}{2} \left(\Pi_{k+\frac{1}{2}} + \Pi_{k-\frac{1}{2}} \right) \times \frac{dh_k}{d\Pi_k}. \quad (6.81)$$

Note that by Proposition 6.5.6, the above scheme is *symplectic* since the discrete Hamiltonian is quadratic.

Simulation results

Simulations are done in Matlab using double precision. Newton's method is used to solve nonlinear equations for implicit schemes. The tolerance of error allowed in Newton method is set to be 10^{-15} , close to machine precision.

For the rigid body example, the initial condition is $\mathbf{\Pi}(0) = (7/8, 5/8, 1/4)^T$. $\mathbb{I}^1 = 7/8$, $\mathbb{I}^2 = 5/8$, and $\mathbb{I}^3 = 1/4$. $\Delta t = 0.1$ for all schemes tested here. Figure 6.4 shows simulation results of the time evolution of Hamiltonian and Casimir functions by VLP on $G \times \mathfrak{g}^*$ (6.75) and (6.73), VLP on $\mathfrak{g} \times \mathfrak{g}^*$ with $\beta = 0$ (6.78)&(6.79), trapezoidal rule (6.80) and symplectic MLP on \mathfrak{g}^* (6.81). For comparison purpose, we also show the results by Runge-Kutta fourth order method (RK4) in the same figure. As an example, the individual trajectories of (Π^1, Π^2, Π^3) by VLP $G \times \mathfrak{g}^*$, together with the reference trajectories, are shown in Figure 6.5. As to the accuracy, Figure 6.6 shows the error plot for the above schemes, verifying that those tested schemes are second order. The results show that though RK4, as a fourth order scheme, generates more accurate individual trajectories, it generates linearly increasing unbounded drifts with finite magnitude in both Hamiltonian and Casimir functions. As comparison, the tested second-order schemes, including the not exactly symplectic trapezoidal rule, preserve the Hamiltonian and Casimir functions well in the sense that the oscillations of those quantities are bounded around the initial values. Thus, qualitatively, these schemes capture the conservative feature of the freely-rotating rigid body system, while by RK4 the system is discretized as a dissipative one. Also notice that the Casimir function is preserved at machine

precision in the VLP on $\mathfrak{g} \times \mathfrak{g}^*$ with $\beta = 0$ scheme, as we expect.

As to the comparison of simulation speed and accuracy among these schemes, VLP on $G \times \mathfrak{g}^*$ needs most CPU time for simulation, while the VLP on $\mathfrak{g} \times \mathfrak{g}^*$ with $\beta = 0$ is the fastest, since it is explicit. Figure 6.6 shows that with small time steps, the VLP on $G \times \mathfrak{g}^*$ has the worst accuracy, and the trapezoidal rule is the most accurate. However, these results depend on the particular system, as the next example shows.

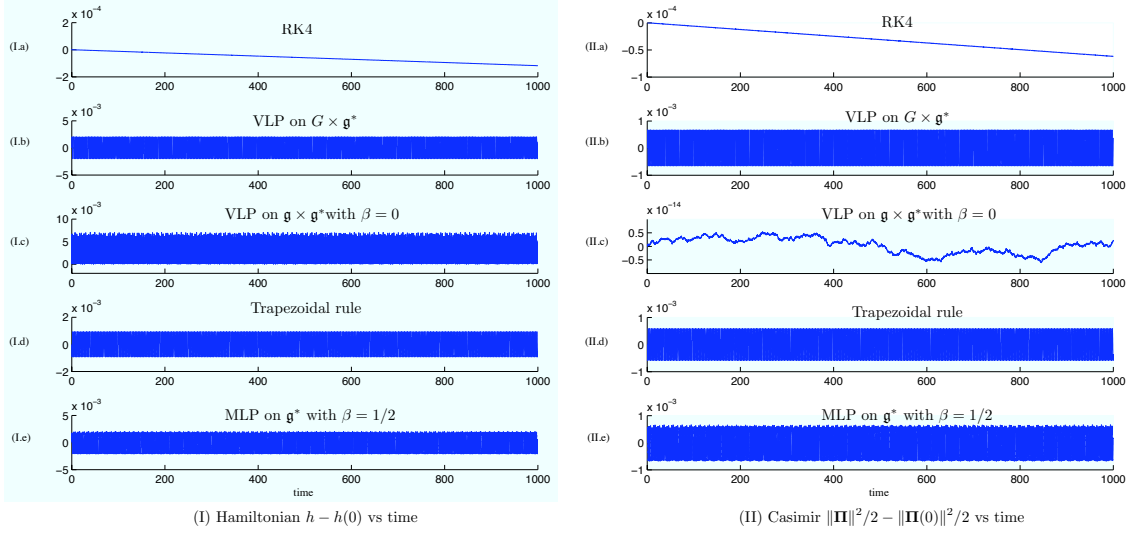


Figure 6.4: Example of the free rigid body rotation problem. $\Delta t = 0.1$. Simulation time $t \in [0, 1000]$. (I): Hamiltonian $h - h(0)$ versus time; (II): Casimir function $\|\Pi\|^2/2 - \|\Pi(0)\|^2/2$ versus time.

6.6.2 Example 2: Dynamics of N point vortices on a sphere

The problem of N point vortices interacting on a sphere is an example of a right-invariant Lie-Poisson system (Pekarsky & Marsden, 1998). It was pointed out in Marsden *et al.* (1999b) that variational Euler-Poincaré integrators can be applied to this system, once one obtains its corresponding Euler-Poincaré representation. However, due to computational difficulty in performing the reduced Legendre transform, the Euler-Poincaré form of the system is not known yet.

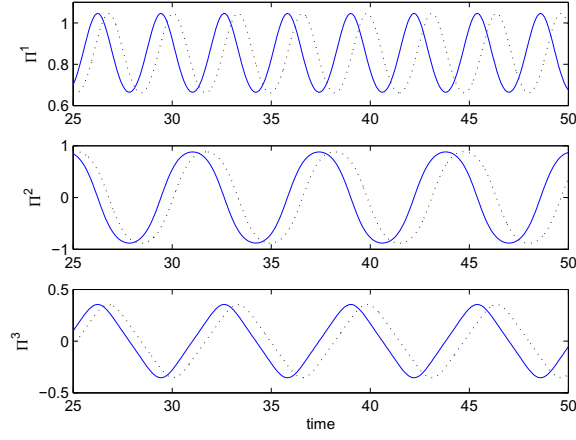


Figure 6.5: The trajectories of $\Pi(t) = (\Pi^1(t), \Pi^2(t), \Pi^3(t))^T$ versus time. Dotted line: RK4 with $\Delta t = 0.001$ as reference; solid line: VLP on $G \times \mathfrak{g}^*$ with time step $\Delta t = 0.1$. Simulation time $t \in [0, 50]$. The time interval displayed in the graph is $[25, 50]$.

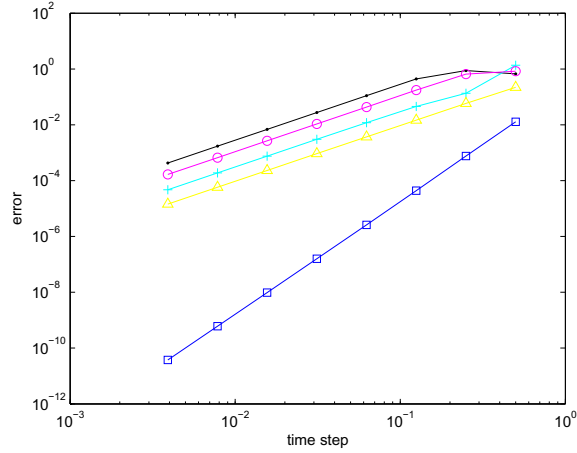


Figure 6.6: Example of the free rigid body rotation problem. Error plot for the schemes RK4 (\square), VLP on $G \times \mathfrak{g}^*$ (\cdot), VLP on $\mathfrak{g} \times \mathfrak{g}^*$ ($+$), Trapezoidal rule (\triangle) and symplectic MLP on \mathfrak{g}^* (\circ). The error is calculated in the time interval $[0, 40]$ by $\text{error} = \frac{1}{K} \sum_{k=0}^{K-1} \|\Pi_{sim}(t_k) - \Pi_{ref}(t_k)\|$, where Π_{sim} is the simulation result and Π_{ref} stands for the reference trajectory generated by RK4 with $\Delta t = 0.001$.

Consider a system of N point vortices interacting on a sphere with radius R . In a Cartesian coordinate system with origin located at the center of the sphere, denote the position vector of the α -th point vortex, with strength Γ^α , as $\mathbf{x}^\alpha = (x^{\alpha 1}, x^{\alpha 2}, x^{\alpha 3})^T$. $\|\mathbf{x}^\alpha\| \equiv R$. Recall the equations of motion expressed in Cartesian

coordinates (Newton, 2001) are

$$\dot{\mathbf{x}}^\alpha = \frac{1}{2\pi R} \sum_{\beta \neq \alpha}^N \Gamma^\beta \frac{\mathbf{x}^\beta \times \mathbf{x}^\alpha}{(l^{\beta\alpha})^2}, \quad (6.82)$$

for $\alpha = 1, \dots, N$, where $l^{\beta\alpha} = \|\mathbf{x}^\beta - \mathbf{x}^\alpha\|$ is the chord distance between the β -th and α -th point vortices on the sphere. The Hamiltonian of this system is

$$h = -\frac{1}{4\pi R^2} \sum_{\beta < \alpha}^N \Gamma^\beta \Gamma^\alpha \ln((l^{\beta\alpha})^2), \quad (6.83)$$

This system possesses a weighted Lie-Poisson (‘LPW’) structure (Pekarsky & Marsden, 1998)

$$\{F, K\}_{LPW}(\mathbf{x}) = \sum_{\alpha=1}^N \frac{R}{\Gamma^\alpha} \mathbf{x}^\alpha \cdot \left(\frac{\partial F}{\partial \mathbf{x}^\alpha} \times \frac{\partial K}{\partial \mathbf{x}^\alpha} \right) \quad (6.84)$$

where real valued function F and $K: \mathbf{x} \mapsto \mathbb{R}$, in which $\mathbf{x} = ((\mathbf{x}^1)^T, \dots, (\mathbf{x}^N)^T)^T \in \mathbb{R}^{3N}$. The system is Lie-Poisson defined on $\mathfrak{g}^* = \mathfrak{so}(3)^* \times \dots \times \mathfrak{so}(3)^* \simeq \mathbb{R}^{3N}$, the dual space of the Lie algebra of the Lie group $G = \text{SO}(3) \times \dots \times \text{SO}(3)$, since it is obtained by a Lie-Poisson reduction from T^*G to \mathfrak{g}^* with a Hamiltonian defined on T^*G which is right invariant under action of G (Pekarsky & Marsden, 1998).

Introduce a set of vector valued variables, $\rho^\alpha = (\rho^{\alpha 1}, \rho^{\alpha 2}, \rho^{\alpha 3})^T \in \mathbb{R}^3 \simeq \mathfrak{so}(3)^*$, $\alpha = 1, \dots, N$, as

$$\rho^\alpha = \frac{\Gamma^\alpha}{R} \mathbf{x}^\alpha. \quad (6.85)$$

Define $\rho = ((\rho^1)^T, \dots, (\rho^N)^T)^T \in \mathbb{R}^{3N} \simeq \mathfrak{g}^*$. The equations of motion in ρ variable can thus be written in Lie-Poisson bracket form

$$\dot{F} = \{F, h\}_{LP} \quad (6.86)$$

with a ‘standard’ (cleaner) Lie-Poisson structure

$$\{F, K\}_{LP}(\rho) = \sum_{\alpha=1}^N \rho^\alpha \cdot \left(\frac{\partial F}{\partial \rho^\alpha} \times \frac{\partial K}{\partial \rho^\alpha} \right). \quad (6.87)$$

The conserved quantities and preserved structure of the system (Pekarsky & Marsden, 1998; Newton, 2001) include its Lie-Poisson structure, its Hamiltonian, its Casimir functions such as $C^\alpha := \|\mathbf{x}^\alpha\|^2 = (R/\Gamma^\alpha)^2 \|\rho^\alpha\|^2 \equiv R^2$, $\alpha = 1, \dots, N$, which imply that all point vortices stay on the sphere, and the three components of the momentum map corresponding to the symmetry group $G_s = \text{SO}(3)$

$$\mathbf{M} = \sum_{i=1}^N \Gamma_i \mathbf{x}^i = \frac{1}{R} \sum_{i=1}^N \rho^i. \quad (6.88)$$

\mathbf{M} is also called the moment of vorticity.

The above setting allows us to put the equations of motion in the intrinsic form of Lie-Poisson systems for the right-invariant case (6.31):

$$\dot{\tilde{\rho}} = -\text{ad}_{dh/d\tilde{\rho}}^* \tilde{\rho}, \quad (6.89)$$

where the tilde map $\rho \mapsto \tilde{\rho}$ gives the skew-symmetric matrix

$$\tilde{\rho} = \begin{pmatrix} \hat{\rho}^1 & & \mathbf{0} \\ & \ddots & \\ \mathbf{0} & & \hat{\rho}^N \end{pmatrix}. \quad (6.90)$$

In this case we identify $\mu = \tilde{\rho} \in \mathfrak{g}^*$ and $\xi = dh/d\tilde{\rho} = \dot{g}g^{-1} \in \mathfrak{g}$, where $g \in G = \text{SO}(3) \times \text{SO}(3) \times \dots \times \text{SO}(3)$ is identified as

$$g = \begin{pmatrix} g^1 & & \mathbf{0} \\ & \ddots & \\ \mathbf{0} & & g^N \end{pmatrix} \quad (6.91)$$

where each $g^\alpha \in \text{SO}(3)$.

Remark 6.6.1. Geometric integrators can also be developed for this system using approaches other than the variational Lie-Poisson one. For example, since the system has a separable Hamiltonian, the splitting method is applicable (Patrick, 2000;

Newton & Khushalani, 2002). Also, the Lie-Poisson Hamiltonian system can be rewritten as other Hamiltonian systems through coordinate transformations (Newton, 2001). For instance, the system can be converted into canonical Hamiltonian form, for which canonical symplectic integrators are applicable. However, in the canonical Hamiltonian representation, the $\text{SO}(3)$ symmetry of the Hamiltonian is broken due to the coordinate transformation. Consequently, in simulations using those canonical symplectic integrators, one in general does not expect that the drifts of the moment of vorticity \mathbf{M} will be bounded over time. Stereographic projection is another coordinate transformation often used in point vortex dynamics, but this approach also breaks the symmetry. In this case, the projected system is still non-canonical and therefore canonical symplectic integrators are not applicable to it.

Schemes of VLP on $G \times \mathfrak{g}^*$

For the right-invariant case we choose $f_{kk+1} = g_k g_{k+1}^{-1}$, $\eta_k = \delta g_k g_k^{-1}$. As we did for the rigid body case, to approximate $\xi(t_k) = \dot{g}(t_k)g(t_k)^{-1}$ by $\xi_k \in \mathfrak{g}$, let

$$\xi_k = \frac{1}{2\Delta t}(f_{kk+1}^T - f_{kk+1}) \in \mathfrak{g}. \quad (6.92)$$

The VLP on $G \times \mathfrak{g}^*$ for the right-invariant case (6.32)&(6.33) is thus in the form

$$\langle \tilde{\rho}_k, (\eta_k f_{kk+1})^T - \eta_k f_{kk+1} \rangle - \langle \tilde{\rho}_{k-1}, (f_{k-1k} \eta_k)^T - f_{k-1k} \eta_k \rangle = 0, \quad k = 1, \dots, K-1; \quad (6.93)$$

$$\frac{1}{2\Delta t}(f_{kk+1}^T - f_{kk+1}) = \frac{dh_k}{d\tilde{\rho}_k}, \quad k = 0, \dots, K-1, \quad (6.94)$$

which will be solved for $f_{kk+1} \in G$ and $\tilde{\rho}_k \in \mathfrak{g}^*$ at each time step. Again use $\langle \mathbf{A}, \mathbf{B} \rangle = \frac{1}{2} \text{Trace}(\mathbf{A}^T \mathbf{B})$ for two skew-symmetric matrices \mathbf{A} and \mathbf{B} . Also, by the same argument used in the rigid body case one shows that η_k here is also skew-

symmetric. Thus by rearrangement of (6.93) one obtains

$$f_{kk+1}\tilde{\rho}_k - \tilde{\rho}_k^T f_{kk+1}^T = \tilde{\rho}_{k-1}f_{k-1k} - f_{k-1k}^T \tilde{\rho}_{k-1}^T, \quad k = 1, \dots, K-1. \quad (6.95)$$

The equations (6.94) and (6.95) are the VLP on $G \times \mathfrak{g}^*$ integrator for the N point vortices problem. Note that we can recover the results in terms of the vortex positions $\{\mathbf{x}_k\}_{k=0}^{K-1}$ by converting $\{\rho_k\}_{k=0}^{K-1}$ using (6.85).

Schemes of VLP on $\mathfrak{g} \times \mathfrak{g}^*$

With $\beta = 0$, the VLP on $\mathfrak{g} \times \mathfrak{g}^*$ (6.51)&(6.52) for the point vortex case is a semi-explicit scheme:

$$\frac{1}{\Delta t}(\tilde{\rho}_k - \tilde{\rho}_{k-1}) = -\frac{1}{2} \text{ad}_{\xi_k}^* (\tilde{\rho}_k + \tilde{\rho}_{k-1}), \quad k = 1, \dots, K-1 \quad (6.96)$$

$$\xi_{k+\frac{1}{2}} = \frac{dh_k}{d\tilde{\rho}_k}, \quad k = 0, \dots, K-1. \quad (6.97)$$

Again it can be rewritten as an *explicit* scheme as what we did in the free rigid-body case: For each α , $\alpha = 1, \dots, N$,

$$\rho_k^\alpha = (\text{Id} - \frac{\Delta t}{2} \xi_k^\alpha)^{-1} (\text{Id} + \frac{\Delta t}{2} \xi_k^\alpha) \rho_{k-1}^\alpha, \quad k = 1, \dots, K-1 \quad (6.98)$$

$$\xi_{k+1}^\alpha = 2 \frac{dh_k}{d\hat{\rho}_k^\alpha} - \xi_k^\alpha, \quad k = 0, \dots, K-1. \quad (6.99)$$

where the $\xi_k^\alpha \in \mathfrak{so}(3)$ is defined by denoting

$$\xi_k = \begin{pmatrix} \xi_k^1 & & \mathbf{0} \\ & \ddots & \\ \mathbf{0} & & \xi_k^N \end{pmatrix}. \quad (6.100)$$

As in the rigid-body case, this scheme guarantees that the Casimir functions $|\rho^\alpha|$, $\alpha = 1, \dots, N$ will be preserved *exactly* in simulation because $\rho_k^\alpha = \text{Cay}(-\Delta t \xi_k^\alpha) \rho_{k-1}^\alpha$ where $\text{Cay} : \mathfrak{so}(3) \rightarrow \text{SO}(3)$.

Schemes of Lie-Poisson integrators on \mathfrak{g}^*

The trapezoidal rule for the point vortex case is, for each α , $\alpha = 1, \dots, N$,

$$\frac{1}{\Delta t}(\rho_{k+1}^\alpha - \rho_k^\alpha) = -\frac{1}{2} \left(\rho_k^\alpha \times \frac{dh_k}{d\rho_k^\alpha} + \rho_{k+1}^\alpha \times \frac{dh_{k+1}}{d\rho_{k+1}^\alpha} \right), \quad (6.101)$$

and the MLP on \mathfrak{g}^* for $\beta = 1/2$ (6.68) for the point vortex case is, for each α , $\alpha = 1, \dots, N$,

$$\frac{1}{\Delta t} \left(\rho_{k+\frac{1}{2}}^\alpha - \rho_{k-\frac{1}{2}}^\alpha \right) = -\frac{1}{2} \left(\rho_{k+\frac{1}{2}}^\alpha + \rho_{k-\frac{1}{2}}^\alpha \right) \times \frac{dh_k}{d\rho_k^\alpha}, \quad (6.102)$$

which is a two-step method. The discrete Hamiltonian is not quadratic so we cannot conclude that this MLP is symplectic by Proposition 6.5.6. Simulation results shown below indicate that it is not symplectic.

Simulation results

To numerically verify the above schemes, we run an ‘inclined ring’ case (See Figure 6.7) where the angles Ψ and θ are arbitrarily chosen. In this case, the radius of the sphere $R = 1$, and there are six identical point vortices with strength $\Gamma^i = 1$, $i = 1, \dots, 6$, initially positioned on the sphere like an inclined ring. It is a stable relative equilibrium (Polvani & Dritschel, 1993; Kurakin, 2003), and the trajectory of each vortex shall be an inclined circle as shown in Figure 6.8.

Figure 6.9 shows simulation results of the time evolution of Hamiltonian, a typical Casimir function $C^1 = ||\mathbf{x}^1||^2$, and the three components of \mathbf{M} , by VLP on $G \times \mathfrak{g}^*$ (6.95)&(6.94), VLP on $\mathfrak{g} \times \mathfrak{g}^*$ with $\beta = 0$ (6.98)&(6.99) and trapezoidal rule (6.101), together with results by RK4 as comparison. As an example, the individual time trajectory of the first point vortex simulated by VLP on $G \times \mathfrak{g}^*$ is also shown in Figure 6.10. Though RK4 does preserve the moment of vorticity \mathbf{M} that is a linear first

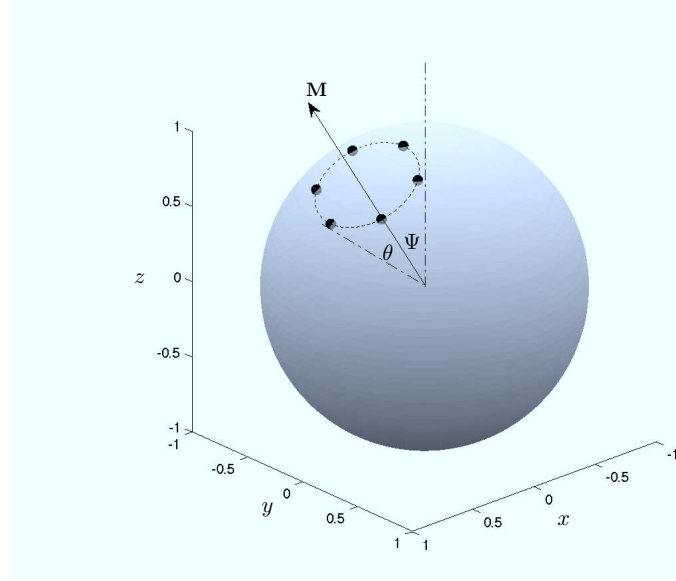


Figure 6.7: Inclined ring case. Initially, the six identical vortices are symmetrically positioned on the surface of the sphere as an ‘inclined ring’. θ is the ‘latitude’ of the vortices if the ring were not inclined, and ψ is the angle of inclination, i.e., the angle between the z axis and the vector from the center of the sphere to the center of the ring, which is also the direction of the initial moment of vorticity \mathbf{M} . \mathbf{M} is parallel to the $x - z$ plane. In this case, $\theta = 20^\circ$ and $\psi = 30^\circ$.

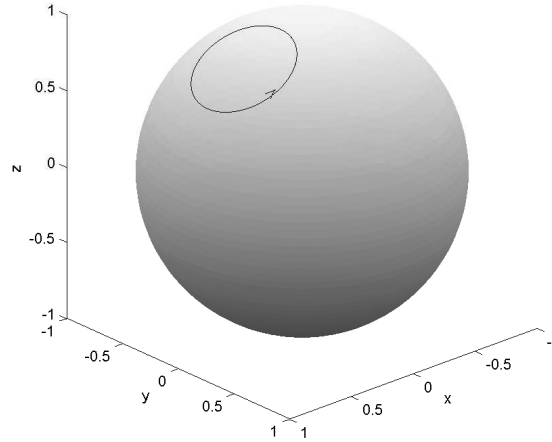


Figure 6.8: In the inclined ring case, the trajectory of each vortex shall be an inclined ring.

integral (Hairer *et al.*, 2006), it generates linearly increasing unbounded drifts with finite magnitude in both Hamiltonian and Casimirs. The drift of Casimir C^α means the trajectories even leave the surface of the sphere. As comparison, in the time in-

terval of simulation the VLP on $G \times \mathfrak{g}^*$ preserves the Hamiltonian, Casimir C^1 , and \mathbf{M} close to the machine precision. Note that the 10^{-14} -level drifts in Hamiltonian and M^2 are due to the Newton method but not the VLP on $G \times \mathfrak{g}^*$ algorithm. The explicit VLP on $\mathfrak{g} \times \mathfrak{g}^*$ with $\beta = 0$ preserves Hamiltonian and x, z components of \mathbf{M} with bounded oscillations, and preserves the Casimir to machine precision, as we expect. The y component of \mathbf{M} oscillates in an envelope with increasing magnitude at 10^{-13} level. This is however not due to the algorithm but related to the errors caused by the coordinate transforms used in the code for the inclined ring. The trapezoidal rule also shows good preservation of conserved quantities. The MLP with $\beta = 1/2$, if tested with $\Delta t = 0.1$ as other schemes, generates trajectories that oscillate sharply and leave the surface of the sphere. Even though with a much smaller $\Delta t = 0.01$ the scheme can generate reasonable trajectories, the Hamiltonian, Casimir and moment of vorticity \mathbf{M} oscillate in envelopes with increasing magnitudes at a finite level (see Figure 6.11). This numerical result indicates that MLP with $\beta = 1/2$ for the point vortex case is not symplectic.

The simulation results, together with the previous theoretical analysis, suggest that the VLP on $G \times \mathfrak{g}^*$, the VLP on $\mathfrak{g} \times \mathfrak{g}^*$ and the trapezoidal rule are good candidates for geometric simulations of the point vortex case. An interesting observation is that the Hamiltonian, though much more complicated than that in the free rigid body case, is preserved nearly to machine precision for VLP on $G \times \mathfrak{g}^*$, and for the trapezoidal rule. Recall that in the free rigid body case the Hamiltonian oscillates for both of these integrators.

Figure 6.12 shows the error plot for the above schemes. We see that for the point vortex case, with small time steps the VLP on $G \times \mathfrak{g}^*$ is the most accurate among those tested schemes, while the VLP on $\mathfrak{g} \times \mathfrak{g}^*$ is the worst, which is different as that for the rigid body case given in Figure 6.6. This comparison implies that the

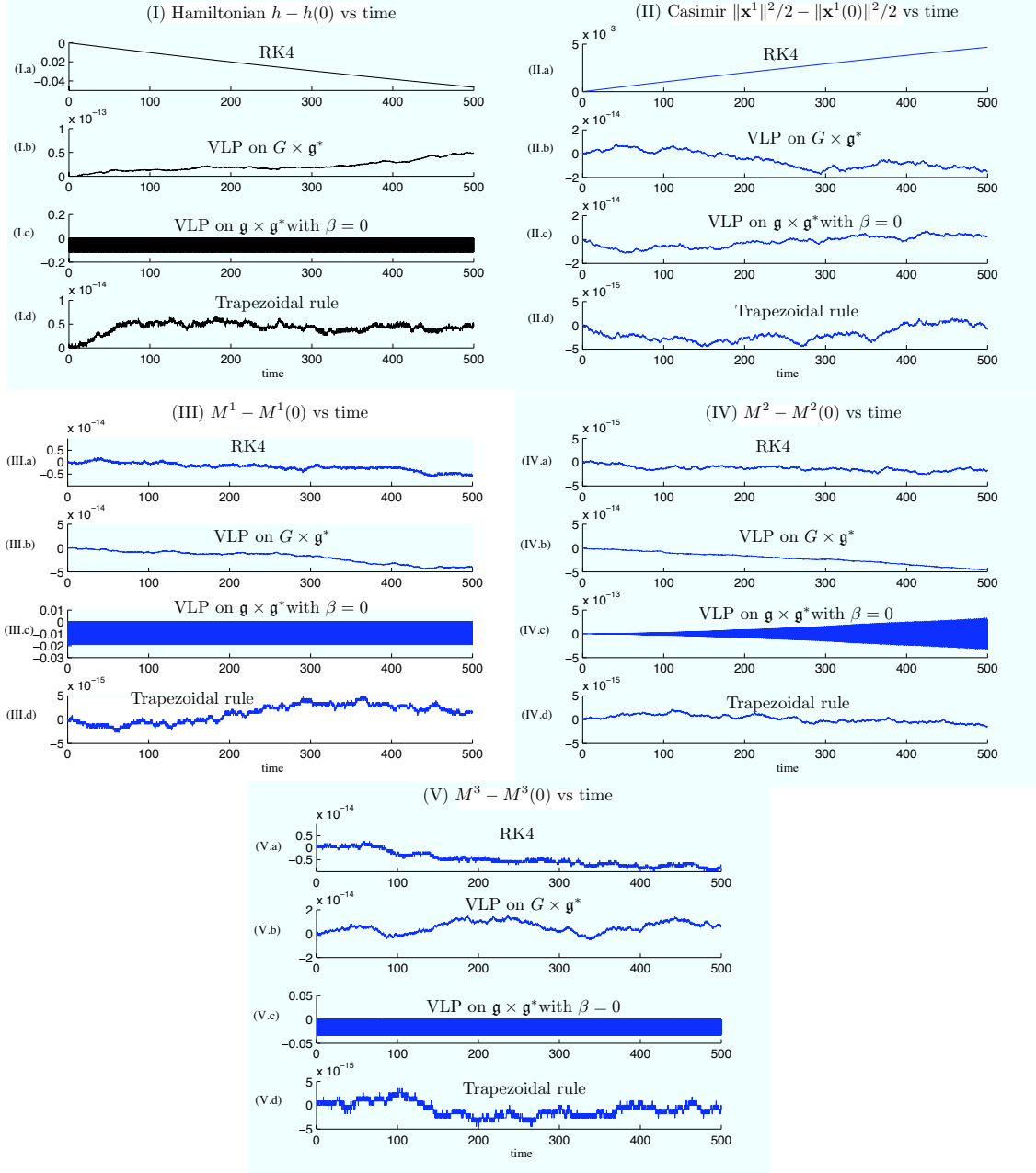


Figure 6.9: The inclined ring case. $\Delta t = 0.1$. Simulation time $t \in [0, 500]$. (I): Hamiltonian $h - h(0)$ versus time; (II): Casimir function $\|\mathbf{x}^1\|^2 - \|\mathbf{x}^1(0)\|^2$ versus time; (III): $M^1 - M^1(0)$ versus time; (IV): $M^2 - M^2(0)$ versus time; (V): $M^3 - M^3(0)$ versus time.

accuracy of these schemes may be Hamiltonian dependent.

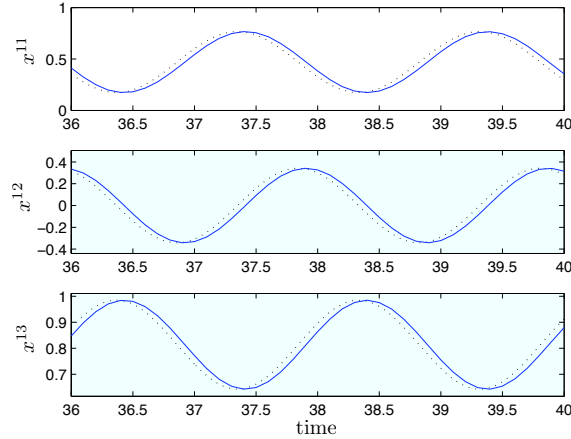


Figure 6.10: The trajectory of the first point vortex, $\mathbf{x}^1(t) = (x^{11}(t), x^{12}(t), x^{13}(t))^T$, versus time. The time interval displayed in the graph is $[36, 40]$. Dotted line: Theoretical trajectory; solid line: VLP on $G \times \mathfrak{g}^*$ with $\Delta t = 0.1$.

6.7 Summary

In this chapter, we presented a systematic approach for construction of Lie-Poisson integrators by discretization of variational principles corresponding to finite-dimensional Lie-Poisson systems. These integrators include a scheme defined on $G \times \mathfrak{g}^*$, a family defined on $\mathfrak{g} \times \mathfrak{g}^*$, a family defined purely on \mathfrak{g}^* and a family defined on \mathfrak{g}^* using a modified Lie-Poisson variational principle. The first three integrators are constructed from the Lie-Poisson variational principle introduced in Cendra *et al.* (2003); the modified Lie-Poisson variational principle used by the last one is proposed in this work and defined only on \mathfrak{g}^* with restricted variations on $\delta\mu$. The schemes on $G \times \mathfrak{g}^*$ and on $\mathfrak{g} \times \mathfrak{g}^*$ are variational (symplectic). In the family of integrators on \mathfrak{g}^* , there is a subset of schemes that are not exactly symplectic but may work well for preservation of conserved quantities, as we see in both numerical examples. Among the modified Lie-Poisson integrators on \mathfrak{g}^* , if the discrete Hamiltonian is quadratic, there is a corresponding symplectic scheme. By backward error analysis, one therefore expects good performance as far as preservation

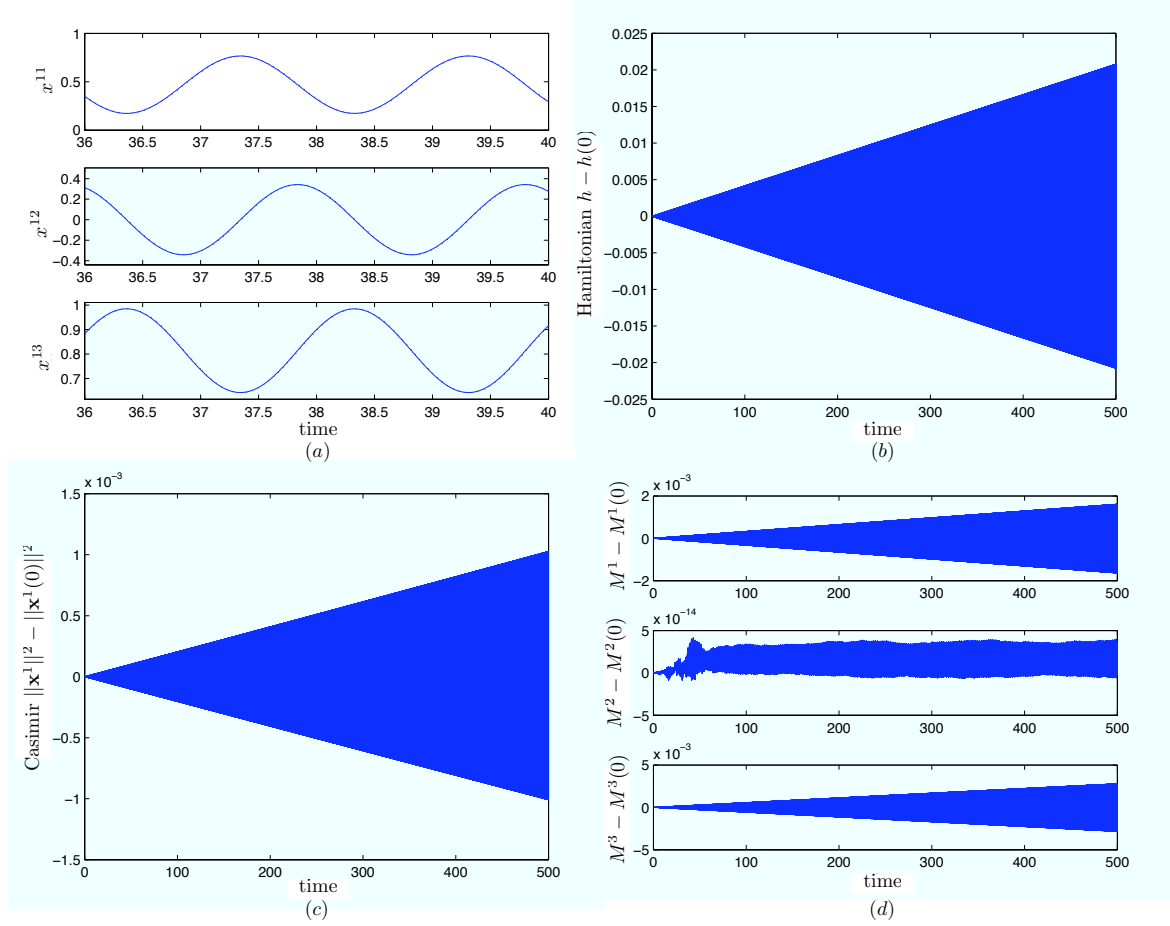


Figure 6.11: Simulation results of the MLP on \mathfrak{g}^* with $\beta = 1/2$. Time step $\Delta t = 0.01$. (a) The trajectory of the first point vortex, $\mathbf{x}^1(t) = (x^{11}(t), x^{12}(t), x^{13}(t))^T$, versus time. The time interval displayed in the graph is $[36, 40]$. Dotted line: Theoretical trajectory; solid line: MLP on \mathfrak{g}^* with $\beta = 1/2$. These two trajectories are almost identical to each other in the graph. (b) Hamiltonian $h - h(0)$ versus time. (c) Casimir function $\|\mathbf{x}^1\|^2 - \|\mathbf{x}^1(0)\|^2$ versus time. (d) Moment of vorticity $\mathbf{M} - \mathbf{M}(0)$ versus time.

of conserved quantities in simulations is concerned. Numerical tests given in the last section confirm these expectations. In particular, we apply those algorithms to the simulations of N point vortices on a sphere, and the algorithms VLP on $G \times \mathfrak{g}^*$ and VLP on $\mathfrak{g} \times \mathfrak{g}^*$ preserve the conservation laws at the discrete level properly. In comparison, in the simulation tests the standard Runge-Kutta fourth-order method does not preserve the Hamiltonian function and the Casimir functions in spite of its higher order of accuracy.

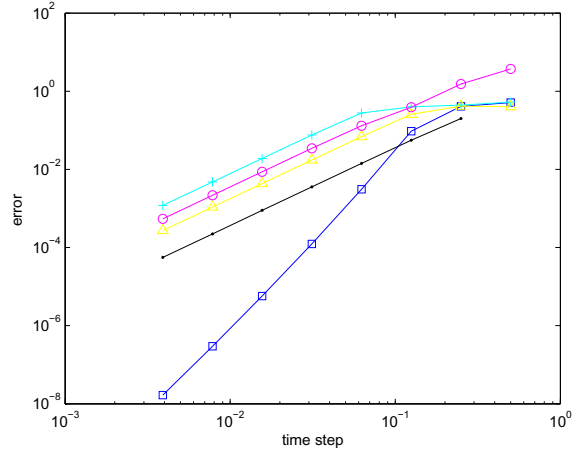


Figure 6.12: The inclined ring case. Error plot for the schemes RK4 (\square), VLP on $G \times \mathfrak{g}^*$ (\cdot), VLP on $\mathfrak{g} \times \mathfrak{g}^*$ with $\beta = 0$ ($+$), Trapezoidal rule (\triangle) and MLP on \mathfrak{g}^* with $\beta = 1/2$ (\circ). The error is calculated in the time interval $[0, 40]$ by $\text{error} = \frac{1}{K} \sum_{k=0}^{K-1} \|\mathbf{x}_{sim}^1(t_k) - \mathbf{x}_{ref}^1(t_k)\|$, where \mathbf{x}_{sim}^1 is the simulated trajectory of the first point vortex and \mathbf{x}_{ref}^1 stands for the theoretical trajectory as reference.

For practical applications, the ultimate goal of our work is to find a general way to construct fast (or even explicit) and stable symplectic/Lie-Poisson integrators defined purely on \mathfrak{g}^* that are easy to use. In this sense, the work presented here is just a beginning. It will also be interesting to apply these integrators to other important Lie-Poisson systems, such as the KdV equation.

Note that higher-order schemes can be constructed by composition methods or using a higher-order approximation of the integral in the variational principle (Marsden & West, 2001).

Chapter 7

Conclusions and future work

7.1 Conclusions

In the first part of the thesis (Chapters 3, 4 and 5), we first show that two widely-used methods in model reduction and system identification for linear time-invariant (LTI) systems, i.e., the approximate balanced truncation (balanced POD) and the eigensystem realization algorithm (ERA), are in fact equivalent in the sense that they generate identical reduced-order models, given the same input data (and assuming infinite-precision arithmetic). ERA is more computationally efficient and adjoint-free. On the other hand, balanced POD provides bi-orthogonal sets of modes that are useful, for example, in system analysis and control design.

Inspired by this equivalence, we construct an ERA algorithm that is also adjoint free for LTI systems with one-dimensional instability.

We then generalize the balanced POD/ERA methods for applications to stable or unstable high-dimensional linear time-periodic systems. Four algorithms are presented, including the lifted balanced POD/lifted ERA algorithms and the periodic

balanced POD/periodic ERA algorithms. The periodic balanced POD/periodic ERA algorithms also lead to model reduction methods for linear time-varying systems.

The lifted ERA method is then used to compute reduced-order models for a linearized time-periodic model around an unstable orbit corresponding to a flow past a two-dimensional flat plate with a periodic forcing. A reduced-order model is then used for observer-based feedback control design for the stabilization of the unstable orbit. Numerical results show that this reduced-order-model based control design approach works well in the sense that the controller stabilizes the unstable orbit, and the reduced-order model equipped with the observer captures well the closed-loop behavior of the full linearized model equipped with the same observer.

In the second part of the thesis (Chapter 6), we present a systematic and general method, in which a variational approach at the Hamiltonian side is used, to develop geometric integrators for Lie-Poisson Hamiltonian systems living in a finite-dimensional space \mathfrak{g}^* , the dual of Lie algebra associated with a Lie group G . These integrators are essentially different discretized versions of the Lie-Poisson variational principle, or a modified Lie-Poisson variational principle proposed in this work. We present three different integrators, including symplectic, variational Lie-Poisson integrators on $G \times \mathfrak{g}^*$ and on $\mathfrak{g} \times \mathfrak{g}^*$, as well as an integrator on \mathfrak{g}^* that is symplectic under certain conditions on the Hamiltonian. These Lie-Poisson integrators are defined directly on the reduced Hamiltonian side. They can be applied to cases where the reduced Lagrangian form is not available and the Euler-Poincaré integrators on the reduced Lagrangian side are not applicable, for instance when the reduced inverse Legendre transform is degenerate or computationally difficult to invert. Examples of applications include simulations of a free rigid body rotation and the dynamics of N point vortices on a sphere. Simulation results verify that

some of these variational Lie-Poisson integrators are good candidates for geometric simulations of those two Lie-Poisson Hamiltonian systems. The problem of N point vortices interacting on a sphere is an example of a case where the reduced Hamiltonian formation is known, but the reduced Lagrangian formation is currently not known.

7.2 Future research directions

ERA for linear systems with more than one unstable eigenvalue. The ERA method is generalized in this thesis for linear systems with a one-dimensional unstable manifold. This method can be also used for a linear system with a higher dimensional unstable manifold by iterating the procedures for the one-dimensional case. However, that will be computationally infeasible if the dimension of the unstable manifold is higher than the order of 10^0 . More efficient methods are of future research interest.

Model reduction methods for nonlinear systems with multiple equilibria and/or periodic orbits. The balanced truncation/ERA methods are designed for linear systems, and generalizing these methods to nonlinear systems is an interesting and challenging problem. One specific interesting direction, as a continuation of the study in this thesis, is to apply the time-varying ERA method (see Section 4.5.2) to a nonlinear system for which the equilibria/periodic orbits are known: linearization about each equilibrium and periodic orbit yields separate linear systems. If the nonlinear dynamics can be described by the equilibria/orbit information and a linear time-varying system that connects the separate linear systems, then the time-varying ERA method can be used to construct a reduced-order

time-varying model that could potentially capture the nonlinear dynamics (together with the equilibria/orbit information).

Observer-based feedback control for three-dimensional flow. The motivation of the study of the two-dimensional model problem considered in Chapter 5 is to develop control design tools for feedback control of wakes of micro-air vehicles at low Reynolds numbers. It would be interesting to apply the approach presented in Chapter 5 to the more realistic three-dimensional flow past a low-aspect-ratio wing. The three-dimensional dynamics is much richer than that in the two-dimensional case, as discussed in Taira & Colonius (2009): depending on the aspect ratio, angle of attack and Reynolds number, the three-dimensional flow past a low-aspect-ratio flat-plate wing can have a stable steady state, a periodic orbit or aperiodic shedding. The aperiodic shedding regime might correspond to a large number of unstable periodic orbits, as commonly occurs in chaotic attractors. The Newton-GMRES method can be applied for seeking those unstable orbits as in the two-dimensional model problem considered in Chapter 5. If there exists a high-lift unstable orbit, then the lifted ERA method can be applied to compute reduced-order models for the linearized time-periodic system about the orbit, and then an observer-based feedback controller can be designed. Note that studies of the three-dimensional flow over a low-aspect-ratio plate have indicated that open-loop forcing at the trailing edge can be beneficial for lift enhancement (Taira *et al.*, 2010). The approach presented in Chapter 5 for the two-dimensional case with periodic forcing could also be applied to the three-dimensional case.

Control of turbulence through stabilization of unstable periodic orbits. Following the discussions above, we note that a continuation study using the Newton-

GMRES method (or other methods) to seek stable/unstable orbits in the three-dimensional flow could lead to a better understanding of the transition to turbulence, for instance if the turbulent flow is comprised of a large (possibly infinite) number of unstable periodic orbits. An interesting direction is to suppress turbulence by the stabilization of a particular unstable orbit using the approach presented in Chapter 5.

Variational integrators for other non-canonical Hamiltonian systems. Recent work by Shashikanth *et al.* (2002); Shashikanth (2005); Shashikanth *et al.* (2008) shows non-canonical Hamiltonian structures for models of a neutrally buoyant, arbitrarily shaped smooth rigid body interacting with N point vortices/vortex rings of arbitrary shape in an infinite two or three-dimensional ideal fluid. These models are useful tools for understanding fish swimming, and it is interesting to construct geometric integrators for numerical simulations of these models. The variational approach applied in Chapter 6 for design of Lie-Poisson integrators can be applied to those systems. However the challenge is that one needs to first establish a corresponding variational principle.

Appendix A

Equivalence between the ROM for projected stable dynamics and the stable part of a ROM for the full unstable system

In this Appendix we show that in balanced POD, the reduced order model (ROM) for the projected system (2.22) that describes stable dynamics of the unstable LTI (2.1) are identical to the stable part of (2.25), the reduced order model of (2.1). This relation becomes important for ERA with application to unstable systems, as shown in Section 3.4, where the modes used in (2.25) are not available.

Proposition A.0.1. *Let A_r, B_r, C_r be the matrices of a reduced model of order r for the projected system given by (2.22), determined by using balanced POD. Then*

$$\Psi_{1r}^* A \Phi_{1r} = A_r; \quad \Psi_{1r}^* B = B_r; \quad C \Phi_{1r} = C_r, \quad (\text{A.1})$$

where Φ_{1r}, Ψ_{1r} are as given in (2.25), the reduced model of order $(r + n_u)$ of sys-

tem (2.1).

Proof. For convenience, here we rewrite the projected system (2.22)

$$\begin{aligned} x_s(k) &= Ax_s(k) + \mathbb{P}_s Bu_s(k); \\ y_s(k) &= C\mathbb{P}_s x_s(k) \end{aligned} \tag{A.2}$$

and the $(r + n_u)$ -dimensional reduced-order model (2.25)

$$\begin{aligned} x_r(k+1) &= \begin{bmatrix} \Psi_{1r}^* A \Phi_{1r} & 0 \\ 0 & \Lambda_u \end{bmatrix} x_r(k) + \begin{bmatrix} \Psi_{1r}^* \\ (S_u^* T_u)^{-1} S_u^* \end{bmatrix} Bu(k); \\ y(k) &= C \begin{bmatrix} \Phi_{1r} & T_u \end{bmatrix} x_r(k). \end{aligned} \tag{A.3}$$

By construction (see Section 2.3), Φ_{1r} and Ψ_{1r} are matrices consisting of the r leading balancing/adjoint modes for the projected system (A.2). Thus,

$$A_r = \Psi_{1r}^* A \Phi_{1r}; \quad B_r = \Psi_{1r}^* \mathbb{P}_s B; \quad C_r = C \mathbb{P}_s \Phi_{1r}. \tag{A.4}$$

Also, Φ_{1r} and Ψ_{1r} are obtained by the method of snapshots and satisfy (see (2.16))

$$\begin{aligned} \Phi_{1r} &= X V_r \Sigma_r^{-\frac{1}{2}} = \begin{bmatrix} A^{m_c P} \mathbb{P}_s B & \dots & \mathbb{P}_s B \end{bmatrix} V_r \Sigma_r^{-\frac{1}{2}}; \\ \Psi_{1r} &= Y U_r \Sigma_r^{-\frac{1}{2}} = \begin{bmatrix} \mathbb{P}_s^* C^* & \dots & (A^*)^{m_o P} \mathbb{P}_s^* C^* \end{bmatrix} U_r \Sigma_r^{-\frac{1}{2}}. \end{aligned}$$

where X and Y are impulse-response snapshots taken for the projected system (A.2) and its adjoint (2.23). By projection properties $\mathbb{P}_s^2 = \mathbb{P}_s$ and $\mathbb{P}_s A = A \mathbb{P}_s$, the realation (A.1) follows. \square

Appendix B

Periodic balanced truncation for linear time-periodic systems: the neutrally stable/unstable case

This work on periodic systems is a generalization to the work for LTI case (Ahuja & Rowley, 2010). The main idea of realizing periodic balanced truncation for a neutrally stable/unstable linear periodic system (4.1) is to decompose the system into a periodic, stable subsystem and a periodic, neutrally stable/unstable subsystem; see Ahuja & Rowley (2010) for the LTI case. A periodic balanced truncation is realized for the stable part, while exact dynamics are kept for the neutrally stable/unstable part, supposing its dimension is small. Since it is often computationally difficult to explicitly obtain the periodic stable subsystem, we suggest to instead find a balanced realization for a projected, stable periodic system. The following are theoretical details.

First, for each time $k, 1 \leq k \leq T$, consider $T_u(k), S_u(k) \in \mathbb{C}^{n \times n_u}$, whose n_u columns

are respectively the right and left neutrally stable/unstable eigenvectors of $F_A(k + T, k) := A(k + T - 1) \cdots A(k)$, where the time-periodic state transition matrix A is defined in (4.1). Choose $T_s(k), S_s(k) \in \mathbb{C}^{n \times n_s}$, each with rank $n_s = n - n_u$, such that $S_s^*(k)T_u(k) = 0$, $S_u^*(k)T_s(k) = 0$. For each k , define a projection onto $E^s(F_A(k + T, k))$, the stable subspace of $F_A(k + T, k)$, by

$$\mathbb{P}_s(k) := T_s(k) (S_s(k)^* T_s(k))^{-1} S_s(k)^*. \quad (\text{B.1})$$

Clearly, $T_u(k), S_u(k), T_s(k), S_s(k), \mathbb{P}_s(k)$ are time T -periodic.

Lemma B.0.2. *For any k , $\mathbb{P}_s(k)$ satisfies*

$$(i) \quad \mathbb{P}_s(k) = I_{n \times n} - T_u(k) (S_u(k)^* T_u(k))^{-1} S_u(k)^*;$$

$$(ii) \quad \mathbb{P}_s(k)^2 = \mathbb{P}_s(k);$$

(iii) $\mathbb{P}_s(k) F_A(k + T, k) = F_A(k + T, k) \mathbb{P}_s(k)$. The eigenvalues of $F_A(k + T, k) \mathbb{P}_s(k)$ include n_u zeros and the n_s stable eigenvalues of $F_A(k + T, k)$.

$$(iv) \quad A(k) \mathbb{P}_s(k) \text{ is a projection onto } E^s(F_A(k + T + 1, k + 1)).$$

Proof. (i)-(iii) are by definition of the projection. To show (iv), consider an eigenvector q of $F_A(k + T, k)$ corresponding to an eigenvalue λ inside the unit circle. On both sides of $F_A(k + T, k)q = q\lambda$, left multiplying $A(k + T)$ and using $A(k + T) = A(k)$, one shows that $A(k)q$ is an eigenvector of $F_A(k + T + 1, k + 1)$ corresponding to λ . It implies for any $z \in E^s(F_A(k + T, k))$, $A(k)z \in E^s(F_A(k + T + 1, k + 1))$. Since $\mathbb{P}_s(k)$ is a projection onto $E^s(F_A(k + T, k))$, the result follows. \square

It follows immediately from (iv) that

Corollary B.0.3. *For any k ,*

$$\mathbb{P}_s(k + 1) A(k) \mathbb{P}_s(k) = A(k) \mathbb{P}_s(k). \quad (\text{B.2})$$

Also, for any $j > 0$,

$$F_{A\mathbb{P}_s}(k+j, k) = F_A(k+j, k)\mathbb{P}_s(k), \quad (\text{B.3})$$

where $F_{A\mathbb{P}_s}(k+j, k) := A(k+j-1)\mathbb{P}_s(k+j-1) \cdots A(k)\mathbb{P}_s(k)$.

By (B.3) and Lemma B.0.2 (iii), one shows that

Corollary B.0.4. *For any k , the matrix $F_{A\mathbb{P}_s}(k+T, k)$ is exponentially stable. Its eigenvalues include n_u zeros and the n_s exponentially stable eigenvalues of $F_A(k+T, k)$.*

Now consider the decomposition of the LTP (4.1).

Lemma B.0.5. *With a coordinate transformation*

$$x(k) = \begin{bmatrix} T_s(k) & T_u(k) \end{bmatrix} \begin{bmatrix} x_s(k) \\ x_u(k) \end{bmatrix}, \quad (\text{B.4})$$

where $x_s(k) \in \mathbb{C}^{n_s}$, $x_u(k) \in \mathbb{C}^{n_u}$, the system (4.1) can be decoupled into an n_s -dimensional exponentially stable T -periodic subsystem

$$x_s(k+1) = A_s(k)x_s(k) + B_s(k)u(k); \quad y_s(k) = C_s(k)x_s(k), \quad (\text{B.5})$$

and an n_u -dimensional neutrally stable/unstable T -periodic subsystem

$$x_u(k+1) = A_u(k)x_u(k) + B_u(k)u(k); \quad y_u(k) = C_u(k)x_u(k), \quad (\text{B.6})$$

where $A_s(k) = (S_s^*(k+1)T_s(k+1))^{-1}S_s^*(k+1)A(k)T_s(k)$, $A_u(k) = (S_u^*(k+1)T_u(k+1))^{-1}S_u^*(k+1)A(k)T_u(k)$, $B_s(k) = (S_s^*(k+1)T_s(k+1))^{-1}S_s^*(k+1)B(k)$, $B_u(k) = (S_u^*(k+1)T_u(k+1))^{-1}S_u^*(k+1)B(k)$, $C_s(k) = C(k)T_s(k)$, $C_u = C(k)T_u(k)$, and $y_s(k) + y_u(k) = y(k)$.

Proof. The subsystems (B.5) and (B.6) are obtained by direct calculation, in which one uses relations $S_s^*(k)T_u(k) = 0$, $S_u^*(k)T_s(k) = 0$, as well as $S_s^*(k+1)A(k)T_u(k) =$

0, $S_u^*(k+1)A(k)T_s(k) = 0$. The latter two relations hold since, similar to the proof of Lemma B.0.2, one can show that the columns of $A(k)T_u(k)$ and $S_u^*(k+1)A(k)$ span $E^u(F_A(k+T+1, k+1))$ and $E^u(F_A(k+T, k))$ respectively.

For any k , consider the $n_s \times n_s$ matrix

$$F_{A_s}(k+T, k) = (S_s^*(k)T_s(k))^{-1}S_s^*(k)F_{A\mathbb{P}_s}(k+T, k+1)A(k)T_s(k).$$

It is easy to check that the n_s eigenvalues of this matrix are those “ n_s exponentially stable eigenvalues” of $F_{A\mathbb{P}_s}(k+T, k)$ in Corollary B.0.4. Thus, the T -periodic subsystem (B.5) is exponentially stable. Similarly, one shows the n_u -dimensional subsystem (B.6) has only neutrally stable/unstable eigenvalues. \square

In practice, before realizing a balanced truncation to the exponentially stable subsystem (B.5), one needs first construct this system. The construction can be very numerically expensive when n_s is large, due to calculations of $T_s(k)$ and $S_s(k)$. On the other hand, $S_u^*(k)$ and $T_u(k)$ can be numerically approximated relatively easily, since n_u is small. Thus, instead of construction of the subsystem (B.5), we compute $\mathbb{P}_s(k) = I_{n \times n} - T_u(k)(S_u^*(k)T_u(k))^{-1}S_u^*(k)$ and consider an n -dimensional system

$$\begin{aligned} x(k+1) &= A(k)\mathbb{P}_s(k)x(k) + \mathbb{P}_s(k+1)B(k)u(k); \\ y(k) &= C(k)\mathbb{P}_s(k)x(k). \end{aligned} \tag{B.7}$$

which by Corollary B.0.4 is exponentially stable. it is easy to check that for this projected system, for any time k , the n_u dimensional subspace $E^u(F_A(k+T, k))$ is neither controllable nor observable. Its controllability and observability Gramians at time k , $W_{c1}(k)$ and $W_{o1}(k)$, by

$$\begin{aligned} W_{c1}(k) &= \sum_{i=-\infty}^{k-1} F_{A\mathbb{P}_s}(k, i+1)\mathbb{P}_s(i+1)B(i)B(i)^*\mathbb{P}_s(i+1)^*F_{A\mathbb{P}_s}(k, i+1)^*; \\ W_{o1}(k) &= \sum_{i=k}^{\infty} F_{A\mathbb{P}_s}(i, k)^*\mathbb{P}_s(i)^*C(i)^*C(i)\mathbb{P}_s(i)F_{A\mathbb{P}_s}(i, k). \end{aligned} \tag{B.8}$$

Exact or approximate balanced truncation of this system can be realized using methods for exponentially stable cases. The following result gives a relation between the balancing modes of this system and those of the exponentially stable subsystem (B.5).

Proposition B.0.6. *For an arbitrary time k , let $\Phi_1(k) \in \mathbb{C}^{n \times n}$ be the balancing transformation for system (B.7) at that time, whose last n_u columns correspond to the n_u zero singular values due to the uncontrollable/unobservable subspace $E^u(F_A(k+T, k))$. Let $\Phi_{1s}(k) \in \mathbb{C}^{n \times n_s}$ be the block including the first n_s columns in $\Phi_1(k)$. Then, $\Phi_s(k) = (S_s(k)^* T_s(k))^{-1} S_s(k)^* \Phi_{1s}(k) \in \mathbb{C}^{n_s \times n_s}$ is the balancing transformation for the subsystem (B.5) at time k . Moreover, $\Phi_{1s}(k) = T_s \Phi(k)$.*

Proof. By definition and given conditions, $W_{c1}(k)W_{o1}(k) = \Phi_1(k)\Sigma_1(k)(\Psi_1(k))^*$, where $\Psi_1(k)^* = (\Phi_1(k))^{-1}$ and the last n_u diagonal entries of the diagonal matrix $\Sigma_1(k)$ are zero. Denote $\Sigma_{1s}(k) \in \mathbb{C}^{n_s \times n_s}$ as the block in $\Sigma_1(k)$ including its upper-left $n_s \times n_s$ entries, and $(\Psi_{1s}(k))^* \in \mathbb{C}^{n_s \times n_s}$ as the block in $(\Psi_1(k))^*$ including its first n_s rows. Note that $\Psi_{1s}(k)^* \Phi_{1s}(k) = I_{n_s \times n_s}$. Clearly $W_{1c}(k)W_{1o}(k) = \Phi_{1s}(k)\Sigma_{1s}(k)\Psi_{1s}(k)^*$.

The controllability and observability Gramians of the system (B.5) at time k , $W_c^s(k)$ and $W_o^s(k)$, read

$$\begin{aligned} W_c^s(k) &= \sum_{i=-\infty}^{k-1} F_{A_s}(k, i+1) B_s(i) B_s(i)^* F_{A_s}(k, i+1)^*; \\ W_o^s(k) &= \sum_{i=k}^{\infty} F_{A_s}(i, k)^* C_s(i)^* C_s(i) F_{A_s}(i, k). \end{aligned} \tag{B.9}$$

Using the definition of $\mathbb{P}_s(k)$, its property $\mathbb{P}_s(k)^2 = \mathbb{P}_s(k)$, and relation (B.3), one

shows by direct calculation that

$$\begin{aligned} W_c^s(k)W_o^s(k) &= (S_s^*(k)T_s(k))^{-1}S_s^*(k)W_{c1}(k)W_{o1}(k)T_s(k) \\ &= (S_s^*(k)T_s(k))^{-1}S_s^*(k)\Phi_{1s}(k)\Sigma_{1s}(k)(\Psi_{1s}(k))^*T_s(k) \end{aligned} \quad (\text{B.10})$$

Let

$$\Phi_s(k) = (S_s(k)^*T_s(k))^{-1}S_s(k)^*\Phi_{1s}(k).$$

By construction $\Phi_{1s}(k) \in E^s(F_A(k+T, k))$, so $T_s(k)\Phi_s(k) = \mathbb{P}_s(k)\Phi_{1s}(k) = \Phi_{1s}(k)$.

One also checks that $(\Phi_s(k))^{-1} = (\Psi_{1s}(k))^*T_s(k)$. Thus,

$$W_c^s(k)W_o^s(k) = \Phi_s(k)\Sigma_{1s}(k)(\Phi_s(k))^{-1}$$

and Φ_s is a balancing transformation for system (B.5). \square

Thus, if at time k , $x_{sB}(k)$ is the “balanced coordinates” of sub-system (B.5) such that $x_s(k) = \Phi_s(k)x_{sB}(k)$, then the “partially balancing” coordinate transformation in original coordinates is $x(k) = \Phi(k) \begin{bmatrix} x_{sB}(k) \\ x_u(k) \end{bmatrix}$, where the T -periodic $\Phi(k) = \begin{bmatrix} \Phi_{1s}(k) & T_u(k) \end{bmatrix}$. Let $\Phi_{1r}(k)$, $\Psi_{1r}(k)$ be matrices including the first r columns of $\Phi_{1s}(k)$ and $\Psi_{1s}(k)$, respectively. Truncation on the stable dynamics part can be done and the reduced T -periodic model of order $(r + n_u)$ is given by

$$\begin{aligned} \begin{bmatrix} x_{sr}(k+1) \\ x_u(k+1) \end{bmatrix} &= \Psi_r(k+1)^*A(k)\Phi_r(k) \begin{bmatrix} x_{sr}(k) \\ x_u(k) \end{bmatrix} + \Psi_r^*(k+1)B(k)u(k); \\ y(k) &= C(k)\Phi_r(k) \begin{bmatrix} x_{sr}(k) \\ x_u(k) \end{bmatrix} \end{aligned} \quad (\text{B.11})$$

$$\text{where } \Phi_r(k) = \begin{bmatrix} \Phi_{1r}(k) & T_u(k) \end{bmatrix}, \Psi_r(k)^* = \begin{bmatrix} (\Psi_{1r}(k))^* \\ (S_u^*(k)T_u(k))^{-1}S_u^*(k) \end{bmatrix}.$$

Appendix C

Proofs of preservation of a symplectic two-form along a Lie-Poisson flow.

Proposition C.0.7. *The Lie-Poisson variational principle (6.6) given in Section 6.2 implies that along a solution flow satisfying Lie-Poisson equations (6.3), a symplectic two-form is preserved. Further, define a map $\phi : G \times \mathfrak{g} \times \mathfrak{g}^* \rightarrow T^*G$ by*

$$\phi(g, \xi, \mu) = (g, T_e L_{g^{-1}}^* \mu), \quad (\text{C.1})$$

then the symplectic two-form on $G \times \mathfrak{g} \times \mathfrak{g}^$ is the pullback $\phi^* \Omega$ of the canonical symplectic form Ω on T^*G .*

Proof. Let

$$S(g, \xi, \mu) = \int_0^T (\langle \mu(t), \xi(t) \rangle - h(\mu(t))) dt. \quad (\text{C.2})$$

Consider the left-invariant case. The differential one-form of S with restricted vari-

ation $\delta\xi = \dot{\eta} + [\xi, \eta]$, where $\eta = g^{-1}\delta g$, is given by

$$\mathbf{d}S(g, \xi, \mu) \cdot (\delta g, \delta\xi, \delta\mu) = \int_0^T \left(\left\langle \delta\mu, \xi - \frac{dh}{d\mu} \right\rangle + \left\langle \mu, \frac{d}{dt}(g^{-1}\delta g) + \text{ad}_\xi g^{-1}\delta g \right\rangle \right) dt. \quad (\text{C.3})$$

Taking exterior derivative of $\mathbf{d}S$ gives

$$\begin{aligned} & \mathbf{d}^2S(g, \xi, \mu) \cdot ((\delta g^1, \delta\xi^1, \delta\mu^1), (\delta g^2, \delta\xi^2, \delta\mu^2)) \\ &= \int_0^T d \left(\left\langle \delta\mu^2, \xi - \frac{dh}{d\mu} \right\rangle + \left\langle \mu, \frac{d}{dt}(g^{-1}\delta g^2) + \text{ad}_\xi g^{-1}\delta g^2 \right\rangle \right) \cdot (\delta g^1, \delta\xi^1, \delta\mu^1) dt \\ & \quad - \int_0^T d \left(\left\langle \delta\mu^1, \xi - \frac{dh}{d\mu} \right\rangle + \left\langle \mu, \frac{d}{dt}(g^{-1}\delta g^1) + \text{ad}_\xi g^{-1}\delta g^1 \right\rangle \right) \cdot (\delta g^2, \delta\xi^2, \delta\mu^2) dt \\ &= \int_0^T \left(\left\langle \delta\mu^2, \delta\xi^1 - \frac{d^2h}{d\mu^2}\delta\mu^1 \right\rangle + \left\langle \mu, \text{ad}_{\delta\xi^1}(g^{-1}\delta g^2) - \frac{d}{dt}(g^{-1}\delta g^1 g^{-1}\delta g^2) - \text{ad}_\xi(g^{-1}\delta g^1 g^{-1}\delta g^2) \right\rangle \right. \\ & \quad \left. + \left\langle \delta\mu^1, \frac{d}{dt}(g^{-1}\delta g^2) + \text{ad}_\xi(g^{-1}\delta g^2) \right\rangle \right) dt \\ & \quad - \int_0^T \left(\left\langle \delta\mu^1, \delta\xi^2 - \frac{d^2h}{d\mu^2}\delta\mu^2 \right\rangle + \left\langle \mu, \text{ad}_{\delta\xi^2}(g^{-1}\delta g^1) - \frac{d}{dt}(g^{-1}\delta g^2 g^{-1}\delta g^1) - \text{ad}_\xi(g^{-1}\delta g^2 g^{-1}\delta g^1) \right\rangle \right. \\ & \quad \left. + \left\langle \delta\mu^2, \frac{d}{dt}(g^{-1}\delta g^1) + \text{ad}_\xi(g^{-1}\delta g^1) \right\rangle \right) dt, \end{aligned}$$

which, by $\delta\xi^i = \frac{d}{dt}(g^{-1}\delta g^i) + \text{ad}_\xi(g^{-1}\delta g^i)$, $i = 1, 2$ and using Jacobi identity, vanishes.

Define a one-form θ_{LP} ('LP' for 'Lie-Poisson') on $G \times \mathfrak{g} \times \mathfrak{g}^*$ as

$$\theta_{LP}(g, \xi, \mu) \cdot (u, v, y) = \langle \mu, g^{-1}u \rangle. \quad (\text{C.4})$$

By integration by parts, along the Lie-Poisson flow the $\mathbf{d}S$ given in (C.3) becomes

$$\begin{aligned} \mathbf{d}S(g, \xi, \mu) \cdot (\delta g, \delta\xi, \delta\mu) &= \int_0^T \left(\left\langle \delta\mu, \xi - \frac{dh}{d\mu} \right\rangle + \langle \text{ad}_\xi^* \mu - \dot{\mu}, \eta \rangle \right) dt + \langle \mu, \eta \rangle \Big|_0^T \\ &= \theta_{LP}(g, \xi, \mu) \cdot (\delta g, \delta\xi, \delta\mu) \Big|_0^T. \end{aligned}$$

It follows that, along the Lie-Poisson flow, since $\mathbf{d}^2S = 0$, the symplectic two-form

$\omega_{LP} = -\mathbf{d}\theta_{LP}$ is preserved. Explicitly,

$$\begin{aligned} \omega_{LP}(g, \xi, \mu) \cdot ((u^1, v^1, y^1), (u^2, v^2, y^2)) \\ = \langle \mu, g^{-1}u^1g^{-1}u^2 - g^{-1}u^2g^{-1}u^1 \rangle + \langle y^2, g^{-1}u^1 \rangle - \langle y^1, g^{-1}u^2 \rangle. \end{aligned} \quad (\text{C.5})$$

This ω_{LP} can be shown to be the pullback $\phi^*\Omega$ of the canonical symplectic two-form Ω on T^*G . The same result holds for the right-invariant case. \square

Proof of Proposition 6.5.4. The proof is similar to that for Proposition C.0.7.

Denote $\frac{dh}{d\mu} = h'(\mu)$. Let

$$S(g, \mu) = \int_0^T (\langle \mu(t), h'(\mu) \rangle - h(\mu(t))) dt. \quad (\text{C.6})$$

Consider the left-invariant case. The differential of S with restricted variation $\delta(h'(\mu)) = \dot{\eta} + [h'(\mu), \eta]$, where $\eta = g^{-1}\delta g$, is given by

$$\begin{aligned} \mathbf{d}S(g, \mu) \cdot (\delta g, \delta \mu) &= \int_0^T (\langle \delta \mu, h'(\mu) \rangle + \langle \mu, \dot{\eta} + \text{ad}_{h'(\mu)} \eta \rangle - \langle \delta \mu, h'(\mu) \rangle) dt \\ &= \int_0^T \left(\left\langle \mu, \frac{d}{dt}(g^{-1}\delta g) + \text{ad}_{h'(\mu)}(g^{-1}\delta g) \right\rangle \right) dt \end{aligned} \quad (\text{C.7})$$

Define a one-form θ_{MLP} ('MLP' stands for modified Lie-Poisson principle) on $G \times \mathfrak{g}^*$

$$\theta_{MLP}(g, \mu) \cdot (u, y) = \langle \mu, g^{-1}u \rangle. \quad (\text{C.8})$$

Along the Lie-Poisson flow, using integration by parts,

$$\mathbf{d}S(g, \mu) \cdot (\delta g, \delta \mu) = \theta_{MLP}(g, \mu) \cdot (\delta g, \delta \mu) \Big|_0^T.$$

So to prove a symplectic two-form $\omega_{MLP} = -\mathbf{d}\theta_{MLP}$ is preserved along the Lie-Poisson flow, it is enough to show that $\mathbf{d}^2S = 0$.

Taking exterior derivative of $\mathbf{d}S$ given in (C.7), one checks that

$$\begin{aligned}
& \mathbf{d}^2 S(g, \mu) \cdot ((\delta g^1, \delta \mu^1), (\delta g^2, \delta \mu^2)) \\
&= \int_0^T d \left(\left\langle \mu, \frac{d}{dt}(g^{-1} \delta g^2) + \text{ad}_{h'(\mu)}(g^{-1} \delta g^2) \right\rangle \right) \cdot (\delta g^1, \delta \mu^1) dt \\
&\quad - \int_0^T d \left(\left\langle \mu, \frac{d}{dt}(g^{-1} \delta g^1) + \text{ad}_{h'(\mu)}(g^{-1} \delta g^1) \right\rangle \right) \cdot (\delta g^2, \delta \mu^2) dt \\
&= \int_0^T \left(\left\langle \mu, -\text{ad}_{h'(\mu)}(g^{-1} \delta g^1 g^{-1} \delta g^2) + \text{ad}_{h''(\mu) \delta \mu^1}(g^{-1} \delta g^2) - \frac{d}{dt}(g^{-1} \delta g^1 g^{-1} \delta g^2) \right\rangle \right. \\
&\quad \left. + \left\langle \delta \mu^1, \text{ad}_{h'(\mu)}(g^{-1} \delta g^2) + \frac{d}{dt}(g^{-1} \delta g^2) \right\rangle \right) dt \\
&\quad - \int_0^T \left(\left\langle \mu, -\text{ad}_{h'(\mu)}(g^{-1} \delta g^2 g^{-1} \delta g^1) + \text{ad}_{h''(\mu) \delta \mu^2}(g^{-1} \delta g^1) - \frac{d}{dt}(g^{-1} \delta g^2 g^{-1} \delta g^1) \right\rangle \right. \\
&\quad \left. - \left\langle \delta \mu^2, \text{ad}_{h'(\mu)}(g^{-1} \delta g^1) + \frac{d}{dt}(g^{-1} \delta g^1) \right\rangle \right) dt \\
&= \int_0^T \left\langle \mu, \text{ad}_{h'(\mu)} \text{ad}_{g^{-1} \delta g^2}(g^{-1} \delta g^1) + \frac{d}{dt}(\text{ad}_{g^{-1} \delta g^2} g^{-1} \delta g^1) \right. \\
&\quad \left. - \text{ad}_{g^{-1} \delta g^2} \left(\frac{d}{dt}(g^{-1} \delta g^1) + \text{ad}_{h'(\mu)}(g^{-1} \delta g^1) \right) + \text{ad}_{g^{-1} \delta g^1} \left(\frac{d}{dt}(g^{-1} \delta g^2) + \text{ad}_{h'(\mu)}(g^{-1} \delta g^2) \right) \right\rangle dt \\
&\quad + \int_0^T (\langle \delta \mu^1, h''(\mu) \delta \mu^2 \rangle - \langle \delta \mu^2, h''(\mu) \delta \mu^1 \rangle) dt
\end{aligned}$$

which vanishes by the symmetry of the second derivative of $h(\mu)$ and using the Jacobi identity

$$\text{ad}_{h'(\mu)} \text{ad}_{g^{-1} \delta g^2}(g^{-1} \delta g^1) - \text{ad}_{g^{-1} \delta g^2} \text{ad}_{h'(\mu)}(g^{-1} \delta g^1) + \text{ad}_{g^{-1} \delta g^1} \text{ad}_{h'(\mu)}(g^{-1} \delta g^2) = 0.$$

Note that the ω_{MLP} on $G \times \mathfrak{g}^*$ is given by

$$\omega_{MLP}(g, \mu) \cdot ((u^1, y^1), (u^2, y^2)) = \langle \mu, g^{-1} u^1 g^{-1} u^2 - g^{-1} u^2 g^{-1} u^1 \rangle + \langle y^2, g^{-1} u^1 \rangle - \langle y^1, g^{-1} u^2 \rangle. \quad (\text{C.9})$$

Same result holds for the right-invariant case. \square

Bibliography

- ÅKERVIK, E., BRANDT, L., HENNINGSON, D. S., HØPPFNER, J., MARXEN, O. & SCHLATTER, P. 2006 Steady solutions of the Navier-Stokes equations by selective frequency damping. *Physics of Fluids* **18**, 068102.
- ÅKERVIK, E., HØPPFNER, J., EHRENSTEIN, U. & HENNINGSON, D. S. 2007 Optimal growth, model reduction and control in a separated boundary-layer flow using global eigenmodes. *Journal of Fluid Mechanics* **579**, 305–314.
- AHUJA, S. 2009 Reduction methods for feedback stabilization of fluid flows. PhD thesis, Princeton University.
- AHUJA, S. & ROWLEY, C. W. 2010 Feedback control of unstable steady states of flow past a flat plate using reduced-order estimators. *Journal of Fluid Mechanics* **645**, 447–478.
- AKERS, J. C. & BERNSTEIN, D. S. 1997 ARMARKOV least-squares identification. In *Proceedings of the ACC*, pp. 186–190. Albuquerque, NM, USA.
- ANTOULAS, A. C. 2005 *Approximation of Large-Scale Dynamical Systems*. SIAM.
- AREF, H. & POMPHREY, N. 1982 Integrable and chaotic motions of four vortices I. the case of identical vortices. *Proceedings of the Royal Society of London A* **380**, 359–387.

- ARNOLD, V. I. 1998 *Topological methods in hydrodynamics, Applied Mathematical Sciences*, vol. 125. Springer.
- ARNOLDI, W. E. 1951 The principle of minimized iterations in the solution of the matrix eigenvalue problem. *Quarterly of Applied Mathematics* **9**, 17–29.
- AUBRY, N., HOLMES, P., LUMLEY, J. L. & STONE, E. 1988 The dynamics of coherent structures in the wall region of a turbulent boundary layer. *Journal of Fluid Mechanics* **192**, 115–173.
- BAGHERI, S., BRANDT, L. & HENNINGSON, D. S. 2009a Input–output analysis, model reduction and control of the flat-plate boundary layer. *Journal of Fluid Mechanics* **620**, 263–298.
- BAGHERI, S., HENNINGSON, D. S., HEPFFNER, J. & SCHMID, P. J. 2009b Input–output analysis and control design applied to a linear model of spatially developing flows. *Applied Mechanics Reviews* **62** (2).
- BAGHERI, S., SCHLATTER, P., SCHMID, P. J. & HENNINGSON, D. S. 2009c Global stability of a jet in cross-flow. *Journal of Fluid Mechanics* **624**, 33–44.
- BAMIEH, B. & PEARSON, J. B. 1992 The H2 problem for sampled-data systems. *Systems and Control Letters* **19**, 1–12.
- BARBAGALLO, A., SIPP, D. & SCHMID, P. J. 2009 Closed-loop control of an open cavity flow using reduced-order models. *Journal of Fluid Mechanics* **641**, 1–50.
- BARKLEY, D. & HENDERSON, R. D. 1996 Three-dimensional floquet stability analysis of the wake of a circular cylinder. *Journal of Fluid Mechanics* **322**, 215–241.

- BAUCHAU, O. A. & WANG, J. 2008 Efficient and robust approaches to the stability analysis of large multibody systems. *Journal of Computational and Nonlinear Dynamics* **3** (011001).
- BOGOMOLOV, V. A. 1977 Dynamics of vorticity at a sphere. *Izvestiya Akademii Nauk SSSR, Mekhanika Zhidkosti i Gaza* **6**, 57–65.
- BOU-RABEE, N. 2007 Hamilton-Pontryagin integrators on Lie groups. PhD thesis, California Institute of Technology.
- BOU-RABEE, N. & MARSDEN, J. E. 2009 Hamilton-Pontryagin integrators on Lie groups Part I: Introduction and structure-preserving properties. *Foundations of Computational Mathematics* **9**, 197–219.
- CABELL, R. H., KEGERISE, M. A., COX, D. E. & GIBBS, G. P. 2006 Experimental feedback control of flow-induced cavity tones. *AIAA Journal* **44** (8), 1807–1815.
- CATTAFESTA, L. N., GARG, S., CHOUDHARI, M. & LI, F. 1997 Active control of flow-induced cavity resonance. AIAA Paper 97-1804.
- CATTAFESTA, L. N., SONG, Q., WILLIAMS, D. R., ROWLEY, C. W. & ALVI, F. S. 2008 Active control of flow-induced cavity oscillations. *Progress in Aerospace Sciences* **44**, 479–502.
- CENDRA, H., MARSDEN, J. E., PEKARSKY, S. & RATIU, T. S. 2003 Variational principles for Lie-Poisson and Hamilton-Poincaré equations. *Moscow Mathematical Journal* **3**, 833–867.
- CHAHLAOUI, Y. & VAN DOOREN, P. 2006 Model reduction of time-varying systems. In *Dimension reduction of large-scale systems*, pp. 131–148. Springer-Verlag.

- CHOI, H., JEON, W.-P. & KIM, J. 2008 Control of flow over a bluff body. *Annual Review of Fluid Mechanics* **40**, 113–39.
- CHOMAZ, J. 2005 Global instabilities in spatially developing flows: Non-normality and nonlinearity. *Annual Review of Fluid Mechanics* **37**, 357–392.
- COLONIUS, T. & TAIRA, K. 2008 A fast immersed boundary method using a nullspace approach and multi-domain far-field boundary conditions. *Computer Methods in Applied Mechanics and Engineering* **197** (25-28), 2131–46.
- CORDIER, L., ABOU EL MAJD, B. & FAVIER, J. 2010 Calibration of POD reduced-order models using Tikhonov regularization. *International Journal for Numerical Methods in Fluids* **63**, 269–296.
- COUPLET, M., BASDEVANT, C. & SAGAUT, P. 2005 Calibrated reduced-order POD-galerkin system for fluid flow modelling. *Journal of Computational Physics* **207**, 192 – 220.
- DJOUADI, S. M., CAMPHOUSE, R. C. & MYATT, J. H. 2008 Empirical reduced-order modeling for boundary feedback flow control. *Journal of Control Science and Engineering* **2008**, Article ID 154956, 11 pages. doi:10.1155/2008/154956.
- DOEDEL, E. J., KELLER, H. B. & KERNEVEZ, J. P. 1991 Numerical analysis and control of bifurcation problems, part II. *International Journal of Bifurcation and Chaos* **1** (4), 745–772.
- DULLERUD, G. E. & PAGANINI, F. 1999 *A Course in Robust Control Theory: A Convex Approach, Texts in Applied Mathematics*, vol. 36. Springer-Verlag.
- EHRENSTEIN, U. & GALLAIRE, F. 2008 Optimal perturbations and low-frequency oscillations in a separated boundary-layer flow. AIAA Paper 2008-4232, 5th AIAA Theoretical Fluid Mechanics Conference.

- FARHOOD, M., BECK, C. L. & DULLERUD, G. E. 2005 Model reduction of periodic systems: a lifting approach. *Automatica* **41**, 1085–1090.
- FUJIMOTO, K. & TSUBAKINO, D. 2008 Computation of nonlinear balanced realization and model reduction based on Taylor series expansion. *Systems and Control Letters* **57**, 283–289.
- GAITONDE, A. L. & JONES, D. P. 2003 Reduced order state-space models from the pulse responses of a linearized CFD scheme. *International Journal for Numerical Methods in Fluids* **42**, 581–606.
- GALLETTI, B., BRUNEAU, C. H., ZANNETTI, L. & IOLLO, A. 2004 Low-order modelling of laminar flow regimes past a confined square cylinder. *Journal of Fluid Mechanics* **503**, 161–170.
- GE, Z. & MARSDEN, J. E. 1988 Lie-Poisson Hamilton-Jacobi theory and Lie-Poisson integrators. *Physics Letters A* **133**, 134–139.
- GUCKENHEIMER, J. & HOLMES, P. J. 1983 *Nonlinear Oscillations, Dynamical Systems, and Bifurcations of Vector Fields, Applied Mathematical Sciences*, vol. 42. New York: Springer-Verlag.
- GUGERCIN, S., SORENSEN, D. C. & ANTOULAS, A. C. 2003 A modified low-rank Smith method for large-scale Lyapunov equations. *Numerical Algorithms* **32**, 27–55.
- HAIRER, E., LUBICH, C. & WANNER, G. 2006 *Geometric Numerical Integration: Structure-Preserving Algorithms for Ordinary Differential Equations*, 2nd edn. Springer-Verlag.
- GAD-EL HAK, M. 2000 *Flow Control: Passive, Active, and Reactive Flow Management*. Cambridge University Press.

- HARTMAN, P. 1964 *Ordinary Differential Equations*. John Wiley and Sons.
- HELMHOLTZ, H. 1858 Über integrale der hydrodynamischen Gleichungen, welche den Wirbelbewegungen entsprechen,. *J. für die reine und angewandte Mathematik* **55**, 25—55.
- HENNINGSON, D. S. & ÅKERVIK, E. 2008 The use of global modes to understand transition and perform flow control. *Physics of Fluids* **20** (031302).
- HOLMES, P., LUMLEY, J. L. & BERKOOZ, G. 1996 *Turbulence, Coherent Structures, Dynamical Systems and Symmetry*. Cambridge, UK: Cambridge University Press.
- HORN, R. A. & JOHNSON, C. R. 1985 *Matrix Analysis*. Cambridge University Press.
- HU, D. Y. & REICHEL, L. 1992 Krylov subspace methods for the Sylvester equation. *Linear Algebra and its Applications* **172**, 283–313.
- ILAK, M. 2009 Model reduction and feedback control of transitional channel flow. PhD thesis, Princeton University.
- ILAK, M., BAGHERI, S., BRANDT, L., ROWLEY, C. W. & HENNINGSON, D. S. 2010 Model reduction of the nonlinear complex Ginzburg-Landau equation. *SIAM Journal on Applied Dynamical Systems* **submitted**.
- ILAK, M. & ROWLEY, C. W. 2008 Modeling of transitional channel flow using balanced proper orthogonal decomposition. *Physics of Fluids* **20** (034103).
- ILLINGWORTH, S. J. 2009 Feedback control of oscillations in combustion and cavity flows. PhD thesis, University of Cambridge.

- JAIMOUKHA, I. M. & KASENALLY, E. M. 1994 Krylov subspace methods for solving large Lyapunov equations. *SIAM Journal on Numerical Analysis* **31**, 227–251.
- JOE, W. T., COLONIUS, T. & MACMYNOWSKI, D. G. 2009 Optimized control of vortex shedding from an inclined flat plate. AIAA Paper 2009-4027, 39th AIAA Fluid Dynamics Conference.
- JOE, W. T., TAIRA, K., COLONIUS, T. & MACMYNOWSKI, D. G. 2008 Closed-loop control of vortex shedding on a two-dimensional flat-plate airfoil at a low Reynolds number. AIAA Paper 2008-0634, 46th AIAA Aerospace Sciences Meeting and Exhibit.
- JUANG, J.-N. 1994 *Applied System Identification*. Prentice-Hall.
- JUANG, J.-N. & PAPPA, R. S. 1985 An eigensystem realization algorithm for modal parameter identification and model reduction. *Journal of Guidance, Control, and Dynamics* **8** (5), 620–627.
- VON KÁRMÁN, T. 1911 Über den Mechanismus des Widerstandes, den ein bewegter Körper in einer Flüssigkeit erfährt. 1. Teil. Göttinger Nachrichten Math-Phys. Klasse, 509-517.
- VON KÁRMÁN, T. 1912 Über den Mechanismus des Widerstandes, den ein bewegter Körper in einer Flüssigkeit erfährt. 2. Teil. Göttinger Nachrichten Math-Phys. Klasse, 547–556.
- KAWAHARA, G. & KIDA, S. 2001 Periodic motion embedded in plane Couette turbulence: regeneration cycle and burst. *Journal of Fluid Mechanics* **449**, 291–300.

- KAWAHARA, G., KIDA, S. & NAGATA, M. 2006 Unstable periodic motion in plane Couette system: the skeleton of turbulence. In *IUTAM Symposium on One Hundred Years of Boundary Layer Research* (ed. G. E. Meier), pp. 415–424. Springer.
- KELLEY, C. T. 2003 *Solving nonlinear equations with Newton's method*. Society for Industrial and Applied Mathematics.
- KIM, J. & BEWLEY, T. R. 2007 A linear systems approach to flow control. *Annual Review of Fluid Mechanics* **39**, 383–417.
- KIRCHHOFF, G. 1876 *Vorlesungen über Mathematische Physik, I*. Leipzig: Teubner.
- KRESSNER, D. 2003 Large periodic Lyapunov equations: algorithms and applications. In *Proceedings of the European Control Conference*. Cambridge, UK.
- KURAKIN, L. G. 2003 On the nonlinear stability of regular vortex polygons and on the nonlinear stability of regular vortex polygons and polyhedrons on a sphere. *Doklady Physics* **48**, 84–89.
- LALL, S., BECK, C. L. & DULLERUD, G. E. 1998 Guaranteed error bounds for model reduction of linear time-varying systems. In *Proceedings of the American Control Conference*, pp. 634–638.
- LALL, S., MARSDEN, J. E. & GLAVAŠKI, S. 2002 A subspace approach to balanced truncation for model reduction of nonlinear control systems. *International Journal of Robust and Nonlinear Control* **12**, 519–535.
- LAUB, A. J., HEATH, M. T., PAGE, C. C. & WARD, R. C. 1987 Computation of system balancing transformations and other applications of simultaneous diagonalization algorithms. *IEEE Transactions on Automatic Control* **32**, 115–122.

- LEE, T., MCCLAMROCH, N. H. & LEOK, M. 2005 A Lie group variational integrator for the attitude dynamics of a rigid body with applications to the 3D pendulum. In *Proceedings of the IEEE Conference on Control Applications*, pp. 962–967.
- LEHOUCQ, R. B., SORENSEN, D. C. & YANG, C. 1998 *ARPACK Users' Guide*. Society for Industrial and Applied Mathematics.
- LEIMKUHLER, B. & REICH, S. 2004 *Simulating Hamiltonian Dynamics*. Cambridge University Press.
- LIM, R. K., PHAN, M. Q. & LONGMAN, R. W. 1998 State-space system identification with identified Hankel matrix. Mechanical and Aerospace Engineering Tech. Report 3045. Princeton University.
- LIU, K. 1997 Identification of linear time-varying systems. *Journal of Sound and Vibration* **206** (4), 487–505.
- LONGHI, S. & ORLANDO, G. 1999 Balanced truncation of linear periodic systems. *Kybernetika* **35**, 737–751.
- LUCHTENBURG, D. K., GÜNTHER, B., NOACK, B. R., KING, R. & TADMOR, G. 2009 A generalized mean-field model of the natural and high-frequency actuated flow around a high-lift configuration. *Journal of Fluid Mechanics* **623**, 283–316.
- LUCHTENBURG, M., TADMOR, G., LEHMANN, O., NOACK, B. R., KING, R. & MORZYNSKI, M. 2006 Tuned pod Galerkin models for transient feedback regulation of the cylinder wake. In *44th AIAA Aerospace Sciences Meeting and Exhibit*. Paper AIAA-2006-1407.

- LUMLEY, J. L. 1967 The structure of inhomogeneous turbulence. In *Atmospheric Turbulence and Wave Propagation* (ed. A. Yaglom & V. Tatarski), pp. 166–78. Moscow: Nauka.
- LUMLEY, J. L. 1970 *Stochastic Tools in Turbulence*. New York: Academic Press.
- MA, Z., AHUJA, S. & ROWLEY, C. W. 2010a Reduced order models for control of fluids using the eigensystem realization algorithm. *Theoretical and Computational Fluid Dynamics* **in press**, DOI: 10.1007/s00162-010-0184-8.
- MA, Z. & ROWLEY, C. W. 2008 Low-dimensional linearized models for systems with periodic orbits, with application to the Ginzburg-Landau equation. AIAA Paper 2008-4196, 4th Flow Control Conference.
- MA, Z. & ROWLEY, C. W. 2010 Lie-Poisson integrators: A Hamiltonian, variational approach. *International Journal for Numerical Methods in Engineering* **82** (13), 1609–1644.
- MA, Z., ROWLEY, C. W. & TADMOR, G. 2010b Snapshot-based balanced truncation for linear time-periodic systems. *IEEE Transactions on Automatic Control* **55** (2), 469–473.
- MAJJI, M., JUANG, J.-N. & JUNKINS, J. L. 2010 Time-varying eigensystem realization algorithm. *Journal of Guidance, Control, and Dynamics* **33** (1), 13–28.
- MARSDEN, J. E., PEKARSKY, S. & SHKOLLER, S. 1999a Discrete Euler-Poincaré and Lie-Poisson equations. *Nonlinearity* **12**, 1647–1662.
- MARSDEN, J. E., PEKARSKY, S. & SHKOLLER, S. 1999b Stability of relative equilibria of point vortices on a sphere and symplectic integrators stability of relative equilibria of point vortices on a sphere and symplectic integrators stability

- of relative equilibria of point vortices on a sphere and symplectic integrators. *Il Nuovo Cimento* **22**, 793–802.
- MARSDEN, J. E. & RATIU, T. S. 1994 *Introduction to mechanics and symmetry*, 2nd edn., *Texts in Applied Mathematics*, vol. 17. Springer-Verlag.
- MARSDEN, J. E. & WEST, M. 2001 Discrete mechanics and variational integrators. *Acta Numerica* **10**, 357–514.
- MCLACHLAN, R. I. 1993 Explicit Lie-Poisson integration and the Euler equations. *Physical Review Letters* **71**, 3043–3046.
- MEYER, R. A. & BURRUS, C. S. 1975 A unified analysis of multirate and periodically time-varying digital filters. *IEEE Transactions on Circuits and Systems* **22**, 162–168.
- MIN, T., KANG, S. K., SPEYER, J. L. & KIM, J. 2006 Sustained sub-laminar drag in a fully developed channel flow. *Journal of Fluid Mechanics* **558**, 309–318.
- MOIN, P. & MOSER, R. 1989 Characteristic-eddy decomposition of turbulence in a channel. *Journal of Fluid Mechanics* **200**, 471–509.
- MOORE, B. C. 1981 Principal component analysis in linear systems: Controllability, observability, and model reduction. *IEEE Transactions on Automatic Control* **26** (1), 17–32.
- MORZYŃSKI, M., STANKIEWICZ, W., NOACK, B. R., KING, R., THIELE, F. & TADMOR, G. 2006 Continuous mode interpolation for control-oriented models of fluid flow. In *Proceedings of the First Berlin Conference on Active Flow Control*.
- NEWTON, P. K. 2001 *The N-vortex Problem: Analytical Techniques*, *Applied Mathematical Sciences*, vol. 145. Springer-Verlag.

- NEWTON, P. K. 2010 The N-vortex problem on a sphere: geophysical mechanisms. *Theoretical and Computational Fluid Dynamics* **24**, 137–149.
- NEWTON, P. K. & KHUSHALANI, B. 2002 Integrable decomposition methods and ensemble averaging for non-integrable N -vortex problems,. *Journal of Turbulence* **1**, 8–17.
- NOACK, B., AFANASIEV, K., MORZYŃSKI, M., TADMOR, G. & THIELE, F. 2003 A hierarchy of low-dimensional models for the transient and post-transient cylinder wake. *Journal of Fluid Mechanics* **497**, 335–363.
- OR, A. C., SPEYER, J. L. & CARLSON, H. A. 2008 Model reduction of input-output dynamical systems by proper orthogonal decomposition. *Journal of Guidance, Control, and Dynamics* **31** (2), 322–328.
- PATRICK, G. W. 2000 Dynamics of perturbed relative equilibria of point vortices on the sphere or plane. *Journal of Nonlinear Science* **10**, 401–415.
- PEKARSKY, S. & MARSDEN, J. E. 1998 Point vortices on a sphere: Stability of relative equilibria. *Journal of Mathematical Physics* **39**, 5894–5907.
- PENZL, T. 2000 A cyclic low-rank Smith method for large sparse Lyapunov equations. *SIAM Journal on Scientific Computing* **21** (4), 1401–1418.
- PENZL, T. 2006 Algorithms for model reduction of large dynamical systems. *Linear Algebra and its Applications* **415**, 322–343.
- POLVANI, L. M. & DRITSCHER, D. G. 1993 Wave and vortex dynamics on the surface of a sphere. *Journal of Fluid Mechanics* **255**, 35–64.

- PULLIN, D. I. & SAFFMAN, P. G. 1991 Long time symplectic integration: the example of four-vortex motion. *Proceedings of the Royal Society of London A* **432**, 481–494.
- REICH, S. 1993 Numerical integration of the generalized Euler equation. *Tech. Rep.* TR 93-20. University of British Columbia.
- ROMA, A. M., PESKIN, C. S. & BERGER, M. J. 1999 An adaptive version of the immersed boundary method. *Journal of Computational Physics* **153**, 509–534.
- ROUSSOPOULOS, K. & MONKEWITZ, P. A. 1996 Nonlinear modeling of vortex shedding control in cylinder wakes. *Physica D. Nonlinear Phenomena* **97**, 264–273.
- ROWLEY, C. W. 2005 Model reduction for fluids using balanced proper orthogonal decomposition. *International Journal of Bifurcation and Chaos* **15** (3), 997–1013.
- ROWLEY, C. W. & JUTTIJUDATA, V. 2005 Model-based control and estimation of cavity flow oscillations. In *Proceedings of the 44th IEEE Conference on Decision and Control*. Seville, Spain.
- ROWLEY, C. W. & MARSDEN, J. E. 2002 Variational integrators for degenerate Lagrangians, with application to point vortices. In *Proceedings of the 41st IEEE CDC*. Las Vegas, NV, USA.
- ROWLEY, C. W., MEZIĆ, I., BAGHERI, S., SCHLATTER, P. & HENNINGSON, D. S. 2009 Spectral analysis of nonlinear flows. *Journal of Fluid Mechanics* **641**, 115–127.
- SAAD, Y. & SCHULTZ, M. H. 1986 GMRES: A generalized minimal residual algorithm for solving nonsymmetric linear systems. *SIAM Journal on Scientific and Statistical Computing* **7** (3), 856–869.

- SAFONOV, M. G. & CHIANG, R. Y. 1989 A Schur method for balanced-truncation model reduction. *IEEE Transactions on Automatic Control* **34** (7), 729–733.
- SAMIMY, M., DEBIASI, M., CARABALLO, E., SERRANI, A., YUAN, X., LITTLE, J. & MYATT, J. H. 2007 Feedback control of subsonic cavity flows using reduced-order models. *Journal of Fluid Mechanics* **579**, 315–346.
- SÁNCHEZ, J., NET, M., GARCÍA-ARCHILLA, B. & SIMÓ, C. 2004 Newton–Krylov continuation of periodic orbits for Navier–Stokes flows. *Journal of Computational Physics* **201**, 13–33.
- SANDBERG, H. 2006 A case study in model reduction of linear time-varying systems. *Automatica* **42**, 467–472.
- SANDBERG, H. & MURRAY, R. M. 2007 Model reduction of interconnected linear systems. *Optimal Control Applications and Methods* **30**, 225–245.
- SANDBERG, H. & RANTZER, A. 2004 Balanced truncation of linear time-varying systems. *IEEE Transactions on Automatic Control* **49** (2), 217–229.
- SCHERPEN, J. M. A. 1993 Balancing for nonlinear systems. *Systems and Control Letters* **21** (2), 143–153.
- SHASHIKANTH, B. N. 2005 Poisson brackets for the dynamically interacting system of a 2D rigid boundary and N point vortices: The case of arbitrary smooth cylinder shapes. *Regular and Chaotic Dynamics* **10**, 1–14.
- SHASHIKANTH, B. N., MARSDEN, J. E., BURDICK, J. W. & KELLY, S. D. 2002 The Hamiltonian structure of a 2-D rigid circular cylinder interacting dynamically with N point vortices. *Physics of Fluids* **14**, 1214–1227.

- SHASHIKANTH, B. N., SHESHMANI, A., KELLY, S. D. & MARSDEN, J. E. 2008 Hamiltonian structure for a neutrally buoyant rigid body interacting with N vortex rings of arbitrary shape: the case of arbitrary smooth body shape. *Theoretical and Computational Fluid Dynamics* **22**, 37–64.
- SHOKOOHI, S. & SILVERMAN, L. M. 1987 Identification and model reduction of time-varying discrete-time systems. *Automatica* **23** (4), 509–521.
- SHOKOOHI, S., SILVERMAN, L. M. & VAN DOOREN, P. 1983 Linear time-variable systems: Balancing and model reduction. *IEEE Transactions on Automatic Control* **28**, 810–822.
- SHUB, M. 1984 Some remarks on dynamical systems and numerical analysis. In *Dynamical Systems and Partial Differential Equations* (ed. L. Lara-Carrero & J. Lewowicz), , vol. VII, pp. 62–92. ELAM.
- SIEGEL, S., COHEN, K. & MCCLAUGHLIN, T. 2003 Feedback control of a circular cylinder wake in experiment and simulation. AIAA Paper 2003-3569.
- SIEGEL, S. G., SEIDEL, J., FAGLEY, C., LUCHTENBURG, D. M., COHEN, K. & MCCLAUGHLIN, T. 2008 Low-dimensional modelling of a transient cylinder wake using double proper orthogonal decomposition. *Journal of Fluid Mechanics* **610**, 1–42.
- SILVA, W. A. & BARTELS, R. E. 2004 Development of reduced-order models for aeroelastic analysis and flutter prediction using the CFL3Dv6.0 code. *Journal of Fluids and Structures* **19**, 729–745.
- SIPP, D., MARQUET, O., MELIGA, P. & BARBAGALLO, A. 2010 Dynamics and control of global instabilities in open-flows: A linearized approach. *Applied Mechanics Reviews* **63** (3), 030801.

- SIROVICH, L. 1987 Turbulence and the dynamics of coherent structures, parts I–III. *Quarterly of Applied Mathematics* **XLV** (3), 561–590.
- SKOGESTAD, S. & POSTLETHWAITE, I. 2005 *Multivariable Feedback Control: Analysis and Design*, 2nd edn. John Wiley and Sons.
- SMITH, T. R. 2003 Low-dimensional models of plane Couette flow using the proper orthogonal decomposition. PhD thesis, Princeton University.
- SMITH, T. R., MOEHLIS, J. & HOLMES, P. 2005 Low-dimensional models for turbulent plane Couette flow in a minimal flow unit. *Journal of Fluid Mechanics* **538**, 71–110.
- TADMOR, G., LEHMANN, O., NOACK, B. R. & MORZYŃSKI, M. 2010 Mean field representation of the natural and actuated cylinder wake. *Physics of Fluids* **22** (034102).
- TAIRA, K. & COLONIUS, T. 2009 Three-dimensional flows around low-aspect-ratio flat-plate wings at low Reynolds numbers. *Journal of Fluid Mechanics* **623**, 187–207.
- TAIRA, K., ROWLEY, C. W. & COLONIUS, T. 2010 Lift enhancement for low-aspect-ratio wings with periodic excitation. *AIAA Journal* (**in press**).
- TOMBS, M. S. & POSTLETHWAITE, I. 1987 Truncated balanced realization of a stable non-minimal state-space reduction. *International Journal of Control* **46** (4), 1319–1330.
- TREFETHEN, L. N. & BAU, D. I. 1997 *Numerical Linear Algebra*. Society for Industrial and Applied Mathematics.

- TUCKERMAN, L. & BARKLEY, D. 2000 Bifurcation analysis for timesteppers. In *Numerical methods for bifurcation problems and large-scale dynamical systems, IMA Volumes in Applied Mathematics and its Applications*, vol. 19, pp. 453–466. Springer-Verlag.
- VARGA, A. 2000 Balanced truncation model reduction of periodic systems. In *Proceedings of the 39th IEEE Conference on Decision and Control*, pp. 2379–2384.
- VARGA, A. & VAN DOOREN, P. 2001 Computational methods for periodic systems – an overview. In *IFAC Workshop on Periodic Control Systems*, pp. 171–176. Como.
- VERRIEST, E. I. & GRAY, W. 2004 Nonlinear balanced realizations. In *Proceedings of the 43rd IEEE Conference on Decision and Control*.
- VERRIEST, E. I. & KAILATH, T. 1983 On generalized balanced realizations. *IEEE Transactions on Automatic Control* **28**, 833–844.
- VISWANATH, D. 2007 Recurrent motions within plane Couette turbulence. *Journal of Fluid Mechanics* **580**, 339–358.
- ZHANG, M. Q. & QIN, M. Z. 1993 Explicit symplectic schemes to solve vortex systems. *Computers & Mathematics with Applications* **26**, 51–56.
- ZHOU, K., DOYLE, J. C. & GLOVER, K. 1996 *Robust and Optimal Control*. New Jersey: Prentice-Hall.
- ZHOU, K., SALOMON, G. & WU, E. 1999 Balanced realization and model reduction for unstable systems. *International Journal of Robust and Nonlinear Control* **9** (3), 183–198.

ZIGLIN, S. L. 1980 Non-integrability of a problem on the motion of four point vortices. *Soviet Mathematics - Doklady* **21**, 296–299.